

# Electron Beam Induced Copper Deposition from Carboxylate Precursors and the Study of Underlying Growth Mechanisms

Présentée le 18 décembre 2020

à la Faculté des sciences et techniques de l'ingénieur  
Laboratoire des matériaux photoniques et caractérisation  
Programme doctoral en science et génie des matériaux

pour l'obtention du grade de Docteur ès Sciences

par

**Luisa BERGER**

Acceptée sur proposition du jury

Prof. V. Michaud, présidente du jury  
Prof. P. Hoffmann, Dr I. Utke, directeurs de thèse  
Prof. P. Swiderek, rapporteuse  
Prof. L. McElwee-White, rapporteuse  
Prof. A. Fontcuberta i Morral, rapporteuse



*"Whatever you choose to do, leave tracks. That means don't do just for yourself, because in the end it's not going to be fully satisfying. You will want to leave the world a little better for you having lived. There is no satisfaction (...) that's equal to knowing that you have made another's life, your community, a little better for your effort."*

*Ruth Bader Ginsburg*





# Acknowledgements

I would like to express my gratitude to my supervisors Dr. Ivo Utke for his invaluable supervision, help and support and Prof. Patrik Hoffmann for our fruitful discussions and his precious advice. I thank Dr. Johann Michler, who gave me the opportunity to work in his laboratory. I would also like to thank the members of my jury: Prof. Petra Swiderek, Prof. Lisa McElwee-White, Prof. Anna Fontcuberta i Morral and Prof. Véronique Michaud.

Furthermore, I want to thank my scientific collaborators Katarzyna Madajska, Prof. Iwona Szymańska and Dr. Katja Höflich for the excellent cooperation and work.

A special thank you goes out to my close colleague Jakub Jurczyk for his precious advice, tireless help, endless patience, countless hours in the lab and his dear friendship. I thank all former and current colleagues at Empa Thun for the heartwarming welcome and inclusion into the group, all collaborations and help. Shoutout to all the colleagues who became friends over the past four years. Especially, I would also like to thank Xavier, Lizzy and Janika for their emotional support and friendship throughout this journey.

Lastly, this thesis would not have been possible without my family: I thank Vini and his family, Fiona and Leandra and my Oma who were my personal cheerleaders over all these years. Special thanks go to my father and Regine for their unlimited support and to my mother for her deep belief in me and my abilities and constantly reminding me: "Eu posso tudo, eu sei tudo".

Thank you, Danke, Obrigada et Merci !



# Abstract

The fabrication of defined and high-quality metal nanostructures is an ongoing topic of research. Direct-write deposition of copper nanostructures is of great value for many fields of research and industrial applications. Focused electron beam induced deposition (FE BID) is an additive fabrication technique with extremely high resolution and versatility. Physisorbed, gaseous precursor molecules are locally dissociated by a finely focused electron beam resulting in volatile fragments which desorb and non-volatile fragments forming the deposit. When applying suitable deposition parameters, these deposits can be as small as the beam diameter and have ideally little to no contamination. For electron beam induced metal deposition, metal-organic compounds are chosen as precursors. However, organic ligand material is often co-deposited, which is detrimental to the deposit's properties.

This work addresses the study of the perfluorinated copper carboxylate  $[\text{Cu}_2(\mu\text{-O}_2\text{CC}_2\text{F}_5)_4]$  ( $\text{Cu}_2(\text{pfp})_4$ ) and its aminated derivatives  $\text{Cu}_2(\text{EtNH}_2)_2(\text{pfp})_4$  and  $\text{Cu}_2(\text{tBuNH}_2)_2(\text{pfp})_4$  as viable FE BID precursors. 25 at.% of copper was achieved with the amine free compound, and 15 at.% with each of the two aminated complexes. Based on the chemical analysis of the deposits, electron-induced dissociation paths were proposed for the adsorbed species, demonstrating the influence of the ligand chemistry and fragmentation on the deposit composition. In parallel, the perfluorinated silver carboxylate  $\text{Ag}_2(\text{pfp})_2$  was reported and compared directly to its copper equivalent. The silver complex yielded up to 74 at.% metal content and exhibited strong susceptibility to varying electron beam densities throughout the deposit.  $\text{Cu}_2(\text{pfp})_4$  did not manifest the same electron sensitivity. Theoretical models, combining analytical solutions with Monte Carlo simulations of primary and backscattered electrons were successfully fitted to the cross sections of deposits from both carboxylates, determining the growth regimes within a single spot deposit. Additionally, two previously reported  $\beta$ -diketonates,  $\text{Cu}(\text{hfac})_2$  and  $\text{Cu}(\text{tbaoc})_2$ , were directly compared to the other Cu(II) precursors with the aim to determine any dependence of the ligand size, electron density or dwell time on the deposit purity. The investigations concluded that the metal content rather depends on the chemistry of the metal-ligand bond than on the ligand size. This applies to both, the variation of ligands and the variation of the metal center.

Furthermore, two copper complexes,  $\text{Cu}(\text{hfac})_2$  and  $\text{Cu}_2(\text{pfp})_4$ , were investigated *in situ* with a dedicated, custom-made setup. The "eQCM" combines a low energy electron source (10-100 eV) with a quartz crystal microbalance and serves to study fundamental processes occurring during FE BI deposition. First results yielded the total dissociation cross section for each precursor at varying electron energies.

Finally, alternative approaches for the electron induced copper deposition from  $\text{Cu}_2(\text{pfp})_4$  were investigated. A two-step post-purification recipe of as-deposited material was reported to yield pure copper crystals (> 97 at.%). Additionally, direct electron beam lithography in a layer of condensed precursor was explored. This room temperature deposition approach yielded in lower metal contents but could potentially produce high resolution deposition.

KEYWORDS: copper, FEBID, carboxylates, electron-induced dissociation, dissociation mechanisms, metal-ligand chemistry, growth regime

# Zusammenfassung

Die Anfertigung definierter, hochqualitativer Metallnanostrukturen ist ein weiterhin aktuelles Forschungsthema. Die direkte Abscheidung von Kupfernanostrukturen ist von grossem Interesse für viele Forschungsbereiche und industrielle Anwendungen. Elektronenstrahlinduzierte Abscheidung (Focused electron beam induced deposition, FEBID) zählt zu den additiven Verfahren mit sehr hoher Auflösung und Flexibilität. Physisorbierte, gasförmige Ausgangsverbindungen werden lokal von einem fokussierten Elektronenstrahl dissoziiert und bilden dabei sowohl flüchtige Fragmente, die desorbieren, als auch nicht-flüchtige Fragmente, die schliesslich die Abscheidung bilden. Durch die Wahl geeigneter Abscheidungsparameter können diese Strukturen so klein wie der Elektronenstrahl werden und haben im Idealfall wenig bis keine Kontaminationen. Für die elektronenstrahlinduzierte Abscheidung von Metallen werden metallorganische Verbindungen als Ausgangsmoleküle gewählt wodurch häufig organische Liganden ebenfalls abgeschieden und so die Eigenschaften der Metallstruktur beeinträchtigt werden.

Diese Arbeit befasst sich mit der Untersuchung des perfluorierten Kupfercarboxylats  $[\text{Cu}_2(\mu\text{-O}_2\text{CC}_2\text{F}_5)_4]$  ( $\text{Cu}_2(\text{pfp})_4$ ) und seiner aminierten Derivate  $\text{Cu}_2(\text{EtNH}_2)_2(\text{pfp})_4$  und  $\text{Cu}_2(\text{tBuNH}_2)_2(\text{pfp})_4$  und ihrer Eignung als FEBID Ausgangsmoleküle.  $\text{Cu}_2(\text{pfp})_4$  erzielte Metallanteile von bis zu 25 at.% und die aminierten Derivate jeweils bis zu 15 at.%. Es wurden elektroneninduzierte Dissoziationsmechanismen für die adsorbierten Moleküle aller Kupferverbindungen aufgestellt und der Einfluss von Liganden und ihrer Fragmentierung auf die Abscheidungszusammensetzung gezeigt. Gleichzeitig wurde das perfluorierte Silbercarboxylat  $\text{Ag}_2(\text{pfp})_2$  untersucht und mit dem äquivalenten Kupferkomplex verglichen. Der Silberkomplex erzielte einen Metallgehalt von bis zu 74 at.% und reagierte empfindlich auf veränderte Elektronenstrahldichten in der Abscheidung. Analytisch gelöste Modelle wurden mit Monte Carlo Simulationen kombiniert und konnten für beide Carboxylate erfolgreich an die experimentellen Werte gefittet werden, sodass die jeweilige Wachstumsordnung den verschiedenen Regionen in Punktabscheidungen zugewiesen werden konnte. Zwei bereits bekannte  $\beta$ -Diketonate,  $\text{Cu}(\text{hfac})_2$  und  $\text{Cu}(\text{tbaoc})_2$ , wurden mit allen Cu-Carboxylaten verglichen, um mögliche Zusammenhänge zwischen Ligandengrösse, Elektronendichte oder Verweilzeit des Elektronenstrahls mit der Abscheidungszusammensetzung zu ermitteln. Aus den Untersuchungen wurde geschlossen, dass nicht die Ligandengrösse, sondern vielmehr die chemischen Eigenschaften der Metall-Ligandenbindung ausschlaggebend für die Zusammensetzung sind.

Weiterhin wurden die zwei Kupferkomplexe  $\text{Cu}(\text{hfac})_2$  und  $\text{Cu}_2(\text{pfp})_4$  *in situ* in einer eigens dafür aufgebauten Kammer untersucht. Die «eQCM» kombiniert eine Elektronenquelle (10-100 eV) mit einer Quarzkristall-Mikrowaage und untersucht grundlegende Prozesse während der FEBID Abscheidung. Erste Werte für den Gesamtdissoziationsquerschnitt für jede Ausgangsverbindung wurden berechnet.

Letztlich wurden alternative elektroneninduzierte Abscheidungstechniken mit  $\text{Cu}_2(\text{pfp})_4$  untersucht. Eine zweistufige Aufreinigung der ursprünglichen Strukturen zeigte die Bildung reiner Kupferkristalle (> 97 at.%). Zusätzlich wurde die direkte Bestrahlung des  $\text{Cu}_2(\text{pfp})_4$ -Kondensats geprüft. Diese Raumtemperaturabscheidung erzielte zwar niedrigere Metallkonzentrationen, dafür könnten zukünftig aber Abscheidungen mit höherer Auflösung erreicht werden.

STICHWORTE: Kupfer, FEBID, Carboxylate, elektroneninduzierte Dissoziation, Dissoziationsmechanismen, Chemie der Metall-Ligandenbindung, Wachstumsordnung

# Table of Contents

Acknowledgements .....	v
Abstract.....	vii
Zusammenfassung.....	ix
Table of Contents.....	xi
List of Figures .....	xiii
List of Tables.....	xx
Abbreviations and Symbols .....	xxi
<b>1 Introduction and Motivation .....</b>	<b>23</b>
1.1 Motivation and Scope of this Thesis.....	26
<b>2 Theoretical Background .....</b>	<b>29</b>
2.1 Focused Electron Beam Induced Deposition (FEBID) of Metals .....	29
2.1.1 <i>Electron-Solid Interaction</i> .....	30
2.1.2 <i>Continuum Model</i> .....	32
2.1.3 <i>Time dependent solutions for pulsed irradiation</i> .....	38
2.1.4 <i>The Impact of the Electron and Precursor Limited Regime on the Deposit</i> .....	40
2.1.5 <i>Process Parameters (dwell time, refreshment time, repetition, step sizes)</i> .....	42
2.2 Quartz Crystal Microbalance (QCM).....	43
<b>3 Experimental Methods.....</b>	<b>45</b>
3.1 Focused Electron Beam Induced Deposition (FEBID) .....	45
3.1.1 <i>Precursors</i> .....	45
3.1.2 <i>Set-Up: Precursor Delivery &amp; Heating, Stage Heating &amp; Manipulation</i> .....	45
3.1.3 <i>Beam Control, Lithography</i> .....	48
3.1.4 <i>Beam Size Determination</i> .....	50
3.2 Monte Carlo Simulations .....	51
3.3 Imaging with Scanning and Transmission Electron Microscopy.....	52
3.4 Chemical Analysis: EDX and Thin Film Correction .....	53
3.5 Atomic Force Microscopy and Deposit Dimensions .....	57
3.6 eQCM setup .....	57
<b>4 Focused Electron Beam Induced Deposition of Group 11 Elements: Silver and Copper from Perfluorinated Carboxylates .....</b>	<b>59</b>
4.1 Precursor Evaporation and Transport in the Gas Phase.....	59
4.2 Experimental Details.....	61
4.3 Results and Discussion.....	62
4.3.1 <i>Deposit Appearance and Chemical Analysis</i> .....	62
4.3.2 <i>Electron Induced Dissociation Paths of <math>\text{Ag}_2(\text{pfp})_2</math> and <math>\text{Cu}_2(\text{pfp})_4</math> in FEBID</i> .....	72
4.3.3 <i>Differences between <math>\text{Ag}_2(\text{pfp})_2</math> and <math>\text{Cu}_2(\text{pfp})_4</math></i> .....	75
4.4 Conclusion.....	77
<b>5 Copper(II) Compounds for Focused Electron Induced Deposition.....</b>	<b>81</b>
5.1 Copper precursors in Focused Electron Beam Induced Deposition .....	81
5.2 Comparing Cu(II) Carboxylate Derivatives and $\beta$ -Diketonates .....	82
5.2.1 <i>Influence of Inter- and Intramolecular Interactions on the FEBID Process</i> .....	84
5.2.2 <i>Deposit Morphology and Deposition Efficiency/Rate</i> .....	85

5.2.3	<i>Chemical Analysis – Local EDX Measurements and Quantification</i> .....	90
5.2.4	<i>Chemical Structure of Copper(II) Complexes and its Effect on Deposition</i> .....	92
5.2.5	<i>Elemental Ratios and possible Dissociation Behavior</i> .....	95
5.3	Conclusion.....	98
<b>6</b>	<b><i>In situ</i> monitoring of FEBID processes</b> .....	<b>101</b>
6.1	Experimental Details .....	101
6.2	Results and Discussion .....	102
6.3	Conclusion.....	105
<b>7</b>	<b>Alternative Approaches to High-Purity Metal Deposition:</b> .....	<b>107</b>
7.1	Post-Experiment Purification of FEBID structures .....	107
7.1.1	<i>Purification methods in FEBID</i> .....	107
7.1.2	<i>Post-Experiment Annealing in Reactive Gases</i> <sup>115</sup> .....	109
7.2	Resist-Based Lithography Techniques.....	113
7.2.1	<i>Electron Beam Lithography (EBL) and Focused Electron Beam Induced Deposition at Cryogenic Temperatures (cryo-FEBID)</i> .....	113
7.2.2	<i>Direct Electron Beam Lithography in a Positive Low-Volatility Precursor Resist</i> .....	115
7.3	Conclusion.....	127
<b>8</b>	<b>Conclusion and Outlook</b> .....	<b>131</b>
<b>9</b>	<b>Appendix: Supplementary Information</b> .....	<b>134</b>
9.1	EDX reference measurements for error estimation .....	134
9.2	Stratagem Thin-Film Correction.....	136
9.3	Parameter Space - Shape Simulation.....	139
9.4	eQCM setup .....	140
	<b>References</b> .....	<b>141</b>
	<b>Curriculum Vitae</b> .....	<b>153</b>



# List of Figures

Figure 1-1	Scheme on precursor choice for metal FEBID with respective challenges (red) and advantages/examples of suitable molecules (green). (a) ideal precursor: evaporated metal or metal salt. (b) inorganic and metalorganic compounds with small, volatile ligands. (c) metalorganic compounds with large organic ligands.....	24
Figure 2-1	Sketch of a typical FEBID set-up. Left: a SEM with electron gun, beam control, detector and internal GIS. Right: Sketch of the local deposition process on the substrate. Molecules are provided through the GIS needle (grey tube) and subsequently dissociated by the electron beam (teal) on the surface (green) into volatile and non-volatile fragments, forming a deposit (orange). .....	29
Figure 2-2	(a) Sketch of the trajectory of a PE beam in a solid, generating BSE and SE with $\lambda$ the mean free path of SE. SE1 generated from PE, SE2 generated from BSE. (b) Energy spectrum of SE and BSE generated in a solid when irradiated with an electron beam (PE) with a primary energy $E(PE)$ . (c) Spatial distribution of SE1 and BSE. All images based on <sup>51,52</sup> .....	30
Figure 2-3	(a) Monte Carlo simulation of electron trajectories of 20 keV Gaussian primary beam with $FW(99.9\%) = 425$ nm in a silicon bulk substrate. Blue: focused PE in vacuum and scattered in bulk substrate, red: emitted BSE, green: SE, some indicated by arrows. (b) Radial distribution of BSE (red) and PE (black) of this simulation. The $FW(99.9\%)$ of the PE beam and the theoretical $r_{BSE}$ (eq. (2-2)) are marked. Simulation of $1 \cdot 10^6$ PE, 200 trajectories from CASINO <sup>55</sup> displayed.....	32
Figure 2-4	(a) radial molecule density $n(r)$ against the distance to the beam center with different $\tau$ , calculated with equation (2-5). (b) radial growth rate $R(r)$ at different $\tau$ , calculated with equation (2-8). The radial electron flux $f(r)$ is plotted in red. Parameters set to typical experimental values in our thermionic emitter system: e-beam with $FWHM=180$ nm, $0.6$ nA, $\sigma=0.1 \text{ \AA}^2$ , $s=1$ , $J=1.52 \cdot 10^{14} \text{ cm}^{-2} \text{ s}^{-1}$ , $V=1.17 \cdot 10^{-22} \text{ cm}^3$ .....	34
Figure 2-5	(a) Radial distribution of the electron flux from a primary electron beam (PE, red) and the emitted backscattered electrons (BSE, blue) generated by the PE in a Si bulk substrate. This illustration shows furthermore the precursor limited (PL, greyblue) and electron limited (EL, orange) growth regimes within the radial distribution. The transition from PL to EL regime lies at the radius where the dissociation rate equals the molecule supply rate: $\sigma f(r) \approx sJ/n_0 + 1/\tau$ . (b) Sketch illustrating half a stationary spot deposit in top view with the center and halo deposit fabricated through the high electron flux in the center and low flux in the outer radii. The theoretical maximum BSE exit range $r_{BSE}$ at 20 keV in Si is marked with a dashed line.....	37
Figure 2-6	Serpentine deposition raster scheme for fabrication of a square deposit. The beam (greyblue) dwells for a given amount of time $t_d$ on one pixel, before moving to the next pixel with a defined step size $\Delta x$ (and $\Delta y$ at the end of the line). Each pixel can be replenished with fresh precursor molecules during a refreshment time $t_r$ . Figure simplified and based on <sup>8</sup> .....	38
Figure 2-7	Different graphs of equation (2-11) illustrating the time dependence of the deposition growth rate $R(t)$ . (a) Dwell time dependence with a fixed refreshment time of $t_r = 10$ ms with changing residence times $\tau$ . (b) Refreshment time dependence at a fixed dwell time $t_d = 100 \mu\text{s}$ with different $\tau$ . (c) Refreshment time dependence with fixed $\tau = 100$ ms and changing dwell times. Other parameters: $V = 1.17 \cdot 10^{-22} \text{ cm}^3$ , $s = 1$ , $J = 1.52 \cdot 10^{14} \text{ cm}^{-2} \text{ s}^{-1}$ , $n_0 = 1.37 \cdot 10^{14} \text{ cm}^{-2}$ , $\sigma = 0.1 \text{ \AA}$ , $f = 1.47 \cdot 10^{19} \text{ cm}^{-2} \text{ s}^{-1}$ .....	40

Figure 2-8	Schemes of deposit purity depending on the electron limited or precursor limited regime. (a) Dependence of the beam current. Deposits from $W(CO)_6$ deposited with a low beam current result to more ligand contamination. Those deposited with a high beam current lead to more ligand desorption and better deposit purity. Based on description from ref. <sup>58</sup> . (b) Two-species deposition scheme of $Co_2(CO)_8$ and hydrocarbons. (i) Precursor adsorption/desorption, (ii) initial electron irradiation forming a deposit. The precursor with the larger dissociation cross section is deposited preferentially (e.g. species A) – deposit is rich in A. (iii) Long dwell times deplete the precursor with the higher cross section (e.g. A), leading increased deposition rate of the other precursor B – deposit is rich in B. (iv) Short dwell times reset the system to initial deposition step, incorporating more species A. Figure (b) and description taken from and based on ref. <sup>15</sup> .	41
Figure 2-9	Scheme of silver deposition in (a) high electron density (PL regime). Ligands cannot desorb and are co-deposited in the high electron density. The deposit is more contaminated. (b) Deposition in low electron density (EL regime). Ligands and fragments can desorb before co-deposition. The deposit is cleaner. Scheme based on Ref. <sup>19</sup> .	42
Figure 2-10	Temperature dependency of AT-cut quartz crystals with different cutting angles $\vartheta$ . The AT-cut shows the least frequency change at room temperature. Temperature changes induce a frequency change that cannot be attributed to the mass change. Figure taken from Sauerbrey. <sup>71</sup>	44
Figure 3-1	$Cu(hfac)_2$ in a glass vial. Left: "pristine", hydrated state. The crystals are green. Right: anhydrous state. After evacuating the vial for several hours, crystal bound water is removed and the precursor changes color to dark blue.	45
Figure 3-2	Gas injection system (a) with needle and (b) without needle.	46
Figure 3-3	(a) Sketch of the positioning of the GIS nozzle with a 380 $\mu m$ opening (inner diameter), 200 $\mu m$ over the substrate and in lateral distance to the deposition area in a typical FEBID experiment. The deposition area includes the whole area, where multiple deposits are fabricated. (b) Simulation of the impinging molecule flux exiting from the nozzle using the parameters from a. The deposition area is marked in orange in a distance between 200 and 500 $\mu m$ from the nozzle exit. The deposition area lies within the regions where 6 - 9% of exiting molecules are available. Simulation parameters: $10^7$ molecules, 256 grid points, uptake coefficient (in nozzle) =0, needle length $l=4mm$ , nozzle angle $\alpha=70^\circ$ , height above substrate $h=200\mu m$ .	47
Figure 3-4	Lithography scan parameters, which can be controlled and defined by XENOS. This includes the shape (e.g. square with side length $L$ ), the step sizes $\Delta x$ and $\Delta y$ (pixel to pixel distance), the dwell time $t_d$ and the writing direction (black: serpentine). Alternative writing directions: (a) spiral, (b) line by line. The refreshment time $t_r$ is the time the beam takes to re-irradiate a pixel position after writing the pattern and it is directly linked to $t_d$ and the pattern size. Furthermore, the lithography system controls how often the pattern is written (repetitions, not shown).	48
Figure 3-5	(a) Scanning electron micrograph of the holey carbon TEM membrane with two 100px wide lines for intensity profiles. (b) Determination of the electron beam profile. The smoothened gray value intensity profile is plotted in grey and its first derivative in light red. The derivative was fitted with a Gaussian curve (solid red), giving the FWHM of the beam.	50
Figure 3-6	Monte Carlo Simulations of an electron beam with 3keV and 7keV interacting with an "CuCOF" and "AgCO" deposit on a silicon substrate. 500 electrons were simulated on an irradiation area of 200 nm diameter, similar to the area probed in the analysis. The	

	figures show 200 trajectories each. The SEM images show the spot deposits from $\text{Cu}_2(\text{pfp})_4$ and $\text{Ag}_2(\text{pfp})_2$ with the analysis positions and the size of the projection of the probed volume (top view). ....	54
Figure 3-7	Sketch of the QCM sensor head with the crystal surface perpendicular to the impinging electron beam.....	58
Figure 4-1	Molecular structure of (a) the $\text{Ag}_2(\text{pfp})_2$ dimer and $\text{Ag}(\text{pfp})$ monomer, (b) $\text{Cu}_2(\text{pfp})_4$ and its monomer. The oxidation state of the metal ions is marked. Both precursors are perfluorinated carboxylates and form dimers in the solid state. In the case of silver, dimers and monomers can co-exist in the gas phase, see text.....	60
Figure 4-2	Spot deposits from (a) $\text{Cu}_2(\text{pfp})_4$ on $\text{AlN}/\text{Si}$ (inset: $60^\circ$ tilt view of center) and (b) $\text{Ag}_2(\text{pfp})_2$ on nat. $\text{SiO}_2/\text{Si}$ . Overlay: radial flux distribution of PE (teal) and BSE (black) from MC simulations. (c) Higher magnification of the Cu deposit center. (d) Higher magnification of the Ag deposit center. Total electron dose for deposition: Cu $0.83\mu\text{C}$ @20keV, Ag $0.15\mu\text{C}$ @25keV. The yellow line marks the theoretical maximum exit range of BSEs at the respective beam energy. ....	62
Figure 4-3	EDX results from local measurements on the spot deposits. Filled: measured in the center of the structures; empty: measured in the halo regions of the structures. Left: fabricated from $\text{Cu}_2(\text{pfp})_4$ ; right: $\text{Ag}_2(\text{pfp})_2$ . The results are background and thin film corrected. PE energies: 3/16keV for Cu, 5/7/10keV for Ag. ....	63
Figure 4-4	Shape simulations of the (a) $\text{Cu}_2(\text{pfp})_4$ and (b) $\text{Ag}_2(\text{pfp})_2$ dot deposits using MC simulations of the radial BSE distribution and the AFM profile of corresponding dot deposits. The shape can be simulated for the growth rate $R(r)$ of the SE1 flux (red, generated from PE), the SE2 flux (blue, generated from BSE) and the sum of both (black, $f(\text{SE1}+\text{SE2})$ ). The shape was fitted to the AFM profiles (grey) by adjusting $\sigma$ , $\tau$ and $J$ . The parameters specific to this fit are noted in the respective graph. Note that the Ag-dot in this AFM featured a large crystal in the central region (arrows) and was not fitted. Other parameters used for simulation see in text. ....	65
Figure 4-5	Square deposits from $\text{Ag}_2(\text{pfp})_2$ with varying deposition parameters. (a) short $t_d$ , short $t_r$ , (b) long $t_d$ , long $t_r$ . The green line marks the region of the high magnification image shown next to each micrograph. Dose: electron dose per area; $t_d$ : dwell time per FWHM; rep.: number of frames repeated for deposition; $t_r$ : refreshment time per FWHM for precursor replenishment. ....	67
Figure 4-6	(a-d) TEM analysis of deposits from $\text{Cu}_2(\text{pfp})_4$ on a 50 nm thick $\text{SiN}_x$ membrane. (a) DF-STEM image of a 25 keV and 1.35 nA FEBID line. The line width is indicated in orange. Note the avoidance of the halo deposit. (c) BF-STEM image showing metal(oxide) crystallites within the FEBID deposit on the membrane. (d) HR-TEM image of two individual metal(oxide) grains on the membrane with distinct lattice planes. (d) FFT of ROIs on HR-TEM image with measured lattice plane angles (blue). (e-h) TEM analysis of deposits from $\text{Ag}_2(\text{pfp})_2$ on a carbon membrane. (e) DF-STEM image of a 25 keV and 0.5 nA FEBID line. The line width is indicated in orange. (f) BF-STEM image showing metal crystallites within the deposit. Twinning is marked with the red arrow. (g) HR-TEM image of two individual metal grains on the membrane with distinct lattice planes. (h) SAED pattern on the line deposit. The diffraction pattern clearly confirms crystallinity of the deposit. The fcc silver diffraction pattern (green) affirms the pure silver structure of the deposited crystallites.....	70
Figure 4-7	Proposed, simplified electron induced dissociation paths based on Table 4-2. (a) $\text{Ag}_2(\text{pfp})_2$ dissociation upon evaporation and upon electron irradiation in the center and halo region. (b.1) $\text{Cu}_2(\text{pfp})_4$ dissociation (non-oxidized center). The first dissociation scheme summarizes all pfp <sup>-</sup> ligands which can potentially leave intact. The second	

dissociation scheme illustrates the dissociation of the remaining ligand into the co-deposited carbonaceous matrix. An additional oxidation step occurring in ambient atmosphere over time  $t$  at room temperature is shown for Cu. (b.2) Note that the actual dissociation path may also occur via fragmentation steps of the intact ligands. Fragmentation mechanism based on measured ratio of elements. .... 73

- Figure 4-8 Local EDX line scan over two individual Ag particles on carbon membrane. Inset: The corresponding BF-STEM image and scan position. No oxidation is visible for the particles. .... 75
- Figure 4-9 (a) Electron withdrawal from  $\text{COO}^-$  group through  $-\text{CF}_2-\text{CF}_3$  chain, leading to harder Lewis base than non-fluorinated carboxylate, i.e. less orbital overlap with metal ion. (b) Electron withdrawal from C1-C2 bond through electronegative oxygen and fluorine, weakening the bond and releasing  $\text{CO}_2$ . (c) Electron withdrawal from C2 by  $-\text{COO}^-$  an,  $-\text{CF}_3$  and F, leading to fluoride release. .... 76
- Figure 5-1 Chemical structures of 5 different Cu(II) precursors as proposed by literature (see text). (a)  $\text{Cu}(\text{hfac})_2$  (b)  $\text{Cu}(\text{tbaoac})_2$  (c)  $[\text{Cu}_2(\mu\text{-O}_2\text{CC}_2\text{F}_5)_4]$  referred to as  $\text{Cu}_2(\text{pfp})_4$  and (d)  $[\text{Cu}_2(\mu\text{-O}_2\text{CC}_2\text{F}_5)_4(\text{EtNH}_2)_2]$  and  $[\text{Cu}_2(\mu\text{-O}_2\text{CC}_2\text{F}_5)_4(\text{tBuNH}_2)_2]$  with A being the N-bound amine ligands, the amine structures are depicted in the inset (blue). The corresponding evaporation temperatures  $T_{\text{GIS}}$  of each precursor is marked beneath the structure. .... 82
- Figure 5-2 Area deposits from different Cu(II) precursors: (a-b)  $\text{Cu}(\text{hfa})_2$ , (c-d)  $\text{Cu}(\text{tbaoac})_2$ , (e-f)  $[\text{Cu}_2(\text{pfp})_4]$ , (g-h)  $[\text{Cu}_2(\text{pfp})_4(\text{EtNH}_2)_2]$  and (i-j)  $[\text{Cu}_2(\text{pfp})_4(\text{tBuNH}_2)_2]$ . The respective total electron dose of each structure, as well as the tilt view ( $60^\circ$ ) are noted. All structures were deposited at 20 keV primary energy and a beam current of 0.59 nA (W-filament) and 1.35 nA (FEG). For each source, the effective dwell times  $t_{d,\text{eff}}$ , as well as the electron dose per frame are noted in the image. Note that the pillar deposit at the corner of each I-deposit originates from the scanning strategy of the instrument, as the beam pauses there after each frame (see Methods). If not noted differently, all scale bars show 1  $\mu\text{m}$ . .... 86
- Figure 5-3 Deposition rates of all five Cu(II) precursors with different sources and effective dwell times  $t_{d,\text{eff}}$ . .... 88
- Figure 5-4 Overview image in tilted view ( $60^\circ$ ) of the  $\text{Cu}(\text{hfac})_2$  sample fabricated with the W-filament SEM. The pillars (black arrows) were programmed to be situated in distance to the squares (white arrows) as "waiting spots" to avoid pillar formation at the corner of the structure. .... 89
- Figure 5-5 Relevant binding modes for coordination within  $\text{Cu}_2(\text{pfp})_4/[\text{Cu}_2(\text{pfp})_4(\text{RNH}_2)_2]$   $\text{R}=\text{Et}, \text{tBu}/\text{Cu}$   $\beta$ -diketonates and  $\beta$ -ketosterates. .... 92
- Figure 5-6 Chemical structure of  $\text{Cu}(\text{tbaoac})_2$  with two types of Cu-O bonds. Grey: ester moiety, weaker Cu-O bond and possible rearrangement reaction (Section 5.2.5). Blue: carbonyl moiety, stronger Cu-O bond. .... 93
- Figure 6-1 QCM mass rates  $R_m$  for  $\text{Cu}_2(\text{pfp})_4$  (black) and  $\text{Cu}(\text{hfac})_2$  (blue) for (a) constant beam current  $I_B = 4 \mu\text{A}$  and for (b) constant beam energy  $E_B = 100 \text{ eV}$ . All experiments were conducted at  $2.7 \cdot 10^{-6} \text{ mbar}$  working pressure. For  $\text{Cu}_2(\text{pfp})_4$  the chamber was heated to  $140^\circ\text{C}$ . Mass rates have an uncertainty of  $\pm 0.06 \text{ pg/s}$ . .... 102
- Figure 6-2 Total deposition cross sections for  $\text{Cu}_2(\text{pfp})_4$  (black) and  $\text{Cu}(\text{hfac})_2$  (blue) in dependence of the primary beam energy at  $I_B = 4 \mu\text{A}$ . .... 104
- Figure 6-3 QCM adsorption and desorption measurements of  $\text{Cu}_2(\text{pfp})_4$  at  $135^\circ\text{C}$  (1) precursor adsorption on a clean crystal. 16.5 monolayers of dimeric precursor were adsorbed. No desorption was observed. (2) New dosing of precursor on physisorbed multilayers

	leads to adsorption of an additional monolayer. (3) FEBID: Electron irradiation with 100 eV and 6 $\mu$ A lead to molecule dissociation and the desorption of probably 8 monolayers of pfp <sup>-</sup> ligands. (4) Readsorption of another 5 monolayers of precursor on the deposit.....	105
Figure 7-1	Spot deposit on SiO <sub>2</sub> /Si (a) as-deposited with 20 keV for 60min, with a relatively smooth and uniform center. A scanning window from previous observation is visible. (b) After annealing for 4h in O <sub>2</sub> flow at 250°C, the smooth matrix is partly removed. (c) After annealing for 15h in a reducing gas mixture, large faceted crystals appear. The green star marks the point of local EDX measurement to prove the presence of pure copper (95 at. %). The orange dashed line marks the theoretical BSE range of this deposit. The graph shows the EDX spectra of deposits from Cu <sub>2</sub> (pfp) <sub>4</sub> at different processing steps. The intensity was normalized to the Si peak. Quantification is summarized in Table Table 7-1. ....	109
Figure 7-2	SEM images showing a line deposited from Cu(hfa) <sub>2</sub> and subsequently annealed at 400°C in the same reducing gas atmosphere as the other structures (2% H <sub>2</sub> / 98% N <sub>2</sub> ). (a) overview image of the right end of the line deposit after annealing. (b) high magnification image of the region marked in a. The table shows EDX quantification results of this line in the as deposited and annealed state. ....	110
Figure 7-3	Sketch of the electron beam lithography (EBL) and ice lithography (IL) process with a positive resist. (a) A resist (pink) spin-coated (EBL) or condensed (IL) onto the substrate. (b) Electron beam irradiation of the resist, changing its solubility (EBL) or evaporating it (IL). (c) EBL: Development of the pattern with a suitable solvent, removing the irradiated part of the resist. (d) Metal thin film deposition on the full sample (via evaporation or electrochemical process). (e) Lift-off process of surplus metal by removing non-irradiated resist with a solvent (EBL) or substrate heating ("melt-off", IL). (f) Final metal structure on the substrate. ....	114
Figure 7-4	Irradiation Pattern of DEBL structures shown in this chapter. All electron doses are noted. ....	116
Figure 7-5	Experimental scheme of Direct EBL in a Cu <sub>2</sub> (pfp) <sub>4</sub> resist. (a) Precursor evaporation through GIS on a cold substrate. (b) Photo of the precursor condensate ("resist"). (c) Electron irradiation of the resist. (d) Pattern development by rinsing for 2 min in ethanol (EtOH) or heating the substrate for precursor evaporation. (e) Optical (upper) and SEM (lower) images of four irradiated structures after development in EtOH. The structures were written in differently thick condensate (gradient center to outside = thick to thin = I to IV). ....	117
Figure 7-6	DEBL structures from Cu <sub>2</sub> (pfp) <sub>4</sub> on a SiO <sub>2</sub> (nat.)/Si substrate after development in EtOH. The shown structures are 5x5 $\mu$ m <sup>2</sup> squares and a dot array with varied e-doses irradiated in (a,c,e) thick and (b,d,f) thin condensate. (a-b) SEM images of four squares deposited with increasing e-dose (left to right). The inset shows the tilted view of parts of the structure. (c-d) AFM measurements of the square deposits with profiles and a 3D image. The average thickness of the structures is marked in the graph. (e-f) SEM images of the dot arrays deposited along with the squares. The e-dose decreased from top to bottom, within each line the dose is constant. The last (right) dot in each line is a long time exposure of 30 ms. The right image shows each array in zoom and tilted view. In (e) delamination of the irradiated condensate is visible. Strongly discernible halos are observed for all structures. The halo sizes i, ii and iii in comparison to the maximum BSE exit radius $r_{BSE,Si}$ are marked in (a-b). ....	120
Figure 7-7	EDX quantification results of the DEBL structures developed (a) in EtOH and (b) by annealing HV. The EDX spectra were recorded locally with 3 keV in within the structure	

	8_4 (filled symbols) and in its respective halo (empty symbols). The position of spectra collection is noted in the inset. The thickness of each deposited structure was determined with AFM and correspond to regions I-IV as in Figure 7-5e. The pristine precursor values are noted for comparison as dashed lines. Note that the x-axis in (b) is shown as logarithmic scale for better illustration of the thin structures. Atomic concentrations have an uncertainty of $\pm 5$ at.% (not noted in this graph).....	121
Figure 7-8	DEBL structures from $\text{Cu}_2(\text{pfp})_4$ on a $\text{SiO}_2(\text{nat.})/\text{Si}$ substrate after development via thermal resist evaporation in HV (substrate heated to $T_s = 190^\circ\text{C}$ ). Left: SEM images of the structures. The halo radii are indicated. Additional SEM image of Square 1 with high magnification image of the lower left corner. Right: AFM image and profile of square 8_4. (a) Results of the thickest resist region (I) with squares 8_1-4 (inset: $60^\circ$ tilt image) and square 1 (c.f. Figure 7-4). The green arrow indicates a copper crystal in the non-irradiated region. (b) Results of the same structures in the thinnest region of the condensate (IV). .....	124
Figure 7-9	EDX spectra of non-irradiated areas in proximity to irradiation fields I-IV (HV annealed sample). Green spectrum: Clean $\text{SiO}_2(\text{nat.})/\text{Si}$ surface was measured outside the condensate area for comparison. ....	123
Figure 7-10	Post-Purification of DEBL structures in region I. (a) The as-deposited structure after development in EtOH. (b) The oxidized structure after 3h in oxygen flow at $300^\circ\text{C}$ . (c) The reduced structure after 3h in form gas at $400^\circ\text{C}$ . Large clusters have formed (see high magnification region below. The graph shows the quantification results of local EDX measurements at each processing step. The empty black data points refer to the local EDX measurement of a large cluster (see high magnification image). They consist of pure copper (96 at.%).....	126
Figure 9-1	EDX reference measurements of Malachite ( $\text{Cu}_2(\text{CO}_3)(\text{OH})_2$ ). (a) Two exemplary EDX spectra of Malachite recorded at 3 keV (blue) and 16 keV (orange). (b) Chemical composition with error bars. The quantification results from EDAX Genesis software (standardless) are within the black error bars (maximum deviation from literature value) in comparison to literature values (black squares, from <a href="http://www.webmineral.com/data/Malachite.shtml">www.webmineral.com/data/Malachite.shtml</a> ). Measured quantification results for Cu, C and O do not exceed a deviation of 5.5 wt.% (4.1 at.%), 1.9 wt.% (3.4 at.%) and 4.2 wt.% (3.2 at.%) respectively.....	134
Figure 9-2	(a) Photograph of a Malachite disk used for EDX. (b) Photograph of the Malachite disk attached and covered with silver paste on an Al-SEM holder. (c) SEM image of the malachite reference sample. The silver paste is visible as well as surface charging arising during electron irradiation.....	135
Figure 9-3	SEM image of the malachite sample in comparison to the optical image (inset). The color differences correspond to different porosity.....	135
Figure 9-4	(a) Thin film thickness $d$ calculated by Stratagem in dependence of a given film density $\rho$ at fixed and variable composition. (b) Deviation of the thin film composition calculated by Stratagem in dependence of a given film density $\rho$ at fixed film thickness $d = 99$ nm (based on AFM measurements). Deviation from $c(\rho = 3 \text{ g/cm}^3)$ as set for all results in this work. ....	136
Figure 9-5	Composition difference (at.%) of various deposits when comparing background subtracted Stratagem results to EDAX results without substrate signal: EDAX quantification result $c(\text{EDAX}) - c(\text{Stratagem})$ . The largest deviations arise for thin halo Ag deposits (red arrows). ....	138

Figure 9-6	Shape simulations for (a-c) $\text{Cu}_2(\text{pfp})_4$ and (d-f) $\text{Ag}_2(\text{pfp})_2$ dot deposits with varying parameters $\sigma$ and $\tau$ . (a and d) The upper panels illustrate the best fit used in Chapter 4.3.1. (b and e) The middle panels illustrate another set of parameters with a good fit. (c and f) The lower panels display two parameter sets each where $\sigma$ and $1/\tau$ from (a/d) were multiplied with the same factor $x$ : $x\sigma$ and $x/\tau$ . (c) left: $x=4$ , right: $x=1/3$ ; (f) left: $x=5$ , right: $x=5/6$ .....	139
Figure 9-7	Drawing of the eQCM chamber. ....	140

# List of Tables

Table 2-1	Some typical values for molecule and electron fluxes, cross sections, residence times and coverages in FEBID experiments with corresponding rates. ....	35
Table 3-1	FWHM and FW(99.9%) of both deposition instruments for beam settings used in deposition. ....	51
Table 3-2	Deposited elements and their characteristic X-Ray energies detected in EDX. ....	53
Table 4-1	Parameters for shape simulation and corresponding transition radius $r_{trans}$ between EL and PL growth regime. ....	66
Table 4-2	Detailed EDX quantification results of the 2D structures from Figure 4-5 with varying parameters. Dose: electron dose per area; $t_d$ : dwell time per FWHM; $t_r$ : refreshment time per FWHM. ....	68
Table 4-3	Elemental ratio of deposits in the center and halo region derived from EDX quantification results (Figure 4-3) and normalized to two metal atoms.* Desorbing species were determined from the difference between pristine precursor and as deposited structures. For $Cu_2(pfp)_4$ only the central measurement is considered, as this is the non-oxidized structure. ....	72
Table 4-4	Classification of the ions forming the precursor complexes into the HSAB theory. ....	77
Table 5-1	Quantification results from local EDX measurements performed on area deposits fabricated with different effective dwell times $t_{d,eff}$ from four different Cu(II) precursors as specified in Figure 5-2. Each precursor was deposited with two different electron sources (W-filament, FEG) and two effective dwell times $t_{d,eff}$ each. <sup>a</sup> ....	90
Table 5-2	List of investigated Cu(II) compounds with corresponding elemental ratios of the pristine precursor, the as deposited structures and desorbing species, as well as the respective evaporation temperatures $T_{GIS}$ and experimental substrate temperatures $T_S$ , which were measured during deposition. The as deposited data was derived from local EDX measurements and the elemental ratios of desorbing species from the difference of pristine precursor and as deposited ratios. ....	95
Table 6-1	Thin-film and background subtracted EDX quantification results of QCM crystals after electron induced deposition with one of the two Cu(II) precursors. ....	103
Table 7-1	Background and thin film corrected EDX quantification results of three dot deposits (on $SiN_x/Si$ bulk) measured in the central pillar (from Chapter 4.3.1) and quantification results of one dot deposit during the purification process (on $SiO_2/Si$ ) measured in the center (c.f. Figure 7-1). All spectra were measured at 3 keV primary beam energy. ....	111
Table 7-2	Halo radii as measured from squares 8_4 in Figure 7-6 and Figure 7-8. ....	118
Table 9-1	Chemical composition of Malachite ( $Cu_2(CO_3)(OH)_2$ ) measured in 8 regions (M01-M08) in comparison to literature values. The values are plotted in Figure 9-1b. ....	135



# Abbreviations and Symbols

## Abbreviations

AFM	Atomic force microscopy
ALD	Atomic layer deposition
BF-STEM	Bright field scanning transmission electron microscopy
BSE	Backscattered electron
CVD	Chemical vapor deposition
DEA	Dissociative electron attachment
DEBL	Direct electron beam lithography
DF-STEM	Dark field scanning transmission electron microscopy
DI	Dissociative ionization
e-dose	electron dose
e-flux	electron flux
EBL	Electron beam lithography
EDX	Energy dispersive X-ray spectroscopy
EI-MS	Electron impact mass spectrometry
EL, PL	Electron flux limited regime, Precursor flux limited regime
FEBID	Focused electron beam induced deposition
FEG	Field emission gun
FIB	Focused ion beam
FW(99.9%)	Full width comprising 99.9% of all electrons (Gauss beam size)
FWHM	Full width at half maximum
GIS	Gas injection system
HR-TEM	High resolution transmission electron microscopy
HSAB	Hard soft acid base theory
MC	Monte Carlo (Simulation)
PE	Primary electron
PVD	Physical vapor deposition
QCM	Quartz crystal microbalance
SE, SE1, SE2	Secondary electron, type 1 (generated by PE), type 2 (generated by BSE)
SEM	Scanning electron microscope
T <sub>GIS</sub>	Temperature of gas injection system
T <sub>S</sub>	Temperature of substrate
ToF-SIMS	Time of flight secondary ion mass spectrometry
UHV	Ultra-high vacuum
Y(SE, BSE)	Secondary or backscattered electron yield (per primary electron)

## Ligands

EtNH <sub>2</sub>	ethylamine
hfac <sup>-</sup>	hexafluoroacetylacetonate
pfp <sup>-</sup>	pentafluoropropionate
tbaoac <sup>-</sup>	tert-butyl acetoacetate
tBuNH <sub>2</sub>	tert-butyl amine

## Symbols

$a$	[cm]	standard deviation Gauss beam
$A_{\text{mol}}$	[cm <sup>2</sup> ]	Molecule area
$\Delta x, \Delta y$	[nm]	Step size in x or y direction
$e_0$	[C]	elementary charge ( $e_0 = 1.602 \cdot 10^{-19}$ C)
$f(r)$	[cm <sup>-2</sup> s <sup>-1</sup> ]	radial electron flux
$I_p$ or $I_B$	[A]	(Primary electron) beam current
$J$	[cm <sup>-2</sup> s <sup>-1</sup> ]	Precursor molecule flux
$M$	[g/mol]	Molecular mass
$N_A$	[mol <sup>-1</sup> ]	Avogadro Number ( $N_A = 6.022 \cdot 10^{23}$ mol <sup>-1</sup> )
$n(r)$	[cm <sup>-2</sup> ]	radial adsorbate density
$n_0$	[cm <sup>-2</sup> ]	adsorbate density
$r$	[nm]	radius from beam center
$r_{\text{BSE}}$	[nm]	theoretical maximum exit radius of backscattered electrons
$R(r, t)$	[nm/s]	radial or time dependent deposition rate (also: growth rate)
$\rho$	[g/cm <sup>3</sup> ]	material/deposit/precursor density
$s$	[-]	physisorption probability
$\sigma$	[cm <sup>2</sup> ]	dissociation cross section
$t_d, t_{d,\text{eff.}}$	[s]	dwelt time, effective dwelt time (per FWHM)
$t_r$	[s]	refreshment time
$\tau$	[s]	residence time
$V$	[cm <sup>-3</sup> ]	volume of deposited material
$V_{\text{mol}}$	[cm <sup>-3</sup> ]	molecule volume

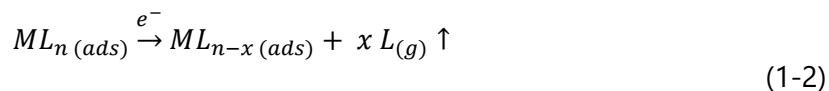
# 1 Introduction and Motivation

The fabrication of metal structures in the nanoscale is still a growing topic in micro- and nanotechnology. Also, physical research and material sciences are interested in nanometer sized patterns and structures to gain more insight in semiconductors, magnetic materials and metal compounds for different sensor applications. To fabricate such structures, often high-resolution top-down or bottom up lithography techniques are used, such as electron beam lithography. However, even advanced lithography techniques bear disadvantages such as multi-step processing, limited process monitoring and the restriction to flat substrates. Furthermore, it is reaching its limits in lateral resolution, making the fabrication of sub-10 nm structures extremely difficult.<sup>1,2</sup>

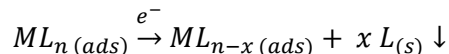
In the family of electron-based lithography, focused electron beam induced deposition (FEBID) presents a direct-write, additive technique. It has a high lateral resolution down to the nm range and the possibility to fabricate complex 2D and 3D structures.<sup>3-7</sup> Hereby, gaseous precursor molecules are introduced into the chamber of a conventional scanning electron microscope (SEM) using a gas injection system (GIS).<sup>8-10</sup> The molecules adsorb reversibly on the sample substrate and are dissociated locally where the electron beam interacts with the substrate. The intramolecular bonds of the precursor molecules are cleaved by electrons, forming volatile fragments which desorb and are pumped away, as well as non-volatile fragments forming the deposit in the desired shape. A variety of materials and metals could be deposited with this technique.<sup>11,12</sup>

Of interest in this work will be the direct deposition of metal structures, in specific the deposition of the two Group 11 metals: silver and copper. The fabrication of pure metal FEBID deposits has shown many challenges in the past. From the large number of metals and transition metals, ranging from titanium over manganese to noble metals like gold, only a small number has successfully been deposited in high purities: Au,<sup>13,14</sup> Co,<sup>15,16</sup> Fe<sup>17</sup> and Si<sup>18</sup> with ~94–100 at. %, Ag<sup>19</sup> with 75 at. % and W<sup>20</sup> with 66 at. %. This is due to the small number of precursors, that have been synthesized or used so far, which are suitable for FEBID.

Impurities in FEBID structures usually arise from ligand co-dissociation in the FEBID process, and to some extent from hydrocarbons and water present in the background of the SEM chamber. While background contamination can only be suppressed by the use of ultra-high vacuum setups, a feature most SEMs do not offer, co-dissociation can be limited by suitable precursor design.

Precursor adsorption and (initial) electron induced dissociation<sup>21</sup>

or



Equations (1-1) and (1-2) describe the adsorption and electron induced dissociation of the precursor molecule as proposed by Ref. <sup>21</sup>. Ideally, the electron induced dissociation of the adsorbed precursor molecule can lead to the ejection of intact ligands, which are volatile themselves (Equation (1-2)). However, the electron irradiation can also lead to the fragmentation and deposition of the ligand ( $L_{(s)}\downarrow$ ), leading to the contamination of the deposited structure with organic material. In order to achieve pure metal structures with FEBID, the co-deposition should be avoided. Therefore, specific precursor design for electron induced deposition is desired. Prospective precursor design which is based on dissociation mechanisms observed in UHV surface studies was summarized.<sup>21-23</sup> The scheme in Figure 1-1 describes the line of thoughts on the search for the ideal FEBID precursor compound.

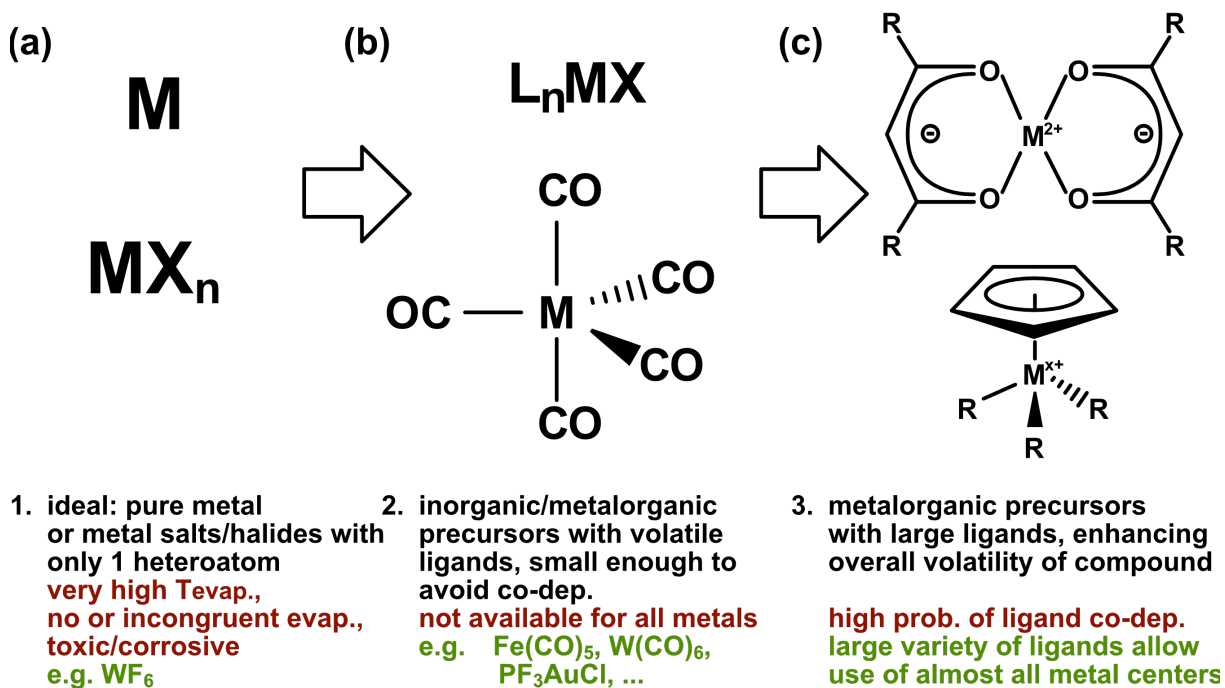


Figure 1-1 Scheme on precursor choice for metal FEBID with respective challenges (red) and advantages/examples of suitable molecules (green). (a) ideal precursor: evaporated metal or metal salt. (b) inorganic and metalorganic compounds with small, volatile ligands. (c) metalorganic compounds with large organic ligands.

In order to prevent any contamination, one could suggest the use of pure metal or metal salts. The first option drops out immediately, as vaporized metals could not be dissociated locally on the substrate by the electron beam, and a uniform metal layer would be achieved. This

technique, however, is better known under the name of physical vapor deposition (PVD). Metal halides can be used as precursors.  $\text{WF}_6$  has been used successfully for the deposition of high-purity tungsten structures at room temperature.<sup>20</sup> Elevated substrate temperatures, however, lead to etching of the  $\text{SiO}_2$  substrate, describing one of the drawbacks of metal halides – they are often corrosive and toxic and therefore undesirable in the use for FEBID.<sup>8</sup> Furthermore, many metal salts have very high evaporation temperatures or evaporate incongruently, limiting the reproducibility.

Therefore, the use of inorganic or metalorganic complexes was investigated (Figure 1-1b). As described by Spencer et al., FEBID precursors should have a small number of ligands which can desorb either by electron irradiation (e.g. CO or halides) or thermal processing (e.g.  $\text{PF}_3$ ).<sup>21</sup> This led to a variety of useful precursors, such as iron and cobalt carbonyls<sup>15–17</sup> forming exceptionally pure deposits. Cisplatin (*cis*- $\text{Pt}(\text{NH}_3)_2\text{Cl}_2$ ) showed to be a potential Pt precursor<sup>24,25</sup> due to the presence of  $\text{NH}_3$ . Under electron irradiation it probably formed reactive hydrogen species, which removed the halide from the deposit. In contrast, chlorine contamination could not be fully removed from the hydrogen-free, carbonyl analogue  $\text{Pt}(\text{CO})_2\text{Cl}_2$ .<sup>26</sup> The inorganic gold precursors  $\text{PF}_3\text{AuCl}$ <sup>13</sup> and  $\text{AuCl}(\text{CO})$ <sup>14</sup> resulted in pure gold structures. Unfortunately, these precursors are extremely air, temperature, moisture and light sensitive, with very short shelf times, making them difficult to use. Small metalorganic gold complexes, which were more stable did not yield as high metal purities.<sup>27</sup> Overall, it should be kept in mind that not all metals yield useful precursors with inorganic ligands such as presented.

Hence, larger metalorganic complexes are explored (Figure 1-1c). Most of the precursors are recruited from the large library of chemical vapor deposition (CVD) or atomic layer deposition (ALD), because these metal-organic compounds have one important feature required in both, CVD/ALD and FEBID: they are volatile and can be transported as intact molecules in the gas-phase from the reservoir into the deposition chamber and onto the sample substrate. A frequently used metalorganic precursor in FEBID is  $\text{MeCpPtMe}_3$ , a platinum precursor utilized in commercially available FEB/FIB systems to form capping layers prior to FIB milling. This precursor results in pure Pt films in CVD in the presence of  $\text{H}_2$ ,<sup>28</sup> but FEBID structures only contain 22 at.% platinum.<sup>8</sup> While the metal-ligand bonds were designed to dissociate thermally in the CVD process, electron induced dissociation in the FEBID process decomposed the larger, organic ligands, which form the contamination of the metal deposits. This is caused by the non-selective bond cleavage during FEBID. A delicate balance between sufficient volatility and little possibility for ligand dissociation has to be found. Recently, new design approaches for small, metalorganic gold precursors were reported, showing that larger halide (or other anionic) ligands increased volatility and the choice of a suitable electron donor ligand increased the compound stability.<sup>23,29</sup> However, it should be noted, that even if a suitable ligand was determined for one metal, this does not always apply to different metals, i.e. the ligands of  $\text{Au}(\text{I})$  complexes do not necessarily lead to similar results with  $\text{Cu}(\text{I})$ . Even though a study of various metal hexafluoroacetates ( $\text{M}(\text{hfac})_2$ ) identified no difference in dissociation,<sup>30</sup> the comparison of different metal carbonyls showed changing deposition results: While  $\text{Fe}(\text{CO})_5$

and  $\text{Co}_2(\text{CO})_8$  yielded high-purity metal deposits,<sup>15–17</sup>  $\text{W}(\text{CO})_6$  resulted in lower metal contents of about 55 at.%.<sup>31</sup> The chemical difference of the transition metals can lead to different dissociation behavior and CO incorporation. This might hold true for other metalorganic compounds and should be kept in mind, when choosing a compound for deposition.

One particularly interesting material which was yet not fully investigated in FEBID is copper. Its excellent properties such as high electrical conductivity, superior to aluminum and tungsten, make copper a promising candidate not only in small-scale electronics but also for mesoscopic physics such as electron transport investigations. Commonly, copper is deposited with chemical vapor deposition (CVD) or physical vapor deposition (PVD) techniques. Both processes have a relatively high throughput and result in pure copper deposits. However, when high lateral resolution and conformality are demanded, these techniques do not give the desired results.

A variety of metal-organic copper precursors has been investigated before, not resulting in pure copper without post-deposition treatment. Up until now, metal contents in as deposited structures did not exceed 25 at.%.<sup>32–36</sup> The incorporation of organic ligand material in the deposit, by insufficient fragment desorption or unintended ligand cross-linking, still poses a major challenge. The dissociation mechanisms of adsorbed species in FEBID were little investigated. Mostly, gas-phase studies or surface science studies of condensed copper precursors were performed so far.<sup>37–39</sup>

As explained above, the typical FEBID approach does not include the condensation of the precursor molecules, nor the ionization or dissociation of gas-phase species. It targets reversibly adsorbed molecules which get replenished continuously during the deposition event. Therefore, *in situ* mass sensing during the FEBID process can shed light on mechanisms that were not accessible by the aforementioned studies. Quartz crystal microbalances (QCM) are a common tool to monitor thin film deposition and are frequently applied in vapor deposition techniques such as ALD.<sup>40</sup> Apart from uniform thin film deposition, QCMs were also implemented in electron and ion beam induced deposition processes to determine deposition rates and cross sections,<sup>41,42</sup> observe precursor adsorption (chemisorption vs. physisorption),<sup>43–45</sup> or autocatalytic growth.<sup>46</sup> The QCM proved to be a versatile tool to investigate mechanisms which are crucial for FEBID.

## 1.1 Motivation and Scope of this Thesis

In order to achieve pure copper deposits in a direct-write approach, new metal-organic complexes were investigated as FEBID precursors. The influence of electron beam exposure and precursor refreshment on deposit composition is a little investigated topic. So is the inherent issue of fast oxidation of copper nanostructures in atmosphere. Dissociation mechanisms of the FEBID process can serve as a lead to explore the new precursor design rules beyond the surface science and gas-phase approaches in controlled environments.

This work aimed to investigate these mechanisms with the help of common chemical analysis methods, such as energy dispersive X-ray spectroscopy (EDX). The qualitative and quantitative analysis of the deposit composition, the deposit shape as well as growth rates were combined with *in situ* mass sensing techniques and theoretical FEBID models to elucidate the dissociation path of both, novel and known metal-organic copper precursors.

Furthermore, this work studied the possibilities of fabricating pure copper structures using alternative strategies, including post-deposition purification and an unconventional resist-based lithography approach.





## 2 Theoretical Background

### 2.1 Focused Electron Beam Induced Deposition (FEBID) of Metals

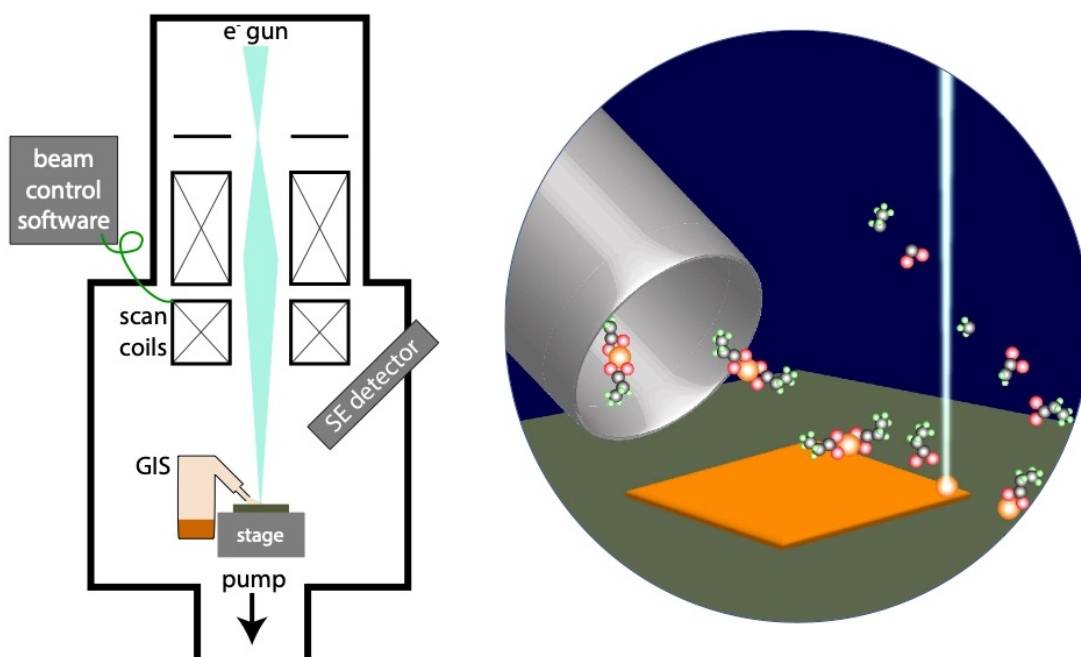


Figure 2-1 Sketch of a typical FEBID set-up. Left: a SEM with electron gun, beam control, detector and internal GIS. Right: Sketch of the local deposition process on the substrate. Molecules are provided through the GIS needle (grey tube) and subsequently dissociated by the electron beam (teal) on the surface (green) into volatile and non-volatile fragments, forming a deposit (orange).

Gas-assisted focused electron beam induced deposition (FEBID) describes a technique for the direct-write fabrication of micro- and nanoscale structures with the electron beam of a scanning electron microscope (SEM). Precursor compounds in a reservoir, the gas injection system (GIS), are evaporated and introduced into the SEM chamber through a small capillary or needle. The molecules physisorb on a substrate of choice and are irradiated by the primary electron beam (PE beam). A dedicated lithography software or the internal SEM scanning system controls the PE beam, fabricating structures via the local dissociation of the precursor molecules.

Initially, electron beam induced deposition was observed as an unintentional side effect in the early stages of transmission and scanning electron microscopy. Hydrocarbons present in the residual gas of the early vacuum chambers adsorbed to the surfaces and were dissociated into non-volatile products in the electron optics and the area of observation.<sup>47</sup> In the 1960s first reports on the potential of this technique arose.<sup>48,49</sup> Nowadays, the contamination through hydrocarbons is avoided by the use of oil-free pumping systems with turbomolecular pumps and a large variety of precursors was introduced. The ongoing research on precursor design

within the FEBID community allow the deposition of numerous materials ranging from insulators/oxides to metals and metal alloys.<sup>12,50</sup>

This chapter will discuss the fundamentals of FEBID, introducing relevant aspects such as the electron-solid interaction, the physical models describing the deposition, processing parameters and their effects on deposit shape and composition.

### 2.1.1 Electron-Solid Interaction

In a SEM, electron beams are generated in an electron source and are focused by a series of lenses to one point on the substrate or target irradiating it with a certain energy. Electron sources can be thermionic emitters (tungsten filaments) or field emission guns (FEG). The electron beam typically has a diameter between a few nanometers and several tens of nanometers and an energy between 1 and 30 keV.

For illustrative reasons, the following part will describe the interaction of a single PE with the solid target as depicted in Figure 2-2a. When arriving at the sample and entering the substrate, the PE immediately starts interacting with the solid. These interactions can be divided into elastic and inelastic collisions. Elastic collisions describe the repulsive or attractive interaction with the sample's atom nuclei or atomic electrons. This interaction results in a trajectory deviation but no energy loss of the PE.

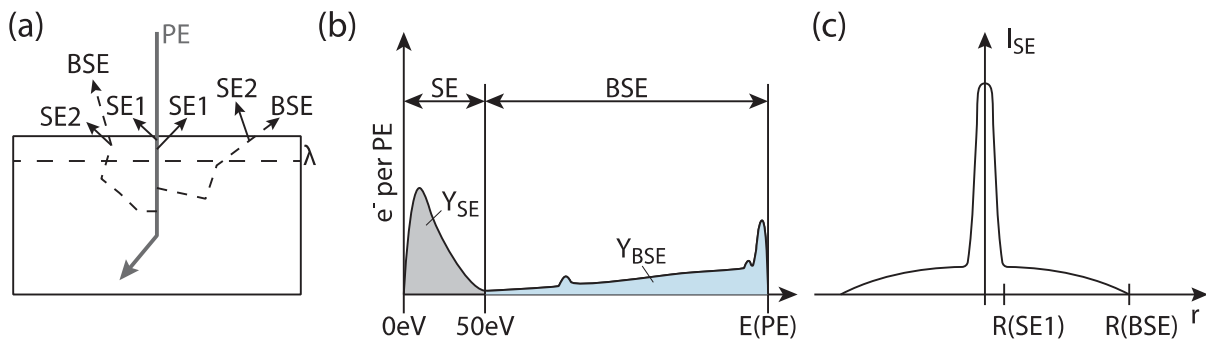


Figure 2-2 (a) Sketch of the trajectory of a PE beam in a solid, generating BSE and SE with  $\lambda$  the mean free path of SE. SE1 generated from PE, SE2 generated from BSE. (b) Energy spectrum of SE and BSE generated in a solid when irradiated with an electron beam (PE) with a primary energy  $E(PE)$ . (c) Spatial distribution of SE1 and BSE. All images based on<sup>51,52</sup>

Inelastic collisions have numerous causes and effects. When interacting with inner shell electrons, they can cause the ionization of atoms by exciting an inner shell electron, eventually inducing the emission of material characteristic X-Rays or Auger electrons. Other inelastic collisions with the crystal lattice or the solid might lead to the generation of phonons or transmit the PE energy otherwise, i.e. as heat and the PE remains in the substrate. The inelastic interaction with weakly bound electrons causes the ejection of low energy electrons, called secondary electrons (SE). A PE can undergo a multitude of these elastic and inelastic collisions, losing energy on its way and changing its direction of travel. This trajectory continues until the

PE either exits the substrate surface as a backscattered electron (BSE) or loses all its kinetic energy within the solid. Each BSE can furthermore generate SE.

As illustrated in the energy spectrum in Figure 2-2b, SE have low energies  $0 \leq E(SE) \leq 50$  eV and therefore mostly short mean free paths  $\lambda$  of only a few nm within a substrate. If SE are generated close enough to the substrate surface ( $d \leq \lambda$ ), they cross the interface and are emitted from the sample. The numbers of SE or BSE generated per PE are called yield ( $Y_{SE}$  and  $Y_{BSE}$ ) and can be determined by the integration of the areas beneath the curves of the spectrum (Figure 2-2b, grey and blue area). These yields depend on the material.

There are two types of emitted SE: Those generated by PE, SE1, and those generated by BSE, SE2 (c.f. Figure 2-2a). Both types have energies in the same spectrum but different emission ranges  $r$  (Figure 2-2c). SE1 are only emitted to close proximity of the PE beam. SE2 however, are emitted wherever BSE are emitted, meaning they have the same range as BSE:  $r(BSE) = r(SE2)$ . The range  $r(BSE)$  depends directly on the beam energy  $E(PE)$  and the substrate material. This maximum exit range was described and calculated theoretically by Kanaya and Okayama<sup>53</sup>. The maximum penetration depth  $R$  (in nm) of PE at an acceleration energy  $E_{PE}$  in a material with the molar weight  $M$  and the atomic number  $Z$

$$R = 2.761 \times 10^{-4} \times \frac{ME_{PE}^{5/3}}{\rho Z^{8/9}} \quad (2-1)$$

is inserted in equation (2-2) describing the maximum exit range of BSE  $r_{BSE}$  in that material

$$r_{BSE} = C \times R \times \frac{\gamma}{1 + \gamma} \quad (2-2)$$

with  $C=1.1$  and  $\gamma=0.19Z^{2/3}$ .

It is also visible from Figure 2-2c that even though the emission ranges for both SE types is different, their yields are similar. SE1 are more localized around  $r=0$ , while SE2 are stretched over the whole range of  $r_{BSE}$ .

To get further insight into the distribution of BSE over the whole radius from the beam center  $r=0$  until  $r_{BSE}$ , Monte Carlo (MC) simulations are useful. The MC method simulates the solid-electron interaction with random numbers and a large number of simulated electrons. Thereby, a good approximate to the trajectories of PE within a material is achieved (Figure 2-3a). The method is described in Chapter 3.2, however, for a detailed discussion the work of Joy can be recommended.<sup>54</sup> With the help of these simulations and a recalculation considering the respective experimental conditions, a radial distribution of BSE emitted during a spot irradiation can be obtained. An example of such a distribution is illustrated in Figure 2-3b.

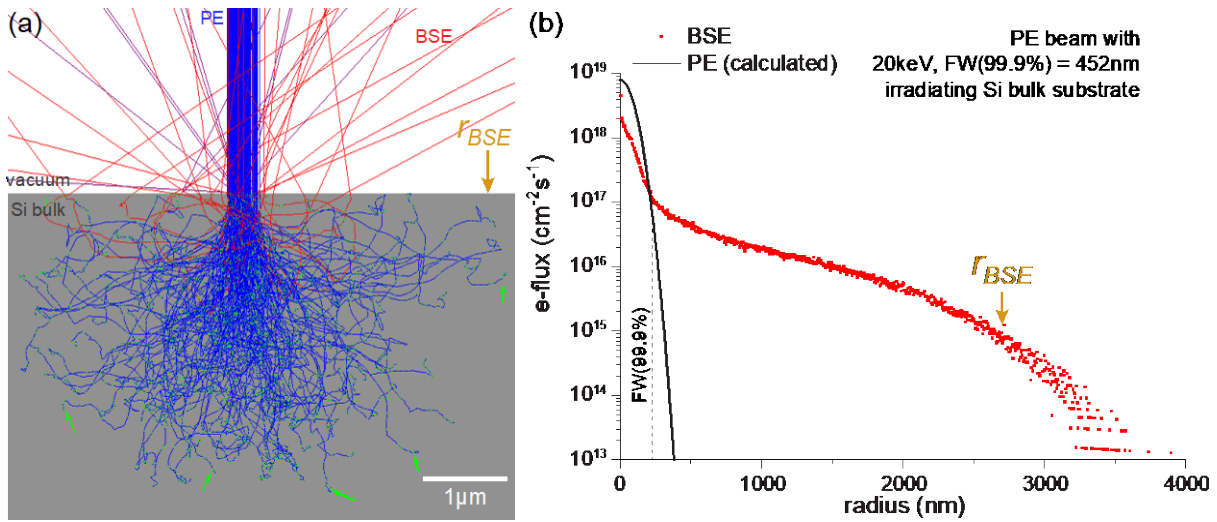


Figure 2-3 (a) Monte Carlo simulation of electron trajectories of 20 keV Gaussian primary beam with  $\text{FW}(99.9\%) = 425 \text{ nm}$  in a silicon bulk substrate. Blue: focused PE in vacuum and scattered in bulk substrate, red: emitted BSE, green: SE, some indicated by arrows. (b) Radial distribution of BSE (red) and PE (black) of this simulation. The  $\text{FW}(99.9\%)$  of the PE beam and the theoretical  $r_{\text{BSE}}$  (eq. (2-2)) are marked. Simulation of  $1 \cdot 10^6$  PE, 200 trajectories from CASINO<sup>55</sup> displayed.

The incident radial flux distribution  $f(r)$  of a typical PE beam can be described by a Gaussian

$$f(r) = \frac{I_p/e}{2\pi a^2} \exp\left(-\frac{r^2}{2a^2}\right) \quad (2-3)$$

with  $I_p$  the beam current (measured experimentally in a Faraday cup),  $e$  the elementary charge,  $a$  the standard deviation of the beam's Gauss profile (obtained experimentally with the knife-edge method, see Chapter 3.1.4) and  $r$  the radial distance to the beam center.

### 2.1.2 Continuum Model

In FEBID the gaseous molecules which adsorbed on the surface of a substrate are locally dissociated by a focused electron beam with a radial flux  $f(r)$ . Simultaneously to the electron flux, the precursor molecules are supplied through a gas injection system (GIS) with a molecule flux  $J$  to the substrate surface with  $(1 - \frac{n}{n_0})$  available adsorption sites, with  $n$  the adsorbate density and  $n_0$  the density of a complete monolayer, and a physisorption probability  $s$ . The molecules stay adsorbed on the surface for a certain amount of time, the residence time  $\tau$ .

The impinging electrons can dissociate the adsorbed molecules with a cross section  $\sigma$ , which depends on the electron energy and the chemical bond it dissociates. Lastly, the molecules can diffuse on the substrate surface. For simplicity, this term will be neglected in the following section.

Combining all the aforementioned situations, the adsorption rate of the molecules in radial distance can be described by <sup>56</sup>

$$\frac{\partial n(r)}{\partial t} = sJ\left(1 - \frac{n(r)}{n_0}\right) - \frac{n(r)}{\tau} - \sigma f(r)n(r) \quad (2-4)$$

For the steady state ( $\frac{\partial n(r)}{\partial t} = 0$ ), the adsorbate density  $n(r)$  can be described in two scenarios:

(A) without electron irradiation,  $f(r)=0$ : 
$$n(r) = \frac{sJ}{sJ/n_0 + 1/\tau} = \theta_{eq} \quad (2-5A)$$

(B) with electron irradiation,  $f(r) \neq 0$ : 
$$n(r) = \frac{sJ}{sJ/n_0 + 1/\tau + \sigma f(r)} \quad (2-5B)$$

Case A describes the situation, when the beam is off, or in regions far away from the beam center ( $r \rightarrow \infty$ ). In this case, the molecules only adsorb and desorb, reaching an equilibrium coverage  $\theta_{eq}$ . In case B, the adsorbed molecules are dissociated with a dissociation rate  $\sigma f(r)$ . The growth rate  $R(r)$  correlates to the molecule density  $n(r)$ , the dissociation rate  $\sigma \cdot f(r)$  and the volume of deposited material  $V$  as:

$$R(r) = V \cdot n(r) \cdot \sigma f(r) \quad (2-6)$$

The deposit volume  $V$  can be calculated with the deposit density and molar mass:

$$V = \frac{M_{dep}}{\rho_{dep} \cdot N_A} \quad (2-7)$$

where  $M_{dep}$  can be calculated from the deposit composition.

Inserting eq. 2-5B for the molecule density reveals the non-proportional behavior of the growth rate on the rates of dissociation  $\sigma \cdot f(r)$ , molecule supply ( $sJ/n_0$ ), and desorption ( $1/\tau$ ):

$$R(r) = V \cdot \frac{sJ}{sJ/n_0 + 1/\tau + \sigma f(r)} \cdot \sigma f(r) \quad (2-8)$$

The deposit shape can then be described by multiplying  $R(r)$  with the total deposition time:

$$Shape(r) = R(r) \cdot t_{tot} \quad (2-9)$$

The three parameters  $f(r)$ ,  $n(r)$  and  $R(r)$  can be plotted in an exemplary graph to explain their correlation to each other at continuous single spot irradiation.

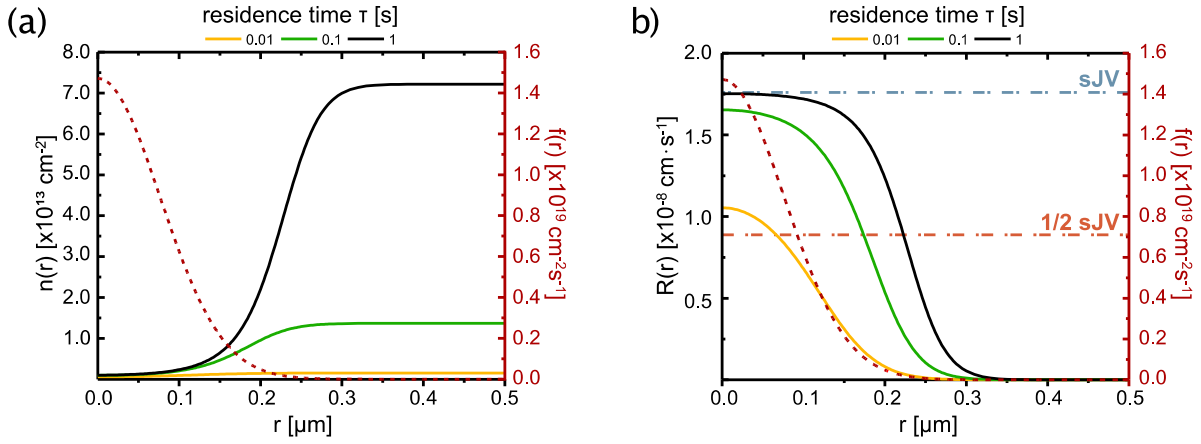


Figure 2-4 (a) radial molecule density  $n(r)$  against the distance to the beam center with different  $\tau$ , calculated with equation (2-5). (b) radial growth rate  $R(r)$  at different  $\tau$ , calculated with equation (2-8). The radial electron flux  $f(r)$  is plotted in red. Parameters set to typical experimental values in our thermionic emitter system: e-beam with FWHM=180nm, 0.6nA,  $\sigma=0.1\text{\AA}^2$ ,  $s=1$ ,  $J=1.52 \cdot 10^{14} \text{ cm}^{-2} \text{ s}^{-1}$ ,  $V=1.17 \cdot 10^{-22} \text{ cm}^3$ .

From Figure 2-4a it is visible, how (without considering surface diffusion) the adsorbate density  $n(r)$  varies within the Gaussian electron beam flux profile (red dashed line). Outside the beam ( $r \rightarrow \infty$ ) the steady state adsorbate density without irradiation becomes  $n(r)=\theta_{eq}$  (c.f. equation (2-5A)) being larger for larger residence times (smaller desorption rate). Inside the beam ( $r \rightarrow 0$ ) the steady state adsorbate density decreases with increasing electron flux and takes a value given by eq. 2-5B. In the example of Figure 2-4 the rates for molecule supply, desorption and dissociation (at  $r=0$ ) are  $sJ/n_0 = 1.1 \text{ s}^{-1}$ ,  $1/\tau = 1-100 \text{ s}^{-1}$  and  $\sigma f_0 = 147.2 \text{ s}^{-1}$ , respectively. Thus, the relation  $\sigma f_0 \gg 1/\tau > sJ/n_0$  holds in the beam center. The steady state value in the beam center depends therefore on the desorption rate and increases with increasing  $\tau$ . The radial growth rate  $R(r)$  increases with increasing electron flux  $f(r)$ . Inside the beam the growth rate is the highest and then decreases with decreasing  $f(r)$  according to eq. (2-6), see also Figure 2-4b. For very low and no electron flux ( $r \rightarrow \infty$ ) the growth rate drops to zero, since there is no more electron induced dissociation taking place. The flat growth rate peak seen in Figure 2-4b represents the maximum value  $R(r) = sJV (= 0.18 \text{ nm/s})$  when  $\sigma f(r) \gg sJ/n_0 + 1/\tau$  (eq. 2-6A). This means all impinging precursor molecules are dissociated by the electrons before they can thermally desorb. An increase of desorption rate  $1/\tau$  (i.e. lowering the residence time) sharpens the growth rate profile but obviously decreases the growth rate maximum.

In this context, two growth regimes in FEBID can be introduced. Depending on the ratio of precursor supply, adsorption and dissociation rate, the deposition can take place in the electron flux limited (EL) regime or the precursor flux limited (PL) regime. In the continuum model, the PL regime describes the radii from the beam center in which the electron induced dissociation rate is higher than the sum of incoming molecule rate and the desorption rate:  $\frac{sJ}{n_0} + \frac{1}{\tau} \ll \sigma f(r)$ . The growth rate is therefore limited by the amount of precursor molecules supplied to the

substrate. As typically the electron beams in SEMs are quite intense (see Table 2-1) and thus imply large dissociation rates, eq. (2-8) becomes around the beam center ( $r \sim 0$ ):

Precursor limited regime (PL): 
$$R(r \sim 0) \cong V \cdot \frac{sJ}{\sigma f(r)} \cdot \sigma f(r) = VsJ \quad (2-8A)$$

In contrast, the EL regime describes the regions of deposition, where the number of molecules supplied to the substrate is higher than the electron flux, so that the growth rate changes with changing electron flux:  $\frac{sJ}{n_0} + \frac{1}{\tau} \gg \sigma f(r)$ . In stationary deposition, this is the case for large radii from the beam center, i.e. at the tails of the electron beam profile and outside of it ( $r \rightarrow \infty$ ). The growth rate in equation (2-8) then becomes proportional to  $f(r)$ :

Electron limited regime (EL): 
$$R(r \rightarrow \infty) \cong V \cdot \frac{sJ}{sJ/n_0 + 1/\tau} \cdot \sigma f(r) \quad (2-8B)$$

Experimentally, these two growth regimes are spatially separated during continuous spot irradiation deposition. The PL regime is usually the growth regime in which a typical constant spot irradiation deposition is taking place. Electron beams used with beam currents of 0.5 – 3 nA lead to very high electron fluxes in the beam center, which are several magnitudes larger than the molecule flux. Table 2-1 summarizes some typical values used in the scope of this work.

Table 2-1 Some typical values for molecule and electron fluxes, cross sections, residence times and coverages in FEBID experiments with corresponding rates.

Total molecule flux (low vapor pressure precursors):		$\sim 10^{14} - 10^{15}$	molec./cm <sup>2</sup> s	19,57
Electron flux (W-emitter, 0.5 - 1 nA):		$\sim 10^{19}$	e <sup>-</sup> /cm <sup>2</sup> s	8
Electron flux (FEG, 0.5 - 3 nA):		$\sim 10^{21}$	e <sup>-</sup> /cm <sup>2</sup> s	8
Typical dissociation cross sections $\sigma$ ,	$\sigma$	$10^{-1} - 1$	Å <sup>2</sup>	
residence times $\tau$ and	$\tau$	$10^{-2} - 1$	s	8
monolayer densities $n_0$	$n_0$	1 - 10	nm <sup>2</sup>	
Rates in FEBID	$\sigma f$	$10^2 - 10^5$	s <sup>-1</sup>	
	$1/\tau$	1 – 100	s <sup>-1</sup>	
	$sJ/n_0$	1 – 10	s <sup>-1</sup>	

Figure 2-5a shows a Monte Carlo simulation of the electron flux of the primary electron beam (PE, red) and emitted backscattered electrons (BSE, blue) plotted against the radius in distance to the beam center. Additionally, a sketch of a spot deposit with corresponding size is illustrated underneath the graph (Figure 2-5b). Here, two regions are marked in the deposit. The high e-flux deposition in the area of the PE beam is labelled as “center deposit”, and the low e-flux deposition in the area of pure BSE contribution is called “halo deposit”.

Figure 2-5 illustrates how stationary spot deposition allows to observe the full gradient of the two growth regimes, EL and PL, in one experiment. Due to the decreasing number of BSEs emitted with increasing distance to the beam center, the deposit underlies the continuum radial growth rate model  $R(r)$  as described in eq. (2-8) (Figure 2-4b). The underlying colors are attributed to the deposition regime. PL (greyblue) deposition takes place when the dissociation rate becomes larger than the sum of the molecule supply and desorption rate given by  $\sigma f \gg sJ/n_0 + 1/\tau$  (see eq. (2-8) and (2-8A)). In the central part of the deposit, where a large number of BSE and SE is emitted and PE are continuously impinging in a high rate, precursor molecules are depleted quickly and cannot replenish in time, leading to a precursor flux limited growth. Contrarily, the EL regime (orange) takes over when  $\sigma f \ll sJ/n_0 + 1/\tau$  (eq. 2-8B).



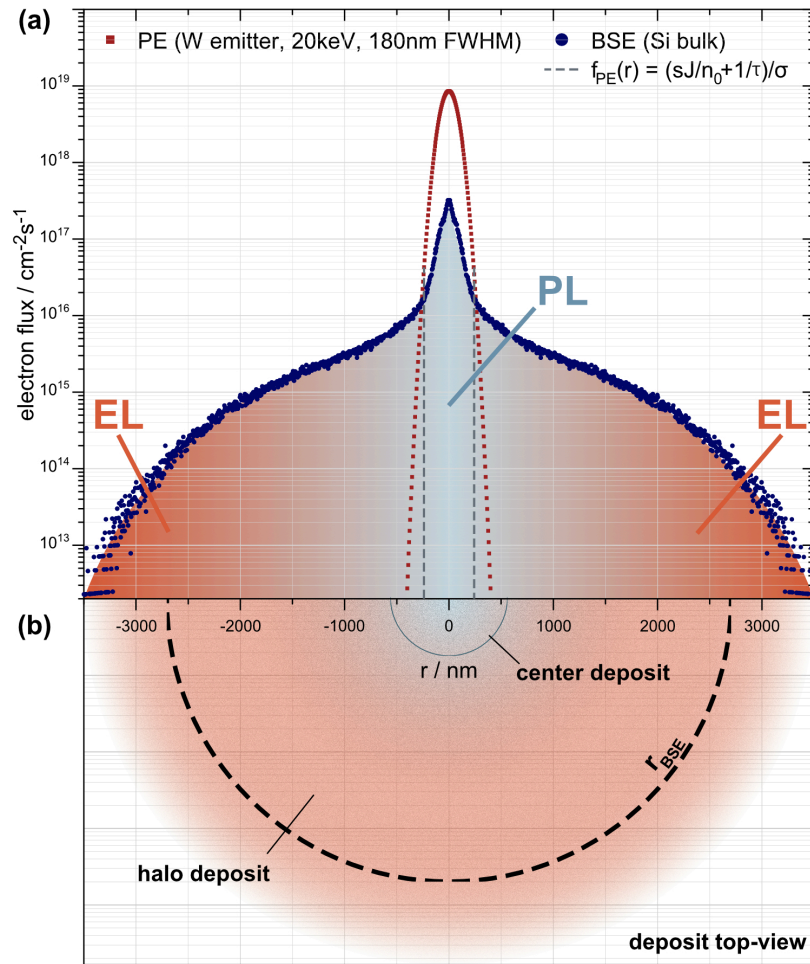


Figure 2-5 (a) Radial distribution of the electron flux from a primary electron beam (PE, red) and the emitted backscattered electrons (BSE, blue) generated by the PE in a Si bulk substrate. This illustration shows furthermore the precursor limited (PL, greyblue) and electron limited (EL, orange) growth regimes within the radial distribution. The transition from PL to EL regime lies at the radius where the dissociation rate equals the molecule supply rate:  $\sigma f(r) \approx sJ/n_0 + 1/\tau$ . (b) Sketch illustrating half a stationary spot deposit in top view with the center and halo deposit fabricated through the high electron flux in the center and low flux in the outer radii. The theoretical maximum BSE exit range  $r_{BSE}$  at 20 keV in Si is marked with a dashed line.

The transition from the PL to EL deposition regime happens towards larger radii and decreasing amount of BSE emission. The transition point can be assigned to the radius, where both sides of the inequation become equal:  $\sigma f \approx sJ/n_0 + 1/\tau$ . Since this is not a sharp transition, the change between both regions is visualized as a color gradient.  $R(r)$  is proportional to the e-flux (eq. (2-8)). Therefore, the deposition rate is significantly smaller at the outer edges of the deposits as BSE fluxes are up to 4 magnitudes smaller than in the center. This leads to thin halo deposits. The theoretical BSE exit radius  $r_{BSE} = 2707$  nm for a 20 keV beam interacting with a silicon substrate is illustrated with a dashed line.<sup>53</sup> Note, that  $r_{BSE}$  is calculated for a 0-dimensional beam (point source), so that this value will always be smaller than the observed and simulated BSE emission range, where the real beam diameter (FWHM) has to be added.

### 2.1.3 Time dependent solutions for pulsed irradiation

So far, the equations were describing the continuous spot deposition only. To write areas, however, the classical FEBID approach consists of a moving beam successively dwelling on neighboring pixels, giving each irradiated pixel the possibility to deplete and replenish with adsorbates. The idea is illustrated in Figure 2-6, showing the scanning path of an electron beam for depositing a square deposit. The electron beam with an electron flux  $f(r)$  and a Gauss shape irradiates each pixel with a dwell time  $t_d$  and subsequently moves on to the next pixel with a defined step size  $\Delta x$  (and  $\Delta y$  when reaching the end of a line). When considering just one pixel of the structure, it gets depleted during the irradiation (dwell) time  $t_d$  and then replenished with fresh precursor by the incoming molecule flux during the refreshment time it takes the beam to come back to this pixel,  $t_r$ . The deposition parameters will be discussed further in sections 2.1.5 - 2.1.5.3.

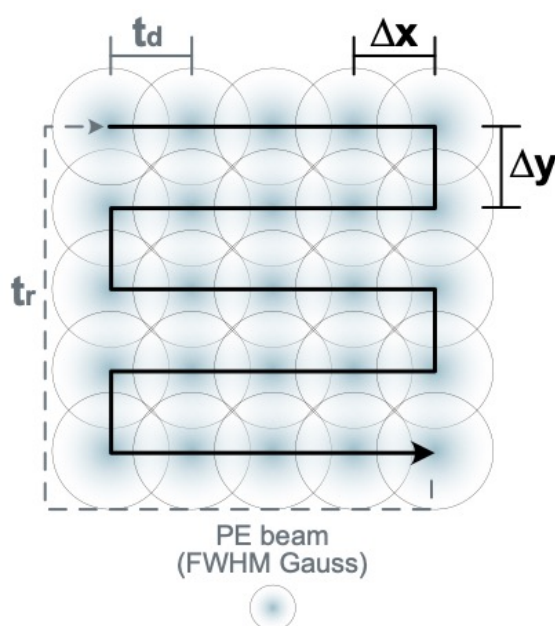


Figure 2-6 Serpentine deposition raster scheme for fabrication of a square deposit. The beam (greyblue) dwells for a given amount of time  $t_d$  on one pixel, before moving to the next pixel with a defined step size  $\Delta x$  (and  $\Delta y$  at the end of the line). Each pixel can be replenished with fresh precursor molecules during a refreshment time  $t_r$ . Figure simplified and based on <sup>8</sup>.

Based on this deposition process, equation (2-4) has a time dependent solution, describing the adsorbate density with: <sup>56</sup>

$$n(t) = Ce^{-kt} + B \quad (2-10)$$

Due to the nature of the experiments, each variable in equation (2-10) has two components for the two situations created by dwelling the beam. When the beam is on, the precursor molecules are depleted by the incoming electron flux. The variables are denoted with the index d. Contrarily, the precursor molecules can be refreshed (replenished) by the incoming molecule flux when the beam is off. The variables are denoted with the index r.

$$k = \begin{cases} k_d = sJ/n_0 + 1/\tau + \sigma f(r) \\ k_r = sJ/n_0 + 1/\tau \end{cases} \quad (2-7A)$$

$$B = \begin{cases} B_d = sJ/k_d \\ B_r = sJ/k_r \end{cases} \quad (2-7B)$$

The time dependent solution for the deposition rate during the dwell time  $R(t)$  is given by: <sup>56</sup>

$$R(t) = V\sigma f \left\{ \frac{(B_r - B_d)}{k_d t_d} \frac{[1 - \exp(-k_r t_r)][1 - \exp(-k_d t_d)]}{1 - \exp(-k_r t_r) \exp(-k_d t_d)} + B_d \right\} \quad (2-11)$$

The results for  $R(t)$  plotted against the dwell time for fixed refreshment time  $t_r$ , as well as  $R(t)$  against the refreshment time  $t_r$  at a fixed dwell time  $t_d$  and a fixed residence time  $\tau$  are illustrated in Figure 2-7.

The graphs in Figure 2-7 depict (a) the dwell time dependent growth rate as well as the refreshment time dependent growth rate with (b) fixed  $t_d = 100 \mu s$  and (c) fixed  $\tau = 100ms$ . In (a) it is visible, that the growth rate plateau increases with short dwell times at large refreshment times, due to minimized molecule depletion during irradiation and their sufficient replenishment. The region of this plateau can be attributed to the electron limited regime (EL), as described earlier in section 2.1.2. With increasing  $t_d$ , the deposition rate shifts towards the precursor limited regime (PL) and reaches a minimum plateau. Here, precursor replenishment is not sufficient, and less molecules are available to be dissociated. Therefore, deposition is taking place with the same deposition rate as in the beam center of continuous irradiation (Continuum Model, equation(2-8)). Overall, the growth rate increases for longer residence times  $\tau$ . Larger  $\tau$  means smaller desorption rates, so that more precursor molecules are available for deposition, when irradiated.

The refreshment time dependent growth rate is plotted in Figure 2-7b-c with a fixed dwell time  $t_d = 100\mu s$  (b), or fixed residence time  $\tau = 100ms$  (c). In both cases, the growth rate is small for short  $t_r$ , since the precursor depletion is larger than the replenishment, meaning that the deposition is taking place in the precursor limited regime (PL). With longer refreshment times, more precursor molecules are replenished and available at the irradiation spot. The deposition rate therefore shifts into the electron limited regime (EL) until it reaches a constant growth rate.

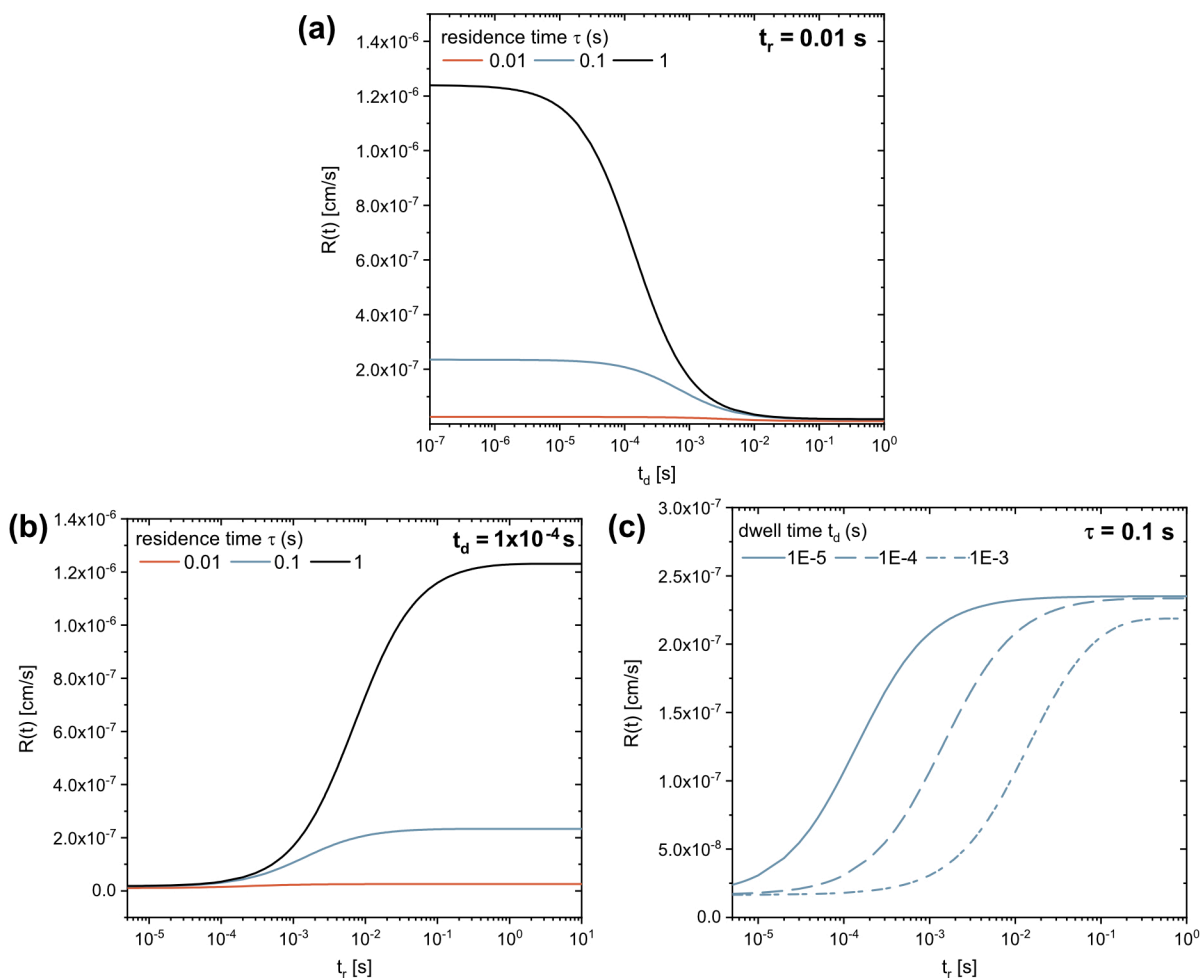


Figure 2-7 Different graphs of equation (2-11) illustrating the time dependence of the deposition growth rate  $R(t)$ . (a) Dwell time dependence with a fixed refreshment time of  $t_r = 10$  ms with changing residence times  $\tau$ . (b) Refreshment time dependence at a fixed dwell time  $t_d = 100 \mu\text{s}$  with different  $\tau$ . (c) Refreshment time dependence with fixed  $\tau = 100$  ms and changing dwell times. Other parameters:  $V = 1.17 \times 10^{-22} \text{ cm}^3$ ,  $s = 1$ ,  $J = 1.52 \times 10^{14} \text{ cm}^{-2}\text{s}^{-1}$ ,  $n_0 = 1.37 \times 10^{14} \text{ cm}^{-2}$ ,  $\sigma = 0.1 \text{ \AA}$ ,  $f = 1.47 \times 10^{19} \text{ cm}^{-2}\text{s}^{-1}$

At longer  $\tau$ , i.e. smaller desorption rates, the deposition rate increases faster, due to more available precursor molecules on the substrate. In contrast,  $R(t)$  increases faster with shorter  $t_d$ , due less depletion during the shorter irradiation, as also shown in Figure 2-7a. In summary, FEBID square deposits can be exposed in the electron or precursor limited regime by changing the dwell and refreshment times of the pixels.

#### 2.1.4 The Impact of the Electron and Precursor Limited Regime on the Deposit

The estimation of the prevailing deposition regime can be crucial for the tuning of the deposition rate and/or the deposition composition. There have been studies on the effect of changing the deposition regime for several cases.

Almost 30 years ago, the PL limited regime was already described as the favorable deposition regime for  $\text{W}(\text{CO})_6$ .<sup>58</sup> The higher amount of electrons in comparison to the present precursor molecules was improving the electrical conductivity as the precursor was dissociated more

completely in high beam currents, leading to the desorption of more CO ligands and cleaner deposits (Figure 2-8a).

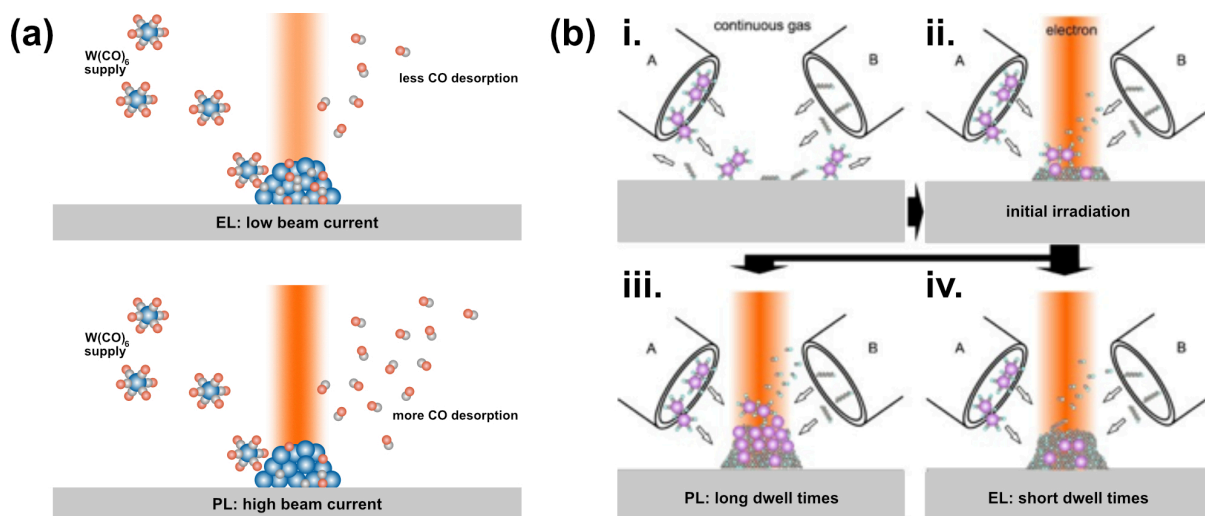


Figure 2-8 Schemes of deposit purity depending on the electron limited or precursor limited regime. (a) Dependence of the beam current. Deposits from  $W(CO)_6$  deposited with a low beam current result to more ligand contamination. Those deposited with a high beam current lead to more ligand desorption and better deposit purity. Based on description from ref. <sup>58</sup>. (b) Two-species deposition scheme of  $Co_2(CO)_8$  and hydrocarbons. (i) Precursor adsorption/desorption, (ii) initial electron irradiation forming a deposit. The precursor with the larger dissociation cross section is deposited preferentially (e.g. species A) – deposit is rich in A. (iii) Long dwell times deplete the precursor with the higher cross section (e.g. A), leading increased deposition rate of the other precursor B – deposit is rich in B. (iv) Short dwell times reset the system to initial deposition step, incorporating more species A. Figure (b) and description taken from and based on ref. 15.

Similar observations were reported for  $Co_2(CO)_8$ .<sup>15,59</sup> It was shown that by changing the dwell time  $t_d$ , the deposit composition could be tuned, meaning that the cobalt content was increased with longer dwell times. The study could model this composition change by extending the time dependent solution for pulsed irradiation to a two-adsorbate system. These two adsorbates were (A) the cobalt precursor and (B) a hydrocarbon representing residual hydrocarbons present in the SEM chamber (Figure 2-8b). The solution could model the composition by showing that for short  $t_d$  both adsorbates are deposited in the EL regime. When increasing  $t_d$ , the hydrocarbons shifted to the PL limited regime, leading to the depletion of these adsorbate species and therefore depositing less carbon. This leads to higher cobalt concentrations at longer  $t_d$  until reaching the steady state plateau ( $t_d \rightarrow \infty$ ).

More recently, these observations were confirmed in magnetic studies for  $Co_2(CO)_8$  deposits. Cleaner structures were achieved at higher e-fluxes.<sup>60</sup> Another study presented how the different regimes could precisely be accessed by varying the flow of an inert carrier gas through the precursor reservoir, varying the precursor flux accordingly.<sup>61</sup> Also here, the highest purities were achieved in the PL regime at higher beam currents and/or lower gas flows. Additionally, the variation of precursor flux within the PL regime was shown to lead to changing Co contents

and deposit shapes emphasizing the importance of not only the impact of PL vs. EL regime but also surface diffusion and molecule desorption rates.<sup>62</sup>

Contrarily to the abovementioned studies, the deposition with the silver carboxylate  $\text{Ag}(\text{O}_2\text{Me}_2\text{Bu})$  lead to cleaner silver crystals in the halo of a continuous spot deposit, where the electron flux is significantly lower than in the center.<sup>19</sup> Therefore, the EL regime lead to improved purity, since less ligands were co-deposited (Figure 2-9).

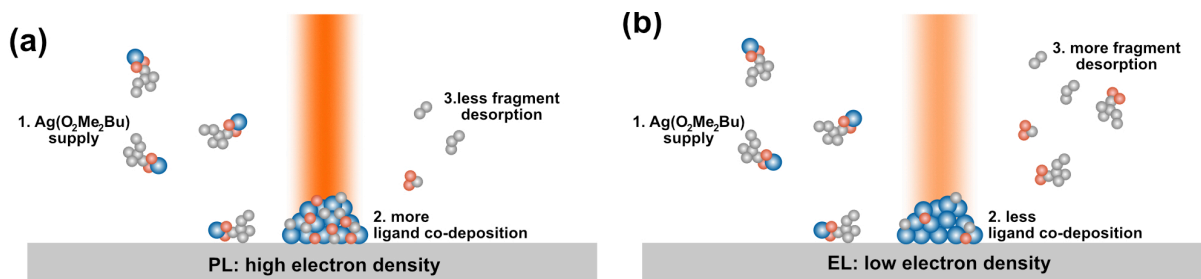


Figure 2-9 Scheme of silver deposition in (a) high electron density (PL regime). Ligands cannot desorb and are co-deposited in the high electron density. The deposit is more contaminated. (b) Deposition in low electron density (EL regime). Ligands and fragments can desorb before co-deposition. The deposit is cleaner. Scheme based on Ref. <sup>19</sup>.

## 2.1.5 Process Parameters (dwell time, refreshment time, repetition, step sizes)

During the FEBID process, a number of parameters have to be set in order to achieve the desired deposit. As mentioned earlier, a lithographic process controls the electron beam, resulting in a certain structure.

This process consists of:

- dwell time  $t_d$ : the time the beam stays on that specified position (pixel).
- refreshment time  $t_r$ : the time each position (pixel) is not irradiated throughout one repetition (frame) and can "refresh" its precursor coverage to pre-irradiation state.
- pattern: what should the structure look like? 1D dot arrays, 2D rectangles or 3D pillars? The lithography software defines the shape with xy coordinates. The beam moves to the specified position for a certain amount of time.
- step size: the distance between two specified positions (pixels) in the pattern. The steps are equidistant throughout the pattern/structure if not defined differently.
- repetitions: the number of times the pattern is irradiated in the same way (the pattern is repeated).

### 2.1.5.1 Dwell Time and Refreshment Time

The two crucial deposition parameters dwell time  $t_d$  and refreshment or replenishment time  $t_r$  were discussed in section 2.1.3. These parameters strongly influence the deposition rate and can shift the growth from the EL to the PL regime.

### 2.1.5.2 Pattern

The big advantage of FEBID over other nanofabrication techniques is that basically any pattern can be chosen for the deposit. Theoretically, there is no limitation to the variety of shapes. The resolution is extremely high since deposition occurs only within and in close proximity to the irradiated area. Of note is that  $\mu\text{m}$ -sized halos can be avoided by using low electron beam energies  $\leq 1\text{ keV}$ . Therefore, 1D dot arrays can be deposited with high precision and 2D shapes of all sorts are achievable. Usually, squares, rectangles, circles or lines are sufficient for many studies and applications. Several reviews have summarized the large variety of e.g. sensor applications achieved by FEBID.<sup>8,12,50</sup> Depending on the software controlling the beam, even the deposition of more complex 2D structures, such as logos or images is possible. This technique has recently been further developed allowing the programming and deposition of complex 3D structures<sup>5-7,63</sup>. 3D structures through the movement of the beam when irradiating with long  $t_d$  can form sophisticated structures such as arches,<sup>64-66</sup> angled segments,<sup>67</sup> pillar arrays<sup>68</sup> and helices.<sup>69,70</sup> The shape and size of the final structure is limited by the growth rate of the respective precursor. Compounds with a high deposition rate are more suitable for 3D deposition.

### 2.1.5.3 Step Size and number of Repetitions

A pattern is defined by a number of pixels that the beam scans over. As illustrated in Figure 2-6, the beam moves by the distance  $\Delta x$  (and  $\Delta y$ ) after having irradiated the previous point for a defined dwell time  $t_d$ . By varying the step size, the same deposit can look very different. The step size was chosen to be as large as the FWHM of the irradiating electron beam to optimize overlap for flat deposition and to keep the effective dwell time close to the pixel dwell time  $t_d$ . If  $\Delta x \ll \text{FWHM}_B$ , the beam will overlap largely with the previously irradiated area, increasing the effective  $t_d$ , increasing the electron dose and increasing precursor depletion. However, if  $\Delta x \gg \text{FWHM}_B$ , there will be no sufficient overlap, leading to a non-uniform thickness deposition, as there are regions between the beam spots which were not sufficiently irradiated, and therefore not enough material deposited.

In addition to the step size, the number of repetitions can be adjusted for a desired deposit thickness. After scanning the pattern with the defined  $\Delta x$  and  $t_d$ , it is usually irradiated in the same manner again for multiple times. Depending on  $t_d$ , the number of repetitions might be higher or lower. For very short  $t_d$ , a large number of repetitions must be chosen, in order to deposit enough volume as the deposited thickness in the short duty cycle (exposure time) is very small. Very long  $t_d$  however, might deposit enough material in less repetitions.

## 2.2 Quartz Crystal Microbalance (QCM)

A quartz crystal microbalance (QCM) consists of a quartz crystal which, due to its piezoelectric properties, oscillates with a known frequency  $f_i$  when applying a potential. The mass change is detected by the frequency change of an oscillating quartz crystal upon addition or removal of

material from its surface. The dependency of  $\Delta f$  on  $\Delta m$  was first described by Sauerbrey in 1959:<sup>71</sup>

$$\Delta f = -\frac{f^2}{N_q \rho_q A} \Delta m = -C_f \frac{\Delta m}{A} \quad (2-12)$$

with  $f$  the crystal Eigenfrequency,  $N_q$  the frequency constant of the crystal,  $\rho_q$  the crystal density,  $A$  the measured area of the crystal and  $\Delta m$  the mass change.

All crystal parameters can be combined in the sensitivity factor  $C_f$ , which is specific for the crystal and its cut. The most common crystal cut is the AT-cut. It corresponds to a cut along a specific crystal plane leading to a crystal frequency of 5-6 MHz. For a typical 6 MHz AT-cut crystal, with  $N_q = 1.67 \cdot 10^4 \text{ Hz} \cdot \text{cm}$ , and  $\rho_q = 2.65 \text{ g} \cdot \text{cm}^{-3}$ , the sensitivity factor becomes  $C_f = 8.13 \cdot 10^7 \text{ Hz/ng} \cdot \text{cm}^{-2}$ . This means that a mass change of  $12.3 \text{ ng/cm}^2$  induces a frequency change of 1 Hz, which can be resolved with a QCM. This corresponds to about  $0.4 \text{ ML/cm}^2$  of  $\text{H}_2\text{O}$ . This shows that the QCM has a sufficiently high resolution to detect the desorption and adsorption of monolayers from copper precursors studied in this work.

The AT-cut quartz crystals are optimized for the use around room temperature. Depending on the exact cut angle, the change in temperatures can cause differently strong changes in frequency, which falsify the results.<sup>71</sup>

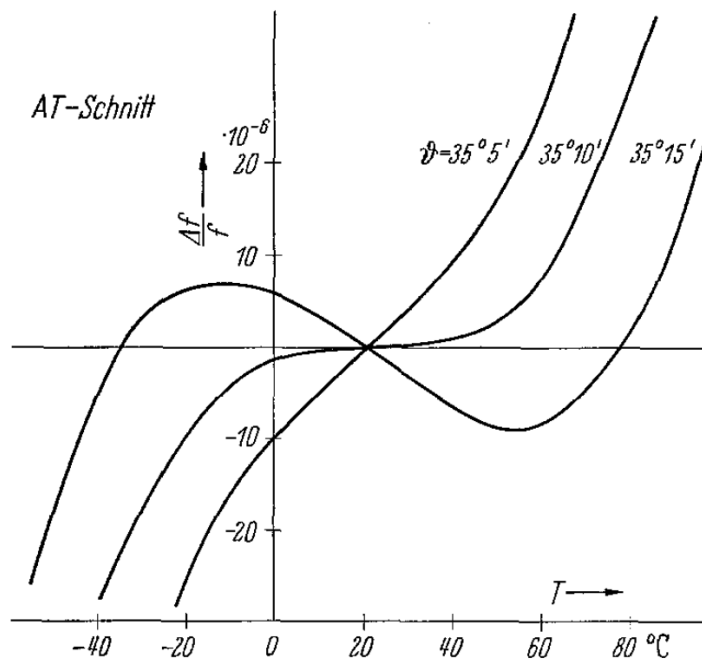


Figure 2-10 Temperature dependency of AT-cut quartz crystals with different cutting angles  $\vartheta$ . The AT-cut shows the least frequency change at room temperature. Temperature changes induce a frequency change that cannot be attributed to the mass change. Figure taken from Sauerbrey.<sup>71</sup>

Different crystal materials or cuts can be used for a linear temperature dependence over larger temperature windows. The frequency change due to temperature shifts can then be subtracted (c.f. experimental Chapter 3.6).



## 3 Experimental Methods

### 3.1 Focused Electron Beam Induced Deposition (FEBID)

#### 3.1.1 Precursors

All carboxylate precursors were synthesized by K. Madajska in the research group of I. Szymańska at the Department for Chemistry, Nicolaus Copernicus University Toruń, Poland. Silver(I) pentafluoropropionate  $[\text{Ag}_2(\mu\text{-O}_2\text{CC}_2\text{F}_5)_2]$  ( $\text{Ag}_2(\text{pfp})_2$ , CAS 509-09-1) is a white, light sensitive solid stored in air at room temperature. Copper(II) pentafluoropropionate  $[\text{Cu}_2(\mu\text{-O}_2\text{CC}_2\text{F}_5)_4]$  ( $\text{Cu}_2(\text{pfp})_4$ ) and its *tert*-butylamine derivative  $[\text{Cu}_2(\mu\text{-O}_2\text{CC}_2\text{F}_5)_4(\text{tBuNH}_2)_2]$  are both a light blue powder stored in air at  $<10^\circ\text{C}$ . The ethylamine derivative  $[\text{Cu}_2(\mu\text{-O}_2\text{CC}_2\text{F}_5)_4(\text{EtNH}_2)_2]$  is a light blue gel also stored in atmosphere at  $<10^\circ\text{C}$ .

Bis(*tert*-butylacetoacetato) copper(II)  $\text{Cu}(\text{tbaoac})_2$  (CAS 23670-45-3) was synthesized by N. Boysen in the research group of A. Devi at the Department of Inorganic Chemistry, University of Bochum, Germany. It is a green powder stored in air at room temperature.

Bis(hexafluoroacetylacetonate) copper(II)  $\text{Cu}(\text{hfac})_2 \cdot x\text{H}_2\text{O}$  (CAS 155640-85-0) were purchased from Sigma-Aldrich. The hydrated compound is made of green crystals stored in air at  $<10^\circ\text{C}$ . When stored in vacuum for longer periods of time, crystal-bound  $\text{H}_2\text{O}$  is removed and the crystals turn dark blue (Figure 3-1).

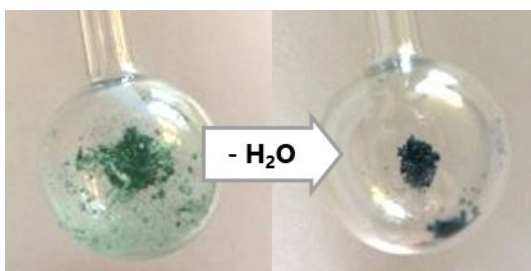


Figure 3-1  $\text{Cu}(\text{hfac})_2$  in a glass vial. Left: "pristine", hydrated state. The crystals are green. Right: anhydrous state. After evacuating the vial for several hours, crystal bound water is removed and the precursor changes color to dark blue.

#### 3.1.2 Set-Up: Precursor Delivery & Heating, Stage Heating & Manipulation

Precursors are delivered to the substrate with an internal gas injection system (GIS). The GIS is made of chemically inert stainless steel and is designed for minimizing molecule path lengths. Prior to filling the precursor, the GIS reservoir and needle are cleaned in ultrasonic baths in 1. acetone and 2. isopropanol for 10 min each. The precursors are filled freshly into the GIS reservoir before each experiment in small amounts (20-40 mg) under the fume hood. The GIS heating is realized through resistive heating of a fitted heating jacket and a PID controller for temperature control. The temperature is measured on the GIS surface with a Type K thermocouple. The precursor gas leaves the reservoir through a capillary made of medical steel

with inner diameter of 0.38 mm. Precursors with very low volatility (e.g.  $\text{Ag}_2(\text{pfp})_2$ ) could also be evaporated with a GIS without capillary but a large linear tube opening of 3mm inner diameter (Figure 3-2).

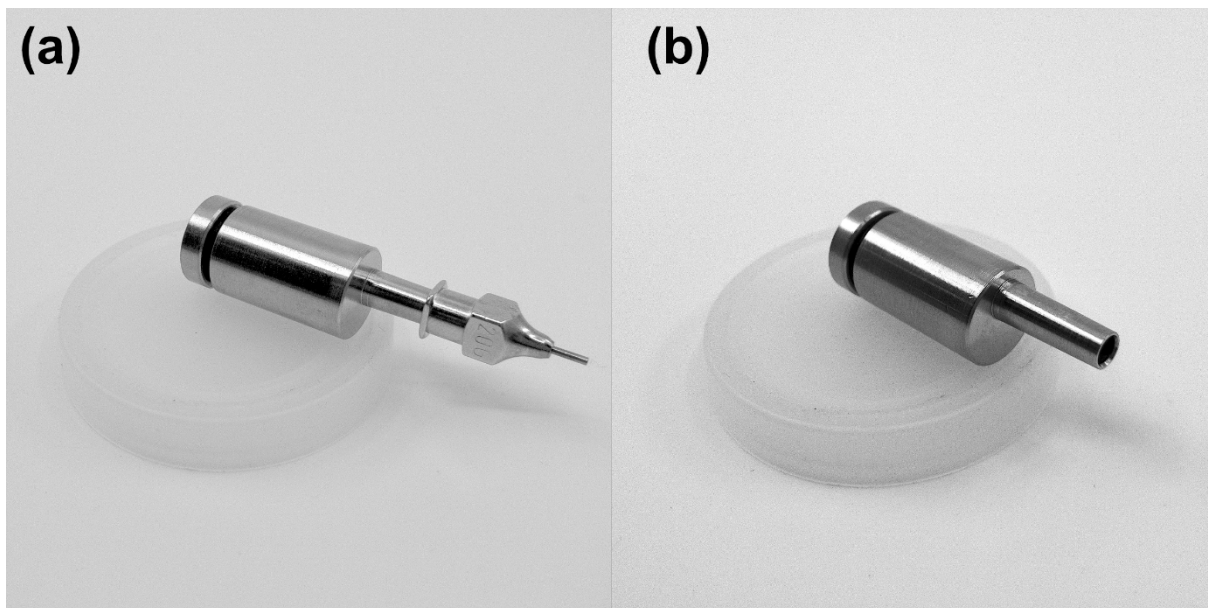


Figure 3-2 Gas injection system (a) with needle and (b) without needle.

For positioning the GIS is mounted on a 3- or 2-axis piezo stage (depending on the microscope). If not noted differently, the capillary opening was positioned in 200-300  $\mu\text{m}$  lateral and 200  $\mu\text{m}$  vertical distance to the deposition area (Figure 3-3a). A simulation of the spatial distribution of all exiting molecules for this experimental setup using the GIS Simulator is provided in Figure 3-3b. The nozzle was simulated to be 200 $\mu\text{m}$  above the substrate, in a 70° angle to the substrate normal with an inner tube diameter of 0.38 mm and 4mm nozzle length (length of the thin needle, c.f. Figure 3-2a). The uptake coefficient was set to 0, so that no molecules will adsorb on the tube walls, and all molecules exit the GIS. The deposition area includes the full area, where multiple structures were fabricated during the experiment, and is marked in orange in a lateral distance of 200-500  $\mu\text{m}$  to the lower tube end. According to the color scale on the right side, 6-9% of all exiting molecules are available for deposition in that area.

The available molecule flux in these regions can then be calculated by multiplying this percentage with the calculated total molecule flux  $J_{\text{tot}}$ :

$$J_{\text{tot}} = \frac{\Delta m}{\Delta t} \frac{N_A}{M} \frac{1}{A_{\text{exit}}} \quad (3-1)$$

with  $\Delta m$  the experimentally determined precursor mass loss,  $\Delta t$  the time during which the precursor was evaporated and exiting the GIS,  $N_A$  the Avogadro's number,  $M$  the molecular mass of the precursor molecule,  $A_{\text{exit}}$  the area of the tube opening.  $\Delta m$  was determined after each experiment by measuring the GIS mass before and after the experiment.

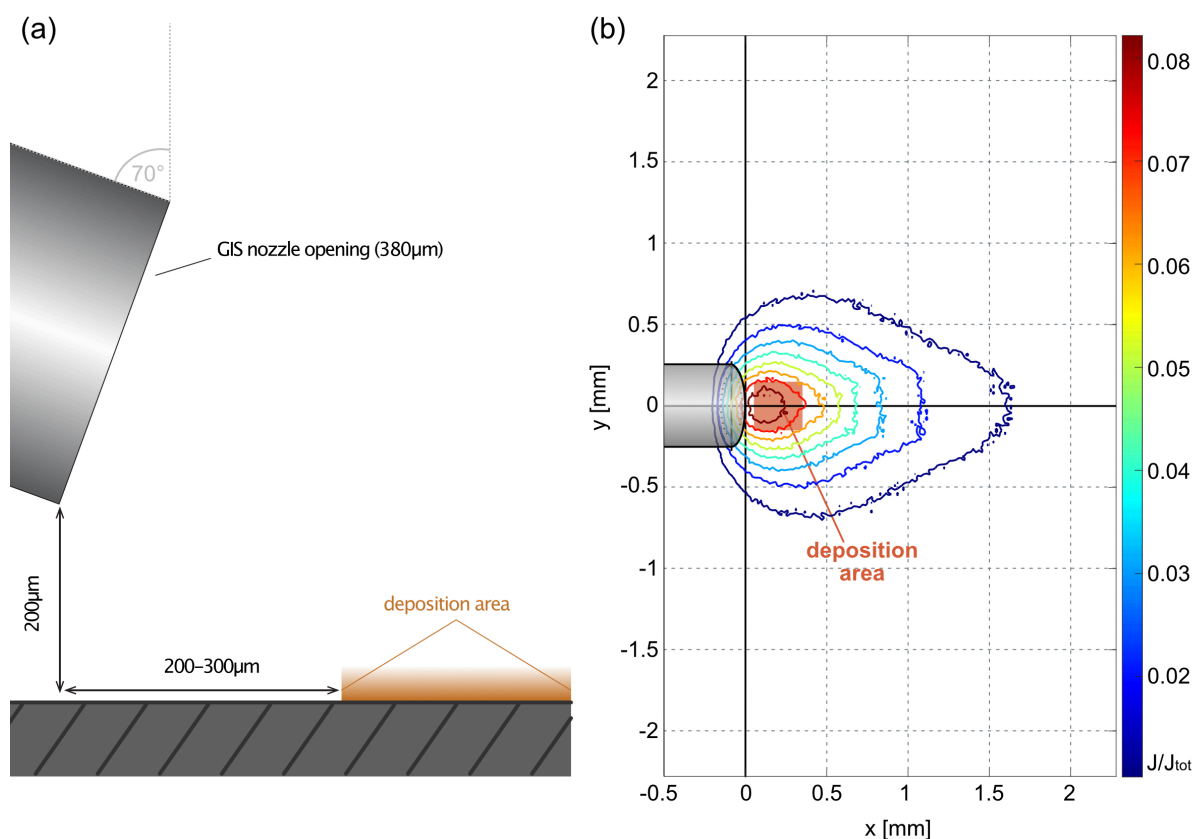


Figure 3-3 (a) Sketch of the positioning of the GIS nozzle with a 380 μm opening (inner diameter), 200 μm over the substrate and in lateral distance to the deposition area in a typical FEBID experiment. The deposition area includes the whole area, where multiple deposits are fabricated. (b) Simulation of the impinging molecule flux exiting from the nozzle using the parameters from a. The deposition area is marked in orange in a distance between 200 and 500 μm from the nozzle exit. The deposition area lies within the regions where 6 - 9% of exiting molecules are available. Simulation parameters:  $10^7$  molecules, 256 grid points, uptake coefficient (in nozzle) = 0, needle length  $l=4\text{mm}$ , nozzle angle  $\alpha=70^\circ$ , height above substrate  $h=200\mu\text{m}$ .

The substrates were attached to a heatable stage with copper clamps in order to avoid any carbon contamination through diffusion originating from adhesive tape or glue. The substrates lay on a solid copper block for uniform heat transfer from the underlying ceramic heating plate. This resistive heater was heated with a constant current source. The temperature was measured with a Type K thermocouple within the copper block. The stage movement was controlled by the SEM system.

For deposition, two scanning electron microscopes were used: a Hitachi S3600 with a thermionic tungsten source and a Philips XL-30 with a field emitter gun (FEG) source.

### 3.1.3 Beam Control, Lithography

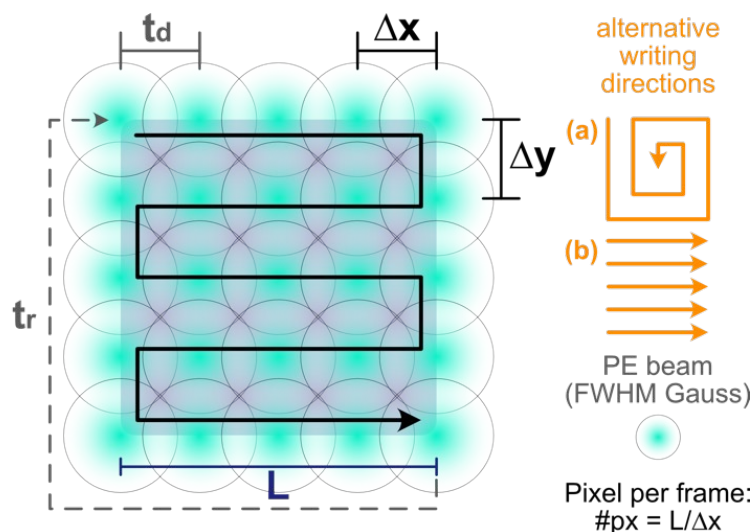


Figure 3-4 Lithography scan parameters, which can be controlled and defined by XENOS. This includes the shape (e.g. square with side length  $L$ ), the step sizes  $\Delta x$  and  $\Delta y$  (pixel to pixel distance), the dwell time  $t_d$  and the writing direction (black: serpentine). Alternative writing directions: (a) spiral, (b) line by line. The refreshment time  $t_r$  is the time the beam takes to re-irradiate a pixel position after writing the pattern and it is directly linked to  $t_d$  and the pattern size. Furthermore, the lithography system controls how often the pattern is written (repetitions, not shown).

For precise irradiation and deposition, the Hitachi S3600 has a XENOS patterning engine with a beam blaster attached for beam control. This lithography software allows the definition of dwell times  $t_d$ , step size  $\Delta x$  and  $\Delta y$  (pixel to pixel distance), number of repetitions, writing direction and shape through individually adjustable protocols (Figure 3-4). If not mentioned otherwise, XENOS square deposits were written with the serpentine writing direction and all other area deposits with a line by line writing direction (internal beam control, see below). XENOS has an inherently implemented waiting time of 30 ms before each frame repetition which needs to be considered in each experiment. All relevant parameters are mentioned in the respective chapters.

Both SEMs can also be controlled through the respective SEM system. They include the irradiation of a full frame (scanning mode) with different scan speeds, area, line and spot irradiation. The area scan irradiates a fraction of the full frame with the same scan speed. A line scan irradiates one single horizontal line of the full frame and during the spot irradiation the beam continuously irradiates one spot. The position of each of those scan modes can be set arbitrarily by the user, as well as the irradiation time (and therefore the number of repetitions of the line or area respectively). The area and line sizes are dependent of the magnification chosen by the user. Furthermore, the user can choose between a set of preset scan speeds for the full frame, area and line scan. In the Hitachi SEM the internal program offers different scanning modes such as "TV" with short dwell times and "Slow Scan" with long dwell times. The following details of the scanning modes are documented in the manual: number of pixels

per line ( $\#px_x$ , x-direction), number of lines per frame ( $\#px_y$ , y-direction), time per frame ("TV") or time per line ("Slow Scan"). From these values, the number of pixels per frame and the pixel dwell time can be derived. With the size of the scanned area (or region of interest, ROI), the step sizes  $\Delta x$  and  $\Delta y$  can be calculated. The area size was determined either by measuring it with the scale bar during deposition, or *ex situ* upon analyzing the deposit size, determining the side lengths  $L$  (c.f. Figure 3-4). The number of repetitions  $n$  was determined by dividing the total deposition time by the time per frame.

$$t_{d,TV} = \frac{t_{frame}}{(\Delta x * \Delta y)} \text{ or } t_{d,slow} = \frac{t_{line}}{\Delta x} \quad (3-2)$$

$$\Delta x = \frac{L_x}{\#px_x} \text{ (if } \Delta x \neq \Delta y, \text{ then } \Delta y = \frac{L_y}{\#px_y} \text{)} \quad (3-3)$$

$$n = \frac{t_{total}}{t_{frame}} \quad (3-4)$$

The XL-30 is equipped with an external imaging software, "Digital Image Scanning System 5" (DISS) v.5.15.13.0 from point electronic GmbH, which allows the definition of scan speed and scan sizes, giving a more direct possibility to define  $t_d$  and step sizes in comparison to the internal SEM system of the Hitachi. However, it is less precise than the XENOS lithography system. The ROI could be set by choosing a magnification and setting it to a size by measuring it with the scale bar. The number of pixels in this ROI is provided or can be set in the DISS software. Furthermore, discrete scan speeds can be chosen by changing the oversampling time. The respective pixel dwell time and time per frame are calculated and provided by the software. By dividing the total deposition time by the time per frame,  $n$  was determined (c.f. equation (3-4)). Both systems use the line by line writing strategy (Figure 3-4b).

The electron dose  $D$  of any deposit will be defined as impinging (electron) charges divided by the respective area. The number of impinging electrons is calculated as the beam current times the total irradiation time,  $I_B \cdot t_{tot}$ , where the probe current is measured in a Faraday cup using a Keithley 6485 picoammeter connected to the SEM stage. The respective areas of square, line, or point (pixel) deposits will be given by  $length^2$ ,  $length \cdot FWHM_B$ , and  $0.25\pi \cdot FWHM_B^2$ , respectively, where  $FWHM_B$  is the full width at half maximum of the (Gaussian) electron beam profile. The doses can also be formulated in terms of the lithography parameters step size (pixel-to-pixel distance)  $\Delta x$ , dwell time per pixel  $t_d$ , and number of frame or line repetitions  $n$ :

$$D_{pixel} = t_d \cdot n \cdot I_B / (0.25\pi \cdot FWHM_B^2) \quad (3-5)$$

$$D_{line} = (L/\Delta x) \cdot D_{pixel} = n \cdot I_B \cdot t_{tot} / (FWHM_B \cdot L) \quad (3-6)$$

$$D_{square} = (L/\Delta x)^2 D_{pixel} = n \cdot I_B \cdot t_{tot} / L^2 \quad (3-7)$$

The term  $L/\Delta x$  defines the number of pixels in a line of length  $L$ . The pixel dose defined by eqn. (3-5) is for an average areal dose and a useful single number for comparison, however, it should be kept in mind that the spatial dose varies within the pixel area according to the impinging and electron beam profile and its interaction with the substrate (c.f. section 2.1.1).

### 3.1.4 Beam Size Determination

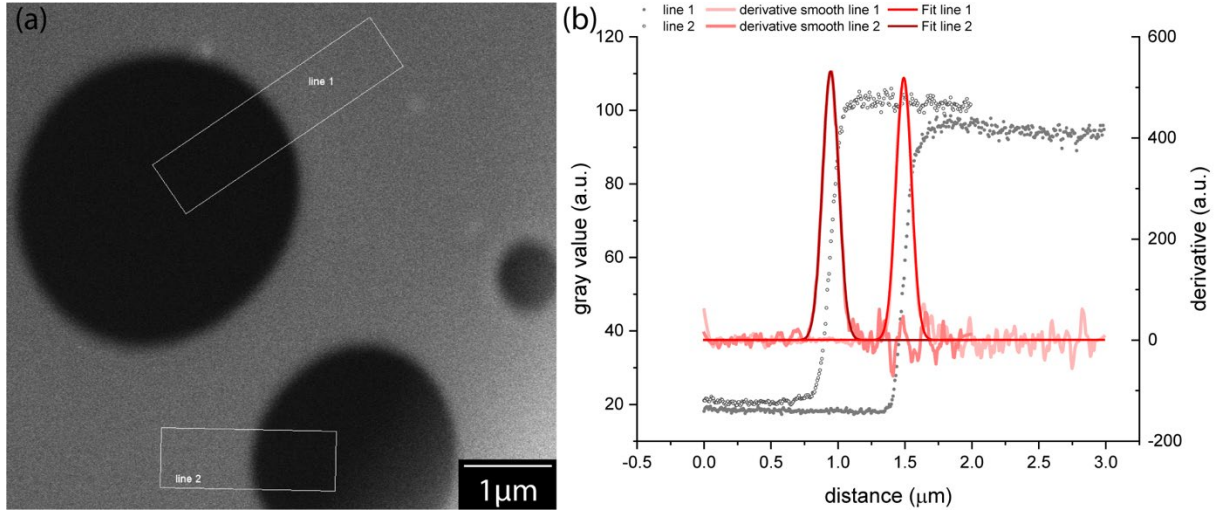


Figure 3-5 (a) Scanning electron micrograph of the holey carbon TEM membrane with two 100px wide lines for intensity profiles. (b) Determination of the electron beam profile. The smoothened gray value intensity profile is plotted in grey and its first derivative in light red. The derivative was fitted with a Gaussian curve (solid red), giving the FWHM of the beam.

The areal intensity distribution of a focused and astigmatism-free electron beam can be well described by a radial Gaussian distribution<sup>8</sup>

$$f(r) = \frac{I_P/e_0}{2\pi a^2} \exp\left(-\frac{r^2}{2a^2}\right) \quad (3-8)$$

With  $I_P$  the beam current of the PE beam,  $e_0$  the elementary charge,  $a$  the standard deviation and  $r$  the radius.

Depending on the settings of acceleration voltage and beam current, the spot sizes of electron beams vary. The beam sizes used during deposition in this work were determined using a modified knife-edge method. For that, holey carbon TEM membranes were imaged in the SEM with the same settings as for the deposition. The advantage of thin carbon membranes (thickness about 10 nm – standard thickness) is that the interaction volume becomes geometrically very small and that carbon has a low Z number and density making elastic interactions less likely. Hence edge effects are minimized compared to steel razor blade approaches. High magnification images of the holes were recorded (Figure 3-5a) and processed with Fiji ImageJ software. Line profiles with 100px line width (to improve the noise levels) were measured over the edges of the holes (Figure 3-5a). These contrast profiles were then smoothened using the built-in Savitzky-Golay method in Origin, with a window size set to 20 (this means 20 data points used in each local regression). The first derivative of these edge profiles corresponds to the beam profile and can be fitted with a Gauss curve (Levenberg Marquardt iteration algorithm) (Figure 3-5b). The full width at half maximum (FWHM) of this Gauss curve was provided by the fit. Using this process, the FWHM of all beam settings were determined.

Usually, the spot or beam sizes mentioned in this work will refer to the full width of the Gauss shaped electron beam profile which includes 99.9% of all electrons, FW(99.9%). It is calculated with the inverted error function from the experimentally obtained FWHM and correlates in the following way:

$$FWHM_B = 2\sqrt{2 \ln 2} \sigma \quad (3-9)$$

and

$$FW(99.9\%) = 2\sigma\sqrt{2}\text{erf}^{-1}(2 \cdot 0.999 - 1) \approx 6.1805\sigma = 2.624FWHM_B \quad (3-10)$$

with  $\sigma$  the standard deviation of the Gauss profile.

All beam sizes used in this work are summarized in Table 3-1. The variation in uncertainties depends on the noise of the recorded images.

Table 3-1 FWHM and FW(99.9%) of both deposition instruments for beam settings used in deposition.

	Beam settings	FWHM	FW(99.9%)
Hitachi S3600	25 keV, 0.25 nA	402 ± 1 nm	1055 nm
	20 keV, 0.46 nA	170 ± 17 nm	446 ± 34 nm
Philips XL-30	25 keV, 1.25 nA	26.34 ± 0.43 nm	69 ± 1 nm

The electron flux (e-flux) of the FEG source is several orders of magnitude higher, than for a W-filament.

## 3.2 Monte Carlo Simulations

The various interactions of electrons with a solid, as listed in detail in chapter 2.1.1, can be simulated with the Monte Carlo (MC) method. This method combines the possibilities and probabilities of scattering events (elastic and inelastic) and the resulting trajectory deviation, with the sampling of random numbers to compute a scattering path for one electron within a solid. By the combination of a large number (usually >1000) of these single trajectories, a significant composition of numerous possibilities is generated, which as a whole, gives a realistic approximation of what really happens.<sup>54</sup>

In this work, the MC software CASINO v3.3.0.4 was used.<sup>55</sup> This most recent version of the software allows the simulation and representation of electron trajectories within a three-dimensional sample with varying materials, which are defined by their stoichiometry, density and vertical and lateral dimensions (thickness and area). It outputs several spatial and spectral distributions including the spatial distributions of the penetration depth of all electrons and the penetration depth of BSEs (which escape the surface), the energy distributions of BSEs and TEs when exiting the substrate as well as the radial distributions of BSE and their energy when leaving the surface at that position.

CASINO distinguishes five types of electrons: (a) primary electrons (PE) originate from the electron source and travel to the sample surface with a given energy determined by the acceleration voltage. Energy and beam diameter are inputs to CASINO. (b) Backscattered electrons (BSE) are scattered PE, which exited the sample to the top, with energies greater than 50 eV. Trajectories, Cartesian energy distribution maps, BSE yield, and spectral (energy) distribution are simulated. (c) Electrons which are not emitted and have energies below 50 eV are considered absorbed. This information is then used for spatial energy distribution and X-Ray generation. (d) Transmitted electrons (TE) exit the sample at the bottom generating an energy distribution of those. (e) Secondary electrons (SE) are electrons emitted from the substrate with energies smaller than 50 eV. Trajectories of SEs are visualized in CASINO mostly within the bulk, however, due to the small  $Y_{SE}$ , almost no emitted SE are displayed.

All electron distributions visualized in this work were obtained by simulating  $10^6$  (bulk substrate) and  $10^8$  electrons (membrane). For trajectory illustrations, however, smaller numbers, i.e. 75 (bulk) and  $10^5$  trajectories (membrane) were used. The number is noted in the respective figures.

CASINO provides the radial distribution of BSE  $N_{CAS}(r)$ , the origin being the center of the primary electron beam distribution. The primary electron beam distribution can be defined as singular zero diameter beam or as Gaussian distribution. The user can enter the experimentally determined beam diameter (FW99.9%, see eq. (3-10)).<sup>72</sup> The radial distributions simulated by CASINO were exported as CSV files and recalculated to get the BSE flux per  $\text{cm}^2$  and second  $f_{BSE}$ :

$$f_{BSE}(r) = \frac{N_{PE,exp.} \cdot Y_{BSE}}{\sum_i N_{CAS}(r)} \cdot N_{CAS} = \frac{\frac{I_B}{e_0} \cdot Y_{BSE}}{\sum_i N_{CAS}(r)} \cdot N_{CAS} \quad \text{with } i = \frac{r_{max}}{\Delta r} \quad (3-11)$$

with  $N_{PE,exp.}$  the calculated number of primary electrons,  $Y_{BSE}$  the BSE yield obtained by CASINO for this simulation,  $I_B$  the experimentally measured current of the primary beam and  $e_0$  the elementary charge.

The primary beam settings of the simulation were adjusted according to the experimental values for each case. The radial PE beam distribution is additionally added to the graphs containing the radial BSE distribution for better visualization.

The physical models implemented for all simulations were the default options based on the MONSEL code from NIST, as they are well-established. SE distributions are not provided by CASINO.

### 3.3 Imaging with Scanning and Transmission Electron Microscopy

All high-resolution scanning electron microscopy (SEM) images were made with a Hitachi S4800 SEM with secondary electron detectors in two positions (upper and lower). Additionally, some images were obtained with a Tescan Mira SEM with an in-lens secondary electron detector.



Transmission electron microscopy analysis on membranes was performed in a JEOL JEM 2200FS TEM with a JEOL EX-24065JGT EDX detector operated at 200 kV in high resolution imaging (HR-TEM), high angle annular dark field scanning (HAADF-STEM) and bright field scanning (BF-STEM) modes. Selected area electron diffraction (SAED) pattern indexing was performed using the CSpot software (version 1.2.0).

### 3.4 Chemical Analysis: EDX and Thin Film Correction

The chemical composition of all structures was determined with energy dispersive X-ray spectroscopy (EDX). The high energy electron beam of the SEM locally irradiates the deposit, exciting the atoms within the structure. During the relaxation process, X-rays with element characteristic energies are emitted and registered by the EDX detector. The resulting graph plots the signal intensity versus the kinetic energy showing which elements are present in the probed sample.

The primary energies used for characterization in this work were set to 7 keV for Ag samples and 3 or 5 keV for Cu samples. These beam energies were used to excite the low energy lines of all ligand material and the metals (Table 3-2).

Table 3-2 Deposited elements and their characteristic X-Ray energies detected in EDX.

Line	C K	N K	O K	F K	CuL	SiK	AgL
Energy (keV)	0.277	0.392	0.525	0.677	0.928	1.740	2.983

For the characterization of thin FEBID deposits and different locations within the deposits, small probe volumes and areas were used. Therefore, excitation energies as low as possible were crucial in this work. As explained in equation (2-1) (Chapter 2.1.1) the penetration depth  $R$  of electrons, and therefore the interaction volume within a substrate, depends on the energy of the PE beam and the material density. Therefore, the interaction volume of a low energy primary beam is significantly smaller than of a high energy beam. For the characterization of the central and halo region of the dot deposits shown for  $\text{Cu}_2(\text{pfp})_4$  and  $\text{Ag}_2(\text{pfp})_2$ , 3 and 7 keV were chosen respectively. These energies were about the double of the characteristic CuL and AgL lines, as to optimize the X-ray emission signal for reliable analysis.

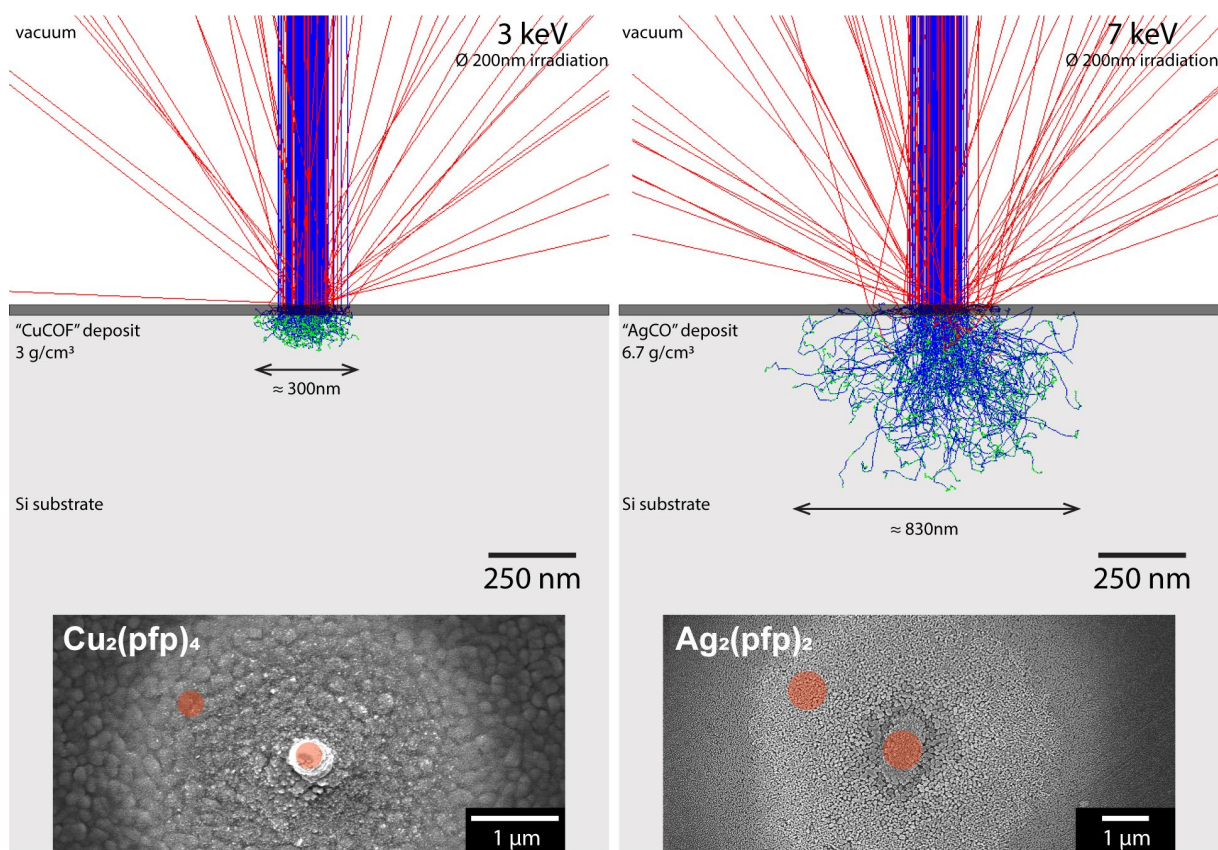


Figure 3-6 Monte Carlo Simulations of an electron beam with 3keV and 7keV interacting with an "CuCOF" and "AgCO" deposit on a silicon substrate. 500 electrons were simulated on an irradiation area of 200 nm diameter, similar to the area probed in the analysis. The figures show 200 trajectories each. The SEM images show the spot deposits from  $\text{Cu}_2(\text{pfp})_4$  and  $\text{Ag}_2(\text{pfp})_2$  with the analysis positions and the size of the projection of the probed volume (top view).

Simultaneously, the excitation volume within the deposit and substrate is sufficiently small to not exceed the region of interest (ROI), i.e. it allows enabling distinct measurements of halo and center where the ratios of electron to molecule flux differ. Figure 3-6 shows the Monte Carlos simulations of the two beam energies used for analysis, 3 and 7 keV. The 3 keV beam is interacting with a 30 nm thick "CuCOF" deposit (density  $3 \text{ g/cm}^3$ ) on a silicon substrate. The 7 keV beam interacts with a 30 m thick "AgCO" deposit ( $6.7 \text{ g/cm}^3$ ). The material density input is discussed further down this chapter. Both simulations show an irradiated area with 200 nm diameter, which corresponds to the probed area during analysis. The primary electrons (blue) scatter in the deposit and substrate depending on their energy. The higher energy beam with 7 keV has a visibly larger interaction volume than the beam with lower energy. The SEM images below the simulations show spot deposits that were analyzed locally with these acceleration energies. The position and projected size of the interaction volume was illustrated as red circles. All spectra were recorded either with a Hitachi S4800 equipped with an EDAX silicon drift detector (SDD) or a TESCAN MIRA equipped with an EDS Octane Plus Silicon Detector from EDAX.

Spectra were recorded and treated with the EDAX Genesis and Team software, to subtract detector background signal and perform a standardless quantification to determine the k-ratios of each element. The k-ratio for each element  $i$  was determined and ZAF-corrected by the software through comparing the measured intensities with standard intensities from the internal database:

$$k\text{-ratio} = \frac{I_{i,meas.}}{I_{i,stand.}} \cdot [ZAF]_i$$

The EDAX software calculates this ratio assuming a uniform composition of all detected elements inside the excitation volume. This assumption is violated for thin films where the excitation volume extends into the substrate and where the matrix effect of the bulk material has to be corrected. This ZAF correction includes: the atomic number effect  $Z$ , which accounts for the change in emitted X-ray intensity through scattering within in the material. The X-ray absorption effect  $A$ , which accounts for the reduction of emitted X-ray signal due to absorption through other elements within the probed material on the way to the detector. And the X-ray fluorescence effect  $F$ , that accounts for increased signal intensities for elements that experience both, electron induced X-ray emission and secondary X-ray induced fluorescence. The fluorescence occurs when the elements excitation energy is smaller than the X-ray energy of other elements in the material.<sup>73</sup>

Further data processing was done with the SAMx Stratagem thin film analysis software.<sup>74</sup> Of note is that this software is integrated part of the Oxford Aztec EDX software for thin film correction. It uses the k-ratio of each detected element obtained from any EDX software to estimate the thickness and/or composition of the analyzed thin film-substrate arrangement. The user defines the sample geometry, i.e. number of layers, and composition, such as substrate material and possible elements in the film. In this work, the thin film stoichiometry was unknown, so all detected elements and corresponding spectral lines were input to the software with the respective k-ratio from the EDX measurement at the given primary beam energy. The deposit thickness was also entered into SAMx Stratagem when AFM measurements were available, simulating the material density. If this data was not available, the layer density was defined according to existing measurements ("CuCOF" 3 g/cm<sup>3</sup>, "AgCO" 6.7 g/cm<sup>3</sup>) and the layer thickness was calculated by the software. The material densities were also based on previous studies which determined the material density of a different fluorinated metal-organic copper precursor<sup>75</sup> and the weight fractions of elements within the deposit ("Ag<sub>2</sub>CO") provided by CASINO. The influence of densities on the thin-film correction can be viewed in the Supplementary Information (Chapter 9.2). The SAMx Stratagem manual notes that thickness estimates however, are only reliable when the sample was measured with multiple acceleration voltages and the high-energy lines. Since this increases the size of ROIs beyond the measured feature sizes, the calculated thicknesses of these deposits were not considered. The layer composition determination however, is more reliable and was calculated with an iterative process through the software. A reference sample for "CuOC" materials is presented in the Supplementary Information (Chapter 9.1).

In order to exclude any signals from contamination on the substrate (i.e. residual gases deposited during analysis), a background subtraction was performed after thin film correction. For that, the background signal with identical settings was recorded outside the deposition area. The background regions were chosen both in close proximity to the FEBID structure and at larger distance to it. Therefore, any co-deposition through large area scan during the FEBID observation process or precursor condensation could be excluded.

Carbon and oxygen background quantities (oxygen only if no oxide layer –native or artificial– was involved) were subtracted directly from the weight percentage  $w$  (in wt.%) of the Stratagem results. The corrected values were then renormalized and transformed to atomic percent using the molar mass of each element involved:

$$x_i [at. \%) = \frac{\frac{w_i}{M_i}}{\sum_j \frac{w_j}{M_j}} \times 100 \quad (3-12)$$

with  $w_i$  the weight fraction of the element  $i$ ,  $M_i$  the molar mass of the element  $i$  and  $w_j$ ,  $M_j$  the respective fractions and molar masses of the other elements  $j$  detected.

The resulting atomic percentages  $x_i$  (in at.%) are the elemental composition of the FEBID structures presented in this work.

This procedure poses some limitation that should be considered in this work. The Stratagem software sets the assumption that all elements defined in the unknown layer are distributed equally in a homogeneous, non-porous film with constant thickness. Most of these assumptions fit the FEBID case. Even though TEM measurements showed the formation of metal(oxide) nanoparticles within a carbonaceous matrix, they can be considered homogeneously distributed as the observed nanoparticles are smaller (typically 4-20 nm, see Figure 4-6 in Chapter 4.3) than the probed region and volume of X-ray generation (300-830 nm, Figure 3-6):

$$V_{NP} \ll V_{probe} \quad (3-13)$$

The constant thickness was provided through the small, local ROIs where the deposits showed no significant change in thickness. The porosity poses the largest source of error here. Especially for some Ag deposits, where large silver crystals were obtained. The procedure was still implemented in the same manner. Based on the reference measurements (Supporting Information, Chapter 9.1), all EDX quantifications have a maximum uncertainty of about 5-10%. For the determination of potential dissociation paths, the deposit atomic contents were normalized and scaled to the metal atomic content of the pristine precursor. Differences between the ligand element atomic contents of pristine precursor and FEBID material were then attributed to volatile fragments leaving during the adsorbate dissociation. The metals were considered nonvolatile within the FEBID temperature range  $< 200^\circ\text{C}$  in this work.

### 3.5 Atomic Force Microscopy and Deposit Dimensions

Atomic Force Microscopy uses the interatomic forces between the microscope's thin tip and the sample. The sharp tip is on an oscillating cantilever, which scans the sample in xy-direction. Due to repulsing and attracting forces between the sharp tip and the surface, the oscillation amplitude and position of the cantilever is altered. While the tip scans the defined area, the cantilever deflection and oscillation are detected by a laser reflecting from the cantilever head on a photodiode. Whenever the topography of the sample changes, the amplitude changes accordingly. The microscope tries to keep this amplitude constant and therefore moves the sample in z-direction up or down while scanning in xy-direction. These xyz-changes are controlled with high precision by a piezo motor. With this, a three-dimensional topography map of the sample was obtained.

In this work, a NT-MDT NTEGRA Spectra system equipped with Bruker Antimony doped Silicon cantilevers was used for all AFM measurements. They were obtained with the tapping mode, where the cantilever oscillates with an amplitude that allows the tip to touch the sample. Scanning frequencies were adjusted constantly according to each sample. All data was treated with Gwyddion v2.42 and v2.55 and Origin.

Deposit volumes were calculated with the deposit heights obtained from AFM profiles and the lateral dimensions (length, width) from AFM and/or SEM images:

$$V = l \cdot w \cdot h$$

### 3.6 eQCM setup

A dedicated vacuum chamber was built from commercially available vacuum parts equipped with CF flanges to ensure possible UHV compatibility. The chamber was equipped with a pressure sensor, electrical feedthroughs, two gas feedthroughs (1/4" VCR connectors) and a turbomolecular pumping system with backing pump (Edwards Vacuum). An electron source, designed by J. Orzagh (Comenius University Bratislava, Slovakia), was mounted on a blind flange and fitted in the chamber. It consists of a W filament and three copper electrodes, which are connected to four electrical power supplies through the electrical feedthrough: (1) for filament heating and electron emission, (2-4) for applying potentials to the electrodes (electron acceleration and beam focusing). An emission current of 2.2 A was set at the filament, to saturate the filament and extract sufficient electrons. Acceleration potentials between 10 and 100 eV were applied to the electrodes. The impinging beam current  $I_B$  was tuned by variation of the electrode potentials.  $I_B$  was measured *ex situ* on a separate metal plate connected to a picoammeter (Keithley 6485). For these measurements, the QCM was removed from the chamber. The electron flux was calculated with Eq. (3-14):

$$f_0 = \frac{\frac{I_B}{e_0}}{\pi \cdot \frac{FWHM^2}{4}} \quad (3-14)$$

with FWHM of the beam derived from visible deposition spot sizes after prolonged irradiation.

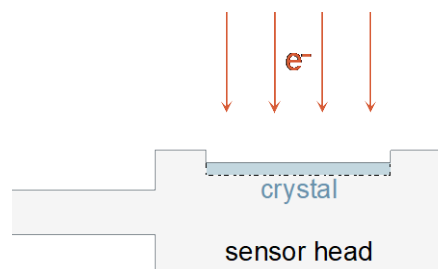


Figure 3-7 Sketch of the QCM sensor head with the crystal surface perpendicular to the impinging electron beam.

The QCM (Colnatec) was placed in the chamber with the quartz crystal surface perpendicular to the electron beam (Figure 3-7). Slight misalignments were compensated by reducing the deposition area  $A_{dep}$  with a factor of 0.9. The company's EON controller system operated the QCM and logged the frequencies over the time of the experiments. All log files were further treated with a custom python script and graphs were created with Origin. Both, AT-cut crystals (Au coated, Inficon) and RC-crystals (Au coated, PhilippTechnologies, USA) were used. The latter were used for their better thermal stability. To remove false mass changes created through temperature changed, a reference curve over the temperature range of interest was recorded. The frequency at the corresponding temperature was used as reference data and subtracted from the raw data.

The precursors were stored in a glass container with a metal-glass seal (CF flange) attached to the gas feedthrough line. The container was separated from the chamber with a bellow valve (Swagelok). The gaseous precursor was fed into the chamber by opening the valve.

The chamber was pumped to a base pressure of  $p_{base} = 1 \cdot 10^{-7}$  mbar. After experiments, the chamber was vented with argon gas. For experiments at elevated temperatures ( $T_{chamber} > RT$ ), the whole chamber was placed inside an oven (Heratherm, ThermoScientific) to ensure uniform heating and exclude the occurrence of hot or cold spots. The pumping system, Ar bottle, electrical power supplies and QCM controller were kept outside the oven.

A detailed plan of the vacuum chamber and its parts can be found in the Appendix, Chapter 9.4.

## 4 Focused Electron Beam Induced Deposition of Group 11 Elements: Silver and Copper from Perfluorinated Carboxylates

This chapter consists of large passages from the following publications:

Berger et al., *ACS Appl. Electron. Mater.* 2020, 2, 7, 1989–1996.

Berger et al., *Beilstein J. Nanotechnol.* 2018, 9, 224–232.

### 4.1 Precursor Evaporation and Transport in the Gas Phase

Silver and copper are highly demanded metals in the nanofabrication and thin film production. Copper is of special interest in microelectronics and ultra large scale integrated circuits (ULSI).<sup>76</sup> Copper deposition with a focused ion beam has already been used for the debugging and repair of integrated circuits, e.g. reconnecting vias.<sup>77</sup> The noble metals gold and silver are known for excellent optical properties in plasmonics, such as surface enhanced Raman spectroscopy (SERS). Plasmonic gold structures were already realized using FEBID.<sup>7,70,78–81</sup> The search for suitable silver precursors is of great interest to advance this field of research and fabricate plasmonic silver nanostructures. Direct silver deposition with an electron beam was previously reported for the condensed and liquid phase (solutions or ionic liquids), but these studies suffered from low resolution, particle embedding in a matrix or the limitation to membrane substrates.<sup>82–86</sup>

Gas-assisted FEBID requires the designated precursors to be introduced into the SEM chamber as a gas. Therefore, these compounds should be sufficiently volatile at room temperature or sublime easily at elevated temperatures. Most precursors used for FEBID are recruited from the large database of volatile metal-organic compounds used in chemical vapor deposition (CVD). The same holds for the precursors discussed in this section. For CVD and FEBID the precursors have to be thermally stable in the gas phase when sublimated in order to be transported intact to the substrate. The compound should not decompose before reaching the substrate where it will be dissociated either thermally (CVD) or by electron irradiation (FEBID).

Group 11 carboxylates make up a group of promising metal organic complexes for both metals, copper and silver. Especially, perfluorinated carboxylates show signs of fulfilling the requirements for gas-assisted FEBID since they are more volatile and thermally more stable than their non-fluorinated analogues. The two species used in this work are silver(I) pentafluoropropionate [ $\text{Ag}_2(\mu\text{-O}_2\text{CC}_2\text{F}_5)_2$ ] and copper(II) pentafluoropropionate [ $\text{Cu}_2(\mu\text{-O}_2\text{CC}_2\text{F}_5)_4$ ]. Their molecular structures are depicted in Figure 4-1. The compounds are referred to as  $\text{Ag}_2(\text{pfp})_2$  and  $\text{Cu}_2(\text{pfp})_4$  in this work. At room temperature,  $\text{Ag}_2(\text{pfp})_2$  is a white, light sensitive powder and  $\text{Cu}_2(\text{pfp})_4$  a light blue powder. Both precursors are stable in atmospheric conditions and have a long shelf time of several years.

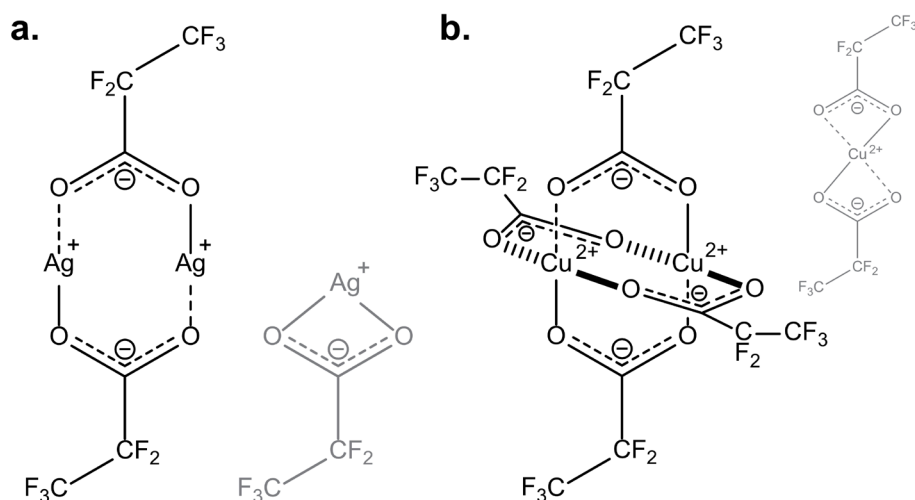


Figure 4-1 Molecular structure of (a) the  $\text{Ag}_2(\text{pfp})_2$  dimer and  $\text{Ag}(\text{pfp})$  monomer, (b)  $\text{Cu}_2(\text{pfp})_4$  and its monomer. The oxidation state of the metal ions is marked. Both precursors are perfluorinated carboxylates and form dimers in the solid state. In the case of silver, dimers and monomers can co-exist in the gas phase, see text.

$\text{Ag}_2(\text{pfp})_2$  and other perfluorinated silver(I) carboxylates were studied intensively already 20 years ago by Szlyk et al.<sup>87,88</sup> They reported the evaporation and subsequent thermal decomposition of those compounds and analyzed them using thermogravimetric analysis (TGA), variable temperature infrared spectroscopy (VT-IR) and gas-phase electron impact mass spectrometry (EI-MS). The TGA results showed the evaporation and decomposition of the silver carboxylates. For better understanding of the thermal behavior, both studies reported the molecular structures of the precursor present in the gas phase. Using VT-IR spectroscopy, the binding modes between  $\text{Ag}^+$  and  $\text{pfp}^-$  were determined and gas phase VT-IR spectra showed mostly the presence of monomeric species until the compound decomposed above 250°C.<sup>88</sup> VT-IR data at 200°C and EI-MS data at 180°C (same range as GIS temperature during FEBID) showed  $\text{Ag}_2(\text{pfp})^+$  and  $\text{C}_2\text{F}_5^-$  species and the presence of characteristic bands for bridging carboxylates (i.e. dimer) but more unidentately and chelating bonded carboxylates. This suggested that  $\text{Ag}_2(\text{pfp})_2$  sublimates as a dimer and simultaneously decomposes into monomers at 180-200°C. Below these temperatures, all three signals were very low, indicating little evaporation. In conclusion, it can be assumed that in the gas phase, the precursor is mostly present as a monomeric species (Figure 4-1a, grey).

$\text{Cu}_2(\text{pfp})_4$  was studied in a similar manner more recently by Piszczek et al.<sup>89</sup> In this report  $\text{Cu}_2(\text{pfp})_4$  was analyzed for comparison to its amine derivate. VT-IR spectra are only available at 280°C which is beyond the thermal decomposition temperature for the  $\text{Cu}_2(\text{pfp})_4$  complex. Some coordinated species were observed, showing that there were still copper containing entities in the gas phase. However, no dimers and only Cu(I) monomeric species were reported at these temperatures.

A more recent publication from Lacko et al.<sup>38</sup> studied the  $\text{Cu}_2(\text{pfp})_4$  complex in the gas phase by mass spectrometry using a cross-beam experiment. A beam of sublimated molecules,



evaporated at 140-160°C (same range as GIS temperature during FEBID), inside a UHV chamber is orthogonally irradiated by a monochromatic electron beam with low energy electrons (c.f. secondary electrons in the FEBID process). The electron induced dissociation fragments were analyzed by mass spectrometry. This group reports the presence of the  $\text{Cu}_2(\text{pfp})_4$  dimer in the gas phase. Monomeric species were only detected upon dissociative electron attachment and were not associated to thermal dissociation during evaporation.

The knowledge of the precursor structure in the gas phase is crucial to the understanding of the gas-assisted FEBID processes described in the following. The modelling of growth rates and description of possible dissociation mechanisms were based on this knowledge.

## 4.2 Experimental Details

Both precursors were synthesized by the group of I. Szymańska at the Nicolaus Copernicus University in Toruń, Poland.

Deposition was done in the Hitachi S3600 SEM with a W-filament on Si bulk substrates with 200 nm  $\text{SiO}_2$  (Ag deposition) and 300 nm AlN or 200 nm  $\text{SiN}_x$  layers (Cu deposition). As copper is known to diffuse into silicon substrates also at low temperatures,<sup>90</sup> the AlN and  $\text{SiN}_x$  layers were chosen as diffusion barrier to prevent copper diffusion into the substrate. Silver deposition with  $\text{Ag}_2(\text{pfp})_2$  was performed at elevated temperatures, both for sufficient precursor evaporation at GIS temperatures of 175°C and substrate temperatures of 160°C to prevent precursor condensation. For copper deposition with  $\text{Cu}_2(\text{pfp})_4$  the GIS was heated to 140°C and the substrate to 130°C. All deposits for TEM investigations were fabricated on thin, electron-transparent membranes.  $\text{Ag}_2(\text{pfp})_2$  on 10nm carbon membranes on a copper grid and  $\text{Cu}_2(\text{pfp})_4$  on a 50nm  $\text{SiN}_x$  membranes on a Si support. In order to enhance the deposition rate of  $\text{Cu}_2(\text{pfp})_4$  a thicker membrane was chosen and deposition for the TEM samples was performed in the Philips XL-30 SEM with a FEG source. The higher e-flux of the FEG source ( $1.59 \cdot 10^{21} \text{ e}^-/\text{cm}^2\text{s}$ ) increases the deposition rate ( $R(r) \propto f(r)$ , c.f. equation (2-8)) in comparison to the W emitter ( $1.45 \cdot 10^{19} \text{ e}^-/\text{cm}^2\text{s}$ ). Additionally, the thicker membrane emits more SEs than the 10nm carbon membrane, leading to a higher SE-flux contributing to the deposition rate.

## 4.3 Results and Discussion

### 4.3.1 Deposit Appearance and Chemical Analysis

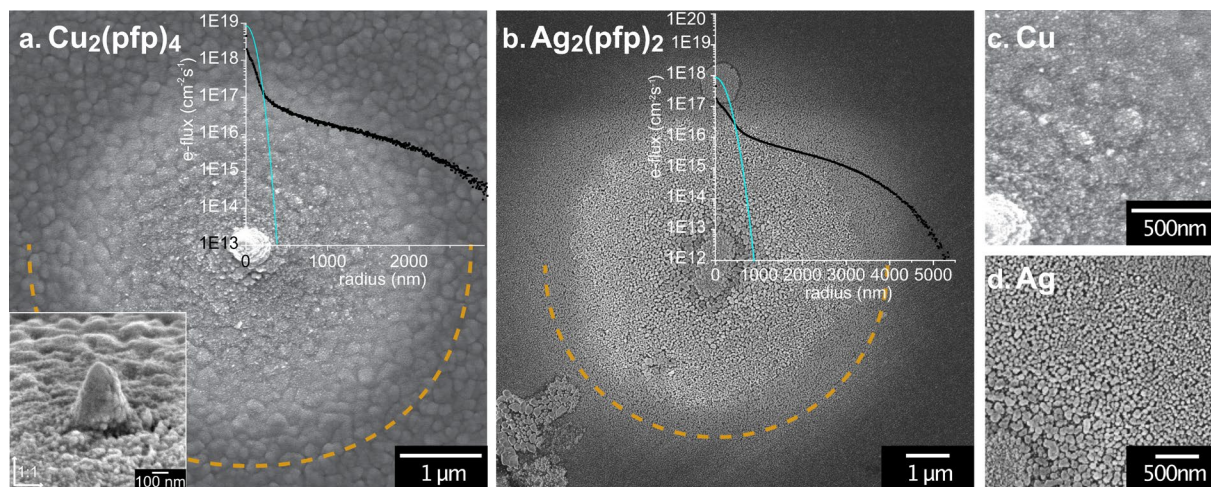


Figure 4-2 Spot deposits from (a)  $\text{Cu}_2(\text{pfp})_4$  on AlN/Si (inset: 60° tilt view of center) and (b)  $\text{Ag}_2(\text{pfp})_2$  on nat.  $\text{SiO}_2/\text{Si}$ . Overlay: radial flux distribution of PE (teal) and BSE (black) from MC simulations. (c) Higher magnification of the Cu deposit center. (d) Higher magnification of the Ag deposit center. Total electron dose for deposition: Cu 0.83  $\mu\text{C}$  @20keV, Ag 0.15  $\mu\text{C}$  @25keV. The yellow line marks the theoretical maximum exit range of BSEs at the respective beam energy.

A simple experiment with which multiple phenomena can be studied is the deposition of a single spot by irradiating one position for a prolonged amount of time. In this work, spot deposits were fabricated from  $\text{Cu}_2(\text{pfp})_4$  and  $\text{Ag}_2(\text{pfp})_2$  on AlN/Si and native  $\text{SiO}_2/\text{Si}$  respectively. Note that the substrate for copper deposition required a diffusion barrier (c.f. section 4.2), limiting the choice of material.

Figure 4-2 depicts the spot deposits from the two precursors. They were deposited with a total electron dose of 0.83  $\mu\text{C}$  at a beam energy of 25 keV for  $\text{Cu}_2(\text{pfp})_4$  and 0.15  $\mu\text{C}$  at 20 keV for  $\text{Ag}_2(\text{pfp})_2$ .

As visible from Figure 4-2a-b, both deposits have a similar appearance featuring a center and a halo region. Each halo region extends almost to the maximum exit range of BSEs as theoretically calculated for each beam energy and substrate according to Okayama-Kanaya<sup>53</sup> (yellow dashed line). For the silver deposition, a thin contrast is visible beyond this radius. When zooming into the central regions of each structure (Figure 4-2c-d), it becomes visible, that the center and halo deposition vary in their appearance. While the copper deposition features a 3-dimensional tip growth in the center (see inset in a), the outer deposition is 2-dimensional and consists of small, high-contrast grains. The silver deposit on the other hand shows no 3-dimensional growth. However, there is a clear distinction in crystallite size between the central and halo deposit as apparent from Figure 4-2d.

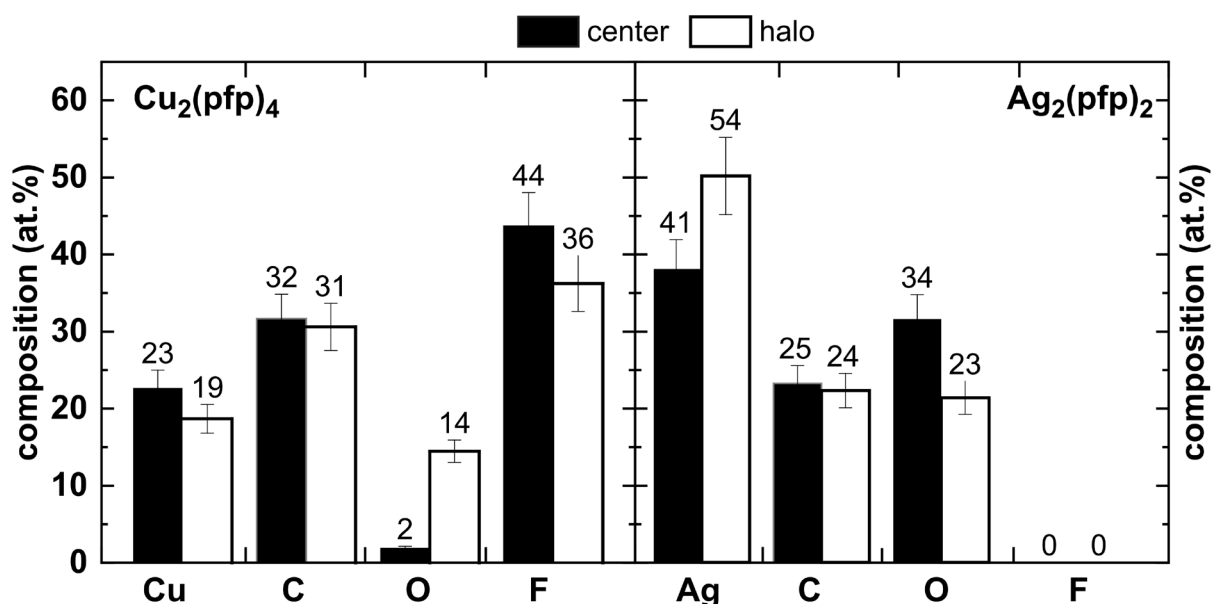


Figure 4-3 EDX results from local measurements on the spot deposits. Filled: measured in the center of the structures; empty: measured in the halo regions of the structures. Left: fabricated from  $\text{Cu}_2(\text{pfp})_4$ ; right:  $\text{Ag}_2(\text{pfp})_2$ . The results are background and thin film corrected. PE energies: 3/16keV for Cu, 5/7/10keV for Ag.

The chemical composition was analyzed in both regions, center and halo, separately. The bar charts in Figure 4-3 display the background and thin film corrected results of the energy dispersive X-ray spectroscopy (EDX) quantification.

The right bar chart shows the quantification results for the structure fabricated from  $\text{Ag}_2(\text{pfp})_2$ . While the carbon and fluorine signals do not change with the deposition region, the metal content does. More silver is detected in the halo region, while the oxygen content increases for the center. The main contaminants for both regions are carbon and oxygen. In contrast to the copper spot, no fluorine was detected in the silver deposit. Apparently, there is a change in dissociation paths for each region when it comes to  $\text{Ag}_2(\text{pfp})_2$ . Contrarily, only little change from one region to another was observed with  $\text{Cu}_2(\text{pfp})_4$ . As evident from the left bar chart, all elements in the deposit from  $\text{Cu}_2(\text{pfp})_4$  have comparable values within the measurement uncertainty, except for oxygen. Carbon and fluorine are with ~30 at.% and ~40 at.% the main contaminants. Oxygen is only present in the halo region of the structure.

As the copper precursor  $\text{Cu}_2(\text{pfp})_4$  is the analogue to  $\text{Ag}_2(\text{pfp})_2$ , the first expectation was a similar deposition behavior. However, the metal content and appearance of the copper structure did not change significantly between the two regions. In contrary, the metal content is constant within the uncertainty of the measurement. A higher e-flux in the beam center led to a higher growth rate than in the halo, so that a 3D tip was formed in the center (Figure 4-2a, inset). The halo region features a notably higher amount of oxygen, which was absent in the central area. The thinner halo region might be stronger affected by post-experiment oxidation during the short transfer time from the deposition to the analytical tool (~2min). Thicker

deposits have a larger volume which is protected against oxidation. After long storage in atmosphere, also the thicker center regions suffered from oxidation.

The variation of crystallites observed in the different regions of the deposits (Figure 4-2) can be attributed to the varying electron flux in the different areas. Figure 4-2a and b include the radial flux distribution of the BSE and PE in each dot deposit, as obtained from Monte Carlo (MC) simulations (c.f. Chapter 3.2). From these MC simulations, the growth rates and deposit shape could be simulated, following the continuum model of FEBID growth (c.f. Chapter 2.1.2):

$$R(r) = V \cdot \frac{sJ}{sJ/n_0 + 1/\tau + \sigma f(r)} \cdot \sigma f(r) \quad (2-8)$$

and

$$Shape(r) = R(r) \cdot t_{tot} \quad (2-9)$$

The shape simulations for  $Cu_2(pfp)_4$  and  $Ag_2(pfp)_2$  are shown in Figure 4-4. Each shape was fitted to an AFM profile of the same ( $Cu_2(pfp)_4$ ) or comparable ( $Ag_2(pfp)_2$ ) dots, shown in grey. The shapes were simulated using both, the electron flux of SE1 (red, generated by the PE beam) and of SE2 (blue, generated by BSEs, see MC simulation). The SE1 flux was calculated by multiplying the PE flux of a Gauss shaped electron beam with the secondary electron yield  $Y_{SE}$ . Similarly, the SE2 flux was obtained by multiplying the radial BSE flux (from MC simulations) with  $Y_{SE}$  and the multiplication factor  $\beta$ . This factor accounts for the higher SE yield of BSEs and has a value  $\beta = 2-3$ .<sup>91</sup> In all simulations, this value was fixed to  $\beta = 2.2$ , since the experimental value was not known.

For each fit, the corresponding experimental data was used to set all parameters. The total molecule flux at the GIS nozzle exit  $J_{tot}$  was obtained from experimentally observed precursor mass loss (eq. (3-1)). The precursor flux available at the irradiation site  $J$  was determined with the GIS simulation (c.f. Chapter 3.1.2). The molecule flux  $J$  is another fit parameter for the central region (precursor limited) and was adjusted for the best fit. The values are in relatively good agreement with the calculated values, as described above. The deposit volume  $V$  was calculated using the deposit density  $\rho$  and molar mass  $M$  (eq. (2-7)). For  $Ag_2(pfp)_2$  deposits,  $\rho_{AgCOF} = 6.7 \text{ g/cm}^3$  (same value as in the Casino simulation and the thin film correction) and the molar mass of the deposit  $M(Ag_1C_{0.6}O_{0.85}F_0) = 129.14 \text{ g/mol}$  were chosen for the simulation. For the  $Cu_2(pfp)_4$  deposit the parameters were set to  $\rho = 3 \text{ g/cm}^3$  (based on literature values)<sup>75</sup> and  $M(Cu_2C_{3.3}O_{1.5}F_{3.8}) = 263.66 \text{ g/mol}$ , as was the composition in the oxidized halo deposit. The monolayer surface density  $n_0$  is the inverse molecule area  $A_{mol}$ . This area was obtained by measuring the largest atom distances in the molecule, using minimum energy calculations in Chem3D.

Finally,  $\sigma$  and  $\tau$  were not accessible experimentally and had to be adjusted to fit the shape to the AFM profile. Note that the shape of the Ag-deposit is very irregular due to the crystallite formation during the deposition process. The dot measured for this simulation featured large crystals at the central region, which are visible in the AFM profile (marked with the arrows). An AFM top view image is shown in the inset for illustration. The values are noted in the respective

graph in Figure 4-4a and b. The parameter space was studied by varying  $\sigma$  and  $\tau$  and show that the values chosen here were the best fit. The parameter space study, where different  $\sigma$  and  $\tau$  were fitted, is described in the Supporting Information (Chapter 9.3).

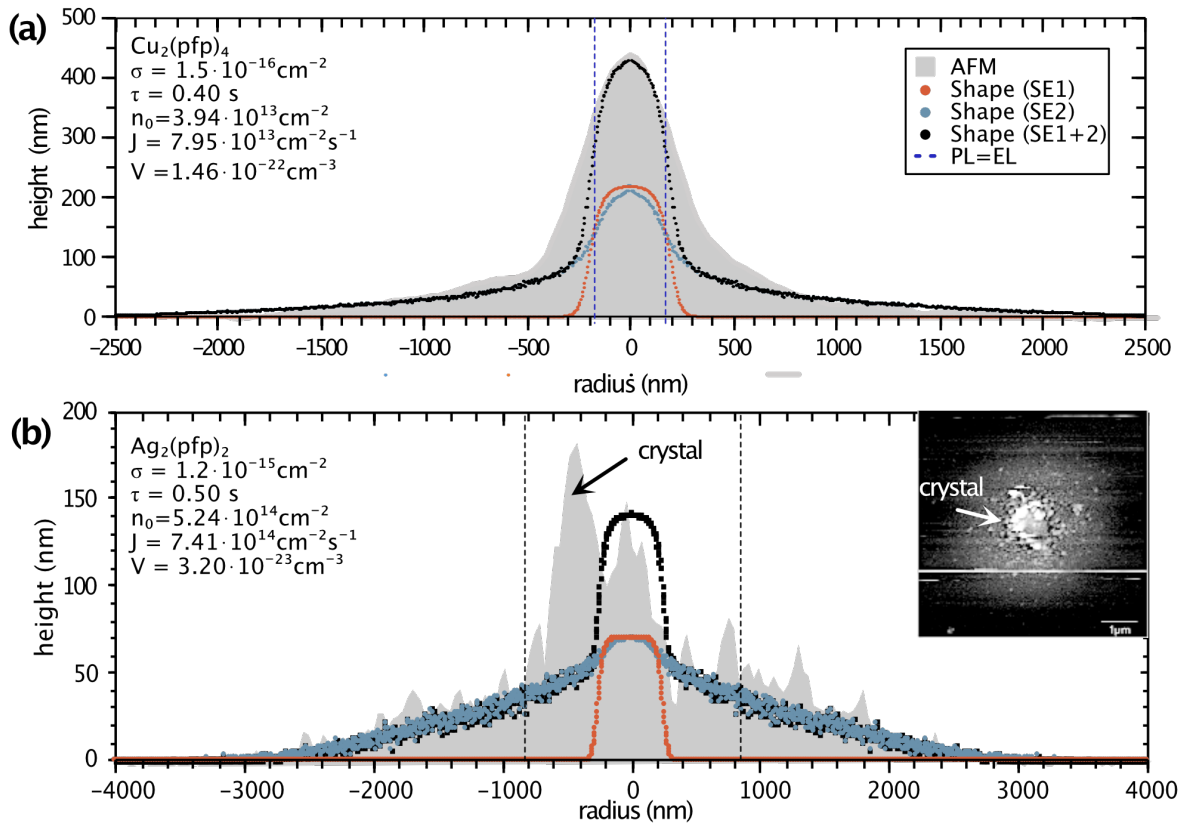


Figure 4-4 Shape simulations of the (a)  $\text{Cu}_2(\text{pfp})_4$  and (b)  $\text{Ag}_2(\text{pfp})_2$  dot deposits using MC simulations of the radial BSE distribution and the AFM profile of corresponding dot deposits. The shape can be simulated for the growth rate  $R(r)$  of the SE1 flux (red, generated from PE), the SE2 flux (blue, generated from BSE) and the sum of both (black,  $f(\text{SE1}+\text{SE2})$ ). The shape was fitted to the AFM profiles (grey) by adjusting  $\sigma$ ,  $\tau$  and  $J$ . The parameters specific to this fit are noted in the respective graph. Note that the Ag-dot in this AFM featured a large crystal in the central region (arrows) and was not fitted. Other parameters used for simulation see in text.

Figure 4-4a illustrates the shape of the  $\text{Cu}_2(\text{pfp})_4$  dot. The center shape could be fitted with the sum of SE1 and SE2 flux, while the halo was fitted with the SE2 flux only. This confirms that the halo deposit corresponds to the emitted BSEs and the generated SE2. The decaying halo thickness fits the decreasing BSE flux, so that a direct correlation can be presumed. Similarly, the  $\text{Ag}_2(\text{pfp})_2$  deposit was fitted. However, the central region was not represented well with this model. This was expected, since the continuous irradiation did not lead to 3D growth in the beam center. This is in contrast to the continuum model. Nevertheless, the halo simulation fit the AFM reasonably well. 3D growth was achieved only by optimizing the precursor replenishment by reducing the beam current and using exposure with a pulsed beam.<sup>57</sup>

A significant difference between halo and center deposit in the  $\text{Ag}_2(\text{pfp})_2$  dot still was observed in Figure 4-2b and d. The center consists of small, less distinguished crystallites which were

deposited by SEs produced by a large number of BSEs and PEs with high fluxes between  $2 \cdot 10^{16}$ - $9 \cdot 10^{17}$  e<sup>-</sup>/cm<sup>2</sup>s. In contrast, the halo material was deposited solely via the interaction of adsorbed precursor molecules with BSE and generated SE2, leading to the deposition of larger crystallites. The particles in the halo appear to be very similarly sized up to a distance of 3.25 μm from the center and slightly smaller until the maximum BSE exit range  $r_{BSE}$  (Figure 4-2b, dashed orange line). Beyond this radius the BSE flux drops below  $2 \cdot 10^{14}$  e<sup>-</sup>/cm<sup>2</sup>s and little or no more deposition is visible. Interestingly, the metal content of the Ag<sub>2</sub>(pfp)<sub>2</sub> was higher in the halo region as visible from Figure 4-3. We attribute this to a lower amount of co-deposited ligand material in this low e-flux region (between  $2 \cdot 10^{14}$  and  $2 \cdot 10^{16}$  BSE/cm<sup>2</sup>s). The e-flux of PE and BSE are plotted in the overlays in Figure 4-2a and b. Towards the center the e-flux was 1-2 orders of magnitude higher than in the halo. As explained in Chapter 2.1.2 (c.f. Figure 2-5) the spot deposits obtained through continuous irradiation, contain both growth regimes, electron limited (EL) and precursor limited (PL). Using  $\sigma$  and  $\tau$  from the shape simulations, it was possible to determine the radius  $r_{trans}$  where the PL regime transitions into the EL regime. The radius was calculated with the SE2 flux of the graphs in Figure 4-2a,b. The values are summarized in Table 4-1.

Table 4-1 Parameters for shape simulation and corresponding transition radius  $r_{trans}$  between EL and PL growth regime.

	$\sigma$ (cm <sup>-2</sup> )	$sJ/n_0 + 1/\tau$ (s <sup>-1</sup> )	radius of transition $r_{trans}$ (nm) ( $\sigma f(r) = sJ/n_0 + 1/\tau$ )	corresponding radii
Cu <sub>2</sub> (pfp) <sub>4</sub>	$1.5 \cdot 10^{-16}$	4.52	$231 \pm 2$	$\simeq$ FW (99.9%)
Ag <sub>2</sub> (pfp) <sub>2</sub>	$1.2 \cdot 10^{-15}$	3.42	$797 \pm 10$	$\simeq 1.5 \cdot \text{FW}(99.9\%)$

The transition radius  $r_{trans}$  for Cu<sub>2</sub>(pfp)<sub>4</sub> measured roughly the size of FW(99.9%), so that the PL regime ends with the edges of the PE beam. Similarly,  $r_{trans}$  for Ag<sub>2</sub>(pfp)<sub>2</sub> was at about 1.5·FW(99.9%). This corresponds very well with the optical change in crystallinity in both deposits. The 3D tip of the copper containing deposit ends at this radius. Also, the crystal size of the silver deposit changes significantly from small clusters to larger crystals at the calculated radius. The different deposition appearances can therefore be attributed to the two different growth regimes. The central parts are deposited in the precursor limited regime (PL) and the halo in the electron limited regime (EL).

However, a significant composition change was only observed for the silver deposit, as explained above. The central region has a higher concentration of contaminants than the halo. This was previously observed for FEBID dots fabricated with a different Ag(I) carboxylate precursor (silver dimethylbutyrate). Also there the silver content within the PE beam area was lower than in the halo.<sup>19</sup> According to literature though, the EL region should be less pure than the PL region (see Chapter 2.1.4). Here however, the EL region exhibits a higher metal purity. This effect was explained by desorption driven growth:



*deposit center:*  $1/\tau \ll \sigma f(r)$

more dissociation than desorption

*deposit halo:*  $1/\tau \geq \sigma f(r)$

less dissociation than desorption

Höflich et al.<sup>19</sup> suggested that adsorbates initially dissociate through electron interaction into deposited metal atoms and volatile, yet still physisorbed ligands. Due to the high electron flux within the PE beam area, deposition is taking place in the PL regime. However, the desorption rate of these volatile ligands is lower than their dissociation rate, resulting in co-deposition and a higher carbon concentration. Outside the PE beam area, in the EL regime, the adsorbates still dissociate by electron impact into deposited metal atoms and volatile physisorbed ligands. Yet the desorption rate of the ligands is larger than their further dissociation by the much lower electron flux, preventing co-deposition and leading to purer silver deposits.<sup>19</sup> This could also account for larger silver crystals in the halo region that could grow without carbon contamination.

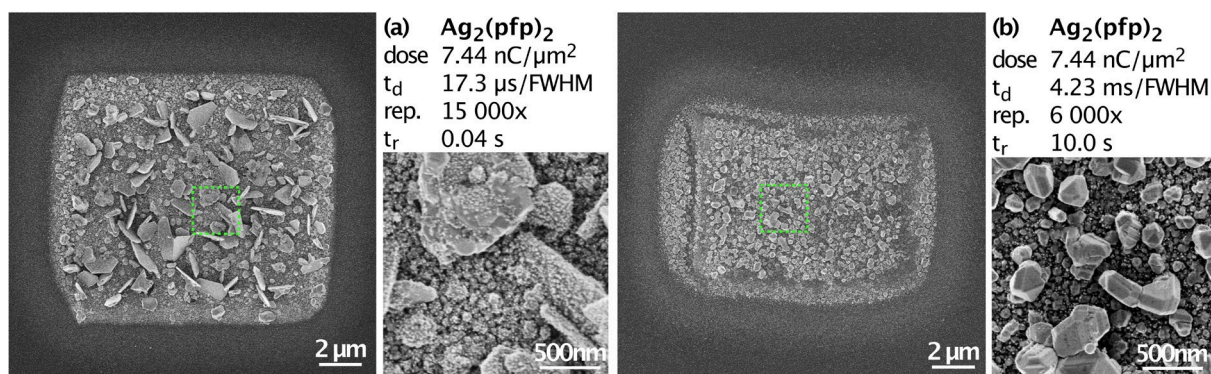


Figure 4-5 Square deposits from  $\text{Ag}_2(\text{pfp})_2$  with varying deposition parameters. (a) short  $t_d$ , short  $t_r$ , (b) long  $t_d$ , long  $t_r$ . The green line marks the region of the high magnification image shown next to each micrograph. Dose: electron dose per area;  $t_d$ : dwell time per FWHM; rep.: number of frames repeated for deposition;  $t_r$ : refreshment time per FWHM for precursor replenishment.

Based on the large differences in the two deposition regions observed for  $\text{Ag}_2(\text{pfp})_2$ , the influence of precursor refreshment times ( $t_r$ ) and dwell times ( $t_d$ ) were studied to see how ligand co-deposition was further influenced by the number of electrons per area and/or time unit. The metal contents and crystallite sizes of 2D area deposits were studied. Figure 4-5 depicts the SEM images of two deposits fabricated with long (a) and short (b) dwell times. While the e-dose was kept constant,  $t_r$  and  $t_d$  were varied. The silver deposits change their appearance radically. On first sight it is visible that for short refreshment times as in Figure 4-5a two-dimensional platelet crystals at a length scale of  $\geq 1 \mu\text{m}$  were formed. With a 250 times longer refreshment time voluminous three-dimensional crystals (length scale  $\approx 200\text{--}500 \text{ nm}$ ) were obtained (Figure 4-5b). Having a more detailed look at the adjacent high magnification images, one can see the same small crystallites ( $\approx 10\text{--}25 \text{ nm}$ ) on top of the platelets as were observed before in the center of the spot (Figure 4-2d). In contrast, the voluminous crystals of Figure 4-5b were not covered with these small crystallites. While the crystallite growth relies on the

absence of co-deposited ligands, this seems not to be the case for the metal content within the structure. The silver content of approximately 70 at.% (Table 4-2) for both deposits is comparable within the uncertainty of the measurement. The porosity of the structures however, can lead to larger measurement deviations (see Chapter 3.4). Still, the similar chemical composition might be due to the fact, that the dwell times are extremely long in both cases, leading to the same deposition regime.

The refreshment time does not only play an important role in the precursor replenishment at the irradiated areas, but also impacts the desorption rate of ligands and/or fragments after initial bond scission. Since the desorption rate  $1/\tau$  is constant, the number of desorbing molecules can only be increased with longer  $t_r$ . More ligands/fragments therefore desorb before being co-deposited, as discussed before, allowing the growth of large crystals (Figure 4-5b).

The crystal sizes seem to depend on the agglomeration time the silver particles have on the hot surface. A short  $t_r$  seems to have stopped the agglomeration of silver atoms to larger crystals and only small crystallites and platelets could be formed.

Table 4-2 Detailed EDX quantification results of the 2D structures from Figure 4-5 with varying parameters. Dose: electron dose per area;  $t_d$ : dwell time per FWHM;  $t_r$ : refreshment time per FWHM

Deposit dose, $t_d$ , $t_r$	element (at.%) <sup>a</sup>			
	Ag	C	O	F
<b>(a) Ag<sub>2</sub>(pfp)<sub>2</sub></b> <b>7.44 nC/μm<sup>2</sup>, 17.3 μs, 0.04 s</b>	76	20	1	3
<b>(b) Ag<sub>2</sub>(pfp)<sub>2</sub></b> <b>7.44 nC/μm<sup>2</sup>, 4230 μs, 10s</b>	69	24	2	5

<sup>a</sup> The measurement uncertainty is  $\pm 5$  at.%

The crystalline nature of the deposits was determined by studying the internal structure of FEBI deposition on thin membranes with transmission electron microscopy (TEM). Ag<sub>2</sub>(pfp)<sub>2</sub> was deposited on a thin carbon membrane and Cu<sub>2</sub>(pfp)<sub>4</sub> on a 50nm SiN<sub>x</sub> membrane (see section 4.2). Figure 4-6 summarizes all TEM data for both precursors. Figure 4-6a and e show the dark field scanning transmission electron microscopy (DF-STEM) images of a single line deposited with 25keV with each precursor. This energy was chosen to achieve a highly focused beam to deposit a line as thin as possible. Note that the Ag deposit was fabricated with the less focused W-filament. For both cases crystallites can be distinguished within the line and deposition is limited to  $67 \pm 2$  nm and  $1.0 \pm 0.1$  μm respectively (c.f. orange marker). Since there is no significant electron scattering as in bulk substrates, no halo deposition is observed and the line width correspond to the FW(99.9%) of the respective primary beam (69 nm for Cu, 1.05 μm for Ag).

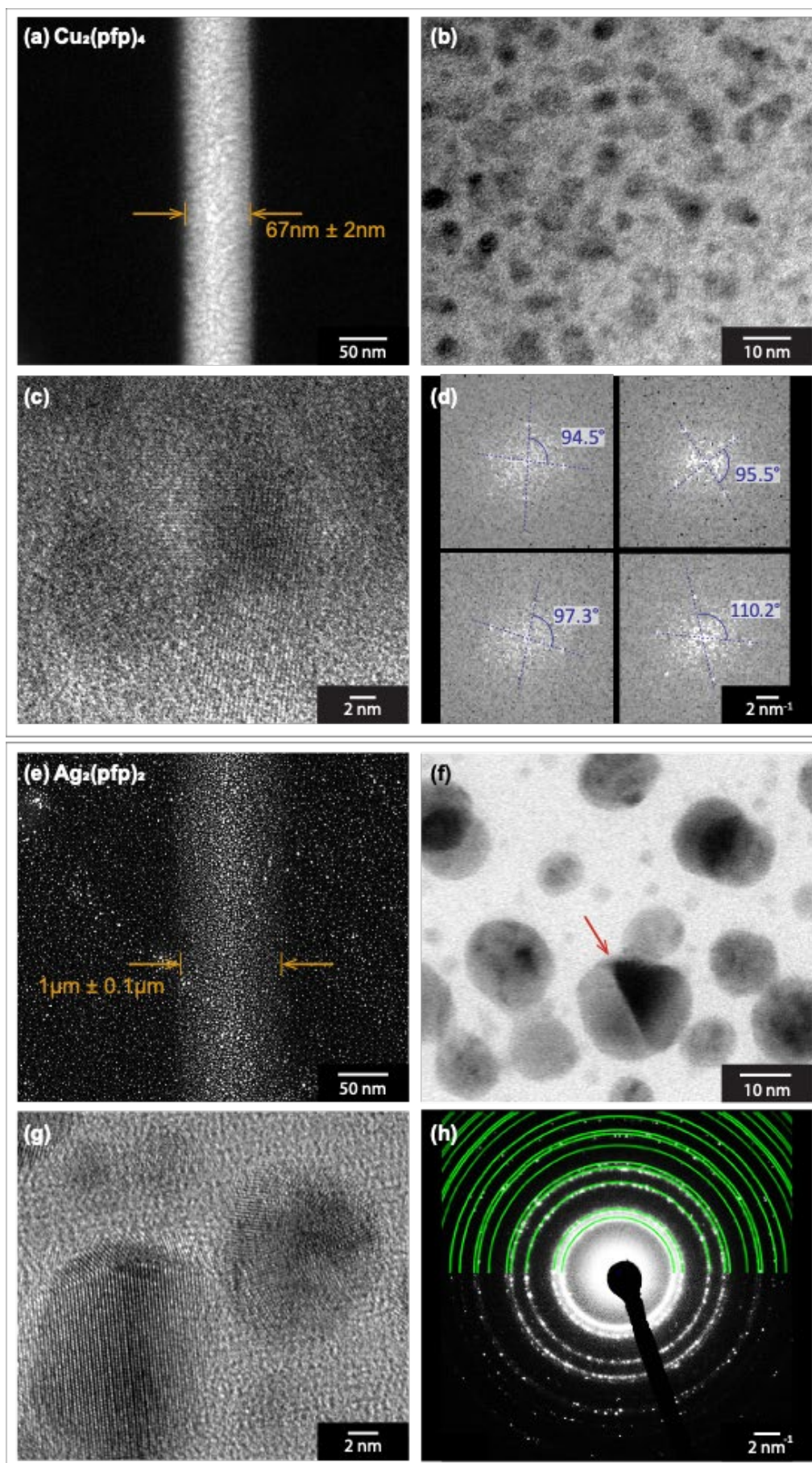
Figures b and f show bright field STEM (BF-STEM) images with higher magnification of individual crystallites. The average crystallite diameter was determined to be  $4.20 \pm 0.95$  nm in the copper deposit and  $17.81 \pm 5.47$  nm in the silver deposit. HR-TEM images of two particles



each (Figure 4-6 c and g) exhibit distinct lattice planes for both metals. The SAED pattern for precise elemental determination was only obtained for Ag and is depicted in Figure 4-6h. It shows clear diffraction rings, confirming the crystalline nature of the particles within the deposit. Furthermore, the fcc pattern of pure silver (green overlay) matches the diffraction pattern well, giving no doubt that pure silver crystallites were obtained in this FEBID process. For the elemental determination of the copper containing crystallites, local FFT patterns were obtained from the HR-TEM images and are shown in Figure d. Lattice plane angles could be obtained from these patterns and are marked in blue. According to the EDX quantification results, the Cu:O ratio in the halo regions indicates the formation of copper(II)oxide (CuO). Since the halo deposit is only about 10 – 80 nm thin, and therefore of comparable thickness to the structures on the membrane, post-experiment oxidation of copper during the sample transfer from the deposition microscope to the analytical tool lead to the formation of CuO. This assumption is further backed by the FFT patterns from the HR-TEM images in Figure 4-6c-d. From these patterns, lattice plane angles were determined as characterization measurement. Three of four angles measure 94.5°, 95.5° and 97.3° and match those from monoclinic CuO very well (95.663° viewed down  $\langle 1-10 \rangle$  and  $\langle 110 \rangle$ ; 95.33° down  $\langle 0-11 \rangle$  and  $\langle 011 \rangle$ ). In one case, the angle of 110.2° matches the cubic Cu<sub>2</sub>O when viewed down the  $\langle 110 \rangle$  axis. Still, we could exclude these particles being pure Cu which also crystallizes in a cubic structure, due to the larger interplanar width measured here (most  $>3 \text{ \AA}$ ). It can therefore, in combination with the EDX data from Figure 4-3, be concluded that two oxides are formed, from which monoclinic CuO is the most likely.

(right)

Figure 4-6 (a-d) TEM analysis of deposits from  $\text{Cu}_2(\text{pfp})_4$  on a 50 nm thick  $\text{SiN}_x$  membrane. (a) DF-STEM image of a 25 keV and 1.35 nA FEBID line. The line width is indicated in orange. Note the avoidance of the halo deposit. (c) BF-STEM image showing metal(oxide) crystallites within the FEBID deposit on the membrane. (d) HR-TEM image of two individual metal(oxide) grains on the membrane with distinct lattice planes. (d) FFT of ROIs on HR-TEM image with measured lattice plane angles (blue). (e-h) TEM analysis of deposits from  $\text{Ag}_2(\text{pfp})_2$  on a carbon membrane. (e) DF-STEM image of a 25 keV and 0.5 nA FEBID line. The line width is indicated in orange. (f) BF-STEM image showing metal crystallites within the deposit. Twinning is marked with the red arrow. (g) HR-TEM image of two individual metal grains on the membrane with distinct lattice planes. (h) SAED pattern on the line deposit. The diffraction pattern clearly confirms crystallinity of the deposit. The fcc silver diffraction pattern (green) affirms the pure silver structure of the deposited crystallites.



### 4.3.2 Electron Induced Dissociation Paths of $\text{Ag}_2(\text{pfp})_2$ and $\text{Cu}_2(\text{pfp})_4$ in FEBID

Based on the findings from the SEM, TEM, EDX and scan parameter studies in the previous section detailed dissociation mechanism for both precursors can be suggested. In order to estimate the fragmentation pattern and number of elements desorbed per precursor molecule, the EDX quantification results from Figure 4-3 were normalized to two metal atoms (as in the pristine precursor). In combination with the gas phase and mass spectrometry studies for  $\text{Cu}_2(\text{pfp})_4$ <sup>38,89</sup> and  $\text{Ag}_2(\text{pfp})_2$ <sup>87,88</sup> the dissociation paths are proposed in Figure 4-7. It should be noted, that these mechanisms were proposed on the basis of mechanisms reported in literature. The nature of desorbing and deposited species could not be determined in the scope of this work.

Table 4-3 Elemental ratio of deposits in the center and halo region derived from EDX quantification results (Figure 4-3) and normalized to two metal atoms.\* Desorbing species were determined from the difference between pristine precursor and as deposited structures. For  $\text{Cu}_2(\text{pfp})_4$  only the central measurement is considered, as this is the non-oxidized structure.

			normalized elemental ratios*				desorbing species <sup>b</sup>		
			M <sup>a</sup>	C	O	F	$\Delta\text{C}$	$\Delta\text{O}$	$\Delta\text{F}$
$\text{Ag}_2(\text{pfp})_2$	prist. precursor		2	6	4	10			
	as deposited	center	2	1.2	1.7	0	4.8	2.3	10
		halo	2	0.9	0.9	0	5.1	3.1	10
$\text{Cu}_2(\text{pfp})_4$	prist. precursor		2	12	8	20			
	as deposited	center	2	2.8	0.2	3.8	9.2	7.8	16.2

\* Atomic ratios have an uncertainty of  $\pm 0.1$ .

<sup>a</sup> M = Ag, Cu

<sup>b</sup>  $\Delta\text{X} = \text{X}(\text{prist.}) - \text{X}(\text{as dep.})$

Figure 4-7a shows the possible dissociation of one  $\text{Ag}_2(\text{pfp})_2$  molecule during the FEBID process where the substrate is heated to  $T_s=160^\circ\text{C}$  in either the center (top) or halo (bottom) region. The number of deposited and desorbed fragments is estimated from the element ratios listed in Table 4-3. They are based on the EDX quantification results from Figure 4-3 and normalized to 2 silver and copper atoms as in the pristine precursors.

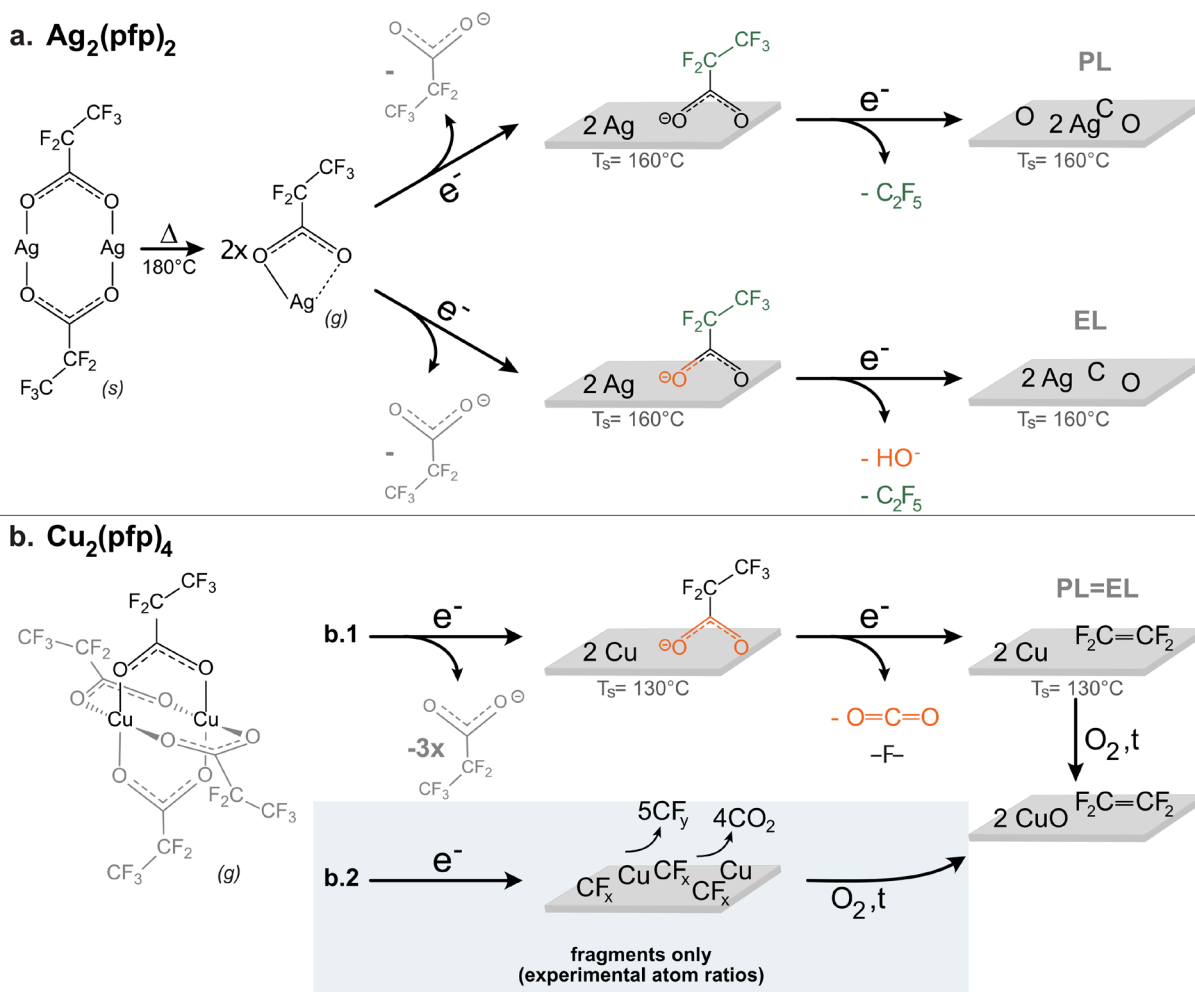


Figure 4-7 Proposed, simplified electron induced dissociation paths based on Table 4-2. (a)  $\text{Ag}_2(\text{pfp})_2$  dissociation upon evaporation and upon electron irradiation in the center and halo region. (b.1)  $\text{Cu}_2(\text{pfp})_4$  dissociation (non-oxidized center). The first dissociation scheme summarizes all pfp<sup>-</sup> ligands which can potentially leave intact. The second dissociation scheme illustrates the dissociation of the remaining ligand into the co-deposited carbonaceous matrix. An additional oxidation step occurring in ambient atmosphere over time  $t$  at room temperature is shown for Cu. (b.2) Note that the actual dissociation path may also occur via fragmentation steps of the intact ligands. Fragmentation mechanism based on measured ratio of elements.

The element ratio indicates that the deposit consists mainly of silver atoms with small traces of carbon and oxygen. This is consistent with the TEM data where silver crystallites are discernible from the surrounding (Figure 4-6e-g). In order to evaporate the  $\text{Ag}_2(\text{pfp})_2$  precursor, it had to be heated to 180°C, leading to the sublimation and simultaneous decomposition of the precursor into monomers (c.f. section 4.1). The subsequent electron induced dissociation is illustrated in two steps: The Ag-L bond scission and desorption of one intact pfp<sup>-</sup> ligand. Subsequently the dissociation of the remaining ligand into the perfluorinated alkyl chain  $\text{C}_2\text{F}_5$  and the remaining carbon and oxygen. Note that the co-deposition of a carbon-oxygen matrix might also be occurring by fragmentation of the other ligands. Particularly in the center region,

i.e. higher electron density or shorter desorption times, more co-deposition was observed, leading to the deposition of smaller Ag crystals (Figure 4-2a and Figure 4-5).

The same approach was taken for  $\text{Cu}_2(\text{pfp})_4$ . The dissociation of one  $\text{Cu}_2(\text{pfp})_4$  molecule during the FEBID process, with a substrate heated to  $130^\circ\text{C}$ , is shown in Figure 4-7b.1. Here the illustration was based additionally on the gas phase experiments from Lacko et al.<sup>38</sup> where the specific dissociation path was reported with the help of mass spectrometry. The ligand loss in the first dissociation step was reported similarly. These bonds were broken through dissociative ionization (DI) finally leading to the release of pure copper ions. While three of the four ligands desorb from the surface (Figure 4-7b, grey), the fourth one gets dissociated by the electron beam, releasing fluoride ( $\text{F}^-$ ) and  $\text{CO}_2$  as also reported in the gas phase during dissociative electron attachment (DEA). The  $\text{CO}_2$  release was reported for electron induced dissociation for other perfluorinated carboxylic acids in the condensed phase.<sup>92</sup> For more Cu(II) carboxylate species, electron induced dissociation mechanisms were proposed from the solid state irradiation. A metal organic framework (MOF) of Cu(II)-oxalate, a simple di-carboxylate, was irradiated with low energy electrons and formed copper nanoparticles under the release of  $\text{CO}_2$ .<sup>93</sup> Also other Cu(II)carboxylate MOFs were studied in the same manner, all releasing  $\text{CO}_2$  and CO upon electron irradiation.<sup>94,95</sup> For precursors in this work, the proposed  $\text{CO}_2$  formation is furthermore in line with the high electronegativity of fluorine, through which the C-C bond between  $\text{C}_2\text{F}_5$  and  $\text{COO}^-$  is weakened and broken easily. This is illustrated and discusses later (Figure 4-9b).

Additionally, the copper deposition includes an important third step: In contrast to silver, copper oxidizes easily in atmospheric conditions. The incorporated crystallites in the deposit (c.f. Figure 4-6a-b) oxidize at room temperature when stored in air and form CuO in a CF matrix. The oxidation was further suggested through TEM measurements (Figure 4-6d). For completeness, a non-specified fragmentation path is illustrated in Figure 4-7b.2, based purely on the elemental ratios. Here, the matrix could be described with an average sum formula of  $\text{C}_3\text{F}_4$  after electron-induced dissociation, but the exact configuration is not known to us; therefore, they are described as " $\text{CF}_x$ " ( $0 \leq x \leq 3$ ) for simplification. Following the same approach, the average desorbing species have the sum formula  $\text{C}_9\text{F}_{16}\text{O}_4$ . Highly simplified, the desorbing fragments are described as " $\text{CO}_2$ " and " $\text{CF}_y$ " ( $2 \leq y \leq 3$ ). The same approach holds true for  $\text{Ag}_2(\text{pfp})_2$ .

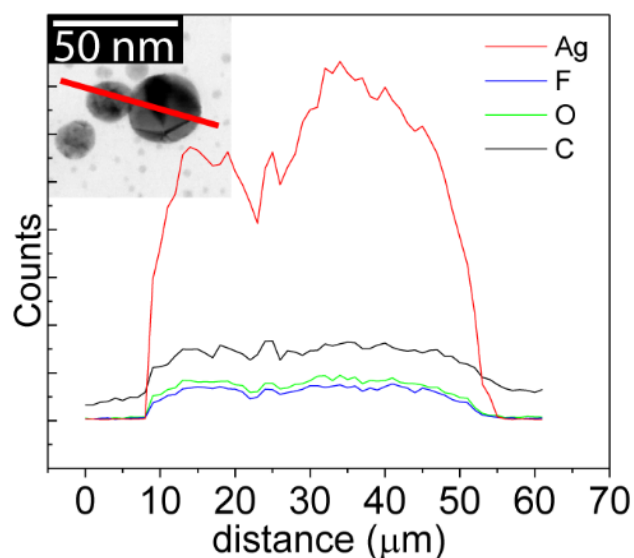


Figure 4-8 Local EDX line scan over two individual Ag particles on carbon membrane. Inset: The corresponding BF-STEM image and scan position. No oxidation is visible for the particles.

Surprisingly, the silver deposits always showed an oxygen signal in the EDX analysis. As demonstrated through SAED (Figure 4-6h) and local EDX scans in the TEM (Figure 4-8), it is not silver that oxidizes. Even over longer periods of time (the TEM samples were stored several weeks in air before being measured), the crystallites exhibit a distinct  $\text{Ag}^0$  pattern and no sign of oxidation. Therefore, the co-deposition of the ligand remaining after the first dissociation step, seems to be different from the one described for  $\text{Cu}_2(\text{pfp})_4$  at the same step. The silver deposit loses all fluorine, while the fresh copper deposit shows no sign of oxygen.

In both cases, the dissociation of the  $\text{pfp}^-$  ligand has the possibility to release  $\text{CO}_2$  via the C-C bond scission, as discussed above. During this dissociation, also  $\text{CF}_3$  can be released. This seems to be a common fragmentation path as shown by EI-MS.<sup>87,88</sup>

#### 4.3.3 Differences between $\text{Ag}_2(\text{pfp})_2$ and $\text{Cu}_2(\text{pfp})_4$

The direct comparison of the quantification results of the deposits from both precursors most obviously arises the question why the metal contents differ so significantly. The most prominent difference between them is the metal center and their oxidation state. As visible from Figure 4-1, the copper compound is a dinuclear  $\text{Cu}^{2+}$  complex and the silver complex a dinuclear  $\text{Ag}^+$  complex with the metal oxidation state +1. This leads to the fact that the copper carboxylate has the double amount of ligands in order to form a neutral compound.

Previous publications have shown that  $\text{Cu}_2(\text{pfp})_4$  is evaporated as a dimer, while  $\text{Ag}_2(\text{pfp})_2$  is primarily present as monomers in the gas phase.<sup>38,87–89</sup> Even though the metal to ligand ratios do not change by dimerization, the  $\text{Ag}_2(\text{pfp})_2$  monomers might have the advantage of having less bonds to cease, since a portion of monomers was shown to be the unidentately bonded complex. The chances to dissociate a single Ag-O bond in that case are much higher, than the chance to dissociate all 8 Cu-O bonds. On the one hand, more electrons might be needed to dissociate more metal-ligand bonds in dimers. On the other hand, multi-ligand dissociation by



one electron was observed in gas-phase experiments, reducing the number of electrons per molecule for deposition.<sup>96</sup> However, this process might not be valid for carboxylates.

The bigger amount of carbon incorporation in the Cu deposit, however, might not be attributed exclusively to the larger number of ligands per metal center. Looking at the chemical nature of the coordination complexes, some well-established theories might apply.

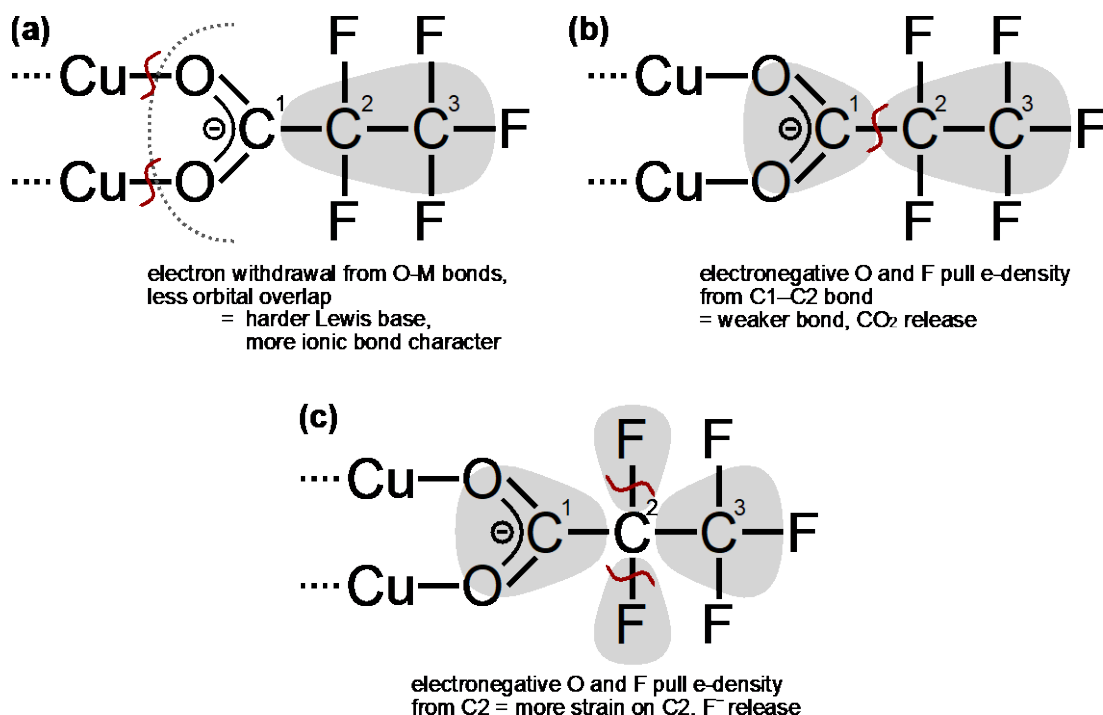


Figure 4-9 (a) Electron withdrawal from  $\text{COO}^-$  group through  $-\text{CF}_2-\text{CF}_3$  chain, leading to harder Lewis base than non-fluorinated carboxylate, i.e. less orbital overlap with metal ion. (b) Electron withdrawal from C1-C2 bond through electronegative oxygen and fluorine, weakening the bond and releasing  $\text{CO}_2$ . (c) Electron withdrawal from C2 by  $-\text{COO}^-$  an,  $-\text{CF}_3$  and F, leading to fluoride release.

A generally well applicable theory in coordination chemistry is the "hard and soft acids and bases" concept (HSAB theory) from Pearson.<sup>97,98</sup> It describes metal (ions) as electron acceptors, i.e. Lewis acids, and ligands as electron donors, i.e. Lewis bases. According to their electronegativity or polarizability these species are then categorized as "hard" or "soft".

According to the HSAB theory, small, highly charged and less polarizable transition metals are *hard* acids due to their tightly bound electron spheres ("small, hard shelled spheres"). Larger, more polarizable and heavier transition metals are *soft* acids and have less strongly bound valence electrons in a more diffuse cloud. Accordingly, ligands are electron donors, i.e. Lewis bases. Small, more electronegative ligands are classified as *hard* donors, and larger, low charged entities as *soft* donors. Table 4-4 summarizes the relevant ions for the precursor complexes used in this work.



Table 4-4 Classification of the ions forming the precursor complexes into the HSAB theory.

$\text{Ag}^+$	$\text{Cu}^{2+}$	$(\text{pfp})^-$
large ionic radius	smaller ionic radius	small electron cloud (high e- affinity of fluorine)
easily polarizable	less polarizable	not polarizable
prefers covalent bonding	-	prefers ionic bonding
soft acid	intermediate acid	hard base

These entities form more stable coordination compounds when combining ions with an alike character. They form either strong ionic bonds (*hard-hard*) or covalent bonds through good orbital overlap (*soft-soft*).

In the case of  $\text{Cu}_2(\text{pfp})_4$  and  $\text{Ag}_2(\text{pfp})_2$  we have the same type of ligand ( $\text{CF}_3\text{-CF}_2\text{-COO}^-$ ) coordinated to a different metal center ( $\text{Cu}^{2+}$  vs.  $\text{Ag}^+$ ). Carboxylic acids are generally classified as hard donors due to the electronegative oxygen forming the M-L bond. It prefers not to share its electrons with the metal center forming bonds with a more ionic character. Furthermore, the perfluorination of the alkyl chain makes the ligands even harder. Figure 4-9a illustrates how the electronegativity of fluorine pulls the electron density towards the alkyl chain and away from the  $\text{-COO}^-$  entity. This makes orbital overlapping and covalent bonding more difficult giving the M-O bond a more ionic character and make this Lewis base even harder than its non-fluorinated analogues.

The metal ions of the compounds used in this work have a different hardness. Cu and Ag are in the same transition metal group 11. Following the trends throughout the periodic system of elements, metal ions become softer down the group. Also, the ion radius of  $\text{Ag}^+$  is larger than of  $\text{Cu}^{2+}$ , making it more polarizable and therefore a softer acid.

Looking at the rule stated above, that hard bases prefer hard acids, we can say that the bond between  $\text{Ag}^+$  and  $\text{O}_2\text{CC}_2\text{F}_5^-$  is generally weaker than between  $\text{Cu}^{2+}$  and  $\text{O}_2\text{CC}_2\text{F}_5^-$ . The bond dissociation enthalpies  $\Delta H^0$  reported by Deng et al. for ion-molecule exchange experiments in the gas phase with non-fluorinated carboxylates affirm this statement<sup>99</sup>. They showed that  $\Delta H^0(\text{Ag-complex}) < \Delta H^0(\text{Cu-complex})$ . This means, the Ag-L bond is easier to dissociate, i.e. by electrons, giving the  $\text{pfp}^-$  ligand more chances to desorb as a free acid from the substrate. In contrast, the Cu-L bond is more difficult to cease giving the ligands less chance to escape before the next electron dissociates it. In combination with the higher amount of ligands per metal atom, this explains the higher concentration of carbon-fluorine material deposited with the  $\text{Cu}_2(\text{pfp})_4$  precursor as shown experimentally.

## 4.4 Conclusion

This chapter showed the electron beam induced deposition of two group 11 carboxylates. The two compounds,  $\text{Ag}_2(\text{pfp})_2$  and  $\text{Cu}_2(\text{pfp})_4$ , were used as a FEBID precursor for the first time.

Stationary dot deposits of both precursors led to the deposition of central spots with the beam's FW(99.9%) and a large surrounding halo deposit induced by BSEs. Both dot deposits were simulated using the continuum FEBID model, so that the transition between two growth regimes could be assigned to the regions. In both cases the PL growth ended with the FW(99.9%) of the beam, which corresponded to the visible deposit change, i.e. 3D growth or crystallite size. The halo could be assigned to the EL growth regime.

$\text{Ag}_2(\text{pfp})_2$  showed a strong sensitivity towards changing electron densities within the beam center and the halo regions, with higher metal contents > 54 at.% in the halo. In contrast to literature knowledge, the metal purity was improved in the EL region. Additionally, the metal content could be improved when scanning the electron beam with long refreshment times so that large silver crystals were obtained with an average silver content of about 70 at.%. This was in line with previously reported influence of ligand/fragment desorption.  $\text{Cu}_2(\text{pfp})_4$  did not exhibit the same sensitivity and resulted in metal contents up to 23 at.%.

TEM investigations of deposits from both precursors revealed the internal structure of those deposits to be nanocrystallites embedded in an amorphous matrix. Ag formed crystallites with an average size of about 18 nm and Cu formed smaller grains of about 4 nm size. SAED confirmed the formation of pure silver crystallites, while the copper crystallites oxidized in atmosphere, as suggested from bulk EDX measurements and FFT patterns of the TEM images. Chemical composition studies were used to describe the electron induced dissociation mechanism of both precursors. The elemental ratios suggested for both compounds, that the electron induced dissociation led to the initial dissociation and desorption of one to three full  $\text{pfp}^-$  ligands and therefore more than 80% of atoms of the pristine precursor.

When depositing  $\text{Ag}_2(\text{pfp})_2$ , no fluorine was incorporated in the deposits. In contrast, deposits from  $\text{Cu}_2(\text{pfp})_4$  featured fluorine as a main contamination compound. Therefore, it was suggested that the dissociation of  $\text{Cu}_2(\text{pfp})_4$  was less complete than of  $\text{Ag}_2(\text{pfp})_2$ . This was ascribed to both, the different metal to ligand ratios of the compounds, but also the larger discrepancy between the hard ligand and soft silver ion according to the HSAB theory. Additionally, it was reported in previous studies, that  $\text{Cu}_2(\text{pfp})_4$  sublimates as an intact dimer, while  $\text{Ag}_2(\text{pfp})_2$  decomposes upon evaporation, forming chelating and monodentately bound monomers, facilitating the dissociation of the Ag-L bond.

Last, the small copper crystallites suffered from easy oxidation upon exposure to atmosphere, drastically deteriorating the metal purity in the deposits. This effect was particularly strong in very thin deposits, where the crystallites were not protected by a carbonaceous matrix, such as was the case for thicker structures and the spot center.

These findings can be useful for the improvement of pure silver and copper deposition. While the silver concentration and crystal growth could be directly influenced by increasing  $t_r$  and reducing  $t_d$ , the copper content was not accessible through these parameters. Contrarily to most volatile FEBID precursors reported in literature, the increase of  $t_d$  for  $\text{Ag}_2(\text{pfp})_2$  led to decreasing metal contents, giving more precedence to the particular FEBID behavior of low-volatility carboxylate precursors. Additionally, this chapter showed how the change of metal

center can drastically alter the electron induced mechanisms in the FEBID process. Also, the results can help to identify and improve the design of other metalorganic copper precursors and the challenges linked to the deposition of copper containing nanostructures.



## 5 Copper(II) Compounds for Focused Electron Induced Deposition

This chapter includes results and passages from the publication:

Berger et al., *ACS Appl. Electron. Mater.* 2020, 2, 7, 1989–1996.

### 5.1 Copper precursors in Focused Electron Beam Induced Deposition

The deposition of copper has been a field of interest due to its preferable performances in (micro)electronics. There has been already a variety of copper compounds reported as FEBID precursors, of which all are  $\beta$ -diketonates.

Early works focused mostly on the use of the fluorinated compound copper(II) bis-hexafluoroacetylacetonate  $\text{Cu}(\text{hfac})_2$ ,<sup>32–35</sup> which was already known as a CVD precursor for Cu thin films<sup>100–107</sup>. It is a fluorinated derivative of  $\text{Cu}(\text{acac})_2$ , a copper complex with relatively high sublimation temperatures between 130 and 140°C as shown for atomic layer deposition<sup>108,109</sup> especially in comparison to  $\text{Cu}(\text{hfac})_2$ , which has an exceptionally high vapor pressure between  $4.34 \cdot 10^{-3}$  and  $1.2 \cdot 10^{-2}$  mbar at room temperature despite being a solid.<sup>110</sup> However, FEBI deposition from  $\text{Cu}(\text{hfac})_2$  was never reported to exceed approx. 15 at.% in the as-deposited state.<sup>32–35</sup>

Derivatives of  $\text{Cu}(\text{hfac})_2$ , such as the Cu(I) complexes  $(\text{hfac})\text{Cu}(\text{vtms})$  (vtms = vinyltrimethylsilane) and  $(\text{hfac})\text{Cu}(\text{dmb})$  (dmb = 3,3-dimethyl-1-butene) have also been reported.<sup>32,33</sup> Both precursors showed sufficiently high volatility at room temperature due to their liquid state. Since they incorporated less carbon atoms in their ligands than  $\text{Cu}(\text{hfac})_2$ , and Cu(I) compounds exhibit higher reactivity, higher metal contents were expected and, indeed, achieved of up to 25 at.%. The compounds' high reactivity is, however, also a drawback. It makes them more difficult to handle as they are highly air-sensitive and decompose easily, even at room temperature. Especially  $(\text{hfac})\text{Cu}(\text{dmb})$  tends to disproportionate into  $\text{Cu}(\text{hfac})_2$  and  $\text{Cu}^0$ . Therefore, no stable precursor transport in the gas phase can be guaranteed, which is crucial for controlled FEBI deposition. As a consequence, the reproducibility with these Cu(I) complexes is diminished.

Nevertheless,  $(\text{hfac})\text{Cu}(\text{vtms})$  is reported regularly in FEBID and FIBID literature as copper precursor for low resistivity deposits<sup>77</sup> and 3D deposition<sup>32,33,111</sup>.

The search for copper precursors suitable for FEBID was continued and a  $\beta$ -ketosterate was reported by Haverkamp et al.<sup>36</sup> They recently published the deposition from the non-fluorinated  $\text{Cu}(\text{tbaoac})_2$  (tbaoac = tertbutyl-acetoacetonato) also resulting in a metal content of around 25 at.%.

This chapter will treat the direct comparison of the copper carboxylate  $\text{Cu}_2(\text{pfp})_4$  with previously reported Cu(II) compounds, i.e.  $\text{Cu}(\text{tbaoac})_2$  and  $\text{Cu}(\text{hfac})_2$ , as well as never reported results from its derivatives  $[\text{Cu}_2(\text{pfp})_4(\text{EtNH}_2)_2]$  and  $[\text{Cu}_2(\text{pfp})_4(\text{tBuNH}_2)_2]$ . This work will concentrate on

the chemical and structural differences of the precursor compounds themselves and the deposits achieved from them.

## 5.2 Comparing Cu(II) Carboxylate Derivatives and $\beta$ -Diketonates

In metal FEBID, two processes are of interest: a) the evaporation and transport of the intact precursor molecule and b) the most efficient dissociation of the metal-ligand (M-L) bond to achieve pure metal structures. Figure 5-1 summarizes the molecular structures of the Cu(II) compounds investigated in the scope of this work, and the corresponding temperatures of the gas injection system (GIS)  $T_{GIS}$ . This temperature is based on FEBID experiments described in the following sections, at which sufficient precursor evaporation was observed experimentally to deposit copper-containing structures.

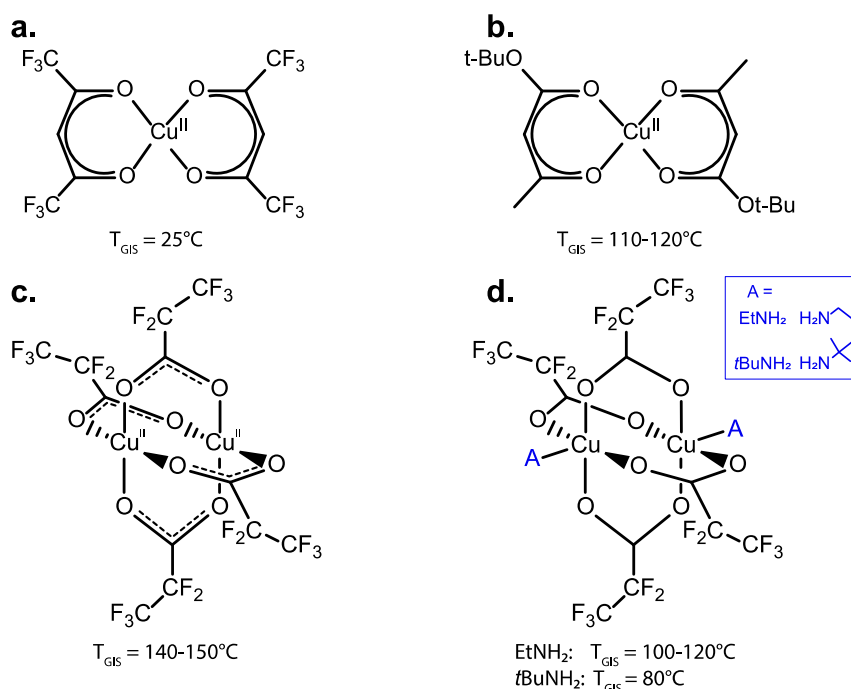


Figure 5-1 Chemical structures of 5 different Cu(II) precursors as proposed by literature (see text). (a)  $\text{Cu}(\text{hfac})_2$  (b)  $\text{Cu}(\text{tbaoac})_2$  (c)  $[\text{Cu}_2(\mu\text{-O}_2\text{CC}_2\text{F}_5)_4]$  referred to as  $\text{Cu}_2(\text{pfp})_4$  and (d)  $[\text{Cu}_2(\mu\text{-O}_2\text{CC}_2\text{F}_5)_4(\text{EtNH}_2)_2]$  and  $[\text{Cu}_2(\mu\text{-O}_2\text{CC}_2\text{F}_5)_4(t\text{BuNH}_2)_2]$  with A being the N-bound amine ligands, the amine structures are depicted in the inset (blue). The corresponding evaporation temperatures  $T_{GIS}$  of each precursor is marked beneath the structure.

For a direct comparison of the precursor's behavior during deposition, a series of experiments with comparable parameters was conducted. The following sections discuss the appearance and chemical composition of square deposits, fabricated with each precursor using (I) short dwell times of 2-3  $\mu\text{s}$ /FWHM and (II) long dwell times of 114-123  $\mu\text{s}$  using two different electron sources. A tungsten thermal emitter (W-filament) and a field emission gun (FEG) were used as electron sources to study any possible difference in deposition due to the electron flux (e-flux). The W-filament had a significantly lower e-flux of  $1.45 \cdot 10^{19} \text{ e}^-/\text{cm}^2\text{s}$  in comparison to the FEG with  $1.59 \cdot 10^{21} \text{ e}^-/\text{cm}^2\text{s}$ . As explained in the theoretical part, the deposition rate  $R(r)$

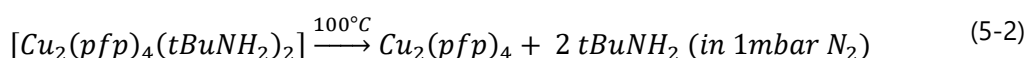
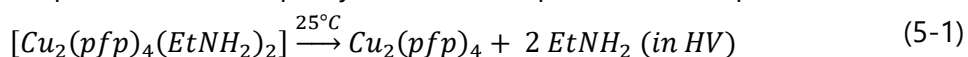
during the FEBID process is directly proportional to the electron flux  $f(r)$ . Additionally, it was shown for the silver carboxylate precursors Ag(dimethylbutyrate) and Ag<sub>2</sub>(pfp)<sub>2</sub> that the e-flux has a direct influence on the deposit composition, due to stronger ligand co-deposition in high e-flux regions.<sup>19,112</sup> This effect was already discussed in Chapter 4 for Ag<sub>2</sub>(pfp)<sub>2</sub> and Cu<sub>2</sub>(pfp)<sub>4</sub> and will be extended to the other four copper precursors in the following sections

.

### 5.2.1 Influence of Inter- and Intramolecular Interactions on the FEBID Process

The evaporation of a compound depends highly on intermolecular interactions, such as Van der Waals (VdW) interactions, hydrogen bridges and electrostatic interactions. As discussed in Section 5.1, fluorination significantly increases the volatility of a compound. Fluorine is the most electronegative element in the periodic table and has therefore a large negative inductive effect (-I effect) within compounds. The -CF<sub>2</sub>-CF<sub>3</sub> groups in Cu<sub>2</sub>(pfp)<sub>4</sub> and its amine derivatives [Cu<sub>2</sub>(pfp)<sub>4</sub>(EtNH<sub>2</sub>)<sub>2</sub>] and [Cu<sub>2</sub>(pfp)<sub>4</sub>(*t*BuNH<sub>2</sub>)<sub>2</sub>], as well as the -CF<sub>3</sub> group in Cu(hfac)<sub>2</sub> pull the electron density towards the ligand ends and away from the rest of the molecule. This weak polarization leads to an accumulation of more negative charge on the ligands, leading to self-repellent properties, which decreases the intermolecular interaction, and increases the volatility of the whole complex.

In the case of [Cu<sub>2</sub>(pfp)<sub>4</sub>(EtNH<sub>2</sub>)<sub>2</sub>] and [Cu<sub>2</sub>(pfp)<sub>4</sub>(*t*BuNH<sub>2</sub>)<sub>2</sub>], the evaporation temperature was observed to be 15-65 K lower than for the non-aminated complex. The amine ligands bonding at the axial position of each copper atom add to the overall size of the coordination complex, leading to more repulsion. This trend is also observable when comparing both amine complexes: the compound with the bulkier *tert*-butyl substituent showed sufficient sublimation at temperatures 10-20 K lower than its ethyl derivative. However, it should be noted that both amines were reported to detach partly from the complex at low temperatures:<sup>39,89</sup>



This raised doubts if these precursors can be transported to the gas phase as intact molecules. However, via supplementary mass spectrometry it was shown that for both cases intact molecules were present in the gas phase, with only minor losses of the amine ligands.

Lastly, the question of why Cu(tbaoac)<sub>2</sub> evaporates at similarly low T<sub>GIS</sub> as Cu<sub>2</sub>(pfp)<sub>4</sub> arises, even though it is an entirely fluorine-free complex and it was stated that fluorination significantly decreases the evaporation temperature. The answer lies in the same principle as previously explained for the amine ligands. The *tert*-butyl moiety on the tbaoac ligand is especially bulky, leading to steric effects. In the solid state, the molecules are less densely packed due to the steric hindrance of the large ligands, decreasing intermolecular VdW-interactions and, thus, facilitating evaporation. Furthermore, the symmetry was broken by introducing an ester residual. This decreased symmetry also decreases molecule packing and possible oligomerization, increasing volatility.<sup>113,114</sup>

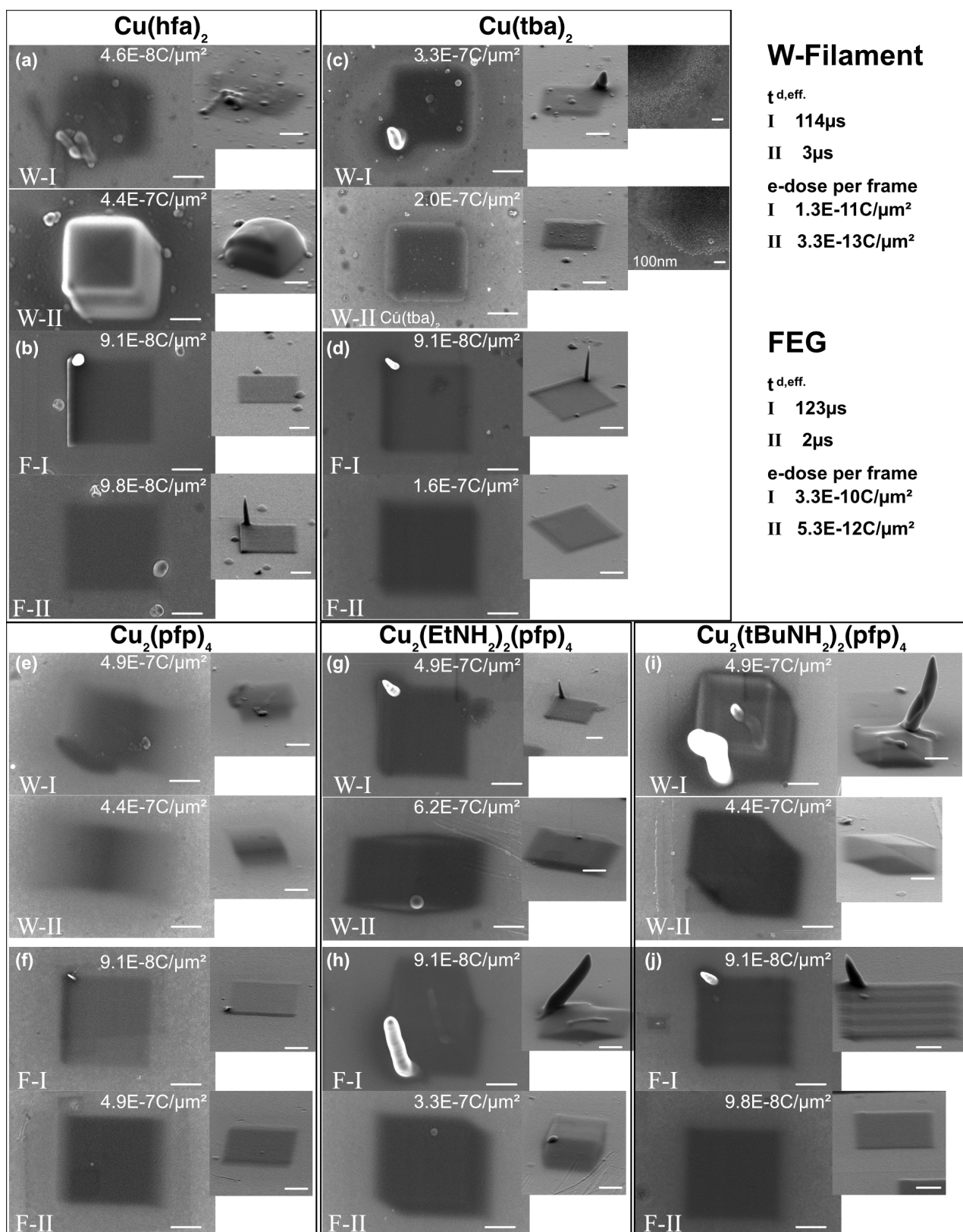


### 5.2.2 Deposit Morphology and Deposition Efficiency/Rate

Figure 5-2 shows square deposits fabricated from the five different Cu(II) precursors illustrated in Figure 5-1. Each precursor was deposited with two different electron sources and two dwell times. The effective dwell time  $t_{d,eff}$  describes the time the electron beam dwells per FWHM without overlap, and is marked in the lower left corner of each SEM image (I/II). The numbers are noted next to the figure. For each source, all structures were deposited with the same electron dose (e-dose) per frame, as noted in Figure 5-2. The total e-dose is noted in the upper right corner of each SEM image and gives an estimate about the deposition rate of each precursor. Generally, it can be observed that for both  $t_{d,eff}$  (W and FEG), sufficient and comparable amounts of material were deposited at similar total electron doses for all precursors. Except for  $\text{Cu(hfa)}_2$ , where Figure 5-2a shows that with longer  $t_{d,eff}$ , significantly more material was deposited, also due to the total e-dose, which is one order of magnitude larger than the short  $t_{d,eff}$ . For the latter case, very little material was deposited. Therefore, it can be assumed that  $\text{Cu(hfac)}_2$  needs high electron doses or a high electron flux to deposit. This is why the structures, which were fabricated with the FEG, are better defined (Figure 5-2b, F-I and F-II). The same trend was observed for  $\text{Cu}_2(\text{pfp})_4$ , where high e-flux deposition with the FEG resulted in better deposits, even at lower total e-doses. This effect is particularly visible when comparing Figure 5-2e (W-I) and f (F-I). The most striking difference in appearance was observed for  $\text{Cu(tbaoac)}_2$ . Low e-flux deposits from the W-filament exhibited high contrast grains within the deposition area, indicating the presence of copper crystallites. Contrarily, high e-flux structures do not show these features. This difference might arise from the slightly higher deposition temperatures used in the W-SEM ( $T_{G,W} = 120^\circ\text{C}$ ,  $T_{S,W} = 134^\circ\text{C}$  /  $T_{G,F} = 110^\circ\text{C}$ ,  $T_{S,F} = 122^\circ\text{C}$ ), so that deposited copper could diffuse and form crystallites, while in the high e-flux system this diffusion was slower. Additionally, more carbon co-contamination inhibited this diffusion. All other precursors did not exhibit any notable difference shown in the SEM images, neither when depositing with a low e-flux (W-filament) or high e-flux (FEG), nor with short (I) or long (II)  $t_{d,eff}$ .

(right)

Figure 5-2 Area deposits from different Cu(II) precursors: (a-b)  $\text{Cu(hfa)}_2$ , (c-d)  $\text{Cu(tbaoac)}_2$ , (e-f)  $[\text{Cu}_2(\text{pfp})_4]$ , (g-h)  $[\text{Cu}_2(\text{pfp})_4(\text{EtNH}_2)_2]$  and (i-j)  $[\text{Cu}_2(\text{pfp})_4(\text{tBuNH}_2)_2]$ . The respective total electron dose of each structure, as well as the tilt view ( $60^\circ$ ) are noted. All structures were deposited at 20 keV primary energy and a beam current of 0.59 nA (W-filament) and 1.35 nA (FEG). For each source, the effective dwell times  $t_{d,eff,i}$ , as well as the electron dose per frame are noted in the image. Note that the pillar deposit at the corner of each I-deposit originates from the scanning strategy of the instrument, as the beam pauses there after each frame (see Methods). If not noted differently, all scale bars show 1  $\mu\text{m}$ .



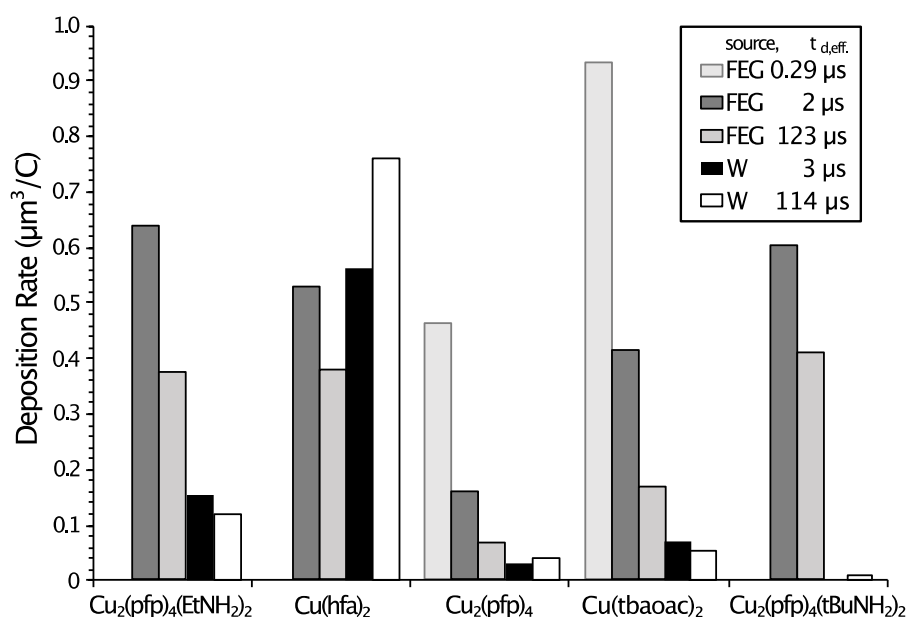


Figure 5-3 Deposition rates of all five Cu(II) precursors with different sources and effective dwell times  $t_{d,eff.}$ .

AFM measurements were performed for all structures to determine the deposition rate  $R$ . The results are summarized in Figure 5-3. The deposition rate per total electron dose is shown as a bar chart. The deposition of pillars, as visible in the SEM images, was not considered in the growth rates, as they do not belong to the effective deposition time and total electron dose of the squares. They rather represent the waiting/refreshment time of each frame. This artefact is discussed later in this chapter.

The carboxylates and Cu(tbaoac)<sub>2</sub> had a higher growth rate at higher electron densities and fluxes, i.e. the FEG source. This, however, is not surprising, since the e-flux of the FEG source is  $1.59 \cdot 10^{21} \text{ e}^-/\text{cm}^2\text{s}$ , which is two orders of magnitudes larger than for the W emitter ( $1.45 \cdot 10^{19} \text{ e}^-/\text{cm}^2\text{s}$ ). With a larger e-flux, the dissociation rate is even larger than the desorption rate, leading to more deposited material. As all experiments were performed with the same acceleration voltage on the same substrates, the energies of SEI and SEII were not changed, so  $\sigma$  did not change either. The only variable in the equation is the electron flux  $f$ , which is larger for the FEG than for the W source.

Furthermore, shorter effective dwell times resulted in faster growth rates than the in the case of long  $t_{d,eff.}$ . This is especially visible for the very short  $t_{d,eff.} = 0.29 \mu\text{s}$ . Cu<sub>2</sub>(pfp)<sub>4</sub> deposited with a significantly slower rate than the aminated analogues Cu<sub>2</sub>(pfp)<sub>4</sub>(RNH<sub>2</sub>)<sub>2</sub> (R = Et, tBu). This trend is in accordance with the time dependent solution of the growth rate  $R(t_d)$ , as described in eq. (2-11) (see Figure 2-7a), where the growth rate increases and saturates for shorter dwell times. Cu(hfac)<sub>2</sub> does not follow this trend and exhibited a much higher growth rate for the low e-flux source (W-filament) and long  $t_{d,eff.}$ . This is also clearly visible in the SEM images in Figure 5-2a, where a thick square deposit is visible.

Generally, all precursors show comparable growth rates between  $\sim 0.4\text{-}0.65 \mu\text{m}^3/\text{C}$  for short  $t_{d,eff.}$  (FEG). Cu<sub>2</sub>(pfp)<sub>4</sub> poses the only exception. This could be attributed specifically to this

experimental series. Here, the  $\text{Cu}_2(\text{pfp})_4$  structures are considerably thinner than in any previous experiments. As the parameter window of this precursor is extremely small ( $T_{\text{GIS}}$ ,  $T_{\text{S}}$ ), the temperatures in this series might not have been favorable, i.e. slightly elevated substrate temperatures might have led to higher desorption rates and decrease the deposition rate. Lower GIS temperatures could decrease the precursor flux, also decreasing the growth rate. The ideal temperature window was experienced to be narrow.

Additionally, Figure 5-2 shows that during the deposition with a low e-flux, a drift was present, leading to elongated deposits, rather than squares (see especially c-e (W-II)). Since the depositions took place at elevated substrate temperatures of 90-135°C (see Methods), a thermal drift of the substrate can occur. In the W emitter SEM, deposition times were two to four times longer than in the FEG system. Therefore, the thermal drift has a significantly larger impact on long term depositions of around 60 min, than on shorter fabrications of around 15 min.

For all short  $t_{d,\text{eff}}$  structures (I), a distinct pillar deposit was observed in one corner of the square. It originated from the time the beam dwells at the beginning of each frame. This is an inherent issue of all SEM systems, where the beam pauses at the start of each scan. This issue was avoided for all W-II structures by defining a waiting spot at a certain distance from the square pattern in the external XENOS patterning machine (see Methods). The spot was therefore relocated. An example is visible in Figure 5-4 (arrows).

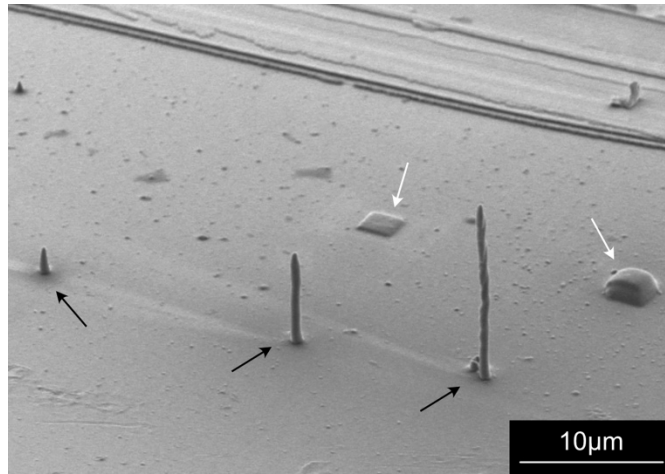


Figure 5-4 Overview image in tilted view (60°) of the  $\text{Cu}(\text{hfac})_2$  sample fabricated with the W-filament SEM. The pillars (black arrows) were programmed to be situated in distance to the squares (white arrows) as “waiting spots” to avoid pillar formation at the corner of the structure.

Unfortunately, the same approach was not feasible for W-I structures, as the short  $t_{d,\text{eff}}$  required extremely large repetition numbers between  $1 \cdot 10^6$  and  $1.5 \cdot 10^6$  repetitions, asking for a different deposition recipe, not allowing the external waiting spot. In the case of F-II deposits, no external waiting spot could be defined due to the lack of a sophisticated lithography system on the FEG SEM. Interestingly, there were no pillar deposits for long  $t_{d,\text{eff}}$ .

### 5.2.3 Chemical Analysis – Local EDX Measurements and Quantification

Table 5-1 Quantification results from local EDX measurements performed on area deposits fabricated with different effective dwell times  $t_{d,eff.}$  from four different Cu(II) precursors as specified in Figure 5-2. Each precursor was deposited with two different electron sources (W-filament, FEG) and two effective dwell times  $t_{d,eff.}$  each.<sup>a</sup>

at.% <sup>b</sup>	Cu(hfac) <sub>2</sub>				Cu(tbaoac) <sub>2</sub>			
	W		FEG		W		FEG	
	I	II	I	II	I	II	I	II
Cu	10	10	11	10	25	20	17	16
C	56	57	64	60	66	69	69	70
O	15	11	20	19	10	11	14	14
F	19	22	5	11	-	-	-	-
N	-	-	-	-	-	-	-	-
at.%	Cu <sub>2</sub> (EtNH <sub>2</sub> ) <sub>2</sub> (pfp) <sub>4</sub>				Cu <sub>2</sub> (tBuNH <sub>2</sub> ) <sub>2</sub> (pfp) <sub>4</sub>			
	W		FEG		W		FEG	
	I	II	I	II	I	II	I	II
Cu	13	13	16	12	15	16	15	13
C	48	48	56	55	55	57	58	60
O	9	10	10	11	8	10	11	10
F	19	19	12	10	17	12	11	11
N	11	10	7	12	6	6	5	5

<sup>a</sup>  $t_{d,eff.}$ : (W-I) 3  $\mu$ s; (W-II) 114  $\mu$ s; (F-I) 2  $\mu$ s; (F-II) 123  $\mu$ s, with the electron sources abbreviated with W for W-filament and for FEG for field emission gun.

<sup>b</sup> Uncertainty of EDX quantification results  $\pm$  5 at.%.

All structures were analyzed in terms of their chemical composition with local EDX measurements. The background and thin-film corrected quantification results for all shown deposits are summarized in Table 5-1. Please note, that for further chemical analysis results for Cu<sub>2</sub>(pfp)<sub>4</sub> in the following we will be referring to Ref. <sup>115</sup> and Chapter 4.

Generally, the metal content seemed not to be heavily influenced by the changing e-fluxes, as previously reported for several silver FEBID precursors.<sup>19,112</sup> For all precursors, the copper content fluctuates within the measurement uncertainty of 5 at.%, with Cu(tbaoac)<sub>2</sub> posing an exception. Overall, it is also observed, that the carbon content had a tendency to increase with the e-flux, i.e. deposits from the FEG SEM having more C incorporated than the comparable deposit from the W-filament. For all fluorine containing precursors, i.e. Cu(hfac)<sub>2</sub>, Cu<sub>2</sub>(EtNH<sub>2</sub>)<sub>2</sub>(pfp)<sub>4</sub> and Cu<sub>2</sub>(tBuNH<sub>2</sub>)<sub>2</sub>(pfp)<sub>4</sub>, the FEG structures exhibited less fluorine incorporation. This could be caused by more efficient C-F cleavage upon higher electron irradiation.

The latter is particularly pronounced for deposits from Cu(hfac)<sub>2</sub>. While all values ranged within the measurement uncertainty when comparing long and short  $t_{d,eff.}$ , slightly more C and O were deposited with high e-fluxes (F-I/FII). This can be assigned to the co-deposition of more hfac-

ligands with a higher electron density of a FEG and simultaneously more C-F bond dissociations.<sup>30</sup> The overall copper content remained at around 10 at.%.

$\text{Cu}(\text{tbaaac})_2$  represented an exception in the trend of W-filament vs. FEG deposition. In contrast to the  $\beta$ -diketonate, this fluorine-free precursor resulted in deposits with a higher copper content at a lower e-flux. This trend was also observed in the SEM, as visible from Figure 5-2b: crystallites with a high contrast could be distinguished from the background, pointing to the possibility of high copper contents. The local EDX quantification confirmed this assumption and showed ~23 at.% Cu content in the W-I and W-II structures. The main contamination was carbon (~68 at.%) and only low amounts of oxygen were incorporated (~10 at.%). Contrarily, a higher amount of oxygen (14 at.%) was co-deposited with the high e-flux of the FEG, reducing the copper content to ~17 at.% at stagnating carbon co-deposition, indicating the co-deposition of the full ligand. A more detailed dissociation pattern will be discussed later in this section.

$\text{Cu}_2(\text{EtNH}_2)_2(\text{pfp})_4$  exhibited little differences between the W and FEG structures. As mentioned above, fluorine contents were lower for the latter case (19 at.% vs. 11 at.%) due to higher carbon contents. In both cases, amine ligands were also incorporated in the structures.

Interestingly, all values lie within the measurement uncertainty for  $\text{Cu}_2(\text{tBuNH}_2)_2(\text{pfp})_4$ , which seemed to always dissociate in the same way, independently from the  $t_{d,eff}$  and e-flux.

However, when comparing the two aminated perfluorocarboxylates  $\text{Cu}_2(\text{EtNH}_2)_2(\text{pfp})_4$  and  $\text{Cu}_2(\text{tBuNH}_2)_2(\text{pfp})_4$ , similar copper contents were achieved, but the nitrogen percentages are significantly lower in the  $\text{tBuNH}_2$  structures. This difference can be assigned to the larger numbers of carbon atoms present in the  $\text{tBuNH}_2$ -ligand (4 C-atoms), which were equally embedded in the structures, as the smaller  $\text{EtNH}_2$  ligands (2 C-atoms). A better overview of how the different ligands and fragments are dissociated and co-deposited can be found in the following section.

## 5.2.4 Chemical Structure of Copper(II) Complexes and its Effect on Deposition

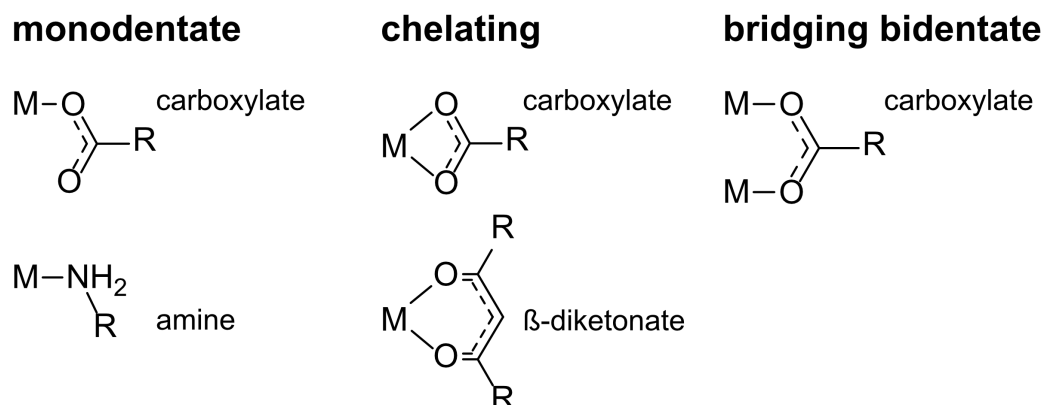


Figure 5-5 Relevant binding modes for coordination within  $\text{Cu}_2(\text{pfp})_4/[\text{Cu}_2(\text{pfp})_4(\text{RNH}_2)_2]$   $\text{R}=\text{Et}, ^t\text{Bu}/\text{Cu}$   $\beta$ -diketonates and  $\beta$ -ketosterates.

Ligands can coordinate to a metal center in different ways. Relevant to the cases presented in this work are monodentate, bidentate chelating and bidentate bridging binding modes. The respective options are illustrated in Figure 5-5. In monodentate coordination, the ligand binds over one atom to the metal center, as it is the case for the amine ligands in  $[\text{Cu}_2(\text{pfp})_4(\text{RNH}_2)_2]$  ( $\text{R}=\text{Et}, ^t\text{Bu}$ ). If a ligand has multiple coordination sites, it may either form a chelate ring around a single metal center, or bridge two metal ions. Here, the bidentate carboxylate and  $\beta$ -diketonate ligand could chose the chelating binding mode where two oxygen atoms bind to one metal center, or a dinuclear species, as in the bridging bidentate mode is possible. The latter is common for carboxylate complexes, while the  $\beta$ -diketonate and  $\beta$ -ketosterate coordinate in a chelating mode.  $\text{Hfac}^-$  and  $\text{tbaoac}^-$  form 6-membered chelate rings with the  $\text{Cu}^{2+}$  ion. For the formation of a neutral complex, two ligands are required to obtain  $\text{Cu}(\text{hfac})_2$  and  $\text{Cu}(\text{tbaoac})_2$ .

Each binding mode has a different coordination strength. Generally, monodentate ligands are weakly bound, followed by bidentate bridging ligands. Chelating ligands again form the most stable complexes within this group. However, these stabilities seem to be mostly relevant in the evaporation process or ligand substitution reactions in solution. In gas-phase and especially upon electron irradiation, other dissociation paths may be accessible.

Upon investigation of the deposits of both, the  $\beta$ -diketonate  $\text{Cu}(\text{hfac})_2$  and  $\beta$ -ketosterate  $\text{Cu}(\text{tbaoac})_2$ , it is visible that the ligands seem to detach well from the metal center even though they are bound quite strongly in the coordination complex via bidentate chelating into a stable, 6-membered ring. Surprisingly,  $\text{Cu}(\text{tbaoac})_2$  resulted in deposits with considerably higher metal content than  $\text{Cu}(\text{hfac})_2$ , even though the  $\text{tbaoac}$ -ligand is bulkier and has more carbon and oxygen than the  $\text{hfac}$ -ligand. The  $\text{tbaoac}$ -ligands can be expected to detach easier, as they are asymmetric, opposing to the symmetric  $\beta$ -diketonate  $\text{Cu}(\text{hfac})_2$ . The higher metal content of 25 at.% for  $\text{Cu}(\text{tbaoac})_2$  deposits can be mostly attributed to the absence of fluorine in the precursor. In the structures from  $\text{Cu}(\text{hfac})_2$  fluorine makes up a significant part of the contamination. In contrast, hydrogen makes up a large part of heteroatoms in the  $\text{tbaoac}$ -



ligands, however, is neither detrimental to the deposit quality, nor is it detected by EDX. It should be noted, however, that the asymmetrical chemical structure of  $\text{Cu}(\text{tbaoac})_2$  (Figure 5-6) has an advantage over the symmetrical  $\text{Cu}(\text{hfac})_2$ . While acetylacetone was shown to decompose into non-volatile carbonaceous material upon electron irradiation,<sup>116</sup> the additional ester residual in  $\text{tbaoac}^-$  could have changed this unfavorable dissociation behavior. Furthermore, the Cu-O bond of the ester moiety (grey underlay) is weaker than the Cu-O bond of the carbonyl group (blue underlay). A thermal decomposition mechanism was reported by Devi et al.<sup>117</sup>, which could give hints for a possible electron induced reaction leading to the efficient ligand removal during the FEBID process and is discussed in more detail in Section 5.2.5.

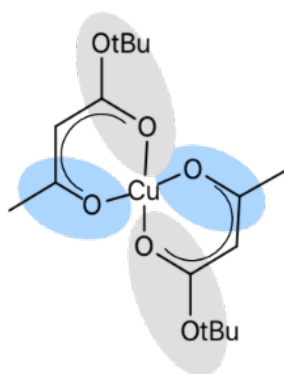


Figure 5-6 Chemical structure of  $\text{Cu}(\text{tbaoac})_2$  with two types of Cu-O bonds. Grey: ester moiety, weaker Cu-O bond and possible rearrangement reaction (Section 5.2.5). Blue: carbonyl moiety, stronger Cu-O bond.

Pentafluoropropionate ( $\text{pfp}^-$ ) prefers the bridging coordination with two  $\text{Cu}^{2+}$  ions, forming dimers. The copper ions in  $\text{Cu}_2(\text{pfp})_4$  are each bound in a square planar configuration to four oxygen atoms. The aminated derivatives have an additional amine ligand in a square pyramidal configuration (see Figure 5-1).<sup>118</sup>

Piszczyk et al. and Sala et al. reported previously that amine ligands were bound only weakly to the complex and showed that the  $\text{EtNH}_2$  and  $t\text{BuNH}_2$  ligands detached upon mild heating in vacuum and  $\text{N}_2$  atmosphere<sup>39,89</sup>. In contrast to these thermal gas-phase studies, this bond seems not to be easily cleaved by electron irradiation, as most FEBID structures contain nitrogen ( $t\text{BuNH}_2$ : ~6 at.%,  $\text{EtNH}_2$ : ~10 at.%, Table 5-1). Accordingly, cross-beam mass spectrometry studies detected amine ligands still coordinated to the copper center, after electron interaction and only a limited formation of naked  $\text{Cu}^+$  ions.<sup>38</sup> In contrast, the theoretically stronger bound carboxylate ligands seem to detach more easily from the metal center, leading to higher metal contents and less carbon contamination. As described in Chapter 4, most of the ligands in  $\text{Cu}_2(\text{pfp})_4$  detach in the first step and form pure copper crystallites embedded in a CF matrix formed through the dissociation of a residual ligands that was still adsorbed on the substrate (C ~30 at.%, F ~40 at%). This seems not to be the mechanism for the aminated carboxylates. The higher carbon contents for both compounds

(*t*BuNH<sub>2</sub> C ~58 at%, EtNH<sub>2</sub> C ~52 at%, Table 5-1) might be an indication of more ligand co-deposition. However, the fluorine contents are far below the numbers of the amine-free complex. This can indicate a more efficient fluoride (F<sup>-</sup>) removal or the co-deposition of mostly the alkyl chains from the amine and the successful removal of large parts of the carboxylate ligands. Additionally, the presence of amine ligands could lead to the removal of fluorine via similar channels as the chlorine removal in cisplatin, where reactive hydrogen species were probably formed through electron irradiation and formed HCl.<sup>24,25</sup>

Lastly, an obvious correlation between the number of heteroatoms within the precursor compound and the resulting metal content of deposits could be expected. Previously, focus was placed to attempt to reduce the number of heteroatoms, especially carbon, within the compounds for FEBID precursors to reduce the contamination of the deposited metal structures through co-deposition. A difficult balance between sufficient volatility and as little heteroatoms as possible resulted from this.

Looking at the direct comparison of the Cu(II) compounds of this work however, it becomes obvious that this is not a correlation as simple as it might seem. All precursor compounds contain between 20 and 26 heteroatoms but result in varying metal contents between 10 and 26 at.%. Similarities can be observed for Cu<sub>2</sub>(pfp)<sub>4</sub> and Cu(tbaoac)<sub>2</sub>, which have differently sized ligands. Cu<sub>2</sub>(pfp)<sub>4</sub> contains only 6 carbon atoms per copper atom, whereas Cu(tbaoac)<sub>2</sub> contains 16 carbon atoms. In total, however, the number of heteroatoms is comparable: 20 and 22, respectively. As described above, both precursors were reported and shown to fabricate deposits with metal contents up to 26 at.%. When only considering the carbon content, the metal purity would be expected to be higher for Cu<sub>2</sub>(pfp)<sub>4</sub>, however, the high amount of fluorine within the precursor is also the largest source of contamination in the deposit. The other three compounds described in this chapter also have comparable numbers of heteroatoms: 26 (Cu(hfac)<sub>2</sub>), 23 (Cu<sub>2</sub>(EtNH<sub>2</sub>)<sub>2</sub>(pfp)<sub>4</sub>) and 25 (Cu<sub>2</sub>(*t*BuNH<sub>2</sub>)<sub>2</sub>(pfp)<sub>4</sub>) and all resulted in similar metal contents from ~10 at.%, ~13 at.% and ~15 at.%, respectively but lower than the other two compounds (Table 5-1). Generally, the chemistry of the ligands shows to be much more relevant for the final dissociation and deposition than the actual size or number of atoms.

## 5.2.5 Elemental Ratios and possible Dissociation Behavior

Table 5-2 List of investigated Cu(II) compounds with corresponding elemental ratios of the pristine precursor, the as deposited structures and desorbing species, as well as the respective evaporation temperatures  $T_{GIS}$  and experimental substrate temperatures  $T_S$ , which were measured during deposition. The as deposited data was derived from local EDX measurements and the elemental ratios of desorbing species from the difference of pristine precursor and as deposited ratios.

compound	pristine precursor					as deposited average					desorbing species <sup>b</sup>				Ratio	$T_{GIS}$	$T_S$
	Cu	C	O	F	N	Cu	C	O	F	N	$\Delta C$	$\Delta O$	$\Delta F$	$\Delta N$			
<b>elemental ratio</b>															$\Delta/prist.$	°C	°C
<b>Cu(hfac)<sub>2</sub></b>	1	10	4	12	-	1.0	5.7	1.5	1.4	-	4.3	2.5	10.6	-	0.67	25-80	25
<b>Cu(tbaoac)<sub>2</sub></b>	1	16	6	-	-	1.0	3.5	0.6	-	-	12.5	5.4	-	-	0.81	110-120	120-135
<b>[Cu<sub>2</sub>(pfp)<sub>4</sub>]<sup>a</sup></b>	2	12	8	20	-	2.0	2.8	0.2	3.8	-	9.2	7.8	16.2	-	0.83	140-150	130-135
<b>[Cu<sub>2</sub>(EtNH<sub>2</sub>)<sub>2</sub>(pfp)<sub>4</sub>]</b>																	
	2	16	8	20	2	2.0	7.6	1.4	2.2	1.5	8.4	6.6	17.8	0.5	0.69	100-120	120-135
<b>[Cu<sub>2</sub>(<sup>t</sup>BuNH<sub>2</sub>)<sub>2</sub>(pfp)<sub>4</sub>]</b>																	
	2	20	8	20	2	2.0	7.8	1.3	1.7	0.7	12.2	6.7	18.3	1.3	0.74	80	90

<sup>a</sup> results from Ref. <sup>115</sup> (c.f. Chapter 4)

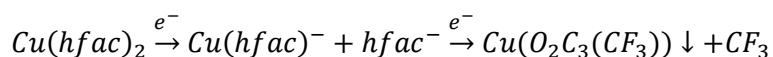
<sup>b</sup>  $\Delta X = X(\text{pristine}) - X(\text{as dep.})$

To identify the electron induced modification of the precursor molecules during the FEBID process, the following section will analyze the structures by considering the elemental ratios of the precursor and the as deposited structures. To this end, the EDX quantification results of all four deposits (W-I/W-II/F-I/F-II) were averaged and renormalized to the number of copper atoms present in one molecule of the pristine precursor. These values are summarized in Table 5-2. Furthermore, the difference between the precursor molecule and the as deposited structure is listed as "desorbing species". These values represent the atoms, which were not deposited but pumped away after dissociation. "Ratio" represents the ratio between the sum of all desorbing species and the sum of all heteroatoms present in the pristine precursor (prist.). As evident from Table 5-2, Cu(tbaoac)<sub>2</sub>, Cu<sub>2</sub>(pfp)<sub>4</sub> and Cu<sub>2</sub>(<sup>t</sup>BuNH<sub>2</sub>)<sub>2</sub>(pfp)<sub>4</sub> dissociated in the most efficient way. Cu(tbaoac)<sub>2</sub> loses 81%, Cu<sub>2</sub>(pfp)<sub>4</sub> 83% and Cu<sub>2</sub>(<sup>t</sup>BuNH<sub>2</sub>)<sub>2</sub>(pfp)<sub>4</sub> 74% of initially present heteroatoms. Cu<sub>2</sub>(EtNH<sub>2</sub>)<sub>2</sub>(pfp)<sub>4</sub> and Cu(hfac)<sub>2</sub> follow closely with 69% and 67% respectively. Based on these ratios and elemental numbers, the electron induced dissociation behavior for each precursor can be suggested. In accordance with thermal and electron induced gas-phase dissociation studies<sup>37-39,89,106,117</sup> the following electron induced dissociation paths can be proposed:

### i. **Cu(hfac)<sub>2</sub>**

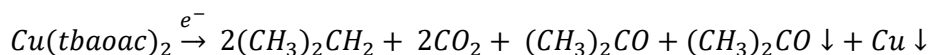
For the fluorinated  $\beta$ -diketonate, thermal dissociation mechanisms proposed by Cohen et al.<sup>106</sup>, showing that Cu(hfac)<sub>2</sub> adsorbs dissociatively on hot surfaces, present in chemical vapor deposition (CVD) processes. The molecule dissociates into Cu(hfac)<sup>+</sup> and hfac<sup>-</sup> and subsequently desorbs Hhfac under recombination with hydrogen. Similar behavior was

found in gas-phase electron attachment studies, where the formation of  $[\text{Cu}(\text{hfac})_2]^-$ ,  $\text{hfac}^-$  and the ligand fragment  $[\text{hfac-H-CF}_3]^-$  (" $\text{O}_2\text{C}_3(\text{CF}_3)$ ") was reported.<sup>37</sup> The desorbing species presented in Table 5-2 indicate that a similar process might be present in the FEBID case. 4 C, 2 O and 10 F atoms can be assigned to desorbing  $\text{hfac}^-$  ( $\text{C}_5\text{O}_2\text{F}_6$ ) and additional detached fluorine ions (or  $\text{CF}_3^+$ ), leaving copper and a partly dissociated  $\text{hfac}^-$  ligand deposited on the substrate. Additionally, C-F bonds can be cleaved by electron irradiation, releasing fluorine from the deposit and explaining the low F concentrations in the FEBID structures.



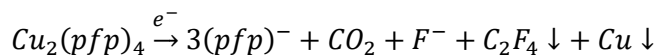
## ii. **Cu(tbaoac)<sub>2</sub>**

The non-fluorinated  $\beta$ -diketonate was previously reported as a CVD precursor by Devi et al. In that study they additionally proposed a thermal dissociation mechanism, where the asymmetrical *tbaoac* ligand easily detaches from the Cu center on the ester side of the ligand. This ester moiety subsequently undergoes an "ene" type rearrangement reaction, forming the volatile isobutene and an acetoacetate intermediate species. The latter quickly decomposes into volatile  $\text{CO}_2$  and acetone, which weakens the second Cu-O bond, forming Cu. In accordance with the desorbing species in Table 5-2, it can be suggested that for each  $\text{Cu}(\text{tbaoac})_2$  molecule, 2 isobutene, 2  $\text{CO}_2$  and 1 acetone molecule are desorbed, while 1 Cu atom and 1 acetone molecule are deposited on the surface. This might also give an explanation to the differences in chemical composition of  $\text{Cu}(\text{tbaoac})_2$  deposits fabricated with low or high e-fluxes. While the low e-flux allowed more acetone molecules to desorb during the deposition process, more were co-deposited in the high e-flux beam of the FEG, leading to higher C and O concentrations (Table 5-2).



## iii. **Cu<sub>2</sub>(pfp)<sub>4</sub>**

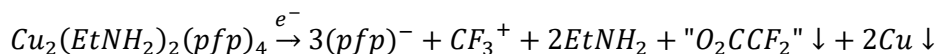
The perfluorinated carboxylate  $\text{Cu}_2(\text{pfp})_4$  loses 83% of its ligand atoms in the electron induced dissociation. The number of desorbed carbon, oxygen and fluorine atoms correspond to the desorption of three full  $\text{pfp}^-$  ligands ( $3^*\text{O}_2\text{C}_3\text{F}_5$ ), as was reported for the gas phase.<sup>38</sup> Dissociative ionization (DI) broke the Cu-O bonds, so that  $\text{Cu}^+$  was released. However, not all ligands desorbed and the remaining ones were dissociated to form F-,  $\text{CO}_2$  and  $\text{F}_2\text{C}=\text{CF}_2$ . The fragments were incorporated in the CF matrix surrounding copper nanoparticles (c.f. Figure 4-6b-c). The proposed  $\text{CO}_2$  formation is in line with the high electronegativity of fluorine, through which the C-C bond between  $\text{C}_2\text{F}_5$  and  $\text{COO}^-$  is weakened and broken easily.



For more details, see Chapter 4 and Ref. <sup>115</sup>

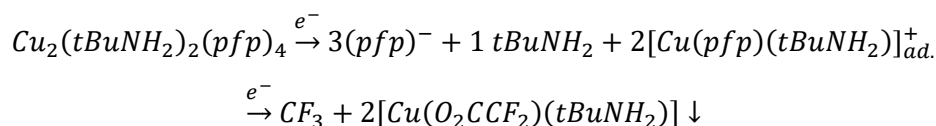
iv. **Cu<sub>2</sub>(EtNH<sub>2</sub>)<sub>2</sub>(pfp)<sub>4</sub>**

The aminated carboxylate Cu<sub>2</sub>(EtNH<sub>2</sub>)<sub>2</sub>(pfp)<sub>4</sub> loses a similar amount of elements as Cu<sub>2</sub>(pfp)<sub>4</sub>. A dissociation mechanism, which is partially similar to the non-aminated analog Cu<sub>2</sub>(pfp)<sub>4</sub>, can be anticipated, leading to the loss of 3 full pfp<sup>-</sup> ligands. In opposition to the analogous carboxylate, the fourth pfp<sup>-</sup> ligand might not be dissociated into CO<sub>2</sub> and F<sub>2</sub>C=CF<sub>2</sub>. The reported fragments were attributed to the amine fragments and not the CO<sub>2</sub> formation, strengthening this hypothesis.<sup>38</sup> The significantly lower amounts of embedded fluorine, as well as the higher amount of incorporated oxygen, indicate that the ligand lost a CF<sub>3</sub> group and a "O<sub>2</sub>C-CF<sub>2</sub>"-fragment was co-deposited instead. This CF<sub>3</sub> cleavage through DEA was reported for the analogous Cu<sub>2</sub>(EtNH<sub>2</sub>)(μ-O<sub>2</sub>CC<sub>3</sub>F<sub>7</sub>)<sub>4</sub> molecule in HR-EELS studies<sup>39</sup> and also detected in small amounts in the positive spectrum of gas-phase experiments.<sup>38</sup> The number of deposited nitrogen atoms, as well as the higher number of C-atoms (4.8 C-atoms more than in Cu<sub>2</sub>(pfp)<sub>4</sub>) strongly indicates the deposition of both EtNH<sub>2</sub> ligands, along with some residual gases. It should be mentioned though, that at the point of the experiment, the Cu<sub>2</sub>(EtNH<sub>2</sub>)<sub>2</sub>(pfp)<sub>4</sub> precursor was not freshly produced and had changed texture over time. The formerly viscous gel had solidified into a harder gel with solid grains. This could indicate the partial loss of amine ligands over time. Ref. <sup>38</sup> and <sup>39</sup> reported this partial loss in vacuum and upon mild annealing, showing that this compound might not be fully stable over time. The larger number of deposited carbon atoms, however, points to the presence of both amine ligands and the change of texture might be assigned to another source.



v. **Cu<sub>2</sub>(tBuNH<sub>2</sub>)<sub>2</sub>(pfp)<sub>4</sub>**

As this compound is very similar to the previously described EtNH<sub>2</sub> compound, a similar dissociation path can be described. Again, three full pfp<sup>-</sup> ligands were desorbed. However, unlike the EtNH<sub>2</sub> groups, only one tBuNH<sub>2</sub> ligand seemed to be deposited in this case. One amine ligand might be desorbing as a full molecule. Even though the amine itself is less volatile than EtNH<sub>2</sub>, the ligand detaches easily from the complex, as reported in literature.<sup>89</sup> The amine ligands were detected to detach at temperatures between 30 and 100°C, which corresponds to the evaporation temperature used in the FEBID experiments (T<sub>GIS</sub>, Table 5-2). It is possible, that the precursor adsorbed onto the surface without the second amine ligand, leading to lower amounts of amine deposited during irradiation. Gas-phase experiments with the same precursors, however, showed no amine loss during the evaporation.<sup>38</sup> The most abundant fragments detected in that study were [Cu(tBuNH<sub>2</sub>)<sub>2</sub>]<sup>+</sup> and [Cu(pfp)(tBuNH<sub>2</sub>)]<sup>+</sup>. The latter case followed by additional pfp-fragmentation could describe our measurements in the most accurate way. Furthermore, Lacko et al. described a highly efficient tBuNH<sub>2</sub> fragmentation, which could be the origin of additional carbon contamination in the FEBID structures of this work.



In all abovementioned cases the suggested dissociation behavior proposed the desorption of 1 or 2 carbon atoms more than the calculated number in this analysis method. This discrepancy may arise from the co-deposition of carbon by residual gases. While the carbon contamination that might have been added during the EDX measurements was eliminated with the background subtraction (see Methods), no co-deposited hydrocarbons present in the deposition instrument could be accounted for. The measured carbon content could therefore include these chamber contaminations, raising the elemental ratios within the structures by 1 or 2 C-atoms.

Moreover, it should be noted, that the dissociation of full pfp<sup>-</sup> ligands was not measured directly for these experiments. The pfp<sup>-</sup> ligands are still likely to undergo fragmentation during electron irradiation and release CO<sub>2</sub>, as was reported for other carboxylates.<sup>92–95</sup> This fragmentation was most probably the reason for C-F contaminations in the FEBID deposits of all pfp-containing precursors.

### 5.3 Conclusion

This chapter showed the electron beam induced deposition of 5 different Cu(II) compounds at different electron densities and dwell times. Two types of precursor classes were investigated. A fluorinated and non-fluorinated β-diketonate: Cu(hfac)<sub>2</sub> and Cu(tbaoac)<sub>2</sub>; and perfluorinated carboxylates with and without additional amine ligands: Cu<sub>2</sub>(pfp)<sub>4</sub>, Cu<sub>2</sub>(EtNH<sub>2</sub>)<sub>2</sub>(pfp)<sub>4</sub> and Cu<sub>2</sub>(tBuNH<sub>2</sub>)<sub>2</sub>(pfp)<sub>4</sub>.

All deposits were analyzed for their deposition rate and chemical composition. The deposition rates were generally larger for short dwell times, which corresponds to the deposition model described in theory. The high e-flux deposits from the FEG source were also deposited at a higher rate, also in accordance with the growth rate model.

Chemical analyses showed little to no difference between high and low electron flux deposits. The C-F bond dissociation was more efficient for higher e-fluxes, leading to less F contamination, but also more carbon incorporation. Even though the amine ligands were reported to be removed easily thermally, they were readily incorporated in the deposits.

Based on the quantification results, elemental ratios of deposited and desorbing species were determined. Dissociation mechanisms for each compound were proposed, which largely agree with fragmentation mechanisms reported in literature. In conclusion, this study showed that the ligand size did not play a major role in metal purity in FEBI deposits. It seems that rather the chemistry of metal-ligand bond type determines the fragmentation behavior and final composition.

This knowledge could be useful for future precursor design in FEBID. Larger ligands are not less favorable for successful metal deposition. Larger ligands which stabilize the metal complex

are desirable, as they facilitate handling and still provide sufficient volatility for gas-assisted deposition. A suitable balance between ideal deposition parameters (waiting and dwell times) and stable, volatile ligands and ligand-fragments could be the right approach for pure metal deposition with FEBID.





## 6 *In situ* monitoring of FEBID processes

Thin-film deposition is often monitored by *in situ* methods determining film growth during deposition. Optical *in situ* techniques such as ellipsometry use the change of optical signal in dependence of the growing film thickness and are often implemented in the deposition of reflective or transparent films.

Film growth can be determined by *in situ* mass sensing. Adsorption, desorption and dissociation processes of metal organic precursors on surfaces can be studied by *in situ* mass monitoring during precursor supply, thermal treatment (i.e. heating, cooling) or other altering processes. An oscillating body experiences a frequency change  $\Delta f$  upon mass change  $\Delta m$ .  $\Delta f$  can be attributed to the mass of material deposited on the oscillating object. Quartz crystal microbalances (QCM) make use of this relationship with oscillating quartz crystals. It is an easy approach to investigate the real process without demanding hardware requirements. A QCM typically can be incorporated in most of the systems without major adjustments. Especially ALD processes have been studied *in situ* with this technique to elucidate the reaction mechanisms.<sup>40</sup> *In situ* QCM measurements were not only used for ALD but also FEBID processes. Such experiments have been conducted before, but only for a limited number of precursors. The group around Sauerbrey was the first to install a system where the electron induced dissociation of organic vapors (from different pump oils and benzene) was studied with a QCM.<sup>41</sup> For that, the quartz crystal was irradiated with a broad electron beam so that adsorbed precursor molecules are dissociated uniformly on the whole surface. As a result, the "polymerization cross sections" could be determined by measuring the mass growth rates in dependency of the electron energy. Similar studies were conducted for  $\text{Fe}(\text{CO})_5$  and  $\text{Cr}(\text{CO})_6$ , demonstrating also the autocatalytic decomposition of those molecules.<sup>46</sup>

Furthermore, similar studies with focused ion beams instead of electrons were conducted with gold and platinum precursors.<sup>42–44</sup> Dubner and Wagner were able to show chemisorption at very low precursor pressures. They demonstrated that approximately one monolayer of  $\text{Me}_2\text{Au}(\text{hfac})$  chemisorbed,<sup>44</sup> demonstrating that QCM measurements are sensitive enough for surface reactions in the range of atomic layers. The observation of ligand desorption upon electron irradiation could therefore be possible. Furthermore, a copper precursor  $(\text{hfac})\text{Cu}(\text{VTMS})$  was investigated in this manner.<sup>45</sup>

This work will investigate the adsorption, desorption and dissociation behavior of the copper compounds addressed in this thesis. The total cross sections will be modelled with the information obtained from the QCM measurements. For this purpose, a dedicated apparatus "eQCM" was designed and built. A detailed description of the setup is available in Chapter 9.4.

### 6.1 Experimental Details

The eQCM setup is described in Chapters 3.6 and 9.4.

The precursors used in this chapter were  $\text{Cu}(\text{hfac})_2$  and  $\text{Cu}_2(\text{pfp})_4$  (details see Chapter 3.1.1).  $\text{Cu}(\text{hfac})_2$  was studied at room temperature, as the precursor has a high vapor pressure without additional thermal energy.<sup>8</sup> For  $\text{Cu}_2(\text{pfp})_4$  the whole setup was heated to 140°C. The temperature was measured through the internal thermocouple of the QCM sensor head.

## 6.2 Results and Discussion

Figure 6-1 shows the mass rates  $R_m$  for  $\text{Cu}_2(\text{pfp})_4$  and  $\text{Cu}(\text{hfac})_2$  at (a) constant beam current ( $I_B = 4 \mu\text{A}$ ) and (b) constant beam energy ( $E_B = 100 \text{ eV}$ ). In (a), the e-flux was  $f_0 = 1.00 \cdot 10^{14} \text{ cm}^{-2} \text{ s}^{-1}$ , which led to deposition in the EL growth regime. All measured beam currents led to EL growth. The eQCM provided  $R_m$  of the deposition process in pg/s by solving the Sauerbrey equation with the recorded frequency change  $\Delta f$  (c.f. Eq. (2-12)). Both precursors exhibited similar deposition behaviors. The mass rate increased slowly for low acceleration voltages ( $E_B < 60 \text{ eV}$ ) and further showed a linear increase until  $E_B = 100 \text{ eV}$  (Figure 6-1a). This corresponds to the maximum beam energy achievable with this setup. A similar energy dependence was observed with benzene in a comparable setup by Kunze et al.<sup>41</sup> In literature, the mass rate reached a maximum at  $E_B > 100 \text{ eV}$  and decreased beyond that. Unfortunately, this maximum could not be observed with the electron energies accessible in the eQCM setup.

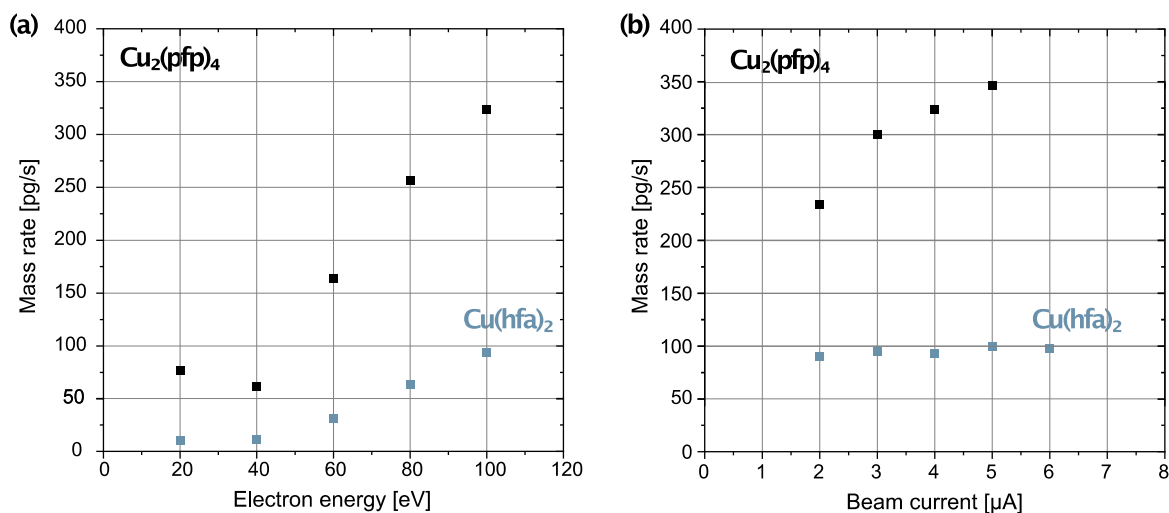


Figure 6-1 QCM mass rates  $R_m$  for  $\text{Cu}_2(\text{pfp})_4$  (black) and  $\text{Cu}(\text{hfa})_2$  (blue) for (a) constant beam current  $I_B = 4 \mu\text{A}$  and for (b) constant beam energy  $E_B = 100 \text{ eV}$ . All experiments were conducted at  $2.7 \cdot 10^{-6} \text{ mbar}$  working pressure. For  $\text{Cu}_2(\text{pfp})_4$  the chamber was heated to 140°C. Mass rates have an uncertainty of  $\pm 0.06 \text{ pg/s}$ .

With increasing beam current, the mass rates increased linear for both precursors for (Figure 6-1b). This is in agreement with the aforementioned benzene studies which also showed a linear dependence on the impinging beam current. Furthermore, this behavior was expected, as the growth rate is proportional to the dissociation rate  $\sigma f_0$  and therefore proportional to  $I_B$  (with  $\sigma = \text{const.}$ , if  $E_B = \text{const.}$ ).

During constant irradiation of the QCM crystal, electron beam induced deposition takes place. The growth rate of this process can be described by the continuum model described in Eq. (2-8). By multiplying the growth rate  $R$  with the deposit density  $\rho$  and deposit area  $A_{dep}$ , the mass rate  $R_m$  can be simulated using the continuum model (see Eq. (6-1))

$$R_m = \frac{sJV}{\frac{sJ}{n_0} + \frac{1}{\tau} + \sigma f_0} \sigma f_0 \cdot \rho A_{dep} \quad (6-1)$$

$\rho$  was estimated from EDX measurements of the deposits (Table 6-1). The chemical analysis shows that a significantly higher amount of carbon was co-deposited with both copper precursors, as compared to the classic FEBID deposits (Chapters 4 and 5). They might arise from the dissociation of background gases or residuals from solvents that were introduced with the precursor. Therefore, the deposit density  $\rho$  was calculated as a weighted ratio of the literature values  $\rho(\text{CuCOF}) = 3.0 \text{ g/cm}^3$  and  $\rho(\text{C}_x\text{O}_y) = 0.94 \text{ g/cm}^3$  (density of carbonaceous matrix).<sup>75</sup>

Table 6-1 Thin-film and background subtracted EDX quantification results of QCM crystals after electron induced deposition with one of the two Cu(II) precursors.

at.% <sup>a</sup>	Cu <sub>2</sub> (pfp) <sub>4</sub>	Cu(hfac) <sub>2</sub>
Cu	4	5
C	87	67
O	7	17
F	2	11
ratio CuCOF : matrix	17 : 83	44 : 56
$\rho \text{ (g/cm}^3\text{)}$	1.29	1.85
<sup>a</sup> measurement uncertainty for EDX $\pm 5\text{at.}\%$		

The values for  $s$ ,  $J$ ,  $V$ ,  $n_0$  and  $\tau$  were obtained from the shape simulation in Chapter 4 (Cu<sub>2</sub>(pfp)<sub>4</sub>) and literature (Cu(hfac)<sub>2</sub>).<sup>8</sup> The electron flux  $f_0$  was calculated as described in Eq. (3-14). A suitable  $\sigma$  was determined for each acceleration voltage  $E_B$  by fitting the simulated values of  $R_m$  to the experimentally obtained values. The values for the total dissociation cross section  $\sigma(E_B)$  are plotted in Figure 6-2a. The  $\sigma(\text{Cu}_2(\text{pfp})_4)$  is almost one order of magnitude larger than  $\sigma(\text{Cu}(\text{hfac})_2)$ . This could be the contribution of the amorphous carbon-oxygen matrix. A high carbon concentration was measured for Cu<sub>2</sub>(pfp)<sub>4</sub>, where up to 83% of the deposit consists of a carbonaceous matrix. This might contribute largely to the total cross section. Kunze et al. determined with the similar experimental setup that benzene had an electron induced dissociation (or polymerization) cross section of  $\sigma(\text{benzene}, 100\text{eV}) = 0.38 \text{ nm}^2$ .<sup>41</sup> Furthermore, the maximum calculated cross section  $\sigma(\text{Cu}_2(\text{pfp})_4, 100\text{eV})$  is about half of the cross section obtained from the shape simulation ( $\sigma = 1.5 \text{ \AA}^2$ , Chapter 4). Nevertheless, both  $\sigma$  values, from the shape simulation and the eQCM, are comparable.

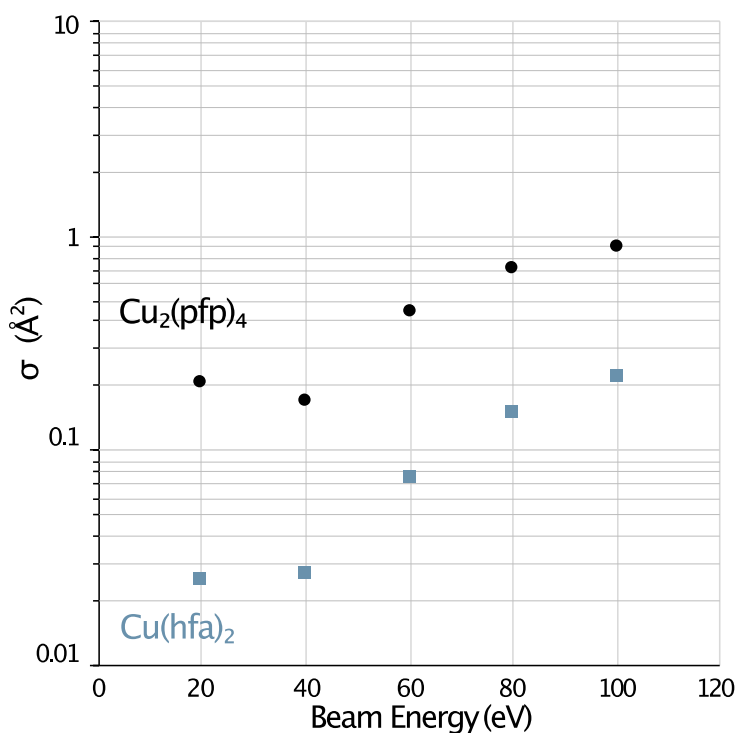


Figure 6-2 Total deposition cross sections for  $\text{Cu}_2(\text{pfp})_4$  (black) and  $\text{Cu}(\text{hfac})_2$  (blue) in dependence of the primary beam energy at  $I_B = 4 \mu\text{A}$ .

First preliminary results were also obtained for adsorption tests, which were done with  $\text{Cu}_2(\text{pfp})_4$  on a pristine QCM crystal. The chamber was heated to  $135^\circ\text{C}$  and precursor was introduced into the chamber. The temperature corrected graph is shown in Figure 6-3. Several observations could be made: (1) The process included the adsorption of precursor multilayers. The measured mass change of 596 ng correspond to 16.5 ML of  $\text{Cu}_2(\text{pfp})_4$  dimers. The weight of 1 ML  $\text{Cu}_2(\text{pfp})_4$  was calculated to be 36.02 ng. After closing the precursor at  $\sim 17:00$  h, no mass change was detected. Hence, no desorption of adsorbed material was observed. (2) Upon reopening the precursor valve ( $\sim 18:00$  h), a single ML of precursor was monitored. (3) With the precursor valve opened, a FEBID experiment was conducted by irradiating the crystal surface with the electron beam (100 eV,  $6 \mu\text{A}$ ) for 30 s. The precursor dissociation was accompanied by a mass loss of 231 ng ( $\sim 19:00$  h). Assuming, that the electron beam dissociated the metal-ligand bond, this mass loss could be attributed to the desorption of 8 ML of  $\text{pfp}^-$  ligands. 1ML  $\text{pfp}^-$  was calculated to weigh 30.14 ng. (4) With the precursor still feeding into the chamber, 173 ng were gained after irradiation. This corresponds to the readsorption of 5 ML  $\text{Cu}_2(\text{pfp})_4$  on the FEBI deposit.

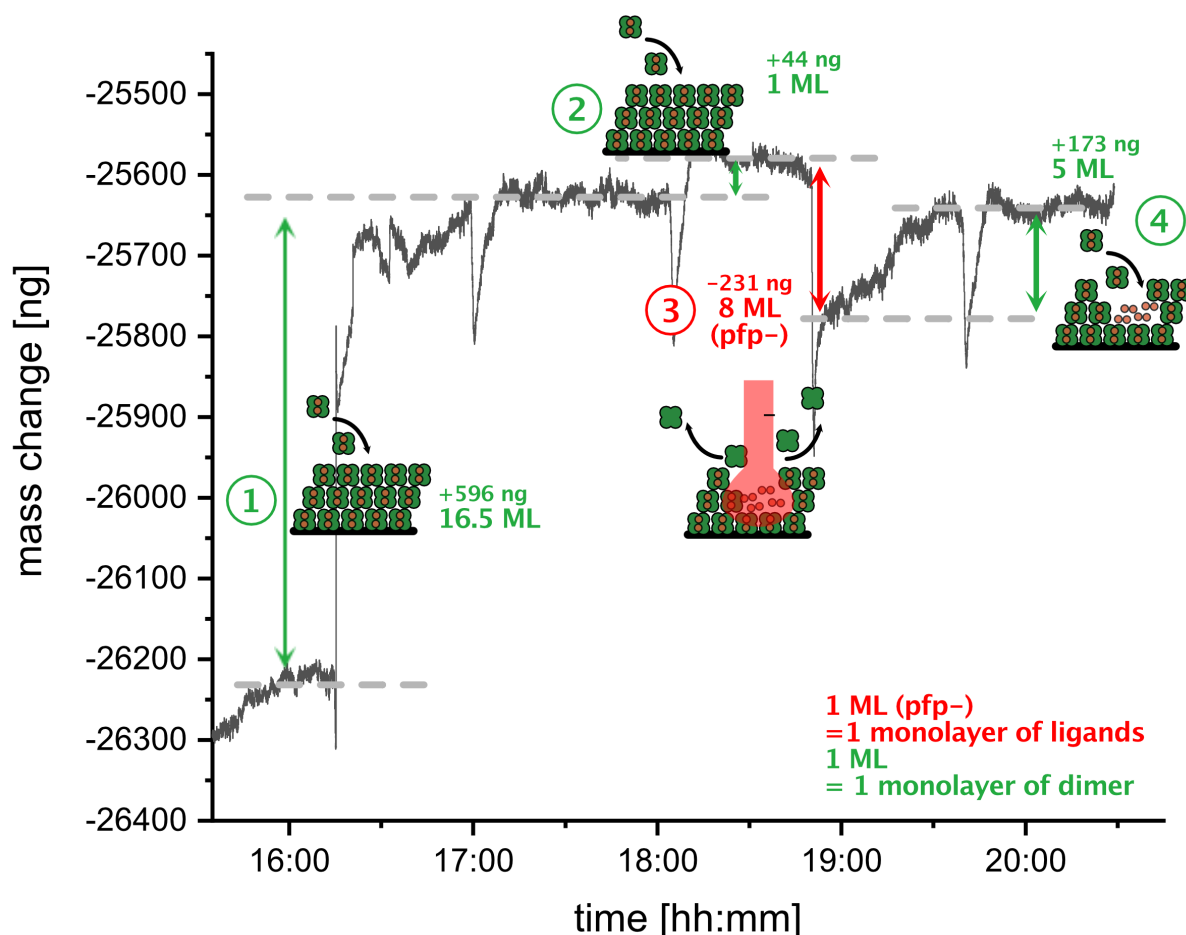


Figure 6-3 QCM adsorption and desorption measurements of  $\text{Cu}_2(\text{pfp})_4$  at  $135^\circ\text{C}$  (1) precursor adsorption on a clean crystal. 16.5 monolayers of dimeric precursor were adsorbed. No desorption was observed. (2) New dosing of precursor on physisorbed multilayers leads to adsorption of an additional monolayer. (3) FEBID: Electron irradiation with 100 eV and 6  $\mu\text{A}$  lead to molecule dissociation and the desorption of probably 8 monolayers of  $\text{pfp}^-$  ligands. (4) Readsorption of another 5 monolayers of precursor on the deposit.

No further adsorption tests were performed at higher temperatures due to technical issues. These conditions, however, represented the FEBID process well, as the substrate temperatures used in the microscopes were also  $135^\circ\text{C}$ . Especially the high resolution of down to 1 ML of precursor, makes this setup promising for future fundamental studies.

### 6.3 Conclusion

This chapter described the setup of the eQCM chamber, in which FEBID processes could be monitored *in situ* via mass change. This setup allowed not only the monitoring of room temperature processes, e.g. with the  $\text{Cu}(\text{hfac})_2$  precursor, but also FEBID at elevated temperatures. For the deposition of  $\text{Cu}_2(\text{pfp})_4$  the whole eQCM chamber was heated to  $140^\circ\text{C}$ , to ensure sufficient precursor evaporation and no condensation on the chamber walls.

From the recorded frequency change, the mass rate  $R_m$  was derived. With this information, the total dissociation cross sections of the continuous FEBI deposition could be obtained by fitting

the continuum model to the experimental data. Chemical analysis of the deposits (with EDX) helped to estimate the best values for the deposit density and volume. By this, a total cross section, similar to the one obtained through shape simulations, was obtained for  $\text{Cu}_2(\text{pfp})_4$ . In future, this setup could provide further insight into more fundamental mechanisms of the FEBID process, such as the study of adsorption and desorption of precursor molecules, as shown in first preliminary results. The adsorption of precursor multilayers, single monolayers and the desorption of ligands upon electron irradiation was presented. Future studies might further allow the determination of molecule residence times  $\tau$  or ligand/fragment desorption through electron irradiation.

## 7 Alternative Approaches to High-Purity Metal Deposition

A challenging goal in focused electron beam induced deposition is the deposition of pure metal nanostructures from metal–organic precursors. The direct deposition of metals from carbon-containing precursors such as silver with purities up to 70 at.%<sup>19,57,112</sup> from a carboxylate or iron,<sup>17</sup> cobalt,<sup>16</sup> and CoFe<sup>119</sup> with purities of 80–90 at.% each from carbonyls were reported in literature. Many high-purity deposits were achieved by autocatalytic dissociation of the precursor molecule on electron induced seed layers. The inorganic precursor PF<sub>3</sub>AuCl<sup>13,120</sup> as well as the carbonyls Fe(CO)<sub>5</sub>,<sup>17</sup> Co<sub>2</sub>(CO)<sub>8</sub>,<sup>121</sup> and Co(CO)<sub>3</sub>NO<sup>122</sup> reported autocatalytic dissociation at room temperature. This means that the initially deposited pure metal seeds, created by electron-induced metal-ligand bond scission, act catalytically upon the cleavage of that same bond. Therefore, further supplied precursor molecules will be dissociated upon arrival to the metal deposit, contributing to the growth of clean metal structures. As a result, very little ligand atoms are co-deposited. This effect however, is not observed for many metals, and mostly in UHV conditions.

For those precursors and systems where no autocatalysis is possible, different approaches were reported to obtain pure metal deposits. The purification of the as-deposited metal-containing material from the carbonaceous matrix will be discussed in the following.

### 7.1 Post-Experiment Purification of FEBID structures

This chapter was taken in large parts from the publication:  
Berger et al., *ACS Appl. Electron. Mater.* 2020, 2, 7, 1989–1996.

#### 7.1.1 Purification methods in FEBID

Typically, the precursors used for FEBID are recruited from the large library of CVD precursors. These were designed and synthesized with the purpose to selectively break the M-L bond thermally with a known and specific energy. As the bond scission energy can be accessed directly by the thermal energy of the hot substrate on which decomposition occurs, very pure metal films can be achieved. In FEBID however, no selectivity is provided by the electrons. As the focused electron beams of SEMs are not monochromatic and, even more importantly, the energy spectrum of emitted SE1 and SE2 is very broad ( $0 \text{ eV} \leq E(\text{SE}) < E(\text{PE})$ ), no direct choice of dissociation energy is possible. Therefore, along with the M-L bond being broken, also any other bond within the ligand might be cleaved, leading to the co-deposition of ligands and the contamination of the metal deposits. As discussed in Chapter 1, the ideal precursor would have no other bonds to be dissociated by the SEs. To improve volatility, however, metalorganic complexes with relatively large ligands have to be chosen for the process.

The co-deposition of carbonaceous material ( $C_xO_yX_z$ , with X being any other heteroatom present in the ligands) was shown to not be avoided but treated instead. The treatment was performed both, *in-situ* during the FEBID process and *ex-situ* after the deposition.

Most purification protocols originated from the necessity to improve the electrical conductivity of Pt containing nanowires from the MeCpPtMe<sub>3</sub> precursor. As deposited structures from this compound typically contain ~15-22 at.% metal in an amorphous carbon matrix. Pt-containing structures from this and other Pt-precursors were shown to be treated after deposition by additional electron irradiation, tuning and improving the conductivity in dependency of the electron dose, as well as the metal content.<sup>123–126</sup> The irradiation with a laser after and during deposition removed the carbon matrix pyrolytically.<sup>127,128</sup> Another approach was the post-experiment irradiation in the presence of (reactive) gases, such as oxygen<sup>129–131</sup> or water<sup>132</sup>, which successfully removed the carbon matrix by oxidation, or NH<sub>3</sub><sup>25,133</sup> for the removal of halides. Similarly, water was used as an oxidative reactive gas *in-situ*, i.e. during the FEBID process, depositing high-purity Pt<sup>134,135</sup> and Au<sup>136</sup> structures. The successful use of reactive gases was reported without electron or photon irradiation, without and with the addition of thermal energy by annealing the structures in the presence of (atomic) oxygen,<sup>137–139</sup> (atomic) hydrogen<sup>126,140,141</sup> or forming gas (a H<sub>2</sub>/N<sub>2</sub> gas mixture).<sup>142,143</sup>

It has to be kept in mind that oxidizing purification protocols, i.e. C removal by water or O<sub>2</sub>, is limited to noble metals, such as gold or platinum, since these metals will not be oxidized themselves in this process. Non-noble metals, which oxidize readily, should be treated with reducing gas atmospheres, i.e. H<sub>2</sub> or forming gas, or in vacuum.

Due to its strong oxidizability, as shown for the deposits of Cu<sub>2</sub>(pfp)<sub>4</sub> in Chapter 4, the purification of copper could not be realized with O<sub>2</sub> or H<sub>2</sub>O. In literature the purification was rather done thermally, instead of chemically. Structures from Cu(hfac)<sub>2</sub>, Cu(hfac)(DMB) and Cu(hfac)(VTMS) were purified by annealing in vacuum, either locally with a laser or globally with a conventional heating stage.<sup>35,144</sup> Both annealing techniques showed the formation of copper nanocrystals through precipitation at the outside of the structure. However, no significant increase in copper content was achieved, meaning that apart from the copper agglomeration, the carbonaceous matrix was not removed.

Therefore, an efficient and complete purification protocol for copper is studied in this chapter.



### 7.1.2 Post-Experiment Annealing in Reactive Gases<sup>115</sup>

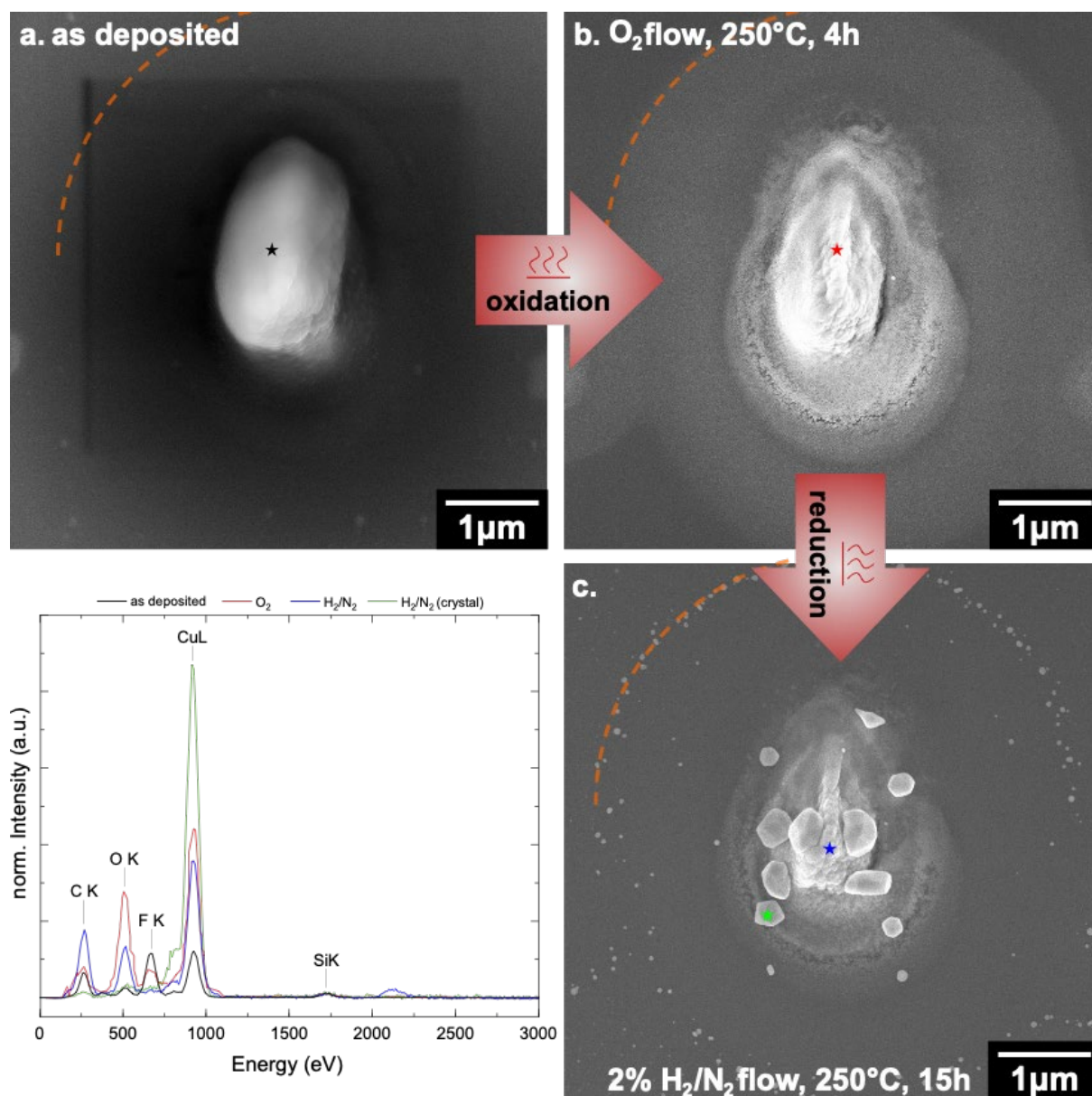


Figure 7-1 Spot deposit on SiO<sub>2</sub>/Si (a) as-deposited with 20 keV for 60min, with a relatively smooth and uniform center. A scanning window from previous observation is visible. (b) After annealing for 4h in O<sub>2</sub> flow at 250°C, the smooth matrix is partly removed. (c) After annealing for 15h in a reducing gas mixture, large faceted crystals appear. The green star marks the point of local EDX measurement to prove the presence of pure copper (95 at. %). The orange dashed line marks the theoretical BSE range of this deposit. The graph shows the EDX spectra of deposits from Cu<sub>2</sub>(pfp)<sub>4</sub> at different processing steps. The intensity was normalized to the Si peak. Quantification is summarized in Table Table 7-1.

The most pressing challenge in the FEBI deposition of this copper precursor is the deposit oxidation when it is exposed to ambient conditions. Post-experiment oxidation can be treated *ex situ* using known purification methods.<sup>142,143</sup> Carbonaceous material from co-deposited ligands can be removed by oxidation via annealing in O<sub>2</sub> atmosphere. However, since copper is a non-noble metal, this oxidation step will also form CuO and Cu<sub>2</sub>O. Therefore, a second

purification step has to be introduced. Subsequent annealing in a reducing gas mixture leads to the formation of  $\text{Cu}^0$ . In this work, a reducing gas mixture of 2%  $\text{H}_2$ /98%  $\text{N}_2$  was used to reduce copper oxide to elemental copper. This procedure proved to be successful and pure copper was obtained. Due to the high mobility of this metal, the initial shape of the deposits could not be maintained and the formation of copper crystals and islands was observed, as depicted in Figure 7-1. The direct annealing in the reducing gas mixture did not lead to full purification because the carbon matrix was not removed. This approach was investigated with a different fluorine containing copper precursor  $\text{Cu}(\text{hfac})_2$  (Figure 7-2).

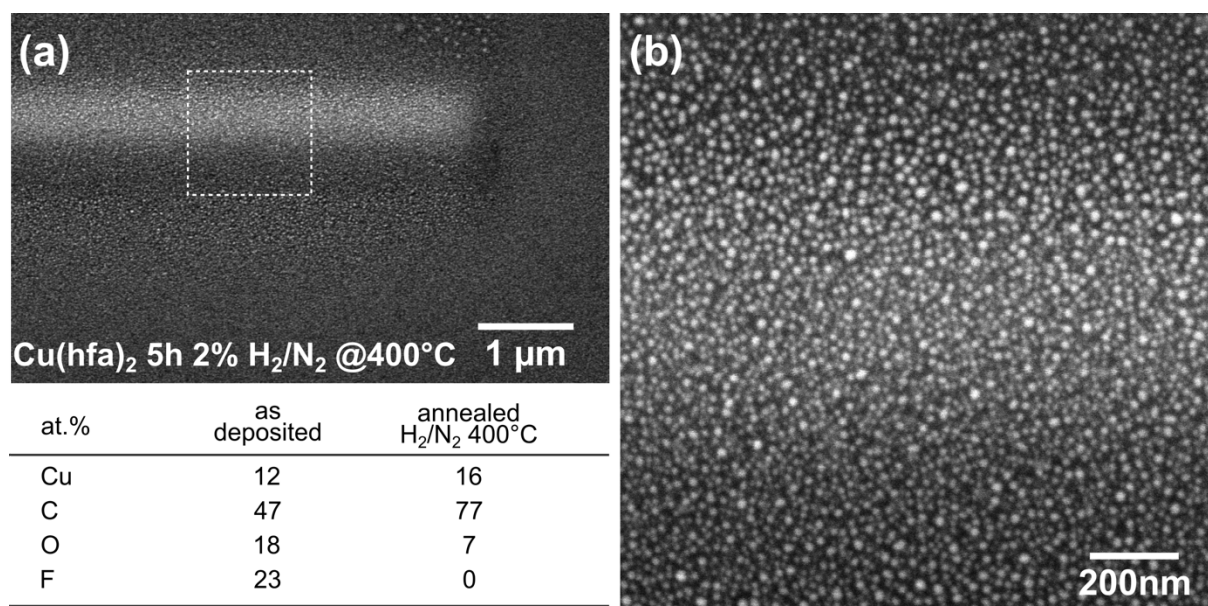


Figure 7-2 SEM images showing a line deposited from  $\text{Cu}(\text{hfa})_2$  and subsequently annealed at 400°C in the same reducing gas atmosphere as the other structures (2%  $\text{H}_2$ / 98%  $\text{N}_2$ ). (a) overview image of the right end of the line deposit after annealing. (b) high magnification image of the region marked in a. The table shows EDX quantification results of this line in the as deposited and annealed state.

The annealing in reducing gas atmosphere only, does not lead to the purification of the structures. The EDX quantification results show that the copper content could not be improved and carbon was not removed. The SEM images in Figure 7-2 show percolation of small particles, similar to HV annealing procedures of this precursor.<sup>35,144</sup> This stands in contrast to the purification process reported by Jurczyk et al., where the carbon content in ruthenium deposits was successfully reduced with forming gas only.<sup>143</sup> This might be due to the fact that perfluorocarbons are more stable at higher temperatures than their respective fluorine-free hydro-carbon compounds. In Ref. <sup>143</sup> all incorporated carbon in the ruthenium deposits originated from non-halogenated allyls. In the as-deposited state, the dot center on the left shows the same appearance as in Figure 4-2 and consists of a relatively smooth, uniform carbonaceous matrix. After annealing it at 250°C for 4h in pure oxygen, the structure appearance changes. Local EDX measurements proved the formation of copper oxide and the presence of residual carbon and fluorine (Figure 7-1, red spectrum). The detailed quantification results are listed in Table 7-1.

Table 7-1 Background and thin film corrected EDX quantification results of three dot deposits (on SiN<sub>x</sub>/Si bulk) measured in the central pillar (from Chapter 4.3.1) and quantification results of one dot deposit during the purification process (on SiO<sub>2</sub>/Si) measured in the center (c.f. Figure 7-1). All spectra were measured at 3 keV primary beam energy.

element (at.%) <sup>a</sup>	average dot deposits		deposit purification	
	as deposited center	O <sub>2</sub> flow, 250°C, 4h center	H <sub>2</sub> /N <sub>2</sub> flow, 250°C, 15h center	crystal
<b>Cu</b>	23	30	26	95
<b>C</b>	32	17	51	5
<b>O</b>	2	44	23	0
<b>F</b>	44	8	0	0

<sup>a</sup> The measurement uncertainty is  $\pm 5$  at. %.

Even though the formation of oxide should lead to a volume increase, the structure collapsed. Therefore, we assume that the carbon–fluorine matrix was partly removed, as is visible from the quantification results. The carbon content dropped from 32 at.% in the as-deposited to 17 at.% in the annealed state. Similar holds true for the fluorine content reducing to 8 at.%. The copper was oxidized, resulting in an almost 1:1 ratio of Cu/O. Since this removal is a function of temperature and time, a longer annealing period or higher temperatures would probably be necessary for complete carbon removal. The second annealing step was performed at 250°C for 15h in the reducing gas mixture. Here, the deposit shape was altered drastically. The deposit developed large, faceted crystals. Local EDX measurements on these large crystals (Figure 7-1c, green star and spectrum) confirm that they are made of pure copper (95 at.%, see Table 7-1). As is visible from the blue spectrum, the dot center still contains some residual carbon and non-reduced CuO due to insufficient annealing temperatures or time. The fluorine was removed completely in this step. Interestingly, a ring of crystals formed around the dot center. When compared to the theoretical BSE range (Figure 7-1, orange dashed line), it becomes visible that the thin halo agglomerated and diffused toward the outside, forming the ring of copper crystals with this exact radius. The local EDX measurement in the center of the structure showed an increase in the contents of carbon (51 at. %) and some non-reduced CuO (Cu 26 and O 23 at. %). Higher carbon contents in the center can be attributed to the migration of purified copper to the large pure copper crystals surrounding the center and thus leaving a residual low copper content carbon matrix in the probed center volume (Figure 7-1c, blue star). Some of the Cu signals from the center might also originate from these large surrounding crystals on top of the center deposit as the volume of X-ray generation at 3 keV ranges up to approximately 56 nm in Cu and 80 nm in the CuCO-FEBID material, assuming a beam diameter of roughly 10 nm during EDX measurements. These observations demonstrate the difficulties that arise during the purification of copper FEBI deposits. Even though the material can be purified, the high mobility of copper prevents the preservation of the initially deposited shape and leads to the agglomerations of large crystals. Nevertheless, the electron irradiation seemed

to have triggered some constraint of further copper diffusion, as they formed a ring precisely at the maximum BSE exit range.

## **7.2 Resist-Based Lithography Techniques**

### **7.2.1 Electron Beam Lithography (EBL) and Focused Electron Beam Induced Deposition at Cryogenic Temperatures (cryo-FEBID)**

Electron Beam Lithography (EBL) is a deposition technique for the fabrication of micro- and nanostructures on the industrial scale. It is mainly used for the fabrication of 2D nanostructures with features in the sub-10nm range.<sup>145</sup> It is a multistep process, consisting of the deposition and irradiation of a resist, the removal of the (non)exposed parts, the deposition of a metal layer and the final lift-off process leaving the intended structure. The process is sketched in Figure 7-3.

The resist is deposited on a substrate with established spin-coating recipes, yielding a uniform layer with known thickness. The resist is subsequently irradiated with a focused electron beam, causing a chemical reaction of the resist molecules. Upon irradiation, the resist becomes either locally soluble or insoluble, depending on if it is a positive or negative tone resist. Positive tone resists undergo a chemical reaction, making the irradiated parts more soluble; negative tone resists crosslink and become insoluble where irradiated by electrons. In the development step, the soluble parts of the resist are removed with a suitable solvent, so that either irradiated or non-irradiated parts of the pattern remain on the substrate. Then, the desired metal thin film is deposited on the entire sample via vapor deposition techniques (sputtering, PVD, CVD or ALD) or electrochemical metal deposition. Finally, the remaining resist is removed with another solvent, removing the excessive metal thin film with it, except on the regions, where the metal was deposited directly on the substrate. This so-called "lift-off" process leaves the desired pattern as a metal structure on the substrate.

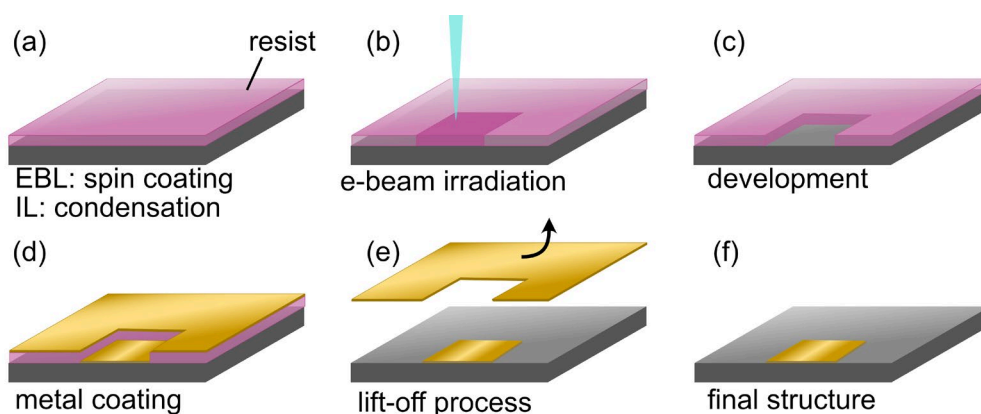


Figure 7-3 Sketch of the electron beam lithography (EBL) and ice lithography (IL) process with a positive resist. (a) A resist (pink) spin-coated (EBL) or condensed (IL) onto the substrate. (b) Electron beam irradiation of the resist, changing its solubility (EBL) or evaporating it (IL). (c) EBL: Development of the pattern with a suitable solvent, removing the irradiated part of the resist. (d) Metal thin film deposition on the full sample (via evaporation or electrochemical process). (e) Lift-off process of surplus metal by removing non-irradiated resist with a solvent (EBL) or substrate heating ("melt-off", IL). (f) Final metal structure on the substrate.

Due to the necessity of uniformly coated resists, EBL is limited to flat surfaces and 2D structures. Even though it is a multistep process, it can produce nanostructures with a high throughput and excellent metal purity. In contrast, FEBID allows the direct-write deposition 2D and 3D structures on any substrate morphology. However, it suffers from large amounts of deposit contamination and low growth rates limiting its use to prototyping and specialized academic use. Ice lithography (IL) presents a technique where EBL and FEBID meet.<sup>146</sup> In IL, a precursor gas (e.g. water or alkanes) is supplied through a gas injection system, similar to FEBID, and condensed onto a cold substrate where it forms a homogeneous ice film. Subsequently, the ice film is irradiated with an electron beam pattern, similar to EBL. In the case of water ice resists, the irradiated parts are removed (positive tone resist) and the pattern is transferred onto the substrate via metal film deposition techniques. The desired metal structures are obtained after the lift-off process, or better called "melt-off", by heating the substrate, or immersing into isopropyl alcohol at room temperature. When using alkane ice, the irradiated pattern undergoes polymerization and the non-irradiated parts can be removed by heating the substrate (negative tone resist). The cross-linked carbon structures stay on the substrate and can for instance be used as a mask for plasma etching.

Unlike spin-coated resists used in EBL, the condensed ice films can also cover irregular, non-flat surfaces, extending the technique to complex substrates and already existing nanostructures.<sup>147</sup> Ultimately, IL was also shown to successfully deposit 3D nanostructures by layer stacking. In contrast to EBL, all irradiation and metallization steps in IL could be performed within the vacuum chamber of the SEM, reducing the fabrication process to a minimum.<sup>148</sup>

A similar approach of resist-based lithography was performed with the common FEBID precursor  $\text{MeCpPtMe}_3$  and  $\text{W}(\text{CO})_6$  as a resist.<sup>149–152</sup> For that the precursor was delivered to the cold substrate with a GIS, forming a layer of precursor ice. Subsequent irradiation with the

focused electron beam of the SEM (focused ion beam in the case of  $(\text{WCO})_6$ ) led to the alteration of the precursor resist. Upon reheating the substrate, the non-irradiated precursor evaporated and left the irradiated patterns on the substrate. This technique represents a direct-write and resist-based deposition of metal-carbon structures with similar composition as the common room temperature FEBID of  $\text{MeCpPtMe}_3$ . However, the growth rate of “cryo-FEBID” is over four orders of magnitude higher than the RT FEBID. Similar to the 3D-IL, also “cryo-FEBID” could achieve 3D deposits by stacking multiple layers.<sup>150</sup>

This section will describe the fabrication of copper structures with an approach similar to “cryo-FEBID”, using the low-volatility precursor  $\text{Cu}_2(\text{pfp})_4$  on a room temperature substrate.

## 7.2.2 Direct Electron Beam Lithography in a Positive Low-Volatility Precursor Resist

### 7.2.2.1 Experimental Details

*Evaporation:* Silicon bulk substrates with a native oxide layer ( $\text{SiO}_2(\text{nat.})$ ) were marked with a small grid of ca. 1 mm step size and placed in the SEM chamber. The precursor  $\text{Cu}_2(\text{pfp})_4$  was filled in a GIS with needle (0.38 mm ID) and introduced into the chamber. Under vacuum, the GIS was heated to  $T_{\text{GIS}} = 140^\circ\text{C}$ . After reaching the temperature, the needle opening was placed 200  $\mu\text{m}$  above the substrate surface at the center of the grid. The precursor was condensed onto the RT substrate for 2.5 h. This process was repeated for all samples mentioned in the following section.

*Irradiation:* The samples were then irradiated with the focused electron beam of the SEM (Hitachi S3600, W-filament) with a primary energy of 25 keV and a beam current of 630 pA. A defined pattern was irradiated, as shown in Figure 7-4. The pattern was written in four different regions of the condensate at four different condensate thicknesses for each sample.

*Development:* After irradiation, the samples were developed in one of the following ways.

- *Condensate dissolution in ethanol (EtOH).* The samples were placed for 2 min into a beaker with clean EtOH and the resist was gently dissolved by hand movement of the beaker. The sample was finally rinsed with fresh EtOH and then dried in air.
- *Resist evaporation in high vacuum (HV).* The samples were placed onto a heatable stage and introduced into the SEM chamber. At a background pressure of  $2 \cdot 10^{-5}$  mbar, the stage was heated to  $198^\circ\text{C}$  over 3.5 h. The temperature was measured within the heated copper block (c.f. Chapter 3.1.2) and on the substrate surface with Type-K thermocouples. The temperatures on the substrate surface did not exceed  $125^\circ\text{C}$ . The max. temperature was held for 35 min. Afterwards the heater was turned off and the sample cooled down in HV.

All samples were analyzed with the analytical HR-SEM with EDX detector (Hitachi S4800) and AFM as discussed in Chapter 3.

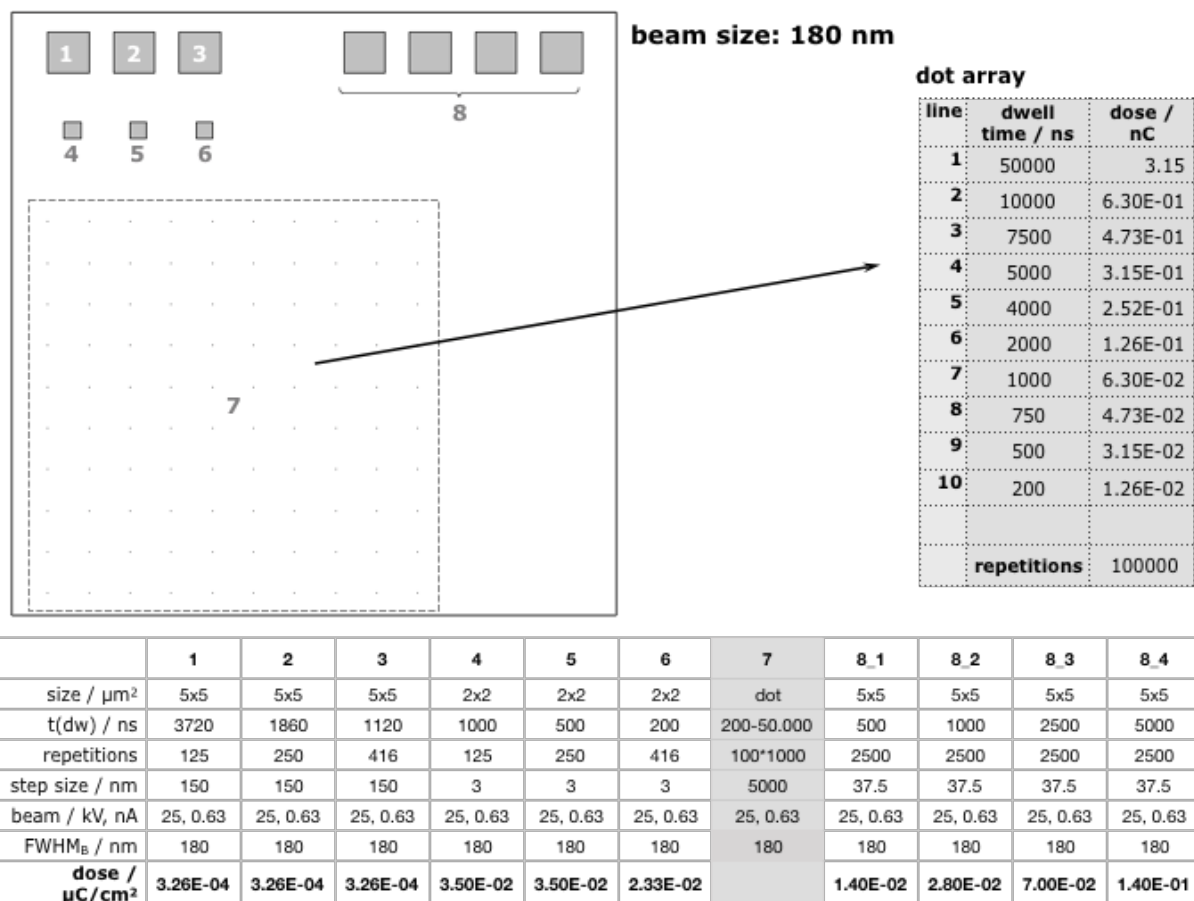


Figure 7-4 Irradiation Pattern of DEBL structures shown in this chapter. All electron doses are noted.

### 7.2.2.2 Results and Discussion

“Cryo-FEBID” is a suitable technique for the deposition of metal containing structures from metal-organic precursors that are volatile at room temperature. A similar approach can be used with low-volatility (LV) precursors such as  $\text{Cu}_2(\text{pfp})_4$ . The compound is stable at room temperature and evaporates only at elevated temperatures ( $T_{\text{GIS}} = 140^\circ\text{C}$ ). For the deposition of the precursor resist, the substrate therefore does not need to be cooled down to cryogenic temperatures but can be held at room temperature.

The “Direct Electron Beam Lithography” (DEBL) is illustrated in Figure 7-5: The resist deposition was realized through evaporation of  $\text{Cu}_2(\text{pfp})_4$  through a GIS with a nozzle diameter of 0.38 mm that was heated to  $140^\circ\text{C}$ . The compound was condensed onto a silicon substrate with native oxide layer ( $\text{SiO}_2(\text{nat.})/\text{Si}$ ) which was held at room temperature (Figure 7-5a). Figure 7-5b shows a photo of one substrate with  $\text{Cu}_2(\text{pfp})_4$  condensate. It is visible as a pear-shaped condensate in all refractive colors, which occurred due to a thickness gradient. This thickness gradient corresponds to the variation in molecule flux arriving on the substrate surface, as was simulated in Figure 3-3b. The condensate thickness decreases from the center to the outside. Therefore, the same deposition pattern was irradiated in four different regions of the resist (Figure 7-5c). Non-irradiated condensate was removed for pattern development either by dissolution in ethanol (EtOH), or by evaporation in the SEM chamber by heating the substrate to  $140^\circ\text{C}$ .



(Figure 7-5d). The results of EtOH development are shown in Figure 7-5e. The pattern consisted of squares and dot arrays of varying electron dose and were imaged with an optical microscope (upper row) and the HR-SEM (lower row). The numbers I to IV correspond to the position of irradiation in the condensate, with I being in the thickest, central part and IV the thinnest, outmost part of the resist. It is evident from the images, that the structures are of different appearance, consistent with the condensate thickness. Thin deposits appear faint (see e-IV), thick deposits show a strong contrast and even interference colors (see e-I).

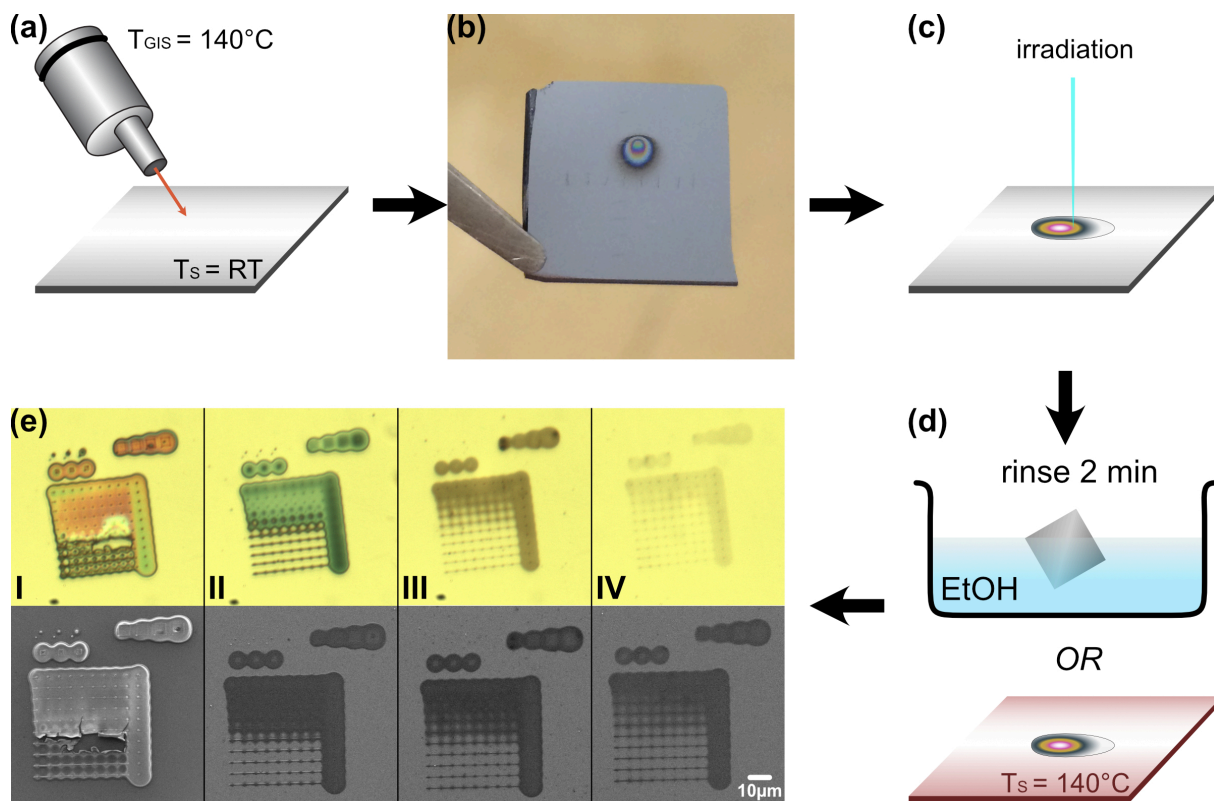


Figure 7-5 Experimental scheme of Direct EBL in a  $\text{Cu}_2(\text{pfp})_4$  resist. (a) Precursor evaporation through GIS on a cold substrate. (b) Photo of the precursor condensate ("resist"). (c) Electron irradiation of the resist. (d) Pattern development by rinsing for 2 min in ethanol (EtOH) or heating the substrate for precursor evaporation. (e) Optical (upper) and SEM (lower) images of four irradiated structures after development in EtOH. The structures were written in differently thick condensate (gradient center to outside = thick to thin = I to IV).

In the following, we will discuss the pattern which was developed in EtOH. The detailed deposition parameters are summarized in the pattern scheme in Figure 7-4. The dots were deposited in an array of 10 dots per line with a distance of  $5\mu\text{m}$ , written from left to right and top down. The arrays were deposited with an inherent bug within the XENOS lithography software, where the last object of an array is irradiated much longer than programmed. Any irregularity in the last row therefore originates in this bug, that could not be solved by the software provider so far. All other dots however were deposited with the dwell times indicated in Figure 7-4. All structures were irradiated according to their numeration (i.e. starting with 1 and ending with 8\_4).

As described above, the pattern was repeatedly deposited in different regions of the condensate, in order to study any changes. A more detailed picture of the two extremities are shown in Figure 7-6. The structures squares 8\_1-4 and the dot array (No. 7) of the thickest and thinnest region, as seen in Figure 7-5 e-I and e-IV, are depicted in detail. The original pattern of the  $5 \times 5 \mu\text{m}^2$  squares in Figure 7-6a-b are indicated by white dashed lines to guide the eye. It is clearly visible, that all squares feature a halo around the squares, originating from BSEs escaping the Si bulk substrate up to a certain radius  $r_{\text{BSE,Si}}$ , which depends on the beam energy. In the case of 25 keV primary energy as used in this experiment, BSEs escape until a radius of  $3.93 \mu\text{m}$ . For both regions, the largest halo around square 8\_4 was measured in the SEM images. Three different distances were measured: i. from the square side to the bright halo edge and ii. the dark halo edge; and iii. from the square corner to the dark halo edge. The values are summarized in Table 7-2:

Table 7-2 Halo radii as measured from squares 8\_4 in Figure 7-6 and Figure 7-8.

halo radius <sup>a</sup>	EtOH		HV annealing		$r_{\text{BSE,Si}}(25\text{keV})$
	(a)	(b)	(a)	(b)	
i. side – bright edge	$3.6 \mu\text{m}$	$1.8 \mu\text{m}$	$3.7 \mu\text{m}$	$2.6 \mu\text{m}$	$3.93 \mu\text{m}$
ii. side – dark edge	$4.3 \mu\text{m}$	$3.9 \mu\text{m}$	$4.5 \mu\text{m}$	$3.6 \mu\text{m}$	
iii. corner – dark edge	$3.5 \mu\text{m}$	$2.9 \mu\text{m}$	$3.7 \mu\text{m}$	$3.4 \mu\text{m}$	

<sup>a</sup> Distances measured by eye in SEM images. Measurement uncertainty is  $\pm 0.05 \mu\text{m}$ .

An increasing halo diameter was observed with increasing e-dose from left to right. This is linked to the increasing number of BSEs being emitted at large radii with increasing e-dose. In these experiments, the e-dose was varied via dwell time variation. Therefore, the smallest e-dose square was deposited with the shortest dwell times at constant e-flux and caused a smaller number of electrons to scatter within the bulk. This means that also the e-dose of BSE was significantly smaller than for long dwell times and was not sufficient to cause electron induced chemistry within the condensate.

For the thick deposit, the radius diverges  $\pm 10\%$  from the theoretical value, with the lateral distance (ii. side-dark halo edge) being larger and the shorter lateral distance (i. side-bright edge) and diagonal distance (iii. corner-halo edge) smaller than the theoretical distance (Table 7-2). The halo of the thinner deposit diverged largely from the theoretical exit radius for distances (i.) and (iii.) At lateral distance ii. however, it shows good agreement. The bright halo edge in the thin deposit therefore corresponds to a threshold where "deposition" changes and is visible as contrast change at shorter range, which could correspond to an electron dose threshold, which was necessary for precursor dissociation.

The discrepancy between the two resist regions I and IV could arise from additional electron scattering within the thick condensate, increasing the halo radius. Also, electron induced dissociation of the condensate could have led the formation of volatile fragments, which could

not desorb from within the resist. This led to a bulging of the resist material, increasing its size and halo diameter. Contrarily, the majority of BSE interacting with the thin condensate were scattered within the bulk substrate.

Since the thickness of the condensate could not be determined beforehand, AFM measurements of the structures were performed after development. The results are shown in Figure 7-6c-d. The graphs depict three profiles over the squares 8\_2-4 (see inset). The average structure thickness was determined to be  $280 \pm 30$  nm and  $8 \pm 3$  nm respectively, showing a direct dependency of the condensate film thickness with the structure thickness. This corresponds to a deposition rate of 1.26 nm/s in the thick deposit, which is about 4 orders of magnitudes larger than a comparable gas-assisted FEBID square ( $< 0.03$  nm/s). The AFM image in Figure 7-6c exhibits three characteristics: a 3D dot on the lower left corner, a 3D dot in the center and a "wall" at the outside edge of each square. The squares were deposited with a spiral writing technique starting from the lower left corner and spiraling inwards. The lithography software dwells longer on the starting point of the structure, leading to the dot on the corner. When spiraling the pattern inwards, more and more beam overlap accumulates a higher effective number of electrons in the center, increasing the deposition rate locally. When irradiating a resist however, no new molecules diffuse towards the irradiation site, therefore an increase of deposition rate is not possible in the classic sense of FEBID growth. This means that either molecules from the surrounding condensate diffused towards the high irradiation points (corner/center), which seems unlikely for the LV-precursor at RT. Or the accumulation of electrons in these regions led to charge accumulation within the thick, non-conductive resist and bulged. Since the AFM and HR-SEM images were taken after EDX measurements, where small areas of the structures were probed with a high beam current, the latter seems a more probable explanation. The dark areas in squares 8\_3 and 8\_4 in Figure 7-6a correspond to the regions of EDX measurement. They are also visible in the 3D AFM image, especially in 8\_3, where the dark area can be identified as a bulge. These features are not visible in the thin condensate structures and can therefore be attributed to the thick resist which trapped volatile fragments.

Figure 7-6e depicts the dot array irradiated in the thick condensate. Here it should be stressed, that the deposit delaminated from the substrate upon development. It is especially apparent in the tilt view image on the right. The delamination could arise from stresses within the thick deposit upon development in EtOH. This is a common challenge in standard EBL and photolithography.

Another notable difference between the thick and thin deposits is the inversed contrast in the SEM images. While the thick structures appear bright in contrast to the substrate, the thin deposits are darker than the surrounding. The bright contrast in Figure 7-6a and e could be attributed to charging effects within the less conductive resist material, rather than a high metal content. Contrarily, the dark contrast in Figure 7-6b and f might have originated from carbonaceous material in the halo and the slightly brighter contrast within the deposition area/center from a higher metal content. As shown in the AFM measurements (Figure 7-6d)

the deposit thickness is uniform over the halo and square deposit, meaning that any charging effects should be uniformly visible as in Figure 7-6a.

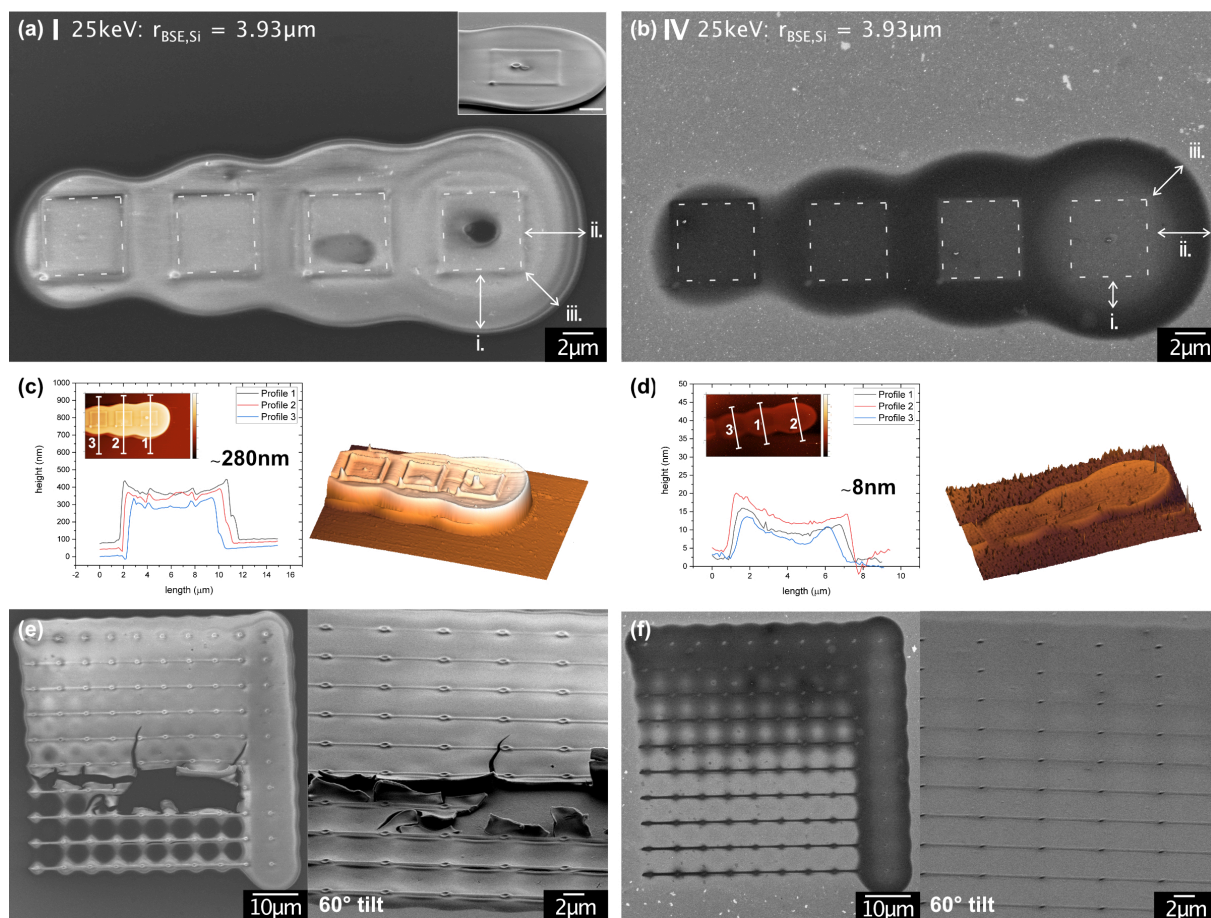


Figure 7-6 DEBL structures from  $Cu_2(pfp)_4$  on a  $SiO_2(nat.)/Si$  substrate after development in EtOH. The shown structures are  $5 \times 5 \mu m^2$  squares and a dot array with varied e-doses irradiated in (a,c,e) thick and (b,d,f) thin condensate. (a-b) SEM images of four squares deposited with increasing e-dose (left to right). The inset shows the tilted view of parts of the structure. (c-d) AFM measurements of the square deposits with profiles and a 3D image. The average thickness of the structures is marked in the graph. (e-f) SEM images of the dot arrays deposited along with the squares. The e-dose decreased from top to bottom, within each line the dose is constant. The last (right) dot in each line is a long time exposure of 30 ms. The right image shows each array in zoom and tilted view. In (e) delamination of the irradiated condensate is visible. Strongly discernible halos are observed for all structures. The halo sizes i, ii and iii in comparison to the maximum BSE exit radius  $r_{BSE,Si}$  are marked in (a-b).

In order to determine the metal contents within the DEBL deposits after development, EDX measurements were locally conducted on the squares 8\_4 within the structures (center) and in the respective halo. The quantification results of each irradiation field in varying condensate thickness are illustrated in Figure 7-7 and are background subtracted and thin film corrected. The values measured in the center (filled symbols) and halo (empty symbols) are noted separately. The pristine precursor composition is noted alongside for comparison (dashed lines). The structure thickness was determined with AFM measurements (c.f. Figure 7-6c-d) and increase from the fields IV to I as illustrated in Figure 7-5e. It should be noted, that in the case

of EtOH development the background signals were clean and only small amounts of carbon and oxygen <2 at.% were detected, which was attributed to background contamination during the EDX measurements. The development process in EtOH was therefore successful, removing any non-irradiated  $\text{Cu}_2(\text{pfp})_4$  residuals.

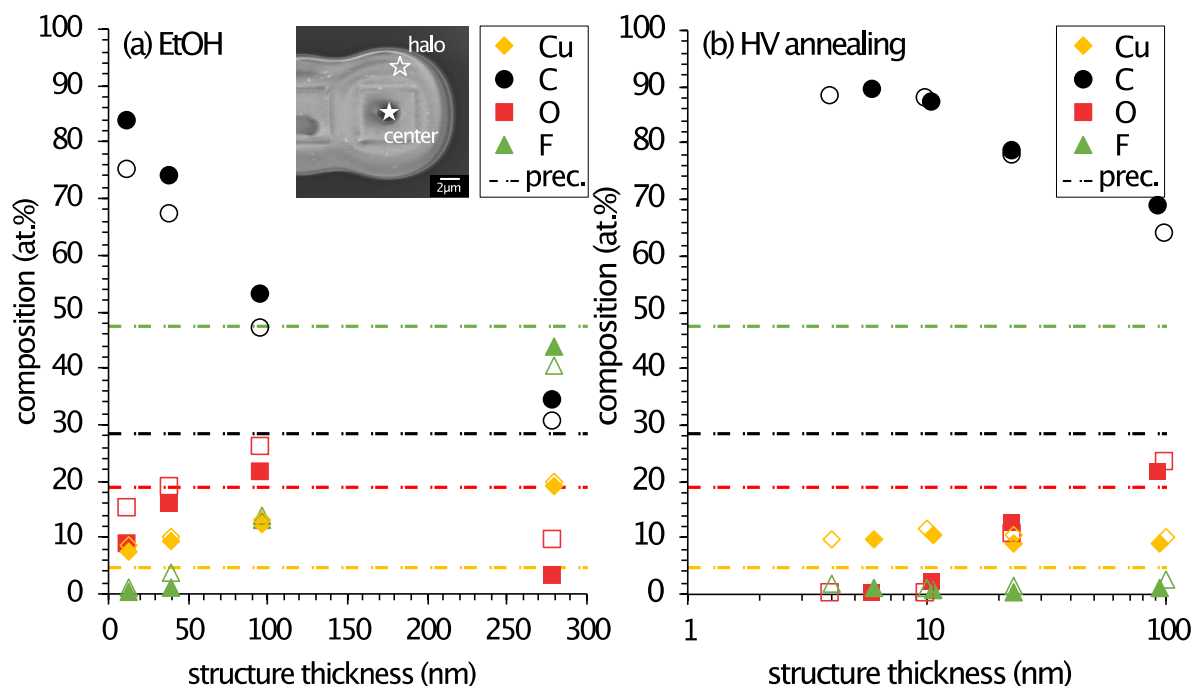


Figure 7-7 EDX quantification results of the DEBL structures developed (a) in EtOH and (b) by annealing HV. The EDX spectra were recorded locally with 3 keV in within the structure 8\_4 (filled symbols) and in its respective halo (empty symbols). The position of spectra collection is noted in the inset. The thickness of each deposited structure was determined with AFM and correspond to regions I-IV as in Figure 7-5e. The pristine precursor values are noted for comparison as dashed lines. Note that the x-axis in (b) is shown as logarithmic scale for better illustration of the thin structures. Atomic concentrations have an uncertainty of  $\pm 5$  at.% (not noted in this graph).

The EDX quantification in Figure 7-7a shows that generally, there was little to no difference between the center and halo regions. All fluctuation lies within the measurement uncertainty of  $\pm 5$  at.%. However, there is a large variation within the differently thick structures, i.e. regions. With increasing thickness, the carbon concentration decreased and the fluorine content increased. While the oxygen content increases with larger thickness, it abruptly drops to <10 at.% for the thickest structure. All values converge towards the original precursor composition but with decreased oxygen and increased copper content (up to 20 at.%). For very thin deposits, the carbon content increased drastically.

The convergence towards precursor composition could be explained by the almost bulk dimension of the resist in region I. The resulting structures were about 280 nm thick and no more substrate signal was detected at 3 keV. It is possible, that electron irradiation polymerized the top layers of the resist, encapsulating the precursor and preventing the desorption of electron-induced fragments. Therefore, the composition within the bulk could not change

significantly from the original composition. Nevertheless, there has been oxygen desorption, as the oxygen content decreased, simultaneously increasing the copper content. The bulky matrix could have been acting as an oxidation barrier, preventing the oxidation of any formed copper particles in this structure.

The lack of oxidation barrier might also be the reason, why thinner deposits have lower copper and higher oxygen concentrations. Copper to oxygen ratios reached  $\text{Cu}:\text{O} = 1:1\text{-}1.5$ , which strongly indicates the formation of  $\text{CuO}$ , as reported for common FEBID structures from  $\text{Cu}_2(\text{pfp})_4$  in Chapter 4. The low fluorine values indicate the electron induced desorption of fluorine containing species.

Other samples were prepared with the same precursor condensation protocol, but a different development process. The structures were developed by annealing the substrate to  $T_s > 140^\circ\text{C}$  in high vacuum (HV,  $2 \cdot 10^{-5}$  mbar base pressure). The EDX quantification results in Figure 7-7b show similar trends for each element. The thickest structure in region I however, did not reach pristine precursor values. This could be assigned to the different development process, where the irradiated structures were annealed to high temperatures, causing an additional alteration of the structures. As apparent from the AFM measurements in Figure 7-8, they are significantly thinner than the corresponding EtOH developed structures. It is probable, that the annealing caused the evaporation of dissociated fragments in the structure, which were encapsulated and trapped in the EtOH sample. This might have led to the shrinkage of the deposit. However, it should be also noted, that the thickness of the condensate could not be determined beforehand. The actual condensate thickness at the area of irradiation was therefore not compared between both samples. Since the condensation step was identical for both samples, it was assumed, that all samples have a similar condensate layer. Figure 7-8 shows the structures 8\_1-4 in the thickest (a, I) and thinnest (b, II) regions of the condensate, analogous to the EtOH sample (Figure 7-6). Corresponding AFM images and line profiles for size determination are shown alongside. Additionally, SEM images are shown of the square deposit 1 (c.f. Figure 7-4) in the respective region. The high magnification image depicts a blow-up of the lower right corner of that deposit.

The SEM and AFM images show a similar appearance compared to the EtOH sample, including the halo around the squares. This was not surprising, as the PE beam energy and substrate density did not change. Therefore, a theoretical exit radius of  $r_{\text{BSE}} = 3.93 \mu\text{m}$  was expected. The halo radii indicated were measured from the SEM images and are noted in Table 7-2. The halo radii lie within the same values as for the EtOH developed sample. The thicker deposits show good agreement with deviations of 5-10% and thin deposits show similar deviations as before. Merely the bright halo edge (i.) is slightly larger than for the EtOH developed sample but is still significantly smaller than  $r_{\text{BSE,Si}}$ .

In square 1 of region I (Figure 7-8a), the formation of locally concentrated crystallites was very well visible. Their size is clearly distinguishable from the thermally induced copper crystals (green arrow) and are more concentrated towards the square's center. They can therefore be

ascribed to the electron induced process. The decreasing number of crystallites towards the corners indicates insufficient electron dose for a uniform deposition. In future, this could be used for the determination of the minimum electron dose necessary for the complete dissociation of the film before development. Square 1 in region IV though (Figure 7-8b) is barely distinguishable from the background. A white line was inserted to guide the eye in the high magnification image. Apart from a slightly darker shade, the irradiated area does not look different from the thermally dissociated precursor. The darker contrast within the structure most probably originates from additional carbon deposition through electron induced dissociation

The most prominent difference to the EtOH developed sample is the presence of bright crystallites in the background of the sample (green arrow in Figure 7-8a). The crystallites outside the irradiated patterns are copper containing clusters which formed upon annealing. The development process probably induced thermal decomposition of the precursor on the entire substrate and due to its high mobility, copper agglomerated into these larger features. In areas where more  $\text{Cu}_2(\text{pfp})_4$  was available, i.e. thicker condensate, the crystals are larger and scattered further apart. In the thin condensate regions, smaller clusters formed and are more numerous and packed more closely.

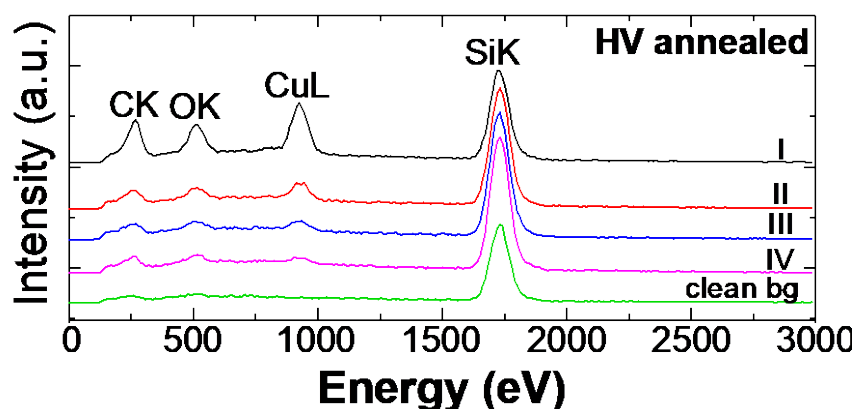


Figure 7-8 EDX spectra of non-irradiated areas in proximity to irradiation fields I-IV (HV annealed sample). Green spectrum: Clean  $\text{SiO}_2(\text{nat.})/\text{Si}$  surface was measured outside the condensate area for comparison.

The EDX background measurement clearly shows the presence of copper and more carbon and oxygen than a clean  $\text{SiO}_2(\text{nat.})/\text{Si}$  surface (Figure 7-9). In order to achieve a clean development process, without thermal decomposition and co-deposition, lower annealing temperatures should be used.



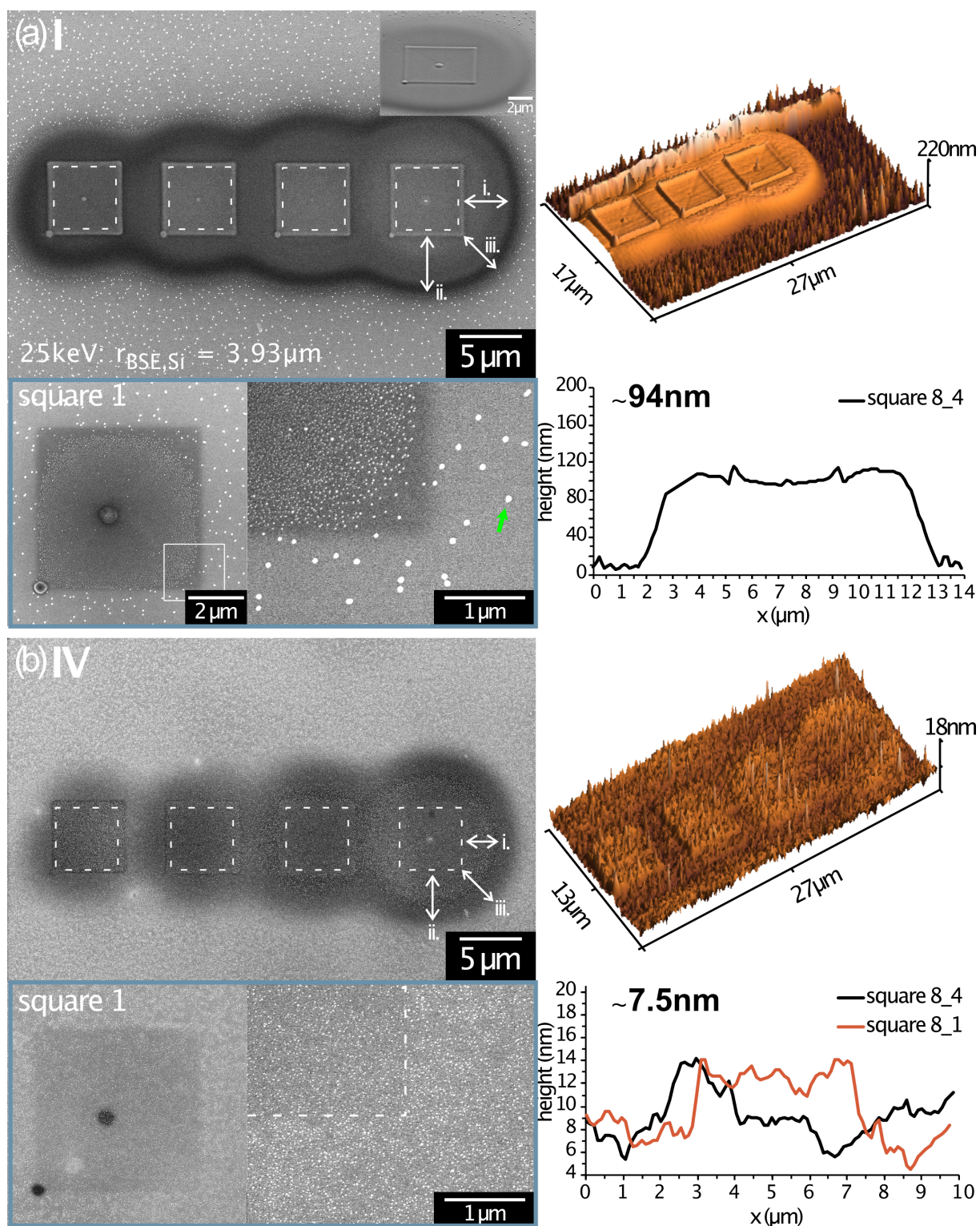


Figure 7-9 DEBL structures from  $\text{Cu}_2(\text{pfp})_4$  on a  $\text{SiO}_2(\text{nat.})/\text{Si}$  substrate after development via thermal resist evaporation in HV (substrate heated to  $T_s = 190^\circ\text{C}$ ). Left: SEM images of the structures. The halo radii are indicated. Additional SEM image of Square 1 with high magnification image of the lower left corner. Right: AFM image and profile of square 8\_4. (a) Results of the thickest resist region (I) with squares 8\_1-4 (inset:  $60^\circ$  tilt image) and square 1 (c.f. Figure 7-4). The green arrow indicates a copper crystal in the non-irradiated region. (b) Results of the same structures in the thinnest region of the condensate (IV).



### 7.2.2.3 Post-Purification of DEBL Structures

Following the 2-step purification protocol described in section 7.1.2, the DEBL structures were annealed subsequently in the reactive gases  $O_2$  and  $H_2/N_2$ . The result of region I (thickest condensate) is summarized in Figure 7-10. The SEM images show the whole irradiation pattern after development (a), after oxidation at  $300^\circ C$  for 3h (b) and after reduction in forming gas at  $400^\circ C$  for 3h (c). The graph shows the quantification results of local EDX measurements taken in square 8\_4 (as above) at each processing step. While the appearance from (a) to (b) did not change significantly, the elemental composition changed notably. Further processing in forming gas changed the appearance drastically. Large clusters precipitated on the irradiated areas. The EDX measurement at the common region (square 8\_4) showed a further decrease in carbon content, an increase in copper content (35 at.%) and an increase in oxygen content, even though it was annealed in a reducing atmosphere. Additionally, the precipitates were locally measured and analyzed with EDX and are shown as the empty symbols in the graph. They turned out to be pure copper clusters (96 at.%), similar to what was observed for the purification of regular FEBI deposits from  $Cu_2(pfp)_4$  as discussed in the previous section of this chapter. The purification of copper containing DEBL structures resulted in the precipitation of pure copper crystals and clusters. The other regions were also analyzed but did not give valuable results. The high annealing temperatures led to the diffusion of copper into the silicon substrate, falsifying the quantification results. The native oxide layer on the Si substrate used for this experiment was not an effective diffusion barrier. Future experiments should therefore be conducted on different substrates with a diffusion barrier (i.e.  $> 200\text{ nm SiO}_2$ ,  $SiN_x$ ,  $AlN$ , ...).

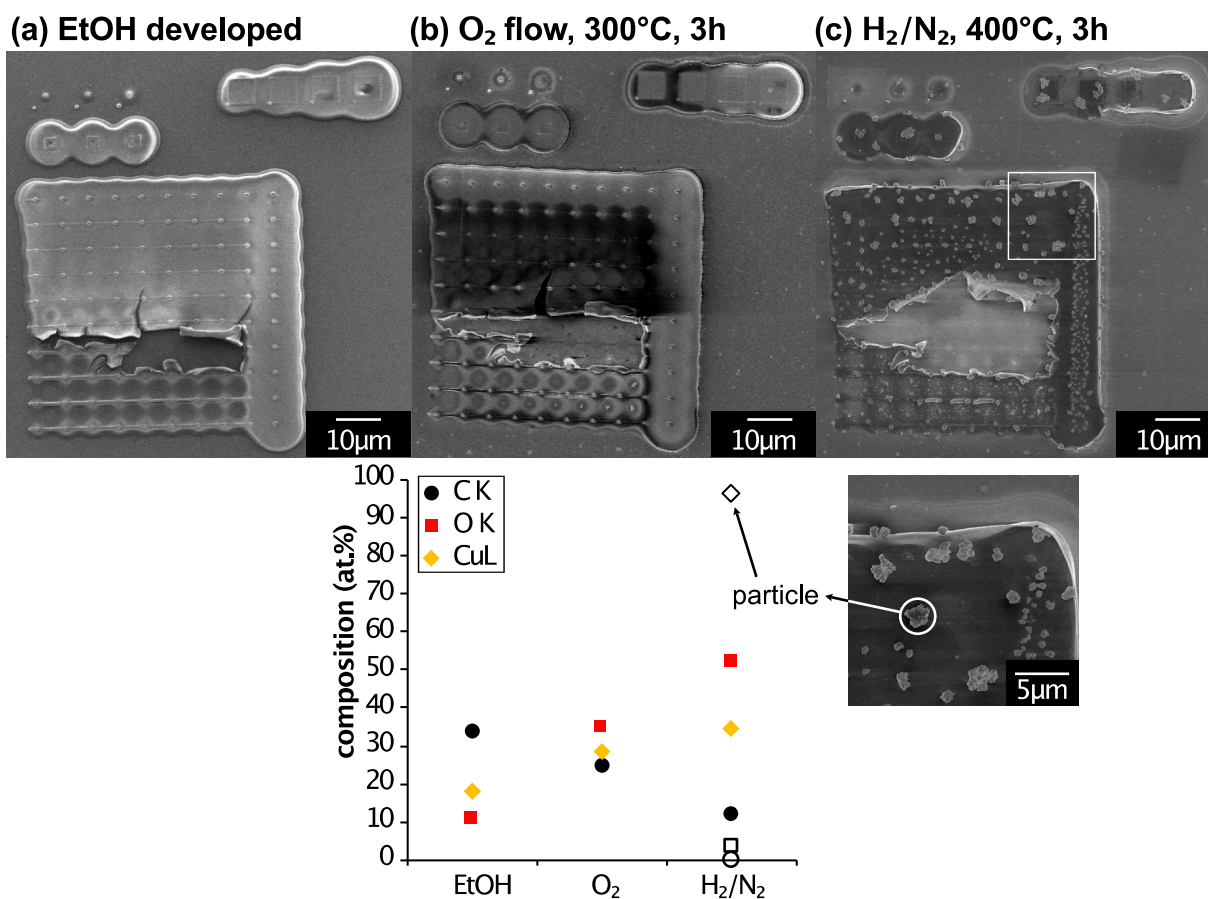


Figure 7-10 Post-Purification of DEBL structures in region I. (a) The as-deposited structure after development in EtOH. (b) The oxidized structure after 3h in oxygen flow at 300°C. (c) The reduced structure after 3h in form gas at 400°C. Large clusters have formed (see high magnification region below). The graph shows the quantification results of local EDX measurements at each processing step. The empty black data points refer to the local EDX measurement of a large cluster (see high magnification image). They consist of pure copper (96 at.%).

### 7.3 Conclusion

In this chapter, alternative deposition and processing techniques were explored for the fabrication of pure copper structures from  $\text{Cu}_2(\text{pfp})_4$ . Both techniques are related to gas-assisted FEBID, as the first part was discussing the post-experimental purification of already deposited structures. The second part covered a possible modification of the gas-assisted process and "cryo-FEBID" for low volatility precursors, here referred to as Direct Electron Beam Lithography (DEBL).

The post-purification of as-deposited FEBID structures was described as a two-step process. Cu-containing FEBID structures from  $\text{Cu}_2(\text{pfp})_4$  were annealed in  $\text{O}_2$  atmosphere to remove the carbonaceous matrix. While the carbon content was successfully lowered, all copper crystallites were oxidized to CuO. Hence, this approach was insufficient. A second annealing step in reducing atmosphere (2%  $\text{H}_2$ /98%  $\text{N}_2$  = forming gas) was introduced. This measure resulted in the reduction of CuO into pure copper crystals with purities >97 at.%. The high mobility of copper upon elevated temperatures caused the agglomeration into larger copper crystals. The metal was shown to diffuse out of the original deposit and shape fidelity was not provided. Interestingly, the copper crystals seemed to have a "diffusion barrier" towards the outside. A ring of copper crystallites formed at the theoretical max. exit radius of BSE  $r_{\text{BSE}}$ . This behavior could not be explained yet and would make an interesting topic of further investigation in future works.

In the second part of this chapter, an alternative deposition approach was studied. Based on the common EBL process and more recent modifications, known as ice lithography and "cryo-FEBID",  $\text{Cu}_2(\text{pfp})_4$  was used as a lithography resist. Since this approach needed neither a metal deposition step, nor cryogenic temperatures for the resist, it was referred to as "Direct Electron Beam Lithography" (DEBL).

$\text{Cu}_2(\text{pfp})_4$  was evaporated onto a substrate which was held at room temperature. The evaporation from the thin GIS needle led to a non-uniform condensate with a thickness gradient from the center outwards. Subsequently, the same pattern was irradiated with the focused electron beam of the SEM, controlled by a lithography software, in four different regions of the condensate. Each pattern was therefore written in differently thick condensate. The patterns were finally developed either by resist dissolution in EtOH or by resist evaporation via annealing in HV. The resulting structures were analyzed and showed the changed condensate thickness in the four regions. The chemical composition changed with the sample thickness. Thin structures showed very high carbon contamination but little to no presence of O and F. The latter was more pronounced for the thermal development process. In contrast, the copper content was relatively constant at ~10 at.% for all thicknesses and processes. The thickest structures developed in EtOH however seemed to have a "capping layer" of polymerized precursor, which prevented the desorption of fragments, and led to a similar elemental composition as the pristine precursor. Additionally, halo deposits surrounding the

structures were studied and showed some potential for the determination of the electron dose necessary to produce deposits.

Finally, both approaches were combined and the DEBL structures were purified with the 2-step protocol described above. Again, high-purity copper crystals (>96 at.%) precipitated and formed large clusters. The carbon matrix could not be fully removed.

In general, the DEBL process has shown to be suitable for the deposition of low volatility precursors and the fabrication of structures within the condensate. It exhibited some advantages over the "classic" gas-assisted FEBID approach. The substrate was held at room temperature during deposition, so that no thermal drift occurred. This is usually an issue of LV precursor FEBID, where the substrate has to be heated to elevated temperatures (e.g.  $\text{Cu}_2(\text{pfp})_4$ :  $T_s = 135^\circ\text{C}$ ). Furthermore, the deposition rate was up to about 4 orders of magnitude larger than for the gas-assisted process and stands in agreement with reports from "cryo-FEBID".<sup>150</sup> In contrast to "cryo-FEBID" however, this RT approach has the advantage, that no water or other contaminants present in the chamber were condensed with the precursor. In addition to the higher deposition rate, this process also allows a higher processing throughput. After preparing the substrates, multiple samples can be irradiated on regular SEM stages, as well as a larger number of patterns are possible, since irradiation times can be reduced drastically. Unfortunately, this process did not offer improved metal contents compared to the gas-assisted FEBID of  $\text{Cu}_2(\text{pfp})_4$ . Another challenge is the sensitivity towards BSE halo deposition, which should be easily avoided by adjusting the electron dose. Furthermore, the thickness and uniformity of the condensate could not be controlled yet. Surely, by exploring the deposition and developing parameters further, this technique might offer more than shown in this limited study.

Different resist deposition techniques were investigated for other precursors, such as  $\text{Cu}_2(\text{pfp})_4(\text{EtNH}_2)_2$ . This precursor was deposited by dip-coating in a precursor-THF solution and subsequent drying, but no deposition results were achieved so far. However, this might be a solution for more uniform and controlled resist thickness. Otherwise, an evaporation method other than the classic GIS configuration (with an angle to the substrate normal) could be used. For symmetric results, the GIS could be placed perpendicular to the substrate surface, so that a directed molecular beam reaches the substrate. This is similar to molecule layer deposition with dedicated Knudsen cells (i.e. used in molecular beam epitaxy, MBE). Also, the distance between substrate and tube exit should be increased, in order to have less localized fluxes and a larger, more uniform condensate.

Future work could expand to the detailed study of electron doses necessary to irradiate and dissociate the condensate, without the formation of halos. When these parameters are determined, high resolution deposits as seen for "cryo-FEBID" and ice lithography will be possible with copper containing precursors as well. After that, large batches of samples can be produced, varying deposit size, thickness and shape and offering a wide range of scientific studies.

Finally, the metal purity could be improved by tweaking the purification protocol. This applies for both, gas-assisted FEBID and DEBL structures. Lower annealing temperatures at longer processing times might avoid the diffusion and agglomeration of copper. However, the removal of the shape sustaining carbon matrix through oxidation might encourage copper migration. Depending on the application, the reduction of copper oxide particles within the FEBID structures without the removal of the carbon matrix might be an option if shape fidelity is necessary. The study of the diffusion behavior of copper on hot substrates could improve the prediction of cluster/precipitate position and size. There might be a potential for making use of the diffusion and agglomeration of copper for the fabrication of pure copper nanoparticles.



## 8 Conclusion and Outlook

This work addressed the topic of direct-write deposition of copper via gas-assisted focused electron beam induced deposition (FEBID). Five different low-volatility Cu(II) compounds were selected for this study, i.e. fluorinated and non-fluorinated  $\beta$ -diketonates and perfluorinated carboxylates with and without additional amine ligands. The latter were reported for the first time as viable FEBID precursors. In parallel, an analogous perfluorinated silver carboxylate was reported and compared to its copper equivalent, to explore the chemical significance of the metal-ligand bond to FEBI deposition.

The direct comparison of the perfluorinated carboxylates  $\text{Cu}_2(\text{pfp})_4$  and  $\text{Ag}_2(\text{pfp})_2$  (with  $\text{pfp}^- = (\mu\text{-O}_2\text{CC}_2\text{F}_5)^-$ ) was performed through the study of spot deposits, which were fabricated via prolonged irradiation of a single spot. These stationary spot deposits served as experimental input for the continuum model, enabling the determination of the regions for different growth regimes. The precursor flux limited regime ended at the FW(99.9%) of the irradiating primary beam, i.e. the central deposition area. Consequently, the halo region, which was purely deposited by BSE contribution, could be assigned to the electron flux limited regime. The chemical and morphological analysis of these deposits showed a changing dissociation behavior for each metal complex. While  $\text{Cu}_2(\text{pfp})_4$  did not show a composition change from one deposition regime to the other,  $\text{Ag}_2(\text{pfp})_2$  featured higher metal purity in the halo, i.e. electron flux limited region. The highest reported metal content for  $\text{Cu}_2(\text{pfp})_4$  was 25 at.%, with copper crystallites that easily oxidized in atmosphere.  $\text{Ag}_2(\text{pfp})_2$  reported a maximum metal content of 74 at.% in its structures and improved crystal growth for long refreshment and short dwell times.  $\text{Cu}_2(\text{pfp})_4$  did not seem to be susceptible to such parameter optimizations.

TEM and EDX characterization showed the formation of metal(oxide) crystallites in a carbonaceous matrix, enabling the proposition of dissociation mechanisms for both precursors. The differences in dissociation and composition could be assigned to the chemical metal-ligand bond characteristics following the HSAB theory.

The aim of the direct comparison of the five copper compounds was to determine a dependence between ligand size and deposit purity. However, only small differences in metal purity were observed.  $\text{Cu}(\text{hfac})_2$ ,  $\text{Cu}_2(\text{EtNH}_2)_2(\text{pfp})_4$  and  $\text{Cu}_2(t\text{BuNH}_2)_2(\text{pfp})_4$  resulted in copper contents of 10, 15 and 15 at.% respectively. Although amine ligands have been reported to detach easily upon heating, they were readily incorporated via electron induced dissociation.  $\text{Cu}(\text{tbaoac})_2$  and  $\text{Cu}_2(\text{pfp})_4$  both yielded up to 25 at.% of metal content, despite the very large ligands of  $\text{Cu}(\text{tbaoac})_2$ . Elemental ratios were derived from the chemical quantification to describe the electron beam induced dissociation paths, as in the case of the  $\text{Ag}_2(\text{pfp})_2$  and  $\text{Cu}_2(\text{pfp})_4$  comparison study.

Thanks to all of the abovementioned FEBID studies, it could be stated that the deposition purity from Cu(II) compounds does not depend on the ligand size or amount of heteroatoms in the

pristine precursor. It is rather the metal-ligand bond chemistry and accessible fragmentation paths of the ligand, that determine the deposit composition. This also became clear for the analogous precursors with changing metal center. The chemistry of Ag(I) ions with the carboxylate ligand differs from the Cu(II)-ligand bond, leading to higher metal purities.

These findings could be beneficial for further FEBID studies and the quest for determining an ideal copper precursor. Rather than using smaller complexes or more reactive Cu(I) complexes, larger ligands which chemically stabilize the whole compound and increase its volatility, could be of advantage. Easy handling and the evaporation of intact molecules is favorable for the FEBID process and might be taken into consideration in future works.

The electron beam induced deposition of two of the abovementioned precursors, Cu(hfac)<sub>2</sub> and Cu<sub>2</sub>(pfp)<sub>4</sub>, were additionally studied *in situ*. To that end, they were introduced in a dedicated "eQCM" setup, which is an (U)HV chamber equipped with a broad electron source (10-100 eV) and a QCM. It was designed and built for *in situ* mass monitoring of FEBID processes at varying temperatures, where uniform heating was ensured by placing the whole chamber in a furnace. Cu(hfac)<sub>2</sub> was investigated at room temperature, and Cu<sub>2</sub>(pfp)<sub>4</sub> at 140°C. For each precursor, the mass rates (in pg/s) were determined at changing acceleration voltages with constant beam current and vice versa. With this data the total dissociation cross sections could be determined, using the FEBID continuum model. The values derived for Cu<sub>2</sub>(pfp)<sub>4</sub> were similar to those determined with the shape simulation approach.

The setup proved to be suitable for the study of more fundamental FEBID processes, but will need improvements to avoid beam-QCM misalignments and the co-deposition of background gases.

Upgrades of the eQCM setup should enable the access to a large variety of information concerning the FEBID process. Besides EBI deposition, also adsorption (i.e. chemi- vs. physisorption) and desorption of precursor molecules, the determination of the residence time  $\tau$ , ligand/fragment desorption upon electron irradiation could shed light on important mechanisms occurring during FEBID.

Finally, alternative approaches to gas-assisted FEBID were explored, with the aim of achieving pure copper structures from Cu<sub>2</sub>(pfp)<sub>4</sub>. The post-purification of FEBID structures was described as a two-step process via annealing in reactive gas atmospheres. Firstly, the carbonaceous matrix was removed through oxidation in O<sub>2</sub> followed by the reduction of CuO to elemental copper in a gas mixture of H<sub>2</sub>/N<sub>2</sub> (forming gas). The purification process successfully yielded pure copper crystals (>97 at.%), however, no shape fidelity was achieved. Annealing at lower temperatures could improve shape fidelity, even though there were indications that the carbon matrix was crucial to inhibit the diffusion and agglomeration of copper outside the initial structure. Nevertheless, it was shown that copper oxide is easily reduced to elemental copper at low concentrations of hydrogen in forming gas (2% H<sub>2</sub>).

An alternative approach that was studied was direct electron beam lithography (DEBL), a room temperature modification of "cryo-FEBID" and EBL, where the condensed Cu<sub>2</sub>(pfp)<sub>4</sub> precursor acted as a positive tone resist. Patterns were irradiated and developed by the removal of non-



irradiated condensate either by dissolution in EtOH or evaporation in HV. The resulting structures were analyzed in terms of composition and height. All had comparable copper contents of only 10 at.% with higher carbon contamination in thinner condensates. Very thick condensates formed a capping layer, which inhibited the desorption of fragments. Furthermore, all structures showed a distinctive halo deposit, which could help to determine the minimum electron dose necessary to dissociate the full condensate layer. Therefore, the halos would be removed and consequently increase the resolution of those structures.

DEBL has some advantages over the typical gas-assisted FEBID process of low-volatility precursors. The irradiation takes place at room temperature, eliminating any thermal drift of the substrate, thereby increasing deposit resolution. The deposition rates are up to 4 orders of magnitude larger than that of gas-assisted FEBID, which would solve the issue of extremely low growth rates of low volatility precursors. It could additionally allow a high throughput of structures, as the irradiation times are significantly shorter and growth rates accordingly higher. In combination with purification techniques, this deposition approach could be an alternative process to the direct-write deposition of copper-containing structures.

To summarize, this thesis explored the dissociation mechanisms of low volatility copper precursors, allowing for continuing the quest for precursors enabling the deposition of pure metal structures via FEBID for future applications.

## 9 Appendix: Supplementary Information

### 9.1 EDX reference measurements for error estimation

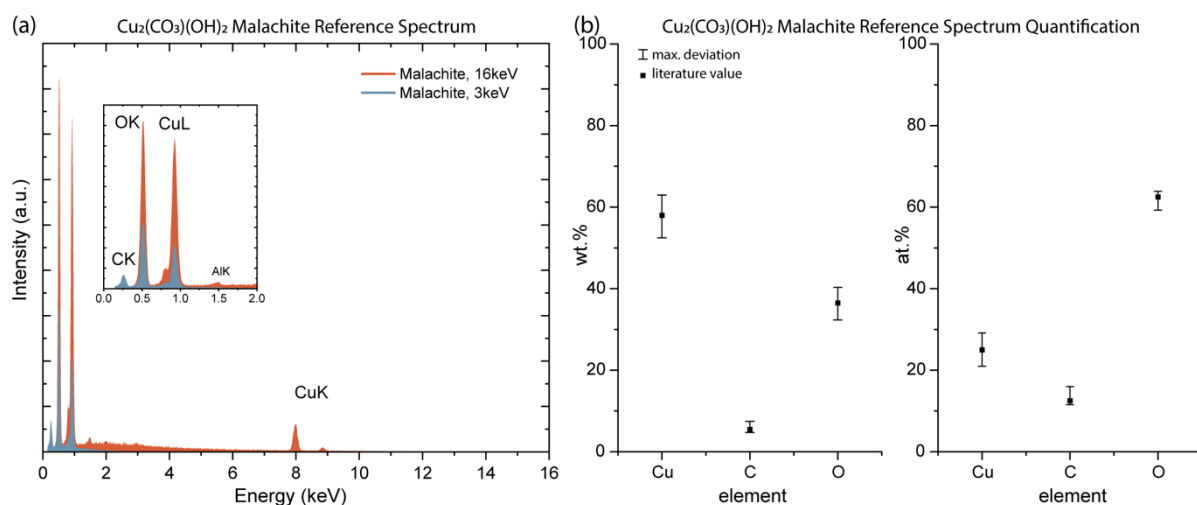


Figure 9-1 EDX reference measurements of Malachite ( $\text{Cu}_2(\text{CO}_3)(\text{OH})_2$ ). (a) Two exemplary EDX spectra of Malachite recorded at 3 keV (blue) and 16 keV (orange). (b) Chemical composition with error bars. The quantification results from EDAX Genesis software (standardless) are within the black error bars (maximum deviation from literature value) in comparison to literature values (black squares, from [www.webmineral.com/data/Malachite.shtml](http://www.webmineral.com/data/Malachite.shtml)). Measured quantification results for Cu, C and O do not exceed a deviation of 5.5 wt.% (4.1 at.%), 1.9 wt.% (3.4 at.%) and 4.2 wt.% (3.2 at.%) respectively.

To determine the average measurement uncertainty of the EDX setup used in this work, a copper carbonate (Malachite,  $\text{Cu}_2(\text{CO}_3)(\text{OH})_2$ ) was measured as reference. For that, a malachite stone was cut into 1.5 mm thick slices and polished. The slices were then attached to an aluminum sample holder with silver paste and partly covered in order to dissipate charges during SEM observation and EDX measurements. In total, 8 regions were measured for reference with either 3 keV or 16 keV primary beam energy (see two exemplary spectra in Figure 9-1a). The quantification results are within the black error bars in Figure 9-1b, marking the maximum deviation from the literature values plotted in the graphs. The measured values do not exceed a deviation of 5.5 wt.% (4.1 at.%) for copper, 1.9 wt.% (3.4 at.%) for carbon and 4.2 wt.% (3.2 at.%) for oxygen. The measurement uncertainties for all EDX measurements in this work can therefore be estimated roughly to max. 5 at.%. The values are listed in Table 9-1.

Table 9-1 Chemical composition of Malachite ( $\text{Cu}_2(\text{CO}_3)(\text{OH})_2$ ) measured in 8 regions (M01-M08) in comparison to literature values. The values are plotted in Figure 9-1b.

	Element	Lit. <sup>a</sup>	M01	M02	M03	M04	M05	M06	M07	M08	+Δ	-Δ
wt. %	Cu	58.01	53.83	52.48	62.03	62.45	57.53	53.99	62.97	56.21	4.96	5.53
	C	5.48	7.46	7.2	5.20	4.90	6.72	6.55	4.71	5.84	1.98	0.77
	O	36.51	38.72	40.32	32.78	32.65	35.75	39.46	32.32	37.96	3.81	4.20
at. %	Cu	25.00	21.78	20.93	28.23	28.64	24.47	22.00	29.12	23.63	4.12	4.07
	C	12.51	15.99	15.21	12.52	11.89	15.14	14.13	11.54	13.00	3.48	0.97
	O	62.50	62.23	63.87	59.25	59.47	60.39	63.87	59.34	63.37	1.37	3.25

<sup>a</sup> from [www.webmineral.com/data/Malachite.shtml](http://www.webmineral.com/data/Malachite.shtml)

It should be noted, that in EDX the measurements with 16 keV a small amount of aluminum was detected (see Figure 9-1a, inset, 1.5 keV). This most likely originated from scattered electrons, that were deviated through surface charging and hit the aluminum sample holder. The surface charging is visible in SEM images, as shown in Figure 9-2c.

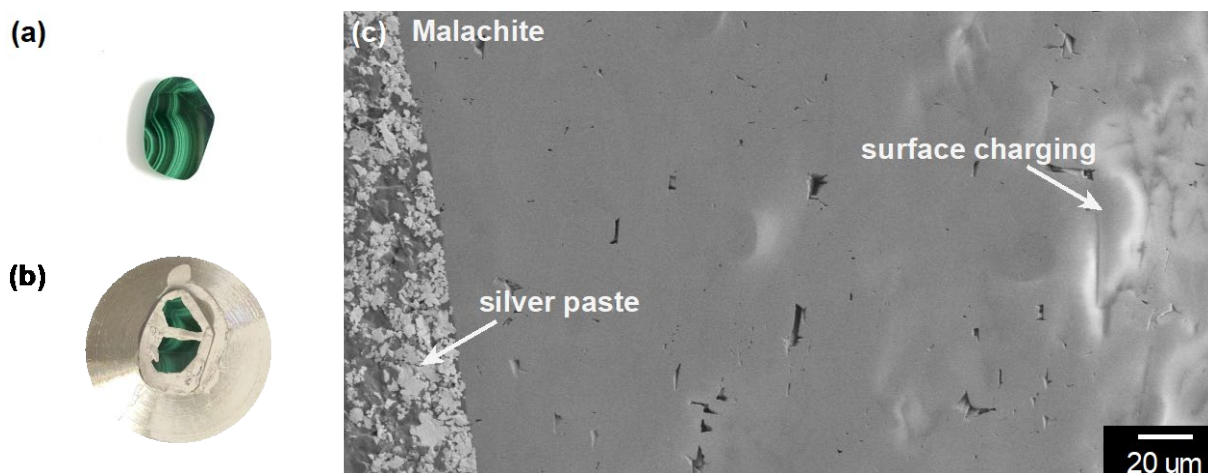


Figure 9-2 (a) Photograph of a Malachite disk used for EDX. (b) Photograph of the Malachite disk attached and covered with silver paste on an Al-SEM holder. (c) SEM image of the malachite reference sample. The silver paste is visible as well as surface charging arising during electron irradiation.



Figure 9-3 SEM image of the malachite sample in comparison to the optical image (inset). The color differences correspond to different porosity.

## 9.2 Stratagem Thin-Film Correction

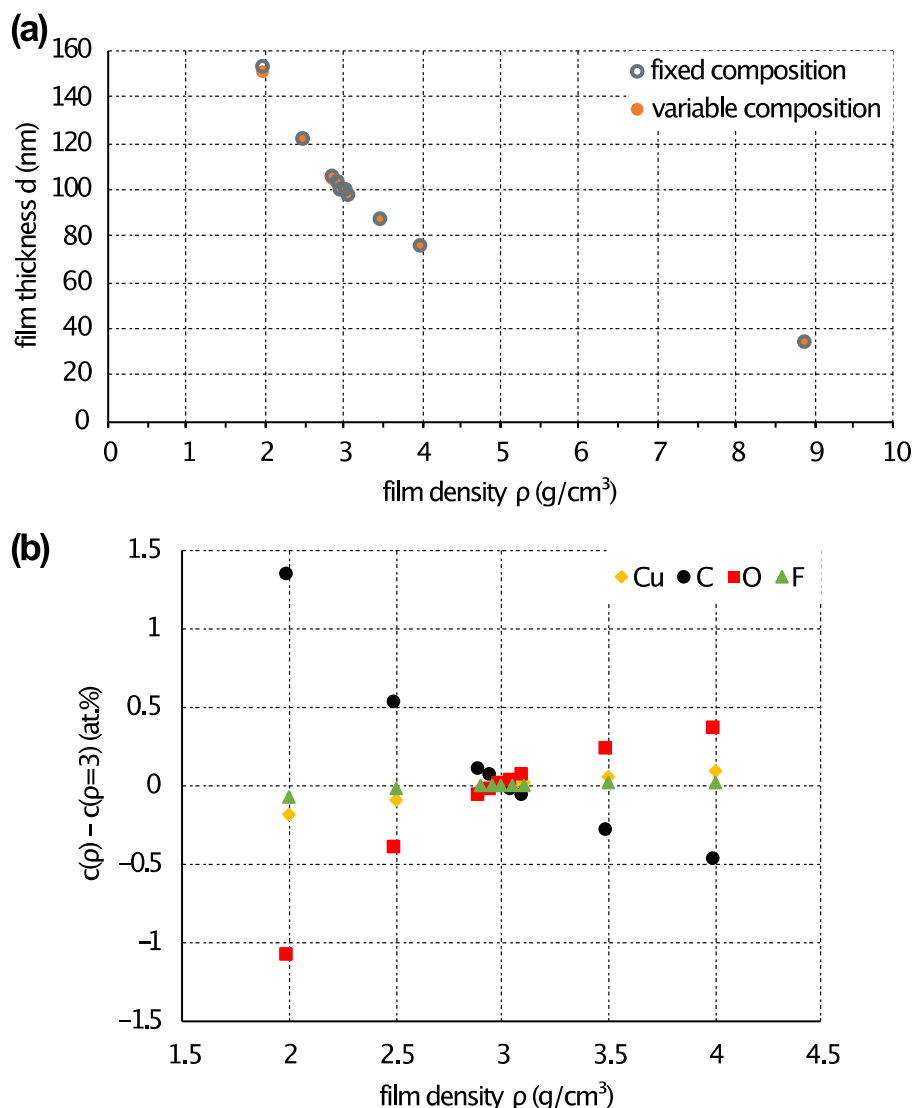


Figure 9-4 (a) Thin film thickness  $d$  calculated by Stratagem in dependence of a given film density  $\rho$  at fixed and variable composition. (b) Deviation of the thin film composition calculated by Stratagem in dependence of a given film density  $\rho$  at fixed film thickness  $d = 99$  nm (based on AFM measurements). Deviation from  $c(\rho = 3 \text{ g/cm}^3)$  as set for all results in this work.

### Influence of Changing Parameters in Stratagem

To determine the influence of varying Stratagem parameters on the calculated composition, the film density  $\rho$  of a measured Cu-FEBID structure from  $\text{Cu}_2(\text{pfp})_4$  was changed by  $\pm 50\%$ . In this work, the "standard density"  $\rho$  was set to  $3 \text{ g/cm}^3$ , according to literature values of similar precursors (see chapter 3.4).<sup>75</sup> Figure 9-4a displays the film thickness change with increasing film density  $\rho$ . The thickness was calculated for both cases, a fixed composition (obtained at  $3 \text{ g/cm}^3$  and used in chapter 7.2.2) and variable composition. In both versions, the film thickness decreased at the same extent. Also, the composition did not change when set variable (not shown). Stratagem calculated the same composition for all densities and merely the

thickness was adjusted. It should be noted, that the film thickness is calculated more reliably when the film was measured at multiple energies.

The film composition therefore only depends on the given film density, if the thickness is fixed to one value. Figure 9-4b shows the absolute difference between the new composition calculation  $c(\rho)$  and the "standard density"  $c(3 \text{ g/cm}^3)$  in at.%. The calculations were done for a fixed thin film thickness  $d = 99 \text{ nm}$  (corresponding to AFM measurements). It is evident from the graph, that the composition changes very little. Fluorine and copper contents are hardly influenced, and even the larger deviations of carbon and oxygen lie within the range of measurement error ( $< 5 \text{ at.}\%$ ).

Differences EDAX Standardless Quantification (exclusion substrate signal) vs. thin film correction

When comparing the differences between the standardless EDAX quantification (neglecting the substrate signal) to the Stratagem results, the deviations are significantly larger. For this purpose, the difference background subtracted Stratagem results were subtracted from the EDAX quantification values for a variety of samples. The results are shown in Figure 9-5. Next to the same experiments as in Figure 9-4, two other samples with  $\text{Cu}(\text{tbaoac})_2$  and  $\text{Ag}_2(\text{pfp})_2$  were added to the comparison. While the difference for  $\text{Cu}_2(\text{pfp})_4$  and  $\text{Cu}(\text{tbaoac})_2$  is relatively small, the measurements of the Ag-halos are largely out of range. In this case, the EDAX quantification overestimated the all values but the fluorine. With increasing PE beam energy (7, 8 and 10 keV) the deviation becomes larger. This is due to the larger interaction volume within the substrate, so that the substrate signal dominates and the exclusion of it falsifies the results. Therefore, the Ag values deviate more than the Cu values, which were recorded with 3 keV PE energy. Additionally, the EDAX quantification cannot account for any oxide layers on the substrate (as necessary for the  $\text{Cu}_2(\text{pfp})_4$  (4nm native  $\text{SiO}_2$ ) and  $\text{Ag}_2(\text{pfp})_2$  (200nm  $\text{SiO}_2$ )). The oxygen signal could not be excluded fully from the quantification, because the deposit could also contain oxygen. This was especially crucial for the detection of metal oxidation (i.e. copper oxides).

Therefore, the Stratagem thin film correction was used confidently in the scope of this work, as even big changes in film density did not influence the atomic composition. Also, the correct subtraction of the substrate, especially oxide layers, was only possible using this method.

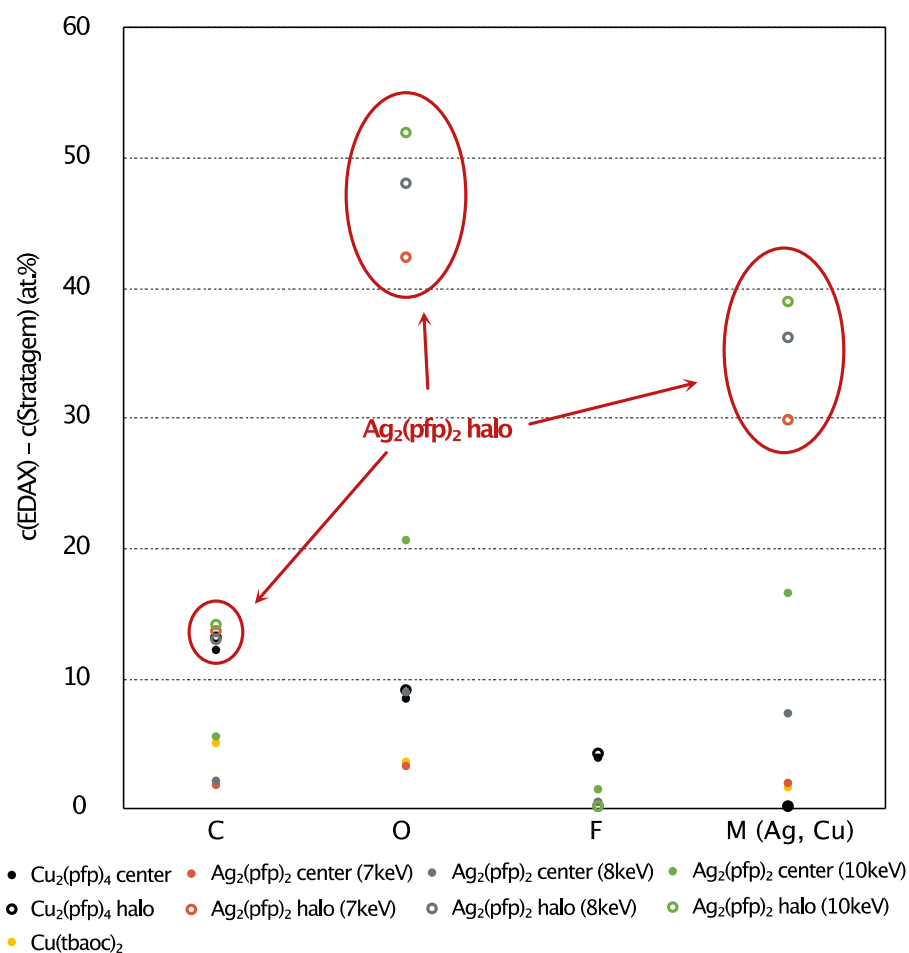


Figure 9-5 Composition difference (at.%) of various deposits when comparing background subtracted Stratagem results to EDAX results without substrate signal: EDAX quantification result  $c(\text{EDAX}) - c(\text{Stratagem})$ . The largest deviations arise for thin halo Ag deposits (red arrows).

### 9.3 Parameter Space - Shape Simulation

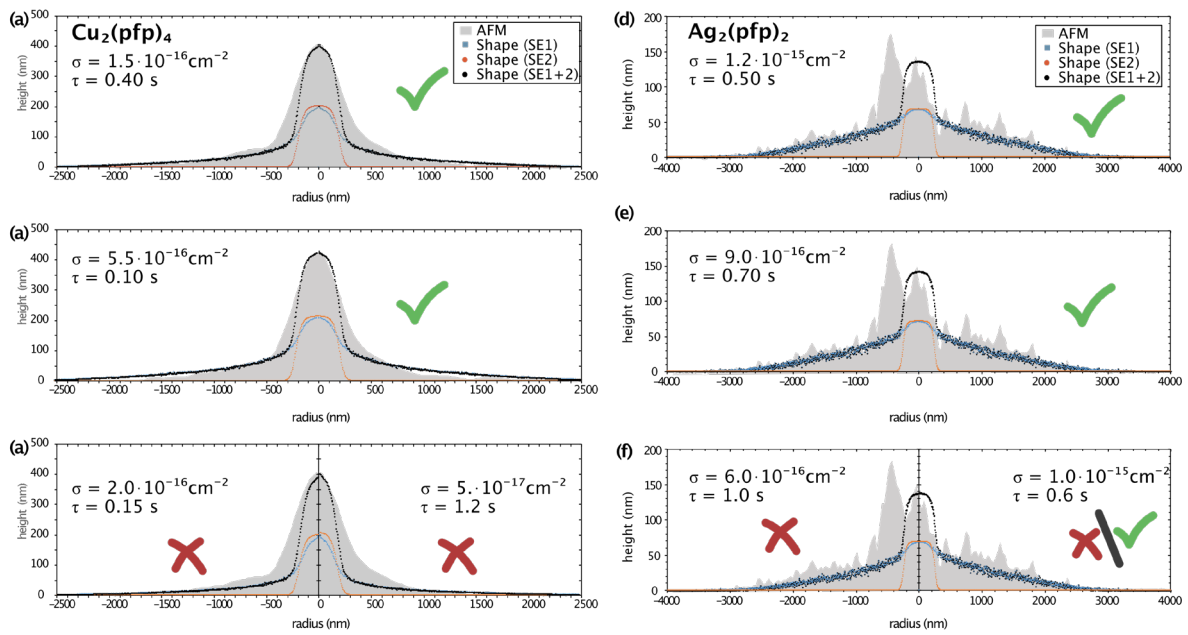


Figure 9-6 Shape simulations for (a-c)  $\text{Cu}_2(\text{pfp})_4$  and (d-f)  $\text{Ag}_2(\text{pfp})_2$  dot deposits with varying parameters  $\sigma$  and  $\tau$ . (a and d) The upper panels illustrate the best fit used in Chapter 4.3.1. (b and e) The middle panels illustrate another set of parameters with a good fit. (c and f) The lower panels display two parameter sets each where  $\sigma$  and  $1/\tau$  from (a/d) were multiplied with the same factor  $x$ :  $x\sigma$  and  $x/\tau$ . (c) left:  $x=4$ , right:  $x=1/3$ ; (f) left:  $x=5$ , right:  $x=5/6$ .

The parameters  $\sigma$  and  $\tau$  were varied to find the best fit of the shape simulation in accordance with the continuum model. Figure 9-6 shows the study of the parameter space. The upper panels (a and d) show the same best fit as in Chapter 4.3.1. The variation of both parameters  $\sigma$  and  $\tau$  are shown in the other panels. (b) and (e) show another possible fit. (c) and (f) illustrate a set of  $\sigma$  and  $\tau$  changed by a factor  $x$ . Since  $\sigma$  and  $\tau$  are inverse proportional ( $1/\tau$ ) in the denominator of the growth rate  $R(r)$ , the same fit could be expected. However, the influence of  $of(r)$  in the numerator is larger, so that no good fit was achieved. Therefore, the panels (a) and (d) were chosen as best fit for the discussion in Chapter 4.

9.4 eQCM setup

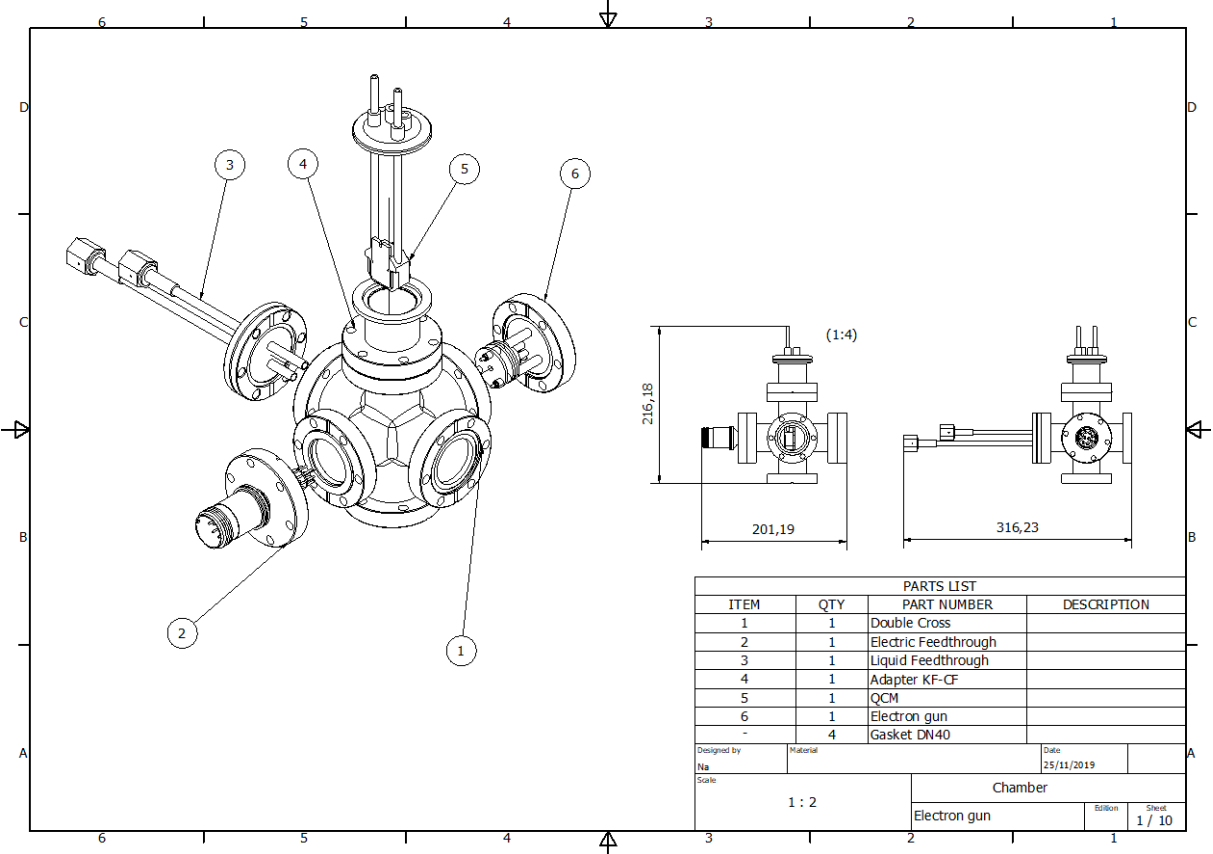


Figure 9-7 Drawing of the eQCM chamber.



## References

- (1) Duan, H.; Manfrinato, V. R.; Yang, J. K. W.; Winston, D.; Cord, B. M.; Berggren, K. K. Metrology for Electron-Beam Lithography and Resist Contrast at the Sub-10 nm Scale. *J. Vac. Sci. Technol. B, Nanotechnol. Microelectron. Mater. Process. Meas. Phenom.* **2010**, *28* (6), C6H11–C6H17. <https://doi.org/10.1116/1.3501359>.
- (2) Manfrinato, V. R.; Zhang, L.; Su, D.; Duan, H.; Hobbs, R. G.; Stach, E. A.; Berggren, K. K. Resolution Limits of Electron-Beam Lithography toward the Atomic Scale. *Nano Lett.* **2013**, *13* (4), 1555–1558. <https://doi.org/10.1021/nl304715p>.
- (3) van Dorp, W. F.; Lazić, I.; Beyer, A.; Götzhäuser, A.; Wagner, J. B.; Hansen, T. W.; Hagen, C. W. Ultrahigh Resolution Focused Electron Beam Induced Processing: The Effect of Substrate Thickness. *Nanotechnology* **2011**, *22* (11), 115303.
- (4) van Dorp, W. F.; Zhang, X.; Feringa, B. L.; Wagner, J. B.; Hansen, T. W.; De Hosson, J. T. M. Nanometer-Scale Lithography on Microscopically Clean Graphene. *Nanotechnology* **2011**, *22* (50), 505303.
- (5) Fowlkes, J. D.; Winkler, R.; Lewis, B. B.; Stanford, M. G.; Plank, H.; Rack, P. D. Simulation-Guided 3D Nanomanufacturing via Focused Electron Beam Induced Deposition. *ACS Nano* **2016**, *10* (6), 6163–6172. <https://doi.org/10.1021/acsnano.6b02108>.
- (6) Jesse, S.; Borisevich, A. Y.; Fowlkes, J. D.; Lupini, A. R.; Rack, P. D.; Unocic, R. R.; Sumpter, B. G.; Kalinin, S. V.; Belianinov, A.; Ovchinnikova, O. S. Directing Matter: Toward Atomic-Scale 3D Nanofabrication. *ACS Nano* **2016**, *10* (6), 5600–5618. <https://doi.org/10.1021/acsnano.6b02489>.
- (7) Winkler, R.; Schmidt, F.-P.; Haselmann, U.; Fowlkes, J. D.; Lewis, B. B.; Kothleitner, G.; Rack, P. D.; Plank, H. Direct-Write 3D Nanoprinting of Plasmonic Structures. *ACS Appl. Mater. Interfaces* **2017**, *9* (9), 8233–8240. <https://doi.org/10.1021/acsnano.6b13062>.
- (8) Utke, I.; Hoffmann, P.; Melngailis, J. Gas-Assisted Focused Electron Beam and Ion Beam Processing and Fabrication. *J. Vac. Sci. Technol. B Microelectron. Nanom. Struct. Process. Meas. Phenom.* **2008**, *26* (4), 1197–1276. <https://doi.org/10.1116/1.2955728>.
- (9) van Dorp, W. F.; Hagen, C. W. A Critical Literature Review of Focused Electron Beam Induced Deposition. *J. Appl. Phys.* **2008**, *104* (8), 81301. <https://doi.org/10.1063/1.2977587>.
- (10) Huth, M.; Porra, F.; Schwalb, C.; Winhold, M.; Sachser, R.; Dukic, M.; Adams, J.; Fantner, G. Focused Electron Beam Induced Deposition: A Perspective. *Beilstein J. Nanotechnol.* **2012**, *3*, 597–619. <https://doi.org/10.3762/bjnano.3.70>.
- (11) Botman, A.; Mulders, J. J. L.; Hagen, C. W. Creating Pure Nanostructures from Electron-Beam-Induced Deposition Using Purification Techniques: A Technology Perspective. *Nanotechnology* **2009**, *20* (37), 372001.
- (12) Huth, M.; Porra, F.; Dobrovolskiy, O. V. Focused Electron Beam Induced Deposition Meets Materials Science. *Microelectron. Eng.* **2017**, *185–186*, 9–28. <https://doi.org/10.1016/j.mee.2017.10.012>.
- (13) Utke, I.; Hoffmann, P.; Dwir, B.; Leifer, K.; Kapon, E.; Doppelt, P. Focused Electron Beam

Induced Deposition of Gold. *J. Vac. Sci. Technol. B Microelectron. Nanom. Struct.* **2000**, *18* (6), 3168–3171. <https://doi.org/10.1116/1.1319690>.

- (14) Mulders, J. J. L.; Veerhoek, J. M.; Bosch, E. G. T.; Trompenaars, P. H. F. Fabrication of Pure Gold Nanostructures by Electron Beam Induced Deposition with Au(CO)Cl Precursor: Deposition Characteristics and Primary Beam Scattering Effects. *J. Phys. D. Appl. Phys.* **2012**, *45* (47). <https://doi.org/10.1088/0022-3727/45/47/475301>.
- (15) Bernau, L.; Gabureac, M.; Erni, R.; Utke, I. Tunable Nanosynthesis of Composite Materials by Electron-Impact Reaction. *Angew. Chemie Int. Ed.* **2010**, *49* (47), 8880–8884. <https://doi.org/10.1002/anie.201004220>.
- (16) Fernández-Pacheco, A.; De Teresa, J. M.; Córdoba, R.; Ibarra, M. R. Magnetotransport Properties of High-Quality Cobalt Nanowires Grown by Focused-Electron-Beam-Induced Deposition. *J. Phys. D. Appl. Phys.* **2009**, *42* (5), 55005.
- (17) Lukasczyk, T.; Schirmer, M.; Steinrück, H.-P.; Marbach, H. Electron-Beam-Induced Deposition in Ultrahigh Vacuum: Lithographic Fabrication of Clean Iron Nanostructures. *Small* **2008**, *4* (6), 841–846. <https://doi.org/10.1002/smll.200701095>.
- (18) Kämpken, B.; Wulf, V.; Auner, N.; Winhold, M.; Huth, M.; Rhinow, D.; Terfort, A. Directed Deposition of Silicon Nanowires Using Neopentasilane as Precursor and Gold as Catalyst. *Beilstein J. Nanotechnol.* **2012**, *3* (1), 534–545. <https://doi.org/10.3762/bjnano.3.62>.
- (19) Höflich, K.; Jurczyk, J.; Zhang, Y.; Puydinger dos Santos, M. V.; Götz, M.; Guerra-Nuñez, C.; Best, J. P.; Kapusta, C.; Utke, I. Direct Electron Beam Writing of Silver-Based Nanostructures. *ACS Appl. Mater. Interfaces* **2017**, *9* (28), 24071–24077. <https://doi.org/10.1021/acsami.7b04353>.
- (20) Matsui, S.; Mori, K. New Selective Deposition Technology By Electron-Beam Induced Surface Reaction. *J. Vac. Sci. Technol. B Microelectron. Nanom. Struct.* **1986**, *4* (1), 299–304. <https://doi.org/10.1116/1.583317>.
- (21) Spencer, J. A.; Rosenberg, S. G.; Barclay, M.; Wu, Y.-C.; McElwee-White, L.; Howard Fairbrother, D. Understanding the Electron-Stimulated Surface Reactions of Organometallic Complexes to Enable Design of Precursors for Electron Beam-Induced Deposition. *Appl. Phys. A* **2014**, *117* (4), 1631–1644. <https://doi.org/10.1007/s00339-014-8570-5>.
- (22) Carden, W. G.; Lu, H.; Spencer, J. A.; Fairbrother, D. H.; McElwee-White, L. Mechanism-Based Design of Precursors for Focused Electron Beam-Induced Deposition. *MRS Commun.* **2018**, *8* (2), 343–357. <https://doi.org/10.1557/mrc.2018.77>.
- (23) Carden, W. G.; Thorman, R. M.; Unlu, I.; Abboud, K. A.; Fairbrother, D. H.; McElwee-White, L. Design, Synthesis, and Evaluation of CF<sub>3</sub>AuCNR Precursors for Focused Electron Beam-Induced Deposition of Gold. *ACS Appl. Mater. Interfaces* **2019**, *11* (12), 11976–11987. <https://doi.org/10.1021/acsami.8b18368>.
- (24) Warneke, J.; Rohdenburg, M.; Zhang, Y.; Orzaghi, J.; Vaz, A.; Utke, I.; De Hosson, J. T. M.; Van Dorp, W. F.; Swiderek, P. Role of NH<sub>3</sub> in the Electron-Induced Reactions of Adsorbed and Solid Cisplatin. *J. Phys. Chem. C* **2016**, *120* (7), 4112–4120. <https://doi.org/10.1021/acs.jpcc.5b12184>.

- (25) Rohdenburg, M.; Martinović, P.; Ahlenhoff, K.; Koch, S.; Emmrich, D.; Götzhäuser, A.; Swiderek, P. Cisplatin as a Potential Platinum Focused Electron Beam Induced Deposition Precursor:  $\text{NH}_3$  Ligands Enhance the Electron-Induced Removal of Chlorine. *J. Phys. Chem. C* **2019**, *123* (35), 21774–21787. <https://doi.org/10.1021/acs.jpcc.9b05756>.
- (26) A. Spencer, J.; Wu, Y.-C.; McElwee-White, L.; Howard Fairbrother, D. Electron Induced Surface Reactions of  $\text{Cis-Pt}(\text{CO})_2\text{Cl}_2$ : A Route to Focused Electron Beam Induced Deposition of Pure Pt Nanostructures. *J. Am. Chem. Soc.* **2016**, *138* (29), 9172–9182. <https://doi.org/10.1021/jacs.6b04156>.
- (27) F. van Dorp, W.; Wu, X.; J. L. Mulders, J.; Harder, S.; Rudolf, P.; T. M. De Hosson, J. Gold Complexes for Focused-Electron-Beam-Induced Deposition. *Langmuir* **2014**, *30* (40), 12097–12105. <https://doi.org/10.1021/la502618t>.
- (28) Xue, Z.; Jane Strouse, M.; Shuh, D. K.; Knobler, C. B.; Kaesz, H. D.; Williams, R. S.; Hicks, R. F. Characterization of (Methylcyclopentadienyl)Trimethylplatinum and Low-Temperature Organometallic Chemical Vapor Deposition of Platinum Metal. *J. Am. Chem. Soc.* **1989**, *111* (24), 8779–8784. <https://doi.org/10.1021/ja00206a002>.
- (29) G. Carden, W.; Pedziwiatr, J.; A. Abboud, K.; McElwee-White, L. Halide Effects on the Sublimation Temperature of  $\text{X-Au-L}$  Complexes: Implications for Their Use as Precursors in Vapor Phase Deposition Methods. *ACS Appl. Mater. Interfaces* **2017**, *9* (46), 40998–41005. <https://doi.org/10.1021/acsami.7b12465>.
- (30) Rosenberg, S. G.; Barclay, M.; Fairbrother, D. H. Electron Induced Surface Reactions of Organometallic  $\text{Metal}(\text{hfac})_2$  Precursors and Deposit Purification. *ACS Appl. Mater. Interfaces* **2014**, *6* (11), 8590–8601. <https://doi.org/10.1021/am501457h>.
- (31) Koops, H. W. P. High-Resolution Electron-Beam Induced Deposition. *J. Vac. Sci. Technol. B Microelectron. Nanom. Struct.* **1988**, *6* (1), 477. <https://doi.org/10.1116/1.584045>.
- (32) Luisier, A.; Utke, I.; Bret, T.; Cicoira, F.; Hauert, R.; Rhee, S.-W.; Doppelt, P.; Hoffmann, P. Comparative Study of Cu-Precursors for 3D Focused Electron Beam Induced Deposition. *J. Electrochem. Soc.* **2004**, *151* (9), C590–C593. <https://doi.org/10.1149/1.1779335>.
- (33) Luisier, A.; Utke, I.; Bret, T.; Cicoira, F.; Hauert, R.; Rhee, S. W.; Doppelt, P.; Hoffmann, P. Comparative Study of Cu Precursors for 3D Focused Electron Beam Induced Deposition. *J. Electrochem. Soc.* **2004**, *151* (8), C535–C537.
- (34) Weber, M.; Koops, H. W. P.; Rudolph, M.; Kretz, J.; Schmidt, G. New Compound Quantum Dot Materials Produced by Electron-beam Induced Deposition. *J. Vac. Sci. Technol. B Microelectron. Nanom. Struct. Process. Meas. Phenom.* **1995**, *13* (3), 1364–1368. <https://doi.org/10.1116/1.587854>.
- (35) Szkudlarek, A.; Vaz, A. R.; Zhang, Y.; Rudkowski, A.; Kapusta, C.; Erni, R.; Moshkalev, S.; Utke, I. Formation of Pure Cu Nanocrystals upon Post-Growth Annealing of Cu–C Material Obtained from Focused Electron Beam Induced Deposition: Comparison of Different Methods. *Beilstein J. Nanotechnol.* **2015**, *6* (1), 1508–1517.
- (36) Haverkamp, C.; Sarau, G.; Polyakov, M. N.; Utke, I.; dos Santos, M. V. P.; Christiansen, S.; Höflich, K. A Novel Copper Precursor for Electron Beam Induced Deposition. *Beilstein J. Nanotechnol.* **2018**, *9*, 1220.
- (37) Engmann, S.; Ómarsson, B.; Lacko, M.; Stano, M.; Matejčík, Š.; Ingólfsson, O. Dissociative

Electron Attachment to Hexafluoroacetylacetone and Its Bidentate Metal Complexes  $M(hfac)_2$ ;  $M = Cu, Pd$ . *J. Chem. Phys.* **2013**, *138* (23), 234309.

- (38) Lacko, M.; Papp, P.; Szymańska, I. B.; Szlyk, E.; Matejčík, Š. Electron Interaction with Copper(II) Carboxylate Compounds. *Beilstein J. Nanotechnol.* **2018**, *9*, 384–398. <https://doi.org/10.3762/bjnano.9.38>.
- (39) Sala, L.; Szymańska, I. B.; Dablemont, C.; Lafosse, A.; Amiaud, L. Response under Low-Energy Electron Irradiation of a Thin Film of a Potential Copper Precursor for Focused Electron Beam Induced Deposition (FEBID). *Beilstein J. Nanotechnol.* **2018**, *9*, 57–65. <https://doi.org/10.3762/bjnano.9.8>.
- (40) Knapas, K.; Ritala, M. In Situ Studies on Reaction Mechanisms in Atomic Layer Deposition. *Crit. Rev. Solid State Mater. Sci.* **2013**, *38* (3), 167–202. <https://doi.org/10.1080/10408436.2012.693460>.
- (41) Kunze, D.; Peters, O.; Sauerbrey, G. Polymerisation Adsorbierter Kohlenwasserstoffe Bei Elektronenbeschuss. *Z. angew. Phys.* **1967**, *22* (2), 69–75.
- (42) Friedli, V.; Santschi, C.; Michler, J.; Hoffmann, P.; Utke, I. Mass Sensor for in situ Monitoring of Focused Ion and Electron Beam Induced Processes. *Appl. Phys. Lett.* **2007**, *90* (5), 53106.
- (43) Dubner, A. D.; Wagner, A. In Situ Measurement of Ion-beam-induced Deposition of Gold. *J. Appl. Phys.* **1989**, *65* (9), 3636–3643.
- (44) Dubner, A. D.; Wagner, A. The Role of Gas Adsorption in Ion-beam-induced Deposition of Gold. *J. Appl. Phys.* **1989**, *66* (2), 870–874.
- (45) Chiang, T. P.; Sawin, H. H.; Thompson, C. V. Surface Kinetic Study of Ion-Induced Chemical Vapor Deposition of Copper for Focused Ion Beam Applications. *J. Vac. Sci. Technol. A Vacuum, Surfaces, Film.* **1997**, *15* (6), 3104–3114. <https://doi.org/10.1116/1.580853>.
- (46) Kunz, R. R.; Mayer, T. M. Electron Beam Induced Surface Nucleation and Low-temperature Decomposition of Metal Carbonyls. *J. Vac. Sci. Technol. B Microelectron. Process. Phenom.* **1988**, *6* (5), 1557–1564.
- (47) Stewart, R. L. Insulating Films Formed Under Electron and Ion Bombardment. *Phys. Rev.* **1934**, *45* (7), 488–490. <https://doi.org/10.1103/PhysRev.45.488>.
- (48) Christy, R. W. Formation of Thin Polymer Films by Electron Bombardment. *J. Appl. Phys.* **1960**, *31* (9), 1680–1683. <https://doi.org/10.1063/1.1735915>.
- (49) Baker, A. G.; Morris, W. C. Deposition of Metallic Films by Electron Impact Decomposition of Organometallic Vapors. *Rev. Sci. Instrum.* **1961**, *32* (4), 458. <https://doi.org/10.1063/1.1717408>.
- (50) De Teresa, J. M.; Fernández-Pacheco, A.; Córdoba, R.; Serrano-Ramón, L.; Sangiao, S.; Ibarra, M. R. Review of Magnetic Nanostructures Grown by Focused Electron Beam Induced Deposition (FEBID). *J. Phys. D: Appl. Phys.* **2016**, *49* (24), 243003.
- (51) Utke, I.; Koops, H. W. P. The Historical Development of Electron Beam Induced Deposition and Etching: From Carbonaceous to Functional Materials. In *Nanofabrication Using Focused Ion and Electron Beams: Principles and Applications*; Utke, I., Moshkalev, S., Russell, P., Eds.; Oxford Series on Nanomanufacturing, 2012; pp 3–35.

- (52) Seiler, H. Secondary Electron Emission in the Scanning Electron Microscope. *J. Appl. Phys.* **1983**, 54 (11). <https://doi.org/10.1063/1.332840>.
- (53) Kanaya, K.; Okayama, S. Penetration and Energy-Loss Theory of Electrons in Solid Targets. *J. Phys. D. Appl. Phys.* **1972**, 5 (1), 43.
- (54) Joy, D. C. *Monte Carlo Modeling for Electron Microscopy and Microanalysis*; Oxford Series in Optical and Imaging Sciences; Oxford University Press: New York, 1995.
- (55) Demers, H.; Poirier-Demers, N.; Couture, A. R.; Joly, D.; Guilmain, M.; de Jonge, N.; Drouin, D. Three-Dimensional Electron Microscopy Simulation with the CASINO Monte Carlo Software. *Scanning* **2011**, 33 (3), 135–146. <https://doi.org/10.1002/sca.20262>.
- (56) Utke, I. FEB and FIB Continuum Models for One Adsorbate Species. In *Nanofabrication Using Focused Ion and Electron Beams: Principles and Applications*; Utke, I., Moshkalev, S., Russell, P., Eds.; Oxford Series on Nanomanufacturing, 2012.
- (57) Höflich, K.; Jurczyk, J. M.; Madajska, K.; Götz, M.; Berger, L.; Guerra-Nuñez, C.; Haverkamp, C.; Szymanska, I. B.; Utke, I. Towards the Third Dimension in Direct Electron Beam Writing of Silver. *Beilstein J. Nanotechnol.* **2018**, 9, 842–849. <https://doi.org/doi:10.3762/bjnano.9.78>.
- (58) Hoyle, P. C.; Ogasawara, M.; Cleaver, J. R. A.; Ahmed, H. Electrical Resistance of Electron Beam Induced Deposits from Tungsten Hexacarbonyl. *Appl. Phys. Lett.* **1993**, 62 (23), 3043–3045. <https://doi.org/10.1063/1.109133>.
- (59) Bernau, L.; Gabureac, M.; Utke, I. Variation of the Metallic Content of Focused Electron Beam Induced Deposition of Cobalt. **2010**. <https://doi.org/10.1002/anie.201004220>.
- (60) Córdoba, R.; Fernández-Pacheco, R.; Fernández-Pacheco, A.; Gloter, A.; Magén, C.; Stéphan, O.; Ibarra, M. R.; De Teresa, J. M. Nanoscale Chemical and Structural Study of Co-Based FEBID Structures by STEM-EELS and HRTEM. *Nanoscale Res. Lett.* **2011**, 6 (1), 592. <https://doi.org/10.1186/1556-276X-6-592>.
- (61) Wachter, S.; Gavagnin, M.; Wanzenboeck, H. D.; Shawrav, M. M.; Belić, D.; Bertagnolli, E. Nitrogen as a Carrier Gas for Regime Control in Focused Electron Beam Induced Deposition. *Nanofabrication* **2014**, 1 (1), 16–22. <https://doi.org/10.2478/nanofab-2014-0002>.
- (62) Pablo-Navarro, J.; Sanz-Hernández, D.; Magén, C.; Fernández-Pacheco, A.; de Teresa, J. M. Tuning Shape, Composition and Magnetization of 3D Cobalt Nanowires Grown by Focused Electron Beam Induced Deposition (FEBID). *J. Phys. D. Appl. Phys.* **2017**, 50 (18), 18LT01. <https://doi.org/10.1088/1361-6463/aa63b4>.
- (63) Fowlkes, J. D.; Winkler, R.; Lewis, B. B.; Fernández-Pacheco, A.; Skoric, L.; Sanz-Hernández, D.; Stanford, M. G.; Mutunga, E.; Rack, P. D.; Plank, H. High-Fidelity 3D-Nanoprinting via Focused Electron Beams: Computer-Aided Design (3BID). *ACS Appl. Nano Mater.* **2018**, 1 (3), 1028–1041. <https://doi.org/10.1021/acsanm.7b00342>.
- (64) Kretz, J.; Rudolph, M.; Weber, M.; Koops, H. W. P. Three-Dimensional Structurization by Additive Lithography, Analysis of Deposits Using TEM and EDX, and Application to Field-Emitter Tips. *Microelectron. Eng.* **1994**, 23 (1–4), 477–481. [https://doi.org/10.1016/0167-9317\(94\)90199-6](https://doi.org/10.1016/0167-9317(94)90199-6).
- (65) Koops, H. W. P. Fabrication and Characterization of Platinum Nanocrystalline Material

Grown by Electron-Beam Induced Deposition. *J. Vac. Sci. Technol. B Microelectron. Nanom. Struct.* **1995**, 13 (6), 2400. <https://doi.org/10.1116/1.588008>.

- (66) Lau, Y. M.; Chee, P. C.; Thong, J. T. L.; Ng, V. Properties and Applications of Cobalt-Based Material Produced by Electron-Beam-Induced Deposition. *J. Vac. Sci. Technol. A* **2002**, 20 (4), 1295–1302. <https://doi.org/10.1116/1.1481040>.
- (67) Gazzadi, G. C.; Frabboni, S.; Menozzi, C. Suspended Nanostructures Grown by Electron Beam-Induced Deposition of Pt and TEOS Precursors. *Nanotechnology* **2007**, 18 (44). <https://doi.org/10.1088/0957-4484/18/44/445709>.
- (68) Koops, H. W. P.; Hoinkis, O. E.; Honsberg, M. E. W.; Schmidt, R.; Blum, R.; Böttger, G.; Kuligk, A.; Liguda, C.; Eich, M. Two-Dimensional Photonic Crystals Produced by Additive Nanolithography with Electron Beam-Induced Deposition Act as Filters in the Infrared. *Microelectron. Eng.* **2001**, 57–58, 995–1001. [https://doi.org/https://doi.org/10.1016/S0167-9317\(01\)00565-2](https://doi.org/https://doi.org/10.1016/S0167-9317(01)00565-2).
- (69) Mølhave, K.; Madsen, D. N.; Dohn, S.; Bøggild, P. Constructing, Connecting and Soldering Nanostructures by Environmental Electron Beam Deposition. *Nanotechnology* **2004**, 15 (8), 1047–1053. <https://doi.org/10.1088/0957-4484/15/8/033>.
- (70) Höflich, K.; Yang, R. Bin; Berger, A.; Leuchs, G.; Christiansen, S. The Direct Writing of Plasmonic Gold Nanostructures by Electron-Beam-Induced Deposition. *Adv. Mater.* **2011**, 23 (22-23), 2657–2661. <https://doi.org/10.1002/adma.201004114>.
- (71) Sauerbrey, G. Verwendung von Schwingquarzen Zur Wägung Dünner Schichten Und Zur Mikrowägung. *Zeitschrift für Phys.* **1959**, 155 (2), 206–222. <https://doi.org/10.1007/BF01337937>.
- (72) Drouin, D.; Couture, A. R.; Joly, D.; Tastet, X.; Aimez, V.; Gauvin, R. CASINO V2.42—A Fast and Easy-to-Use Modeling Tool for Scanning Electron Microscopy and Microanalysis Users. *Scanning* **2007**, 29 (3), 92–101. <https://doi.org/10.1002/sca.20000>.
- (73) Goldstein, J. I.; Newbury, D. E.; Echlin, P.; Joy, D. C.; Lyman, C. E.; Lifshin, E.; Sawyer, L.; Michael, J. R. Quantitative X-Ray Analysis: The Basics. In *Scanning Electron Microscopy and X-ray Microanalysis: Third Edition*; Goldstein, J. I., Newbury, D. E., Echlin, P., Joy, D. C., Lyman, C. E., Lifshin, E., Sawyer, L., Michael, J. R., Eds.; Springer, Boston, MA: Boston, MA, 2003; pp 391–451. [https://doi.org/10.1007/978-1-4615-0215-9\\_9](https://doi.org/10.1007/978-1-4615-0215-9_9).
- (74) SAMx. STRATAGem 4.4 User's Manual. 2008.
- (75) Utke, I.; Friedli, V.; Michler, J.; Bret, T.; Multone, X.; Hoffmann, P. Density Determination of Focused-Electron-Beam-Induced Deposits with Simple Cantilever-Based Method. *Appl. Phys. Lett.* **2006**, 88 (3), 31906. <https://doi.org/10.1063/1.2158516>.
- (76) Murarka, S. P. Multilevel Interconnections for ULSI and GSI Era. *Mater. Sci. Eng. R Reports* **1997**, 19 (3–4), 87–151. [https://doi.org/10.1016/S0927-796X\(97\)00002-8](https://doi.org/10.1016/S0927-796X(97)00002-8).
- (77) Gannon, T. J.; Gu, G.; Casey, J. D.; Huynh, C.; Bassom, N.; Antoniou, N. Focused Ion Beam Induced Deposition of Low-Resistivity Copper Material. *J. Vac. Sci. Technol. B Microelectron. Nanom. Struct.* **2004**, 22 (6), 3000–3003. <https://doi.org/10.1116/1.1826065>.
- (78) Höflich, K.; Becker, M.; Leuchs, G.; Christiansen, S. Plasmonic Dimer Antennas for Surface Enhanced Raman Scattering. *Nanotechnology* **2012**, 23 (18), 185303.

- (79) Haverkamp, C.; Höflich, K.; Jäckle, S.; Manzoni, A.; Christiansen, S. Plasmonic Gold Helices for the Visible Range Fabricated by Oxygen Plasma Purification of Electron Beam Induced Deposits. *Nanotechnology* **2017**, *28* (5), 055303. <https://doi.org/10.1088/1361-6528/28/5/055303>.
- (80) Woźniak, P.; De Leon, I.; Höflich, K.; Haverkamp, C.; Christiansen, S.; Leuchs, G.; Banzer, P. Chiroptical Response of a Single Plasmonic Nanohelix. *Opt. Express* **2018**, *26* (15), 19275. <https://doi.org/10.1364/oe.26.019275>.
- (81) Höflich, K.; Feichtner, T.; Hansjürgen, E.; Haverkamp, C.; Kollmann, H.; Lienau, C.; Silies, M. Resonant Behavior of a Single Plasmonic Helix. *Optica* **2019**, *6* (9), 1098. <https://doi.org/10.1364/optica.6.001098>.
- (82) Abargues, R.; Marqués-Hueso, J.; Canet-Ferrer, J.; Pedrueza, E.; Valdés, J. L.; Jiménez, E.; Martínez-Pastor, J. P. High-Resolution Electron-Beam Patternable Nanocomposite Containing Metal Nanoparticles for Plasmonics. *Nanotechnology* **2008**, *19* (35), 355308. <https://doi.org/10.1088/0957-4484/19/35/355308>.
- (83) Roy, P.; Lynch, R.; Schmuki, P. Electron Beam Induced In-Vacuo Ag Deposition on TiO<sub>2</sub> from Ionic Liquids. *Electrochem. commun.* **2009**, *11* (8), 1567–1570. <https://doi.org/https://doi.org/10.1016/j.elecom.2009.05.051>.
- (84) Halka, V.; Schmid, M. J.; Avrutskiy, V.; Ma, X.; Schuster, R. Electron-Beam-Induced Deposition of Metallic Microstructures from a Molten-Salt Film on Conductive and Nonconductive Substrates. *Angew. Chemie Int. Ed.* **2011**, *50* (20), 4692–4695. <https://doi.org/10.1002/anie.201006560>.
- (85) Ocola, L. E.; Joshi-Imre, A.; Kessel, C.; Chen, B.; Park, J.; Gosztola, D.; Divan, R. Growth Characterization of Electron-Beam-Induced Silver Deposition from Liquid Precursor. *J. Vac. Sci. Technol. B* **2012**, *30* (6), 06FF08. <https://doi.org/10.1116/1.4765629>.
- (86) Bresin, M.; Nehru, N.; Hastings, J. T. Focused Electron-Beam Induced Deposition of Plasmonic Nanostructures from Aqueous Solutions. *Proc. SPIE 8613, Adv. Fabr. Technol. Micro/Nano Opt. Photonics VI* **2013**, 861306.
- (87) Szłyk, E.; Piszczek, P.; Chaberski, M.; Goliński, A. Studies of Thermal Decomposition Process of Ag(I) Perfluorinated Carboxylates with Temperature Variable IR and MS. *Polyhedron* **2001**, *20* (22–23), 2853–2861. [https://doi.org/10.1016/S0277-5387\(01\)00898-1](https://doi.org/10.1016/S0277-5387(01)00898-1).
- (88) Szłyk, E.; Piszczek, P.; Grodzicki, A.; Chaberski, M.; Goliński, A.; Szatkowski, J.; Błaszczuk, T. CVD of AgI Complexes with Tertiary Phosphines and Perfluorinated Carboxylates—A New Class of Silver Precursors. *Chem. Vap. Depos.* **2001**, *7* (3), 111–116. [https://doi.org/10.1002/1521-3862\(200105\)7:3<111::AID-CVDE111>3.0.CO;2-V](https://doi.org/10.1002/1521-3862(200105)7:3<111::AID-CVDE111>3.0.CO;2-V).
- (89) Piszczek, P.; Szymańska, I. B.; Talik, E.; Heimann, J. Deposition of Thin Copper Layers Using Copper(II) Carboxylate Complexes with Tert-Butylamine as New CVD Precursors. *Chem. Vap. Depos.* **2013**, *19* (7–8–9), 251–259. <https://doi.org/10.1002/cvde.201207049>.
- (90) Hall, R. N.; Racette, J. H. Diffusion and Solubility of Copper in Extrinsic and Intrinsic Germanium, Silicon, and Gallium Arsenide. *J. Appl. Phys.* **1964**, *35* (2), 379–397. <https://doi.org/10.1063/1.1713322>.
- (91) Reimer, L. *Scanning Electron Microscopy*; Springer Berlin Heidelberg, 1998.

- (92) Martin, I.; Bertin, M.; Domaracka, A.; Azria, R.; Illenberger, E.; Lafosse, A. Chemistry Induced by Low-Energy Electrons in Condensed Multilayers of Pure Small Organic Acids. *Int. J. Mass Spectrom.* **2008**, *277* (1–3), 262–268. <https://doi.org/10.1016/J.IJMS.2008.06.003>.
- (93) Rückriem, K.; Grotheer, S.; Vieker, H.; Penner, P.; Beyer, A.; Götzhäuser, A.; Swiderek, P. Efficient Electron-Induced Removal of Oxalate Ions and Formation of Copper Nanoparticles from Copper(II) Oxalate Precursor Layers. *Beilstein J. Nanotechnol.* **2016**, *7* (1), 852–861. <https://doi.org/10.3762/bjnano.7.77>.
- (94) Ahlenhoff, K.; Preischl, C.; Swiderek, P.; Marbach, H. Electron Beam-Induced Surface Activation of Metal-Organic Framework HKUST-1: Unraveling the Underlying Chemistry. *J. Phys. Chem. C* **2018**, *122* (46), 26658–26670. <https://doi.org/10.1021/acs.jpcc.8b06226>.
- (95) Ahlenhoff, K.; Koch, S.; Emmrich, D.; Dalpke, R.; Götzhäuser, A.; Swiderek, P. Electron-Induced Chemistry of Surface-Grown Coordination Polymers with Different Linker Anions. *Phys. Chem. Chem. Phys.* **2019**, *21* (5), 2351–2364. <https://doi.org/10.1039/c8cp07028h>.
- (96) T P, R. K.; Björnsson, R.; Barth, S.; Ingólfsson, O. Formation and Decay of Negative Ion States up to 11 eV above the Ionization Energy of the Nanofabrication Precursor  $\text{HFeCo}_3(\text{CO})_{12}$ . *Chem. Sci.* **2017**, *8* (9), 5949–5952. <https://doi.org/10.1039/C7SC01927K>.
- (97) G. Pearson, R. Hard and Soft Acids and Bases. *J. Am. Chem. Soc.* **1963**, *85* (22), 3533–3539. <https://doi.org/10.1021/ja00905a001>.
- (98) Pearson, R. G. The HSAB Principle — More Quantitative Aspects. *Inorganica Chim. Acta* **1995**, *240* (1–2), 93–98. [https://doi.org/10.1016/0020-1693\(95\)04648-8](https://doi.org/10.1016/0020-1693(95)04648-8).
- (99) Deng, H.; Kebarle, P. Bond Energies of Copper Ion-Ligand L Complexes  $\text{CuL}_2^+$  Determined in the Gas Phase by Ion-Ligand Exchange Equilibria Measurements. *J. Am. Chem. Soc.* **1998**, *120* (12), 2925–2931. <https://doi.org/10.1021/ja973814x>.
- (100) Li, H.; Reeves, R. R. Copper Film Deposition by Hydrogen Atom Reactions with Copper Compounds. *MRS Proc.* **1990**, *203*. <https://doi.org/10.1557/PROC-203-341>.
- (101) Lecohier, B.; Philippoz, J. M.; Calpini, B.; Stumm, T.; Van Den Bergh, H. The Influence of Water Vapor on the Selective Low Pressure CVD of Copper. *J. Phys. IV Fr.* **1991**, *02* (C2), C2-279-C2-286.
- (102) Lecohier, B. Thesis: Etude et Developpement de Techniques de Deposition Selective Du Cuivre, Ecole Polytechnique Federale de Lausanne, Lausanne, CH, 1992, Vol. PhD.
- (103) Lecohier, B.; Calpini, B.; Philippoz, J.; Stumm, T. van den; Van den Bergh, H. Selective Low Pressure Chemical Vapor Deposition of Copper: Effect of Added Water Vapor in Hydrogen or Helium Carrier Gas. *Appl. Phys. Lett.* **1992**, *60* (25), 3114–3116.
- (104) Lecohier, B.; Calpini, B.; Philippoz, J.; Van den Bergh, H. Low-pressure Chemical Vapor Deposition of Copper: Dependence of the Selectivity on the Water Vapor Added to a Hydrogen or Helium Carrier Gas. *J. Appl. Phys.* **1992**, *72* (5), 2022–2026.
- (105) Lecohier, B.; Calpini, B.; Philippoz, J.; Van den Bergh, H.; Laub, D.; Buffat, P. A. Copper Film Growth by Chemical Vapor Deposition Electrical and Optical Measurements in Real Time, and Studies of Morphology. *J. Electrochem. Soc.* **1993**, *140* (3), 789–796.
- (106) Cohen, S. L.; Liehr, M.; Kasi, S. Mechanisms of Copper Chemical Vapor Deposition. *Appl.*



- Phys. Lett.* **1992**, 60 (1), 50–52. <https://doi.org/10.1063/1.107370>.
- (107) Cohen, S. L.; Liehr, M.; Kasi, S. Selectivity in Copper Chemical Vapor Deposition. *Appl. Phys. Lett.* **1992**, 60 (13), 1585–1587.
- (108) Utriainen, M.; Kröger-Laukkanen, M.; Johansson, L.-S.; Niinistö, L. Studies of Metallic Thin Film Growth in an Atomic Layer Epitaxy Reactor Using  $M(\text{acac})_2$  ( $M=\text{Ni, Cu, Pt}$ ) Precursors. *Appl. Surf. Sci.* **2000**, 157 (3), 151–158. [https://doi.org/10.1016/S0169-4332\(99\)00562-0](https://doi.org/10.1016/S0169-4332(99)00562-0).
- (109) Tripathi, T. S.; Karppinen, M. Efficient Process for Direct Atomic Layer Deposition of Metallic Cu Thin Films Based on an Organic Reductant. *Chem. Mater.* **2017**, 29 (3), 1230–1235. <https://doi.org/10.1021/acs.chemmater.6b04597>.
- (110) Temple, D.; Reisman, A. Chemical Vapor Deposition of Copper from Copper (II) Hexafluoroacetylacetonate. *J. Electrochem. Soc.* **1989**, 136 (11), 3525–3529.
- (111) Utke, I.; Luisier, A.; Hoffmann, P.; Laub, D.; Buffat, P. A. Focused-Electron-Beam-Induced Deposition of Freestanding Three-Dimensional Nanostructures of Pure Coalesced Copper Crystals. *Appl. Phys. Lett.* **2002**, 81 (17), 3245–3247. <https://doi.org/10.1063/1.1517180>.
- (112) Berger, L.; Madajski, K.; Szymańska, I. B.; Polyakov, M. N.; Jurczyk, J.; Guerra-Núñez, C.; Höflich, K.; Utke, I. Gas Assisted Silver Deposition with a Focused Electron Beam. *Beilstein J. Nanotechnol.* **2018**, 9, 224–232. <https://doi.org/10.3762/bjnano.9.24>.
- (113) Hubert-Pfalzgraf, L. G.; Guillon, H. Trends in Precursor Design for Conventional and Aerosol-Assisted CVD of High- $T_c$  Superconductors. *Appl. Organomet. Chem.* **1998**, 12 (3), 221–236. [https://doi.org/10.1002/\(SICI\)1099-0739\(199803\)12:3<221::AID-AOC693>3.0.CO;2-O](https://doi.org/10.1002/(SICI)1099-0739(199803)12:3<221::AID-AOC693>3.0.CO;2-O).
- (114) McElwee-White, L. Design of Precursors for the CVD of Inorganic Thin Films. *Dalt. Trans.* **2006**, No. 45, 5327–5333. <https://doi.org/10.1039/B611848H>.
- (115) Berger, L.; Jurczyk, J.; Madajski, K.; Edwards, T. E. J.; Szymańska, I.; Hoffmann, P.; Utke, I. High-Purity Copper Structures from a Perfluorinated Copper Carboxylate Using Focused Electron Beam Induced Deposition and Post-Purification. *ACS Appl. Electron. Mater.* **2020**, 2 (7), 1989–1996. <https://doi.org/10.1021/acsaelm.0c00282>.
- (116) Warneke, J.; Van Dorp, W. F.; Rudolf, P.; Stano, M.; Papp, P.; Matejčík, Š.; Borrmann, T.; Swiderek, P. Acetone and the Precursor Ligand Acetylacetonate: Distinctly Different Electron Beam Induced Decomposition? *Phys. Chem. Chem. Phys.* **2015**, 17 (2), 1204–1216. <https://doi.org/10.1039/c4cp04239e>.
- (117) Devi, A.; Goswami, J.; Lakshmi, R.; Shivashankar, S. A.; Chandrasekaran, S. A Novel Cu(II) Chemical Vapor Deposition Precursor: Synthesis, Characterization, and Chemical Vapor Deposition. *J. Mater. Res.* **1998**, 13 (3), 687–692. <https://doi.org/10.1557/JMR.1998.0086>.
- (118) Szymańska, I. B. Gaseous Phase Studies of New Copper(II) Carboxylate Complexes with Tert-Butylamine as Potential Precursors for Chemical Vapor Deposition (CVD). *Polyhedron* **2013**, 50 (1), 200–207. <https://doi.org/10.1016/J.POLY.2012.10.046>.
- (119) Porra, F.; Pohl, M.; Müller, J.; Barth, S.; Biegger, F.; Gspan, C.; Plank, H.; Huth, M. Direct Writing of CoFe Alloy Nanostructures by Focused Electron Beam Induced Deposition from a Heteronuclear Precursor. *Nanotechnology* **2015**, 26 (47), 475701.

- (120) Utke, I.; Götzhäuser, A. Small, Minimally Invasive, Direct: Electrons Induce Local Reactions of Adsorbed Functional Molecules on the Nanoscale. *Angew. Chemie Int. Ed.* **2010**, *49* (49), 9328–9330. <https://doi.org/10.1002/anie.201002677>.
- (121) Muthukumar, K.; Jeschke, H. O.; Valentí, R.; Begun, E.; Schwenk, J.; Porraati, F.; Huth, M. Spontaneous Dissociation of  $\text{Co}_2(\text{CO})_8$  and Autocatalytic Growth of Co on  $\text{SiO}_2$ : A Combined Experimental and Theoretical Investigation. *Beilstein J. Nanotechnol.* **2012**, *3* (1), 546–555. <https://doi.org/10.3762/bjnano.3.63>.
- (122) Vollnhals, F.; Drost, M.; Tu, F.; Carrasco, E.; Späth, A.; Fink, R. H.; Steinrück, H. P.; Marbach, H. Electron-Beam Induced Deposition and Autocatalytic Decomposition of  $\text{Co}(\text{CO})_3\text{NO}$ . *Beilstein J. Nanotechnol.* **2014**, *5* (1), 1175–1185. <https://doi.org/10.3762/bjnano.5.129>.
- (123) Frabboni, S.; Gazzadi, G. C.; Felisari, L.; Spessot, A. Fabrication by Electron Beam Induced Deposition and Transmission Electron Microscopic Characterization of Sub-10-nm Freestanding Pt Nanowires. *Appl. Phys. Lett.* **2006**, *88* (21), 213116. <https://doi.org/10.1063/1.2206996>.
- (124) Schwalb, C. H.; Grimm, C.; Baranowski, M.; Sachser, R.; Porraati, F.; Reith, H.; Das, P.; Müller, J.; Völklein, F.; Kaya, A.; Huth, M. A Tunable Strain Sensor Using Nanogranular Metals. *Sensors* **2010**, *10* (11), 9847–9856. <https://doi.org/10.3390/s101109847>.
- (125) Porraati, F.; Sachser, R.; Schwalb, C. H.; Frangakis, A. S.; Huth, M. Tuning the Electrical Conductivity of Pt-Containing Granular Metals by Postgrowth Electron Irradiation. *J. Appl. Phys.* **2011**, *109* (6), 63715. <https://doi.org/10.1063/1.3559773>.
- (126) Spencer, J. A.; Barclay, M.; Gallagher, M. J.; Winkler, R.; Unlu, I.; Wu, Y. C.; Plank, H.; McElwee-White, L.; Fairbrother, D. H. Comparing Postdeposition Reactions of Electrons and Radicals with Pt Nanostructures Created by Focused Electron Beam Induced Deposition. *Beilstein J. Nanotechnol.* **2017**, *8* (1), 2410–2424. <https://doi.org/10.3762/bjnano.8.240>.
- (127) Roberts, N. A.; Magel, G. A.; Hartfield, C. D.; Moore, T. M.; Fowlkes, J. D.; Rack, P. D. In Situ Laser Processing in a Scanning Electron Microscope. *J. Vac. Sci. Technol. A* **2012**, *30* (4), 41404. <https://doi.org/10.1116/1.4731254>.
- (128) Roberts, N. A.; Fowlkes, J. D.; Magel, G. A.; Rack, P. D. Enhanced Material Purity and Resolution via Synchronized Laser Assisted Electron Beam Induced Deposition of Platinum. *Nanoscale* **2013**, *5* (1), 408–415. <https://doi.org/10.1039/C2NR33014H>.
- (129) Stanford, M. G.; Lewis, B. B.; Noh, J. H.; Fowlkes, J. D.; Roberts, N. A.; Plank, H.; Rack, P. D. Purification of Nanoscale Electron-Beam-Induced Platinum Deposits via a Pulsed Laser-Induced Oxidation Reaction. *ACS Appl. Mater. Interfaces* **2014**, *6* (23), 21256–21263. <https://doi.org/10.1021/am506246z>.
- (130) Plank, H.; Noh, J. H.; Fowlkes, J. D.; Lester, K.; Lewis, B. B.; Rack, P. D. Electron-Beam-Assisted Oxygen Purification at Low Temperatures for Electron-Beam-Induced Pt Deposits: Towards Pure and High-Fidelity Nanostructures. *ACS Appl. Mater. Interfaces* **2014**, *6* (2), 1018–1024. <https://doi.org/10.1021/am4045458>.
- (131) Lewis, B. B.; Stanford, M. G.; Fowlkes, J. D.; Lester, K.; Plank, H.; Rack, P. D. Electron-Stimulated Purification of Platinum Nanostructures Grown via Focused Electron Beam Induced Deposition. *Beilstein J. Nanotechnol.* **2015**, *6*, 907–918. <https://doi.org/10.3762/bjnano.6.94>.

- (132) Geier, B.; Gspan, C.; Winkler, R.; Schmied, R.; D. Fowlkes, J.; Fitzek, H.; Rauch, S.; Rattenberger, J.; D. Rack, P.; Plank, H. Rapid and Highly Compact Purification for Focused Electron Beam Induced Deposits: A Low Temperature Approach Using Electron Stimulated H<sub>2</sub>O Reactions. *J. Phys. Chem. C* **2014**, *118* (25), 14009–14016. <https://doi.org/10.1021/jp503442b>.
- (133) Rohdenburg, M.; Boeckers, H.; Brewer, C. R.; McElwee-White, L.; Swiderek, P. Efficient NH<sub>3</sub>-Based Process to Remove Chlorine from Electron Beam Deposited Ruthenium Produced from ( $\eta^3$ -C<sub>3</sub>H<sub>5</sub>)Ru(CO)<sub>3</sub>Cl. *Sci. Rep.* **2020**, *10* (1), 10901. <https://doi.org/10.1038/s41598-020-67803-y>.
- (134) Langford, R. M.; Ozkaya, D.; Sheridan, J.; Chater, R. Effects of Water Vapour on Electron and Ion Beam Deposited Platinum. *Microsc. Microanal.* **2004**, *10* (S02), 1122–1123. <https://doi.org/DOI: 10.1017/S1431927604883417>.
- (135) Mehendale, S.; Mulders, J. J. L.; Trompenaars, P. H. F. A New Sequential EBID Process for the Creation of Pure Pt Structures from MeCpPtMe<sub>3</sub>. *Nanotechnology* **2013**, *24* (14), 145303. <https://doi.org/10.1088/0957-4484/24/14/145303>.
- (136) Shawrav, M. M.; Taus, P.; Wanzenboeck, H. D.; Schinnerl, M.; Stöger-Pollach, M.; Schwarz, S.; Steiger-Thirsfeld, A.; Bertagnolli, E. Highly Conductive and Pure Gold Nanostructures Grown by Electron Beam Induced Deposition. *Sci. Rep.* **2016**, *6*, 34003. <https://doi.org/10.1038/srep34003>  
<https://www.nature.com/articles/srep34003#supplementary-information>.
- (137) Botman, A.; Mulders, J. J. L.; Weemaes, R.; Mentink, S. Purification of Platinum and Gold Structures after Electron-Beam-Induced Deposition. *Nanotechnology* **2006**, *17* (15), 3779–3785. <https://doi.org/10.1088/0957-4484/17/15/028>.
- (138) Sachser, R.; Reizh, H.; Huzel, D.; Winhold, M.; Huth, M. Catalytic Purification of Directly Written Nanostructured Pt Microelectrodes. *ACS Appl. Mater. Interfaces* **2014**, *6* (18), 15868–15874. <https://doi.org/10.1021/am503407y>.
- (139) Wnuk, J. D.; Gorham, J. M.; Rosenberg, S. G.; Madey, T. E.; Hagen, C. W.; Fairbrother, D. H. Atomic Radical Abatement of Organic Impurities from Electron Beam Deposited Metallic Structures. *J. Vac. Sci. Technol. B* **2010**, *28* (3), 527–537. <https://doi.org/10.1116/1.3378142>.
- (140) Begun, E.; Dobrovolskiy, O. V.; Kompaniets, M.; Sachser, R.; Gspan, C.; Plank, H.; Huth, M. Post-Growth Purification of Co Nanostructures Prepared by Focused Electron Beam Induced Deposition. *Nanotechnology* **2015**, *26* (7). <https://doi.org/10.1088/0957-4484/26/7/075301>.
- (141) Botman, A.; Hesselberth, M.; Mulders, J. J. L. Improving the Conductivity of Platinum-Containing Nano-Structures Created by Electron-Beam-Induced Deposition. *Microelectron. Eng.* **2008**, *85* (5), 1139–1142. <https://doi.org/https://doi.org/10.1016/j.mee.2007.12.036>.
- (142) Langford, R. M.; Wang, T.-X.; Ozkaya, D. Reducing the Resistivity of Electron and Ion Beam Assisted Deposited Pt. *Microelectron. Eng.* **2007**, *84*, 784–788. <https://doi.org/10.1016/J.MEE.2007.01.055>.
- (143) Jurczyk, J.; Brewer, C. R.; Hawkins, O. M.; Polyakov, M. N.; Kapusta, C.; McElwee-White, L.; Utke, I. Focused Electron Beam-Induced Deposition and Post-Growth Purification Using

the Heteroleptic Ru Complex ( $\eta^3\text{-C}_3\text{H}_5$ )Ru(CO)<sub>3</sub>Br. *ACS Appl. Mater. Interfaces* **2019**, *11* (31), 28164–28171. <https://doi.org/10.1021/acsami.9b07634>.

- (144) Puydinger dos Santos, M. V; Szkudlarek, A.; Rydosz, A.; Guerra-Nuñez, C.; Béron, F.; Pirola, K. R.; Moshkalev, S.; Diniz, J. A.; Utke, I. Comparative Study of Post-Growth Annealing of Cu(hfac)<sub>2</sub>, Co<sub>2</sub>(CO)<sub>8</sub> and Me<sub>2</sub>Au(acac) Metal Precursors Deposited by FEBID. *Beilstein J. Nanotechnol.* **2018**, *9*, 91–101. <https://doi.org/doi:10.3762/bjnano.9.11>.
- (145) Chen, Y. Nanofabrication by Electron Beam Lithography and Its Applications: A Review. *Microelectron. Eng.* **2015**, *135*, 57–72. <https://doi.org/https://doi.org/10.1016/j.mee.2015.02.042>.
- (146) Zhao, D.; Han, A.; Qiu, M. Ice Lithography for 3D Nanofabrication. *Sci. Bull.* **2019**, *64* (12), 865–871. <https://doi.org/https://doi.org/10.1016/j.scib.2019.06.001>.
- (147) Han, A.; Kuan, A.; Golovchenko, J.; Branton, D. Nanopatterning on Nonplanar and Fragile Substrates with Ice Resists. *Nano Lett.* **2012**, *12* (2), 1018–1021. <https://doi.org/10.1021/nl204198w>.
- (148) Hong, Y.; Zhao, D.; Liu, D.; Ma, B.; Yao, G.; Li, Q.; Han, A.; Qiu, M. Three-Dimensional in Situ Electron-Beam Lithography Using Water Ice. *Nano Lett.* **2018**, *18* (8), 5036–5041. <https://doi.org/10.1021/acs.nanolett.8b01857>.
- (149) Bresin, M.; Thiel, B. L.; Toth, M.; Dunn, K. A. Focused Electron Beam-Induced Deposition at Cryogenic Temperatures. *J. Mater. Res.* **2011**, *26* (3), 357–364. <https://doi.org/10.1557/jmr.2010.59>.
- (150) Bresin, M.; Toth, M.; Dunn, K. A. Direct-Write 3D Nanolithography at Cryogenic Temperatures. *Nanotechnology* **2013**, *24* (3), 035301. <https://doi.org/10.1088/0957-4484/24/3/035301>.
- (151) Córdoba, R.; Orús, P.; Strohauser, S.; Torres, T. E.; De Teresa, J. M. Ultra-Fast Direct Growth of Metallic Micro- and Nano-Structures by Focused Ion Beam Irradiation. *Sci. Rep.* **2019**, *9* (1), 1–10. <https://doi.org/10.1038/s41598-019-50411-w>.
- (152) De Teresa, J. M.; Orús, P.; Córdoba, R.; Philipp, P. Comparison between Focused Electron/Ion Beam-Induced Deposition at Room Temperature and under Cryogenic Conditions. *Micromachines* **2019**, *10* (12). <https://doi.org/10.3390/mi10120799>.

# Curriculum Vitae

Luisa Berger

Weissensteinstrasse 104  
3007 Bern, Schweiz  
+41 78 864 05 71  
luisa.berger@gmx.de

## Work Experience

- since 11/2016    PhD Student  
Empa Thun, Switzerland  
Laboratory for Mechanics of Materials and Nanostructures
- 06/2017 –  
07/2017    Visiting PhD  
Comenius University Bratislava, Slovakia  
Department for Experimental Physics
- 01/2016 –  
07/2016    Student Research Assistant  
Friedrich-Alexander University Erlangen-Nürnberg, Germany  
Department of Physical Chemistry II
- 05/2012 –  
05/2015    Working Student  
Areva GmbH, Erlangen, Germany  
Health, Safety and Environment/Radiation Protection

## Education

- since 11/2016    PhD Studies, Material Science  
Empa Thun and EPFL Lausanne, Switzerland  
EDMX Material Science and Engineering  
"Electron Beam Induced Copper Deposition from Carboxylate Precursors  
and the Study of Underlying Growth Mechanisms"
- 08/2017    International Graduate Summer School for Science Journalism  
Concordia University, Montreal, Canada  
"Projected Futures: Experimental Science Journalism Studies"
- 10/2013 –  
09/2016    Master Studies, M.Sc. Chemistry  
Friedrich-Alexander University Erlangen-Nürnberg, Germany  
Thesis at the Department of Physical Chemistry II  
"FEBID on Surface Anchored Metal Organic Frameworks"
- 09/2014    Summer School on Physics and Chemistry of Nanomaterials  
"TS&PCnano-2014", 5<sup>th</sup> Russian-German Travelling Seminar 2014, Russia
- 10/2010 –  
09/2013    Bachelor Studies, B.Sc. Chemistry  
Friedrich-Alexander University Erlangen-Nürnberg, Germany  
Thesis at the Department of Physical Chemistry I

1998 – European Baccalaureate  
2010 European School Munich, Germany

### **Awards**

01/2020 SAOG Poster Prize: 2nd Place  
"High-Purity Cu and Ag Structures from Perfluorinated Carboxylates using Focused Electron Beam Induced Deposition"  
36<sup>th</sup> Annual SAOG Meeting, Fribourg, Switzerland

09/2017 Prize for Best Poster  
"Gas Assisted Silver Deposition with a Focused Electron Beam"  
4<sup>th</sup> Annual CELINA Meeting, Porto, Portugal

### **Conference Contributions**

07/2016 FEBIP 2016, Poster TU Vienna, Austria  
"Focused Electron Beam Induced Processing on Surface-Anchored Metal-Organic Frameworks"

07/2017 EUFN 2017, Oral Presentation TU Graz, Austria  
"Gas Assisted Silver Deposition via Focused Electron Beam"

09/2017 4<sup>th</sup> Annual CELINA Meeting, Poster Porto, Portugal  
"Gas Assisted Silver Deposition with a Focused Electron Beam"

11/2017 Empa PhD Symposium, Poster Empa Dübendorf, Switzerland  
"Gas Assisted Silver Deposition with a Focused Electron Beam"

03/2018 DPG Spring Meeting, Oral Presentation TU Berlin, Germany  
"Exploring new Copper Complexes for FEBID"

07/2018 FEBIP 2018, Oral Presentation Modena, Italy  
"Exploring new Copper Complexes for FEBID"

09/2018 B-MRS Meeting 2018, Oral Presentation Natal, Brazil  
"3D Printing by Focused Electron Beam Induced Deposition and Purification of Silver Nanostructures"

01/2020 36<sup>th</sup> Annual SAOG Meeting, Poster Fribourg, Switzerland  
"High-Purity Cu and Ag Structures from Perfluorinated Carboxylates using Focused Electron Beam Induced Deposition"

## Publications

Berger L., Madajska K., Szymanska I., Höflich K., Polyakov M.N., Jurczyk J., Guerra-Nuñez C., Utke I. "Gas assisted silver deposition with a focused electron beam", *Beilstein Journal of Nanotechnology* **2018**, 9, 224.

Höflich K., Jurczyk J., Madajska K., Götz M., Berger L., Guerra-Nuñez C., Haverkamp C., Szymanska I., Utke I. "Towards the third dimension in direct electron beam writing of silver", *Beilstein Journal of Nanotechnology* **2018**, 9, 842.

Drost M., Tu F., Berger L., Preischl C., Zhou W., Gliemann H., Wöll C., Marbach H. "Surface Anchored Metal-Organic Frameworks as Versatile Resists for Gas-Assisted E-Beam Lithography: Fabrication of Sub-10 Nanometer Structures", *ACS Nano* **2018**, 12, 3825.

Berger L., Jurczyk J., Madajska K., Edwards T.E.J., Szymańska I., Hoffmann P., Utke I. "High-Purity Copper Structures from a Perfluorinated Copper Carboxylate using Focused Electron Beam Induced Deposition and Post-Purification", *ACS Applied Electronic Materials* **2020**, 2, 1989.

Jurczyk J., Glessi C., Madajska K., Berger L., Nyrud J. I. K., Szymańska I., Kapusta C., Tilset M., Utke I. "Vacuum vs Ambient Pressure Inert Gas Thermogravimetry: A Study of Silver Carboxylates", *submitted to Journal of Thermal Analysis and Calorimetry*

Jurczyk J., Madajska K., Berger L., Brockhuis L., Edwards T., Höflich K., Kapusta C., Szymańska, I., Utke I. "Ligand size and chain length study of silver carboxylates in focused electron beam induced deposition", *submitted to Chemistry of Materials*